

Aluminum powder as recyclable energy carrier: Population balance modelling of oxide smoke formation

Dissertation

zur Erlangung des akademischen Grades

**Doktoringenieur
(Dr.-Ing.)**

von M. Sc. Jannis Finke

geb. am 09.10.1997 in Minden

genehmigt durch die Fakultät für Verfahrens- und Systemtechnik der Otto-von-Guericke-Universität Magdeburg

Gutachter:

Dr. Fabian Sewerin
Prof. Dr.-Ing. Andreas Kempf
apl. Prof. Dr.-Ing. habil. Gábor Janiga

Promotionskolloquium am 01.04.2025

Abstract

Against the background of our society's endeavour towards a sustainable energy economy, in the past decade, a variety of different technologies has emerged to tackle the challenge of global warming. While particular concepts have already been developed to maturity, metal powders have recently been hypothesized as recyclable and carbon-free energy carriers as part of an on-demand oxidation-reduction cycle, on the consumer side of which the metal powder is burned while releasing heat and condensed oxides as main reaction products.

This thesis focuses on aluminum which not only qualifies as a potential metal fuel due to its high energy density, availability and handling safety, but has also been investigated in detail for its reaction kinetics. At high temperatures, aluminum particles can be burned exothermally in oxidizing atmospheres in a similar way to carbon-based particulate fuels. The produced aluminum oxide is solid under ambient conditions and may form through two distinct chemical pathways. On the one hand, vaporized aluminum initiates homogeneous gas phase combustion, leading to the condensation of aluminum oxide into very fine smoke droplets. On the other hand, heterogeneous reactions at the particle surface cause a direct conversion of aluminum into aluminum oxide, rendering the fuel particle biphasic. At present, the formation of oxide smoke fines poses major challenges to the oxide recovery from dust flames and the closure of the metal fuel cycle. The smoke's size distribution influences natural deposition and emission mechanisms and, consequently, plays a decisive role in the design of gas-particle separation devices. With the objective of elucidating the oxide smoke dynamics and identifying operating conditions promoting the formation of larger smoke droplets, we propose a comprehensive modelling approach that permits a prediction of the smoke size distribution alongside gas and particle surface compositions.

Physically, on the spatially localized level, the oxide droplet size distribution is influenced by the ambient gas phase composition and shaped by the mutual competition of nucleation, condensational surface growth, evaporation/dissociation and coagulation. The heat release and dispersion temperature, on the other hand, are affected by chemical reactions, phase transition and radiation. In this thesis, the oxide smoke droplets are described in a Eulerian fashion by harnessing a population balance description that is informed by a complete set of droplet formation and interaction kinetics and allows for analyzing the interaction,

competition and mutual reinforcement of the relevant physical processes. In a first step, the population balance framework is applied in a perfectly stirred reactor and a partially stirred reactor. These simplified model formulations are representative of the dynamics in a single grid cell of a spatially inhomogeneous laminar reactive flow solver or a one-point, one-time probability density function description. As key novelty in this context, the partially stirred reactor model is extended to account for the presence of a reactive surface with small-scale variability in terms of surface composition. Detailed gas phase and heterogeneous surface kinetics, including NO_x formation, are taken into account.

In a next step, we present a fully Eulerian framework for modelling the combustion of a single spatially resolved aluminum particle. In order to describe the reacting gas-droplet dispersion, we combine the population balance equation governing the smoke size distribution with tailored balance laws for gas phase species as well as the dispersion mass, momentum and enthalpy, while the detailed kinetic framework is augmented by the transport parameters governing species differential diffusion, droplet diffusion and thermophoresis. The major novelties of our physical model lie with the prediction of the smoke size distribution at every location in the flow domain, the accommodation of size-sensitive kinetics and transport processes as well as the prediction of possible NO_x pollutants in a spatially resolved fashion. Based on a comparison of our model predictions with available experimental measurements, we calibrate the droplet formation kinetics and, finally, validate the model while attesting a very good agreement. Ultimately, the spatio-temporally resolved single particle model is instrumented to estimate the emissions of a burning aluminum particle over the course of its conversion. Here, a particular feature is the incorporation of a time-varying particle morphology, including an oxide lobe. Our predictions of the particle burning times and residue sizes for different initial particle diameters are found to agree well with available experimental data. In order to demonstrate the controllability of the combustion products' sizes, an analysis of the effect of a varying pressure on our predictions is performed for all three configurations.

Lastly, we present the fundamentals of a modelling framework for turbulent metal dust flames encountered in practically relevant metal dust burners. Within the scope of a partially stirred reactor, the model is shown to allow for the individual assessment of polydispersity and turbulence influencing the particle-laden flow.

Kurzzusammenfassung

Vor dem Hintergrund unserer gesellschaftlichen Bestrebung hin zu einer nachhaltigen Energiewirtschaft ist im letzten Jahrzehnt eine Vielzahl an unterschiedlichen Technologien aufgekommen, um die Herausforderung der Erderwärmung zu bewältigen. Während einzelne Konzepte bereits ausgereift sind, wurden Metallpulver kürzlich als wiederverwendbare und kohlenstofffreie Energieträger als Teil eines bedarfsgesteuerten Oxidations-Reduktions-Kreislaufs vorgeschlagen, auf dessen Verbraucherseite das Metallpulver verbrannt wird, wobei Wärme und kondensierte Oxide als primäre Reaktionsprodukte freigesetzt werden.

Im Mittelpunkt dieser Dissertation steht Aluminium, das sich nicht nur aufgrund seiner hohen Energiedichte, Verfügbarkeit und sicheren Handhabung als potenzieller metallischer Treibstoff eignet, sondern auch hinsichtlich seiner Reaktionskinetik im Detail untersucht wurde. Aluminiumpartikel können bei hohen Temperaturen in oxidierenden Umgebungen exotherm verbrannt werden, ähnlich zu kohlenstoffbasierten partikulären Treibstoffen. Das gebildete Aluminiumoxid ist bei Umgebungsbedingungen fest und kann über zwei unterschiedliche chemische Pfade gebildet werden. Einerseits initiiert verdampftes Aluminium eine homogene Gasphasenverbrennung, die zu einer Kondensation von Aluminiumoxid in sehr feine Rauchtröpfchen führt. Andererseits verursachen heterogene Reaktionen an der Partikeloberfläche eine direkte Umwandlung von Aluminium in Aluminiumoxid, wodurch das Treibstoffpartikel zweiphasig wird. Zurzeit stellt die Bildung von feinen Oxidrauchtröpfchen eine große Herausforderung für die Oxidrückgewinnung aus Staubflammen und die Schließung des Kreislaufs der metallischen Treibstoffe dar. Die Größenverteilung des Rauchs beeinflusst natürliche Ablagerungs- und Emissionsmechanismen und spielt folglich eine entscheidende Rolle in der Auslegung von Gas-Partikel-Trennapparaten. Mit der Zielsetzung die Oxidrauchdynamik zu beleuchten und Betriebsbedingungen zu identifizieren, die die Bildung größerer Rauchtröpfchen begünstigen, schlagen wir einen umfassenden Modellierungsansatz vor, der eine Vorhersage der Rauchgrößenverteilung zusammen mit der Gas- und Partikeloberflächenzusammensetzung erlaubt.

Physikalisch gesehen wird die Größenverteilung der Oxidtröpfchen räumlich lokalisiert durch die umgebende Gasphasenzusammensetzung beeinflusst und durch den gegensei-

tigen Wettbewerb von Nukleation, kondensationsbedingtem Oberflächenwachstum, Verdampfung/Dissoziation und Koagulation geformt. Die Wärmefreisetzung und Dispersions-temperatur werden hingegen durch chemische Reaktionen, Phasenübergänge und Strahlung bestimmt. In dieser Arbeit werden die Oxidrauchtröpfchen aus einer Eulerschen Sichtweise beschrieben, indem wir uns eine Populationsbilanzbeschreibung zu Nutze machen, die auf einer vollständigen Tröpfchenbildungs- und -interaktionskinetik basiert und eine Analyse der Interaktion, des Wettbewerbs und der gegenseitigen Verstärkung der relevanten physikalischen Prozesse ermöglicht. In einem ersten Schritt wird das Populationsbilanzrahmenwerk in einem perfekt gemischten Reaktor und einem imperfekt gemischten Reaktor angewendet. Diese vereinfachten Modellformulierungen sind repräsentativ für die Dynamik in einer einzelnen Gitterzelle eines Löserturbinen für räumlich inhomogene laminare reaktive Strömungen oder einer *one-point, one-time probability density function*-Beschreibung. Als entscheidende Neuheit in diesem Kontext wird das Modell des imperfekt gemischten Reaktors erweitert, um die Gegenwart einer reaktiven Oberfläche mit kleinskaliger Variabilität hinsichtlich der Oberflächenzusammensetzung zu berücksichtigen. Hierbei wird eine detaillierte Gasphasen- und heterogene Oberflächenkinetik, einschließlich NO_x -Bildung, verwendet.

In einem nächsten Schritt präsentieren wir ein vollständig Eulersches Rahmenwerk zur Modellierung der Verbrennung eines einzelnen räumlich aufgelösten Aluminiumpartikels. Um die reagierende Gas-Tröpfchen-Dispersion zu beschreiben, kombinieren wir die Populationsbilanzgleichung, die die Rauchgrößenverteilung bestimmt, mit angepassten Bilanzgesetzen für die Gasphasenspezies sowie Dispersionsmasse, -impuls und -enthalpie, während das detaillierte kinetische Rahmenwerk um räumliche Transportparameter, welche die differenzielle Diffusion von Spezies, Tröpfchendiffusion und -thermophorese bestimmen, ergänzt wird. Die wesentlichen Neuheiten unseres physikalischen Modells liegen in der Vorhersage der Rauchgrößenverteilung an jedem Punkt im Strömungsgebiet, der Berücksichtigung einer größsensensitiven Kinetik und größsensensitiver Transportprozesse sowie der Vorhersage möglicher NO_x -Schadstoffe in einer räumlich aufgelösten Art und Weise. Anhand eines Vergleichs unserer Modellvorhersagen mit verfügbaren experimentellen Messungen kalibrieren wir die Tröpfchenbildungskinetik und validieren letztlich das Modell, wobei wir eine sehr gute Übereinstimmung feststellen. Schließlich wird das räumlich-zeitlich aufgelöste Einzelpartikelmodell instrumentalisiert, um die Emissionen eines bren-

nenden Aluminiumpartikels im Verlauf seiner Umwandlung abzuschätzen. Dabei stellt die Einbeziehung einer zeitlich variierenden Partikelmorphologie, einschließlich einer Oxidkappe, eine konkrete Neuerung dar. Wir stellen fest, dass unsere Vorhersagen der Partikelbrennzeiten und Rückstandsgrößen für verschiedene initiale Partikeldurchmesser gut mit verfügbaren experimentellen Daten übereinstimmen. Um die Kontrollierbarkeit der Größe der Verbrennungsprodukte zu demonstrieren, führen wir eine Analyse der Auswirkung eines variierenden Drucks auf unsere Vorhersagen für alle drei Konfigurationen durch.

Abschließend präsentieren wir die Grundlagen eines Modellierungsrahmenwerks für turbulente Metallstaubflammen, wie sie in praktisch relevanten Metallstaubbrennern anzutreffen sind. Im Rahmen eines imperfekt gemischten Reaktors wird gezeigt, dass das Modell die individuelle Beurteilung von Polydispersität und Turbulenz, welche die partikelbeladene Strömung beeinflussen, ermöglicht.

Table of Contents

| | |
|--|-------------|
| Table of Contents | VII |
| List of Figures | XI |
| List of Tables | XVII |
| Nomenclature | XIX |
| 1 Introduction | 1 |
| 1.1 Metal fuel cycle | 1 |
| 1.2 Characteristics of aluminum combustion | 2 |
| 1.3 Objectives, literature review and scientific contributions | 5 |
| 2 The perfectly stirred reactor | 13 |
| 2.1 Chapter introduction | 13 |
| 2.2 Physical description of the interacting phases and thermochemistry . . . | 14 |
| 2.2.1 Gas phase chemistry | 15 |
| 2.2.2 Reactive surfaces and heterogeneous surface reactions | 17 |
| 2.2.3 Dispersed oxide droplets | 19 |
| 2.2.4 Dispersion characteristics | 20 |
| 2.3 Governing equations | 22 |
| 2.4 Kinetic framework | 24 |
| 2.4.1 Droplet formation and interaction kinetics | 25 |
| 2.4.2 Heat and mass exchange within the dispersion | 38 |
| 2.4.3 Heat and mass exchange between dispersion and reactive surface | 44 |
| 2.4.4 Thermal radiation | 46 |
| 2.4.5 Characteristic time scales of droplet formation and interaction . | 49 |
| 2.5 Numerical methods | 50 |

Table of Contents

| | | |
|----------|--|-----------|
| 2.6 | Aluminum combustion at atmospheric pressure | 51 |
| 2.6.1 | Gas phase chemistry without NO_x formation | 52 |
| 2.6.2 | Effect of nitrogen oxide formation | 55 |
| 2.7 | Aluminum combustion at elevated pressures | 58 |
| 2.7.1 | Extensions of the kinetic framework | 58 |
| 2.7.2 | Effect of varying operating pressures | 59 |
| 2.8 | Chapter conclusions | 61 |
| 3 | The partially stirred reactor | 63 |
| 3.1 | Chapter introduction | 63 |
| 3.2 | Governing equations | 64 |
| 3.2.1 | A partially stirred reactor model | 64 |
| 3.2.2 | A partially stirred reactor model including a reactive surface | 66 |
| 3.3 | Numerical methods | 68 |
| 3.4 | Aluminum combustion at atmospheric pressure | 68 |
| 3.5 | Aluminum combustion at elevated pressures | 72 |
| 3.6 | Chapter conclusions | 73 |
| 4 | A steadily burning aluminum particle | 75 |
| 4.1 | Chapter introduction | 75 |
| 4.2 | Gas phase, surface and droplet formation kinetics | 77 |
| 4.2.1 | Gas and surface chemistry | 78 |
| 4.2.2 | Droplet formation kinetics | 79 |
| 4.3 | Governing equations | 83 |
| 4.3.1 | Species transport and chemical reactions | 83 |
| 4.3.2 | Droplet transport and phase transition | 85 |
| 4.3.3 | Dispersion mass, momentum and enthalpy balances | 88 |
| 4.3.4 | Enthalpy balance inside the fuel particle | 91 |
| 4.4 | Flux-matching interface conditions | 93 |
| 4.4.1 | Species mass fluxes | 94 |
| 4.4.2 | Droplet mass fluxes | 95 |
| 4.4.3 | Enthalpy flux | 95 |
| 4.4.4 | Solution procedure | 96 |

| | | |
|----------|--|------------|
| 4.5 | Numerical methods | 98 |
| 4.5.1 | General aspects | 98 |
| 4.5.2 | Decoupling of droplet formation and gas phase chemistry | 100 |
| 4.5.3 | Performance of the transport fractional step | 103 |
| 4.6 | Combustion characteristics at atmospheric pressure | 106 |
| 4.6.1 | Aluminum particle combustion in an O ₂ /Ar mixture | 108 |
| 4.6.2 | Aluminum particle combustion in air | 121 |
| 4.7 | Combustion characteristics at elevated pressures | 127 |
| 4.8 | Chapter conclusions | 134 |
| 5 | Unsteady morphological changes of a burning aluminum particle | 137 |
| 5.1 | Chapter introduction | 137 |
| 5.2 | Fuel particle properties and morphology | 138 |
| 5.3 | Modifications and extensions of the single particle combustion model | 142 |
| 5.3.1 | Biphasic fuel particle | 142 |
| 5.3.2 | Flux-matching interface conditions | 143 |
| 5.4 | Numerical methods | 143 |
| 5.5 | Aluminum particle combustion including a varying particle morphology | 144 |
| 5.5.1 | Combustion process | 144 |
| 5.5.2 | Composition of emitted exhaust fumes | 148 |
| 5.5.3 | Burning times and residue sizes | 149 |
| 5.6 | Chapter conclusions | 150 |
| 6 | Developments towards a turbulent metal dust flame | 153 |
| 6.1 | Chapter introduction | 153 |
| 6.2 | Modelling framework | 155 |
| 6.2.1 | Eulerian Monte Carlo scheme | 156 |
| 6.2.2 | Treatment of polydispersity | 158 |
| 6.2.3 | Treatment of turbulence | 159 |
| 6.2.4 | Comparison of stochastic models | 161 |
| 6.3 | A partially stirred reactor for turbulent aluminum dust flames | 162 |
| 6.3.1 | Governing equations | 162 |
| 6.3.2 | Analysis of the interaction between polydispersity and turbulence | 167 |

Table of Contents

| | |
|--|------------|
| 6.4 Chapter conclusions | 168 |
| 7 Conclusions | 171 |
| 7.1 Summary | 171 |
| 7.2 Outlook | 176 |
| Bibliography | 179 |
| Appendix A Droplet formation kinetics | 205 |
| A.1 Changes in the chemical potential during gas-to-liquid phase transitions | 205 |
| A.2 Theory of enhancement factors for particle collisions | 207 |
| A.3 Overview of physical assumptions | 211 |
| Appendix B Monte Carlo method for a PaSR featuring a reactive surface | 213 |
| Appendix C Derivation of the dispersion balance laws | 215 |
| C.1 Mass | 216 |
| C.2 Momentum | 217 |
| C.3 Enthalpy | 219 |
| Appendix D Newton method for solving the triple point angle equation | 221 |

List of Figures

| | | |
|------|--|----|
| 1.1 | Schematic illustration of the metal fuel cycle | 2 |
| 1.2 | Schematic of aluminum particle combustion mechanisms | 4 |
| 1.3 | Schematic of an aluminum-fuelled large-scale burner including the transition to the metal dust and single particle level | 7 |
| 1.4 | Schematic illustration of the investigated reactors | 9 |
| 2.1 | Schematic illustration of the link between a perfectly stirred reactor and a spatially resolved single particle | 14 |
| 2.2 | Schematic overview of the interacting phases and their kinetic interdependencies | 15 |
| 2.3 | Illustration of the gas-surface interface and the atomic site convention | 18 |
| 2.4 | Schematic overview of the kinetic variables determining the condensation of polysized $\text{Al}_2\text{O}_3(l)$ droplets and their interrelations | 25 |
| 2.5 | Comparison of the equilibrium vapour pressure of gaseous Al_2O_3 | 28 |
| 2.6 | Illustration of the Kelvin effect | 28 |
| 2.7 | Change in Gibbs free energy as a function of cluster size | 31 |
| 2.8 | Comparison of the standard chemical potentials | 33 |
| 2.9 | Schematic illustration of the species-bound enthalpy fluxes and the conductive heat fluxes leaving the reactive surface | 45 |
| 2.10 | Temperature dependency of the Planck mean absorption coefficient | 48 |
| 2.11 | Temporal change in the chemical gas phase composition and the surface composition in a PSR without NO_x chemistry | 53 |
| 2.12 | Time evolution of supersaturation and temperature in a PSR without NO_x chemistry | 53 |
| 2.13 | Temporal change of the $\text{Al}_2\text{O}_3(l)$ droplet size distribution in a PSR without NO_x chemistry | 54 |

List of Figures

| | | |
|------|---|-----|
| 2.14 | Temporal evolution of the characteristic time scales, the critical nuclei size and the mean droplet diameter in a PSR without NO _x chemistry | 55 |
| 2.15 | Temporal change in the chemical composition of the gas phase and the surface composition in a PSR with NO _x chemistry | 56 |
| 2.16 | Time evolution of the supersaturation, temperature and droplet size distribution in a PSR with NO _x chemistry | 57 |
| 2.17 | Temporal evolution of the characteristic time scales, the critical nuclei size and the mean droplet diameter in a PSR with NO _x chemistry | 58 |
| 2.18 | Oxide smoke droplet size distributions and time evolution of the mean droplet diameter in a PSR for different operating pressures | 60 |
| 2.19 | Time evolution of temperature and evaporated Al(B) mass in a PSR for different reactor pressures | 61 |
| 3.1 | Schematic illustration of the micro-scale heterogeneity in a partially stirred reactor | 65 |
| 3.2 | Influence of micro-mixing intensity on the mean dispersion temperature and the mean mole fraction of NO in a PaSR with NO _x chemistry | 69 |
| 3.3 | Influence of micro-mixing intensity on the mean smoke size distribution | 70 |
| 3.4 | Mean droplet diameter and the mean share of Al ₂ O ₃ (B) on the reactive surface for different time scale ratios in a PaSR | 71 |
| 3.5 | Change in temperature and mean droplet diameter with pressure and mixing intensity | 72 |
| 4.1 | Illustration of the interacting phases involved in the combustion of an aluminum particle | 78 |
| 4.2 | Temperature dependency of the thermal conductivity of aluminum | 93 |
| 4.3 | Illustration of the particle-dispersion interface | 94 |
| 4.4 | Schematic illustration of the cell blocking scheme | 100 |
| 4.5 | Time evolution of temperature and Al ₂ O ₃ (l) concentration in a PSR at atmospheric pressure obtained with different combinations of nucleation kinetics and coupling strategies | 102 |

| | | |
|------|--|-----|
| 4.6 | Grid convergence study in droplet size space based on the time evolutions of temperature, droplet volume fraction and total droplet number density in a PSR | 109 |
| 4.7 | Grid convergence study in droplet size space based on the droplet size distribution in a PSR | 109 |
| 4.8 | Geometry and inflow boundary conditions for the flow of an O ₂ /Ar gas mixture around a spherical burning aluminum particle | 113 |
| 4.9 | Comparison of the radial AlO, Al ₂ O ₃ (l) and temperature profiles for the Al-O ₂ /Ar case obtained from CFD predictions with experiments | 114 |
| 4.10 | Comparison of the radial AlO, Al ₂ O ₃ (l) and temperature profiles for the Al-O ₂ /Ar case obtained from CFD-PBE predictions with experiments | 115 |
| 4.11 | Spatial distributions of the droplet volume fraction and total droplet number density obtained from CFD-PBE calculations of the Al-O ₂ /Ar case | 116 |
| 4.12 | Comparison of the radial AlO, Al ₂ O ₃ (l) and temperature profiles obtained from CFD-PBE calculations of the Al-O ₂ /Ar case for three different nucleation rates with experiments | 117 |
| 4.13 | Comparison of the radial oxide smoke size distribution and the mean droplet diameter obtained from CFD-PBE calculations using the RKK nucleation rate with and without coagulation in the Al-O ₂ /Ar case | 118 |
| 4.14 | Comparison of the line-of-sight integrated Al ₂ O ₃ (l) profiles obtained from CFD-PBE calculations of the Al-O ₂ /Ar case using the RKK nucleation rate with experiments | 121 |
| 4.15 | Contour plots for a spatially resolved Al-particle steadily burning in air | 122 |
| 4.16 | Contour plots of the droplet volume fraction and the total droplet number density as well as their rates-of-change due to droplet formation in air. | 123 |
| 4.17 | Radial scatter plot of the heat release rates in air | 124 |
| 4.18 | Comparison of the radial AlO, Al ₂ O ₃ (l) and temperature profiles obtained from CFD-PBE predictions using the RKK nucleation rate without coagulation in air with experiments | 125 |
| 4.19 | Radial droplet size distribution and profiles of the mean droplet diameter as well as the characteristic time scales of nucleation and growth in air | 126 |

List of Figures

| | | |
|------|---|-----|
| 4.20 | Contour plots for a spatially resolved Al-particle steadily burning in air at $p = 5$ bar | 129 |
| 4.21 | Contour plots for a spatially resolved Al-particle steadily burning in air at $p = 10$ bar | 129 |
| 4.22 | Contour plots of the droplet volume fraction and the total droplet number density in air at elevated pressures | 131 |
| 4.23 | Radial droplet size distribution and profiles of the mean droplet diameter in air at elevated pressures | 131 |
| 4.24 | Contour plots of the droplet volume fraction and the total droplet number density in air at elevated pressures including coagulation | 132 |
| 4.25 | Radial droplet size distribution and profiles of the mean droplet diameter in air at elevated pressures including coagulation | 132 |
| 4.26 | Radial profiles of the characteristic time scales of nucleation, growth and coagulation in air at elevated pressures | 133 |
| 4.27 | Droplet size distribution and profiles of the mean droplet diameter along the outflow in air at elevated pressures including coagulation | 134 |
| 5.1 | Geometrical description of the cap-body morphology | 139 |
| 5.2 | Schematic of the law of cosines applied to the cap-body morphology | 140 |
| 5.3 | Schematic of the physical pathway to the particle geometry | 142 |
| 5.4 | Spatial distributions of the temperature and advective droplet velocity as well as the droplets' volume fraction and total number density | 145 |
| 5.5 | Change in time of the particle's Al- and Al_2O_3 -masses and the mean body and cap temperatures as well as the smoke deposition rates | 146 |
| 5.6 | Spatial smoke distribution | 147 |
| 5.7 | Radial profiles of the total droplet number density and the droplet volume fraction | 148 |
| 5.8 | Temporal change in the cumulative smoke size distribution emitted across the outflow boundary | 149 |
| 5.9 | Bar plots of the oxide smoke and NO_x emissions for different initial particle diameters | 149 |

| | | |
|------|---|-----|
| 5.10 | Comparison of the predicted particle burning time and residue diameter with experimental measurements and correlations for different initial particle diameters | 150 |
| 6.1 | Illustration of the particle property distribution represented in terms of the particle phase scalars | 157 |
| 6.2 | Illustration of the top-level fluctuation in the initial property distribution due to turbulence | 160 |
| 6.3 | Time evolutions of the particle property distribution obtained with the PBE-PDF approach and a Lagrangian stochastic model | 162 |
| 6.4 | Phenomenological illustration of the diffusive particle exchange between different realizations in a PaSR for dust flames | 165 |
| 6.5 | Time evolution of ensemble statistics of particle temperature and oxide fraction in a PaSR for aluminum dust flames | 168 |
| A.1 | Upper and lower limits of the London–van der Waals potentials for the non-retarded and retarded cases | 209 |
| A.2 | Enhancement factors for the coagulation of two $\text{Al}_2\text{O}_3(l)$ droplets in the kinetic and continuum regimes | 211 |
| B.1 | Monte Carlo method for solving the PaSR equation | 214 |
| C.1 | Material volume of a gas-droplet dispersion | 215 |
| D.1 | Residual of the non-linear equation governing the triple point angle | 221 |

List of Tables

| | | |
|-----|---|-----|
| 2.1 | Coefficients for the non-linear fits of the coagulation enhancement factors | 38 |
| 2.2 | Coefficients of the polynomial fit for the temperature dependency of the Planck mean absorption coefficient of $\text{Al}_2\text{O}_3(l)$ droplets | 49 |
| 4.1 | Coefficients of the polynomial fit for the temperature dependency of the thermal conductivity of Al | 92 |
| 4.2 | Spatial grid convergence analysis for an Al-particle steadily burning in an O_2/Ar mixture | 111 |
| 4.3 | Comparison of the average runtimes per time step for Al particle combustion in an O_2/Ar mixture | 112 |
| 4.4 | Maximum droplet volume fraction and total droplet number density along the radial coordinate for the CFD-PBE simulations in the Al- O_2/Ar case | 117 |

Nomenclature

Physical quantities

| | |
|--------------------------|---|
| α | Triple point angle |
| α_{mac} | Mass accommodation coefficient |
| α_{mix} | Exponential prefactor for micro-mixing |
| α_V | Volumetric coefficient of thermal expansion |
| $\alpha_{\text{mix},p}$ | Particle mixing parameter |
| \bar{c}_k | Mean thermal speed of molecules of species k |
| \bar{c}_{kl} | Relative mean thermal speed of molecules of species k and l |
| \bar{N} | Cumulative droplet number density |
| \bar{W}_k | Wiener process associated with k th sample |
| \bar{X}_k | Normalized mole fraction of species k |
| $\bar{X}_{\text{los},k}$ | Line-of-sight integrated normalized mole fraction of species k |
| $\bar{\sigma}$ | Concentration-weighted average collision diameter |
| \bar{r} | Inverse integral transformation for coagulation enhancement factors |
| \bar{x} | Integral transformation for coagulation enhancement factors |
| β | Droplet coagulation rate |
| β^{con} | Droplet coagulation rate in continuum regime |
| β^{kin} | Droplet coagulation rate in kinetic regime |

Nomenclature

| | |
|--------------------------------|---|
| \mathbf{C} | Parameters quantifying turbulent effects |
| \mathbf{c} | Sample space variable associated with \mathbf{C} |
| \mathbf{C}_I | Parameters quantifying turbulent effects of I th realization |
| χ_p | Sample space variable associated with particle oxide fraction |
| \mathcal{D}'_{12} | Relative Stokes–Einstein diffusion coefficient including viscous retardation |
| $\mathcal{D}_1, \mathcal{D}_2$ | Stokes–Einstein diffusion coefficients of two interacting droplets |
| \mathcal{D}_k | Diffusion coefficient of species k into the rest of the mixture |
| \mathcal{D}_l | Stokes–Einstein diffusion coefficient of droplets |
| \mathcal{D}_{12} | Relative Stokes–Einstein diffusion coefficient of two interacting droplets (or particles) |
| \mathcal{D}_{kl} | Binary diffusion coefficient of species k into l |
| \mathcal{D}_p | Stokes–Einstein diffusion coefficient of particles |
| $\Delta\eta$ | Proportionality factor for increment in droplet number density |
| $\Delta\mu$ | Difference in chemical potential between liquid and gas phase |
| $\Delta\mu^i$ | Difference between chemical potential of a bulk gas and liquid molecule of substance i |
| $\Delta\varepsilon_l$ | Instantaneous increment in droplet volume fraction |
| $\Delta\xi_l$ | Instantaneous increment in droplet surface density |
| ΔG | Change in Gibbs free energy due to cluster formation |
| ΔG_{bulk} | Bulk contribution to change in Gibbs free energy of formation |
| ΔG_{max} | Maximum energy barrier of droplet nucleation |
| ΔG_{surf} | Surface contribution to change in Gibbs free energy of formation |
| $\Delta h_{f,k}^0$ | Mass-specific enthalpy of formation of species k |

XX

| | |
|-------------------|---|
| ΔN | Instantaneous increment in droplet number density |
| Δn_0 | Fluctuation in critical molecule number |
| ΔT | Instantaneous temperature increment |
| ΔT_m | Temperature range for blending coefficient |
| ΔY_k | Instantaneous increment in mass fraction of species k |
| δ'_k | Stoichiometric coefficient of species k in phase transition reaction |
| δ_k | Mass share of species k in phase transition |
| \dot{s} | Surface reaction rates |
| \dot{s}_{BUS} | Surface reaction rates (bulk and surface species only) |
| \dot{g}_i | Rate-of-change of droplet phase scalar i |
| \dot{M}_0^C | Rate-of-change of zeroth moment of smoke size distribution due to coagulation |
| \dot{M}_0^N | Rate-of-change of zeroth moment of smoke size distribution due to nucleation |
| \dot{M}_1^G | Rate-of-change of first moment of smoke size distribution due to growth |
| \dot{m}_l^G | Rate-of-change of liquid phase mass due to growth |
| $\dot{m}_{p,l}$ | Droplet mass flow rate at fuel particle surface |
| \dot{q}_b | Heat flux into bulk |
| \dot{q}_d | Heat flux into dispersion |
| $\dot{q}_{rad,l}$ | Emissive power associated with droplet radiation |
| \dot{q}_{rad} | Emissive power |
| \dot{R} | Droplet nucleation rate |
| \dot{R}_{CNT} | Droplet nucleation rate of Classical Nucleation Theory |

Nomenclature

| | |
|---------------------------------|--|
| \dot{R}_{EA0} | Droplet nucleation rate with vanishing activation energy |
| \dot{R}_{ICCT} | Droplet nucleation rate of Internally Consistent Classical Theory |
| \dot{R}_{RKK} | Droplet nucleation rate of Reiss-Kegel-Katz nucleation theory |
| \dot{r}_k | Rate-of-change of primary variable k |
| $\dot{s}_{\mathcal{G}}$ | Cumulative production rate of gas species due to surface reactions |
| \dot{s}_{dep} | Kinetic droplet deposition rate |
| \dot{s}_k | Surface reaction rate of species k |
| \dot{s}_l | Droplet deposition mass flux |
| \dot{s}_N | Source term associated with localized droplet formation |
| \dot{s}_v | Droplet deposition rate |
| \dot{s}_{ε_l} | Rate-of-change of droplet volume fraction due to localized droplet formation |
| \dot{s}_{ξ_l} | Rate-of-change of droplet surface density due to localized droplet formation |
| $\dot{\mathbf{g}}$ | Rates-of-change of droplet phase scalars |
| $\dot{\omega}_{\text{rad},h_g}$ | Rate-of-change of gas phase enthalpy due to thermal radiation |
| $\dot{\omega}_{\text{rad},h}$ | Rate-of-change of dispersion enthalpy due to thermal radiation |
| $\dot{\omega}_{\text{rad},k}$ | Rate-of-change of gas phase scalar k due to thermal radiation |
| $\dot{\omega}_{g,k}$ | Rate-of-change of gas phase scalar k due to gas phase reactions |
| $\dot{\omega}_{gl,k}$ | Rate-of-change of gas phase scalar k due to gas-liquid phase transition |
| $\dot{\omega}_{s,k}$ | Rate-of-change of gas phase scalar k due to surface reactions |
| $\dot{\omega}_g$ | Rates-of-change of gas phase scalars due to gas phase chemistry |
| $\dot{\omega}_s$ | Rates-of-change of gas phase scalars due to surface chemistry |

| | |
|--------------------------|---|
| $\dot{\omega}_{gl}$ | Rates-of-change of gas phase scalars due to gas-liquid phase transition |
| $\dot{\mathbf{r}}_g$ | Rates-of-change of gas composition |
| $\dot{\epsilon}_l$ | Rate-of-change of droplet volume fraction |
| $\dot{m}''_{Al,s}$ | Surface-averaged mass flux of Al at fuel particle surface |
| \dot{M}_0 | Rate-of-change of total droplet number density |
| ϵ | Thermal particle emissivity |
| Γ | Surface site density |
| γ | Surface density of reactive surface |
| \mathbf{H} | Droplet phase scalars |
| \mathbf{h} | Sample space variable for droplet phase scalars |
| \mathbf{H}^{in} | Inflow droplet charge |
| $\mathbf{H}^{(i)}$ | Droplet charge of i th realization/fluid element |
| κ_P | Planck mean absorption coefficient |
| κ_T | Isothermal compressibility |
| $\kappa_{P,g}$ | Planck mean absorption coefficient of gas phase |
| $\kappa_{P,l}$ | Planck mean absorption coefficient of liquid phase |
| $\kappa_{P\lambda_w}$ | Spectral Planck mean absorption coefficient |
| \mathcal{K} | Jacobian of residual |
| λ | Thermal dispersion conductivity |
| λ_g | Thermal gas conductivity |
| λ_k | Thermal conductivity of species k |
| λ_l | Thermal droplet conductivity |
| λ_p | Thermal conductivity of fuel particle |

Nomenclature

| | |
|--|--|
| λ_w | Wave length |
| $\lambda_{\text{mfp},g}$ | Mean free path of gas mixture |
| $\lambda_{\text{mfp},k}$ | Specific mean free path of species k |
| λ_{mfp} | Mean free path of gas molecules |
| $\lambda_{g,s}$ | Thermal gas conductivity at fuel particle surface |
| $\lambda_{p,s}$ | Thermal conductivity of fuel particle at fuel particle surface |
| $\lambda_{w,\text{min}}, \lambda_{w,\text{max}}$ | Minimum/maximum wave length |
| $\langle d \rangle$ | Mean droplet diameter |
| \mathbf{L} | Linear momentum associated with dispersion inside control volume |
| \mathcal{M} | Micro-mixing operator |
| \mathcal{M}_g | Micro-mixing operator on part of gas composition |
| \mathcal{M}_p | Micro-mixing operator on part of dust particles |
| μ | Dynamic dispersion viscosity |
| μ^0 | Standard chemical potential |
| μ_l^i | Chemical potential of a bulk liquid molecule of substance i |
| μ_v^i | Chemical potential of a bulk gas molecule of substance i |
| μ^{pure} | Chemical potential of a pure substance |
| $\mu_l^{i,\text{pure}}$ | Chemical potential of a bulk liquid molecule of a pure substance i |
| $\mu_v^{i,\text{pure}}$ | Chemical potential of a bulk gas molecule of a pure substance i |
| μ_g | Laminar dynamic viscosity of gas |
| μ_k | Laminar dynamic viscosity of species k |
| μ_l^0 | Standard chemical potential of liquid phase |
| μ_l^{pure} | Chemical potential of pure liquid phase |

| | |
|---------------------------------|--|
| μ_n^0 | Standard chemical potential of a cluster with n molecules |
| μ_v^0 | Standard chemical potential of vapour phase |
| μ_v^{pure} | Chemical potential of pure vapour phase |
| \mathbf{n} | Outward-pointing surface unit normal vector |
| \mathbf{n}_s | Outward-pointing surface unit normal vector at fuel particle surface |
| $\mathbf{n}_{\mathbf{p}_p}$ | Outward-pointing surface unit normal vector in particle property space |
| \mathcal{N}_r | Index of refraction |
| ν | Proportionality constant to link instantaneous increments in droplet volume fraction and surface density |
| $\omega_{\delta \rightarrow 0}$ | Infinitesimal control volume in state space |
| ω_{δ} | Control volume in state space |
| $\Omega_{kk}^{(2,2)*}$ | Viscosity collision integral of species k |
| $\Omega_{kl}^{(1,1)*}$ | Diffusion collision integral of species k and l |
| $\partial\mathcal{V}$ | Surface of material/control volume |
| $\mathbf{P}_{p,k}^{\text{in}}$ | Particle property vector of k th sample drawn from inflow <i>pdf</i> |
| $\mathbf{P}_{p,k}^{(I)}$ | Particle property vector of k th sample in I th realization/fluid element |
| Φ^{Ha} | Hamaker potential |
| Φ^N | Non-retarded London–van der Waals potential |
| Φ^R | Retarded London–van der Waals potential |
| Φ_{LvdW} | London–van der Waals potential |
| ϕ_k | Sample space variable for gas phase scalar k |
| Φ_L^N | Lower limit of the non-retarded London–van der Waals potential |
| Φ_U^N | Upper limit of the non-retarded London–van der Waals potential |

Nomenclature

| | |
|--------------------------|---|
| Φ_{kl} | Kernel for dynamic viscosity |
| Φ | Gas phase scalars/composition |
| ϕ | Sample space variable for gas phase scalars |
| Φ^{in} | Inflow gas composition |
| $\Phi^{(i)}$ | Gas composition of i th realization/fluid element |
| ψ_k | Sample space variable for surface scalar k |
| Ψ | Surface scalars/composition |
| ψ | Sample space variable for surface scalars |
| $\Psi^{(i)}$ | Surface composition of i th surface element |
| \mathbf{q} | Conductive heat flux |
| \mathcal{R} | Residual |
| ρ | Dispersion density |
| ρ_1 | Density of fuel particle body |
| ρ_2 | Density of fuel particle cap |
| ρ_g | Gas density |
| ρ_k | Partial density of species k |
| ρ_l | Density of the liquid phase |
| ρ_N | Total particle number density |
| $\rho_N^{(I)}$ | Total particle number density in I th realization/fluid element |
| ρ_p | Fuel particle density |
| σ_l | Surface tension of liquid phase |
| $\sigma_{\text{int},12}$ | Surface tension associated with fuel particle cap-body interface |
| $\sigma_{\text{int},1}$ | Surface tension associated with fuel particle body-gas interface |

| | |
|-------------------------|---|
| $\sigma_{\text{int},2}$ | Surface tension associated with fuel particle cap-gas interface |
| σ_{kl} | Reduced collision diameter of molecules of species k and l |
| σ_k | Collision diameter of molecules of species k |
| τ | Characteristic time scale |
| τ_{adv} | Decorrelation time scale due to advective transport |
| τ_{mix} | Micro-mixing time scale |
| τ_{res} | Residence time scale |
| τ_C | Characteristic time scale of coagulation |
| τ_G | Characteristic time scale of growth |
| τ_N | Characteristic time scale of nucleation |
| τ_p | Sample space variable associated with particle temperature |
| τ_{int} | Particle interaction time scale |
| $\tau_{\text{mix},p}$ | Particle mixing time scale |
| $\boldsymbol{\tau}$ | Viscous stress tensor |
| \mathbf{t} | Cauchy traction |
| Bi | Biot number |
| Kn | Knudsen number |
| Re_p | Particle Reynolds number |
| St | Stokes number |
| θ_σ | Reduced surface tension |
| θ_k | Surface site fraction of species k |
| $\tilde{\sigma}_l$ | Change of droplet surface tension with temperature |
| \tilde{A}_p | Modified particle property advection rate |

Nomenclature

| | |
|--|--|
| \tilde{G} | Prefactor of droplet growth rate |
| \tilde{s}_1 | Entropy per molecule |
| \tilde{v}_1 | Volume per molecule |
| \tilde{x} | Transformed integration range for coagulation enhancement factors |
| \tilde{D} | Viscous correction factor for relative Stokes–Einstein diffusion coefficient |
| $\tilde{\delta}$ | Size of control volume in state space |
| \mathbf{u} | Bulk flow velocity |
| $\mathbf{u}_{d,l}^{\varepsilon_l}$ | Diffusion velocity associated with droplet volume fraction |
| $\mathbf{u}_{d,l}^{\xi_l}$ | Diffusion velocity associated with droplet surface density |
| \mathbf{u}_c | Correction velocity for Hirschfelder–Curtiss approximation |
| \mathbf{u}_k | Transport velocity of gas species k |
| \mathbf{u}_l | Droplet transport velocity |
| \mathbf{u}_s | Stefan flow velocity |
| \mathbf{u}_t | Thermophoretic velocity |
| $\mathbf{u}_{d,k}$ | Diffusion velocity of gas species k |
| $\mathbf{u}_{d,l}$ | Droplet diffusion velocity |
| $\mathbf{u}_{l,s}$ | Droplet transport velocity at fuel particle surface |
| $\mathbf{u}_{t,s}$ | Thermophoretic velocity at fuel particle surface |
| $\Upsilon_{\text{Al}_2\text{O}_3(\text{B})}$ | Share of condensed Al_2O_3 that is bound to the surface |
| ε_g | Gas volume fraction |
| ε_l | Droplet volume fraction |
| φ_1, φ_2 | Wetting angles |

| | |
|----------------------------|--|
| φ_{12} | Auxiliary wetting angle |
| \mathcal{V} | Material/control volume |
| \mathcal{W} | Coagulation enhancement factor |
| \mathcal{W}^{con} | Coagulation enhancement factor in continuum regime |
| \mathcal{W}^{kin} | Coagulation enhancement factor in kinetic regime |
| \mathbf{x} | Physical location vector |
| \mathbf{x}_i | Position of droplet i in physical space |
| ξ_{adv} | Uniformly distributed variable for decorrelation of surface and dispersion composition |
| ξ_{out} | Uniformly distributed variable for replacement of samples due to inflow/outflow |
| ξ_l | Droplet surface density |
| \mathbf{Y} | Species mass fractions |
| \mathbf{Y}_{in} | Species mass fractions in free-stream |
| \mathbf{y}_s | Independent surface variables |
| \mathbf{Y}_s | Species mass fractions at fuel particle surface |
| \mathbf{Z} | State vector of a fluid-surface element pair |
| \mathbf{z} | Sample space variable for fluid-surface element pair composition |
| $\mathbf{Z}^{(i)}$ | State vector of i th realization/fluid-surface element pair |
| ζ_k | Number of reaction sites occupied by one molecule of surface species k |
| A | Surface area of reactive surface |
| a_{cor} | Correlation parameter for burning time |
| A_H | Hamaker constant |

Nomenclature

| | |
|---------------------|--|
| A_l | Surface area of droplets |
| A_p, \mathbf{A}_p | Particle property advection rate |
| B_k | Specific transmitted bulk mass of species k |
| C | Cunningham slip correction factor |
| C_{mix} | Micro-mixing constant |
| C_p | Mass-specific dispersion heat capacity |
| C_R | Material constant for retarded London–van der Waals potential |
| c_s | Speed of sound |
| $C_{p,g}$ | Mass-specific gas heat capacity |
| $C_{p,k}$ | Mass-specific heat capacity of species k |
| $C_{p,l}$ | Mass-specific droplet heat capacity |
| $C_{p,p}$ | Mass-specific heat capacity of fuel particle |
| d_0 | Nuclei diameter |
| d_1 | Diameter of a single $\text{Al}_2\text{O}_3(1)$ molecule |
| D_p | Fuel particle diameter |
| D_p | Particle property diffusion rate |
| D_r | Residue diameter |
| d_v | Lennard-Jones collision diameter of a vapour molecule |
| $d_{c,12}$ | Axial distance between fuel particle cap and body centers |
| $D_{p,0}$ | Initial fuel particle diameter |
| $dp'_{p,i}$ | Change in property space variable associated with i th sample at time t' |
| $E_{b\lambda_w}$ | Spectral blackbody emissive power |

| | |
|--|---|
| $f_{\Phi, \mathbf{H}}^{\text{in}}$ | Joint scalar <i>pdf</i> associated with inflow gas composition and droplet charge |
| $f_{\Phi, \{\mathbf{P}_{p,i}\}}^{\text{in}}$ | Joint scalar <i>pdf</i> associated with inflow gas composition and particle phase scalars |
| $f_{\mathbf{C}}$ | <i>pdf</i> associated with \mathbf{C} |
| F_{LvdW} | London–van der Waals force |
| $f_{\mathbf{Z}}$ | <i>pdf</i> associated with fluid-surface element pair composition |
| f_N | <i>pdf</i> associated with particle number density |
| f_N^{in} | Inflow particle property <i>pdf</i> |
| $f_{\Phi, \mathbf{H}}$ | Joint scalar/marginal <i>pdf</i> associated with gas composition and droplet charge |
| $f_{\Phi, \Psi, \mathbf{H}}$ | Joint scalar <i>pdf</i> associated with gas composition, surface composition and droplet charge |
| $f_{\Phi, \{\mathbf{P}_{p,i}\}}$ | Joint scalar <i>pdf</i> associated with gas composition and particle phase scalars |
| f_{Φ} | Marginal <i>pdf</i> associated with gas composition |
| f_{Ψ} | Marginal <i>pdf</i> associated with surface composition |
| $f_{\{P_{p,i}\} \{P'_{p,j}\}}$ | Transition <i>pdf</i> associated with particle phase scalars |
| $f_{\{P_{p,i}\}}$ | Master density associated with particle phase scalars |
| f_{N, n_s} | Discrete particle property <i>pdf</i> |
| G | Droplet growth rate |
| G^{con} | Droplet growth rate in continuum regime |
| G^{kin} | Droplet growth rate in kinetic regime |
| G_{μ} | Gibbs free energy |

Nomenclature

| | |
|-------------------------------|---|
| G_{μ}^0 | Standard Gibbs free energy |
| H | Dispersion enthalpy inside control volume |
| h | Mass-specific dispersion enthalpy |
| H^0 | Enthalpy at standard pressure |
| h_g | Mass-specific gas enthalpy |
| h_i | Sample space variable for droplet phase scalar i |
| h_k | Mass-specific enthalpy of species k |
| h_l | Mass-specific heat capacity of the liquid phase |
| k_f | Forward reaction rate |
| M | Dispersion mass inside control volume |
| m | Dispersion mass |
| m_1 | Mass of a single $\text{Al}_2\text{O}_3(\text{l})$ molecule |
| m_g | Gas phase mass |
| M_k | k th moment of droplet size distribution |
| m_k | Mass of species k |
| m_l | Liquid phase mass |
| M_p | Particle mass |
| m_p | Sample space variable associated with particle mass |
| $m_{p,\text{Al}_2\text{O}_3}$ | Balanced mass of fuel particle cap |
| $m_{p,\text{Al}}$ | Balanced mass of fuel particle body |
| N | Number density |
| n | Number of molecules |
| $N(\cdot)$ | Size/property distribution |

| | |
|------------|--|
| $N^{(I)}$ | Particle number density in I th realization/fluid element |
| n_0 | Critical number of molecules in a cluster |
| n_1, n_2 | Refractive and absorption indices |
| n_{adv} | Number of samples to switch surface composition due to advective decorrelation |
| n_{cor} | Correlation index for burning time |
| N_{in} | Free-stream droplet number density |
| n_{out} | Number of samples to be replaced with samples carrying the inflow composition |
| n_f | Number of realizations/fluid-surface element pairs to approximate the <i>pdf</i> |
| n_r | Number of realizations/fluid elements |
| N_s | Droplet number density at fuel particle surface |
| n_S | Number of gas species |
| n_s | Number of particle phase scalars/samples |
| n_{pp} | Number of particle properties |
| N_{n_s} | Discrete representation of particle number density |
| P | Mechanical pressure |
| p | Thermodynamic pressure |
| P'_p | Particle property at time t' |
| $P'_{p,i}$ | Particle property of i th sample at time t' |
| $p'_{p,i}$ | Property space variable associated with i th sample at time t' |
| p_e^{Rp} | Equilibrium vapour pressure over fuel particle surface |
| p_0 | Standard pressure |

Nomenclature

| | |
|-----------------------------|---|
| p_1 | Arbitrary pressure level |
| p_e | Equilibrium vapour pressure |
| p_e^r | Equilibrium vapour pressure over spherical interface with radius r |
| P_p, \mathbf{P}_p | Particle property (vector) |
| p_p, \mathbf{p}_p | Particle property space variable |
| p_v | Vapour pressure |
| $p_{Al,s}$ | Aluminum partial pressure at fuel particle surface |
| $p_{p,i}, \mathbf{p}_{p,i}$ | Property space variable associated with i th sample |
| $P_{p,k}, \mathbf{P}_{p,k}$ | Particle property (vector) of k th sample |
| Q | General observable |
| r | Droplet radius |
| r_0 | Critical nucleus radius |
| r_1, r_2 | Radii of two interacting droplets |
| r_{adv} | Auxiliary variable to compute number of samples to switch surface composition |
| r_{out} | Auxiliary variable to compute number of samples to be flushed out |
| R_p | Fuel particle radius |
| r_R | Retardation distance |
| $r_{int,12}$ | Radius associated with fuel particle cap-body interface |
| $r_{int,1}$ | Radius associated with fuel particle body-gas interface |
| $r_{int,2}$ | Radius associated with fuel particle cap-gas interface |
| $R_{p,0}$ | Initial fuel particle radius |
| S | Supersaturation |

| | |
|-------------------------------|--|
| S^0 | Entropy at standard pressure |
| s_1 | Surface area of a single $\text{Al}_2\text{O}_3(l)$ molecule |
| S_{\max} | Maximum admissible supersaturation |
| s_b | Blending coefficient |
| T | Temperature |
| t | Time parameter |
| t' | Point in time |
| T_0 | Reference/standard temperature |
| t_{end} | Simulation time |
| T_{in} | Free-stream temperature |
| T_{ref} | Reference background temperature |
| t_b | Burning time |
| T_p | Particle temperature |
| T_s | Temperature at fuel particle surface |
| $T_{b,\text{Al}_2\text{O}_3}$ | Boiling temperature of Al_2O_3 |
| $T_{b,\text{Al}}$ | Boiling temperature of Al |
| $T_{m,\text{Al}_2\text{O}_3}$ | Melting temperature of Al_2O_3 |
| $T_{m,\text{Al}}$ | Melting temperature of Al |
| $T_{p,0}$ | Initial fuel particle temperature |
| $T_{p,\text{Al}_2\text{O}_3}$ | Mean temperature of fuel particle cap |
| $T_{p,\text{Al}}$ | Mean temperature of fuel particle body |
| V | Reactor volume |
| v, w | Droplet volume/size |

Nomenclature

| | |
|--------------------------------|---|
| v_0 | Nuclei volume |
| V_1 | Geometric volume of fuel particle body |
| v_1 | Volume of a single $\text{Al}_2\text{O}_3(l)$ molecule |
| V_2 | Geometric volume of fuel particle cap |
| v_i | Volume of droplet i |
| v_r | Right boundary of droplet volume/size space |
| $V_{p,\text{Al}_2\text{O}_3}$ | Balanced volume of fuel particle cap |
| $V_{p,\text{Al}}$ | Balanced volume of fuel particle body |
| W | Mean molecular weight of gas phase |
| W_k | Molecular weight of species k |
| W_l | Molecular weight of liquid phase |
| W_s | Mean molecular weight of gas phase at fuel particle surface |
| X_{eff} | Effective oxidizer concentration |
| $x_{\text{TP}}, y_{\text{TP}}$ | Triple point coordinates |
| X_k | Mole fraction of gas species k |
| X_p | Particle oxide fraction |
| X_v | Mole fraction of vapour |
| $x_{c,12}$ | Axial location of center associated with fuel particle cap-body interface |
| $x_{c,1}$ | Axial location of fuel particle body center |
| $x_{c,2}$ | Axial location of fuel particle cap center |
| $X_{k,s}$ | Mole fraction of species k at fuel particle surface |
| Y_k | Mass fraction of species k |
| $Y_{k,s}$ | Mass fraction of species k at fuel particle surface |

Z_e Collision frequency of vapour molecules at equilibrium

Z_v Collision frequency of vapour molecules

Chemical symbols

$(\cdot)_n$ Species clusters with n molecules

(\cdot) Gaseous species or species in general

$(\cdot) (B)$ Bulk species

$(\cdot) (l)$ Liquid species

$(\cdot) (S)$ Surface species

$(\cdot) (s)$ Solid species

$[\cdot]$ Mass concentration

Al_2O_2 Dialuminum dioxide

Al_2O_3c c-isomer of Aluminum(III) oxide (aluminum oxide)

Al_2O_3/c Aluminum(III) oxide (aluminum oxide) in either of its isomeric forms

Al_2O_3 Aluminum(III) oxide (aluminum oxide)

Al_2O Aluminum(I) oxide (dialuminum monoxide)

AlN Aluminum nitride

AlO_2 Aluminum dioxide

AlO Aluminum(II) oxide (aluminum monoxide)

Al Aluminum

Ar Argon

CO_2 Carbon dioxide

H_2O Water

Nomenclature

| | |
|----------------------|---------------------------------------|
| N_2O | Nitrous oxide (dinitrogen (mon)oxide) |
| N_2 | Nitrogen |
| NO_2 | Nitrogen dioxide |
| NO_3 | Nitrate |
| NO | Nitric oxide (nitrogen (mon)oxide) |
| N | Atomic nitrogen |
| O_2 | Oxygen |
| O | Atomic oxygen |

Physical constants

| | |
|--|---------------------------|
| $\hbar_P = 1.054572 \times 10^{-34} \text{ Js}$ | Reduced Planck constant |
| $\sigma_{SB} = 5.670374 \times 10^{-8} \text{ W}/(\text{m}^2\text{K}^4)$ | Stefan–Boltzmann constant |
| $c = 299792458 \text{ m/s}$ | Speed of light in vacuum |
| $h_P = 6.626070 \times 10^{-34} \text{ J/Hz}$ | Planck constant |
| $k_B = 1.380649 \times 10^{-23} \text{ J/K}$ | Boltzmann constant |
| $N_A = 6.022141 \times 10^{23} \text{ 1/mol}$ | Avogadro constant |
| $R = 8.314463 \text{ J}/(\text{molK})$ | Universal gas constant |

Numerical quantities

| | |
|----------------------------|--------------------------|
| \mathcal{D} | Physical diffusivity |
| \mathcal{D}_{art} | Artificial diffusivity |
| Δt | Time step size |
| Δt_n | Size of n th time step |

| | |
|-------------------------|---|
| Δx | FV-cell width in one direction |
| Δx_{\min} | Minimum FV-cell width in one direction |
| $\ \mathbf{u}\ _{\max}$ | Maximum flow speed inside computational domain |
| Φ | General scalar quantity |
| Φ_d | Value of Φ at center of downwind cell |
| Φ_f | Cell face value of Φ |
| Φ_u | Value of Φ at center of upwind cell |
| Ψ_{TVD} | Flux limiter |
| $\Psi_{\text{TVD},k}$ | Flux limiter of species k |
| CFL | CFL number |
| CFL _L | CFL number associated with momentum transport |
| \tilde{r} | Radial distance |
| $\varepsilon_{l,\max}$ | Maximum droplet volume fraction inside computational domain |
| a_i | Fit coefficients |
| $M_{0,\max}$ | Maximum of total droplet number density inside computational domain |
| r | Radial coordinate |
| r_Φ | Ratio of two upwind gradients of Φ |
| T_{\max} | Maximum temperature inside computational domain |
| t_n | n th point in time |
| $T_{p,\text{avg}}$ | Average particle temperature |
| u | Flow velocity in one direction |
| u_{in} | Inflow velocity |
| u_c | Correction velocity in one direction |

Nomenclature

| | |
|------------------|----------------------|
| w_{int} | Interpolation weight |
| x | Axial coordinate |

Operators, functions & mathematical symbols

| | |
|-------------------------------------|---|
| $(\cdot) : (\cdot)$ | Tensor contraction |
| $(\cdot) \cup (\cdot)$ | Union of two sets |
| $(\cdot) \leftarrow (\cdot)$ | Replacement |
| $(\cdot) \otimes (\cdot)$ | Tensor product |
| $(\cdot)^T$ | Transposition |
| $(\cdot)^{-1}$ | Inversion |
| $\arccos(\cdot)$ | Inverse cosine |
| $\delta(\cdot)$ | Dirac's δ -distribution |
| $\dot{(\cdot)}$ | Time derivative |
| $\exp(\cdot)$ | Natural exponential function |
| $\hat{(\cdot)}$ | Functional dependency |
| I | Identity matrix |
| $\langle \cdot \rangle$ | Averaging operator |
| $\langle \cdot \rangle_{n_r}$ | Monte Carlo estimator for mean with respect to realizations |
| $\langle \cdot \rangle_{n_s}$ | Monte Carlo estimator for mean with respect to property samples |
| $\langle \cdot \rangle_{n_s}^{(I)}$ | Monte Carlo estimator for mean with respect to property samples in I th realization |
| $(\cdot) _{(\cdot)}$ | Evaluation |
| $ \cdot $ | Absolute value |

| | |
|--|---|
| $ \{\cdot\} $ | Cardinality of a set |
| $\lfloor \cdot \rfloor$ | Floor function |
| $\lim_{(\cdot) \rightarrow (\cdot)} (\cdot)$ | Limit of a function |
| $\ln(\cdot)$ | Natural logarithm function |
| $\ \cdot\ $ | Euclidean norm |
| $\max(\cdot)$ | Maximum of arguments |
| $\min(\cdot)$ | Minimum of arguments |
| $\nabla \cdot (\cdot)$ | Divergence |
| $\nabla(\cdot)$ | Gradient |
| $\mathcal{N}(\cdot; a, b)$ | Normal distribution with mean a and variance b |
| $\partial(\cdot)/\partial(\cdot)$ | Partial derivative |
| \sim | Associated with |
| $\sin(\cdot), \cos(\cdot)$ | Sine and cosine |
| $\text{std}_{n_r}(\cdot)$ | Monte Carlo estimator for standard deviation with respect to realizations |
| $\text{std}_{n_s}(\cdot)$ | Monte Carlo estimator for standard deviation with respect to property samples |
| $\text{vol}(\cdot)$ | Volume operator |
| $\{\cdot\}_{i=1}^n$ | Ensemble/set containing n elements |
| $d(\cdot)$ | Differential |
| $d(\cdot)/d(\cdot)$ | Derivative |
| $D(\cdot)/Dt$ | Material time derivative |
| $d^2(\cdot)/d(\cdot)^2$ | Second derivative |

Nomenclature

$f(\cdot|\cdot)$ Conditional *pdf*

Spaces & sets

\mathcal{A} Set of aluminum oxide isomers

\mathcal{B} Bulk species labels

\mathcal{G} Gas phase species labels

\mathbb{N} Natural numbers

$\Omega_{\mathbf{c}}$ Sample space associated with \mathbf{c}

$\Omega_{\mathbf{x}}$ Physical space/flow domain

Ω_v Droplet volume/size space

$\Omega_v \times \Omega_{\mathbf{x}}$ State space

$\Omega_{\mathbf{p}_p}, \Omega_{\mathbf{p}_p}$ Particle property space

$\partial\Omega_v$ Boundary of droplet volume/size space

$\partial\Omega_{\mathbf{p}_p}$ Boundary of particle property space

\mathcal{S} Surface species labels

Abbreviations

NO_x General term for nitrogen oxides

pdf Probability density function

CFD Computational fluid dynamics

CNT Classical nucleation theory

EA0 Non-activated nucleation theory

EMC Eulerian Monte Carlo

| | |
|------|---|
| FV | Finite volume |
| ICCT | Internally consistent classical theory |
| IEM | Interaction-by-exchange-with-the-mean (model) |
| ODE | Ordinary differential equation |
| PaSR | Partially stirred reactor |
| PBE | Population balance equation |
| PDF | Probability density function (approach) |
| PSR | Perfectly stirred reactor |
| RKK | Reiss-Kegel-Katz nucleation theory |
| SDE | Stochastic differential equation |
| TP | Triple point |
| TVD | Total variation diminishing |

Chapter 1

Introduction

As part of our society's endeavour to transition to a sustainable energy economy based on renewable energy sources, the storage, long-distance trade and demand-controlled release of energy turn into timely engineering challenges. Out of the candidate energy carriers and energetic materials that are presently investigated, metals are particularly advantageous as they are characterized by a large energy density which exceeds that of many hydrocarbon fuels and batteries and may be released at immense power densities upon direct combustion in air [12]. Contrary to hydrogen-based concepts, as powdered materials, metals can be safely stored, handled and traded by repurposing existing distribution infrastructure. Moreover, metallic energy carriers offer the potential for retrofitting of coal-fired power plants [36] omitting the necessity to establish new facilities. Currently, metals are deployed in many applications ranging from solid propellants [37] and batteries [102] to pyrotechnics [6] and chemical looping combustion [1, 2, 108]. In recent years, however, metal powders have been hypothesized as potential recyclable and carbon-free energy carriers suitable for long distance trade and long term storage that could aid our transition to a sustainable energy economy [12, 13, 109, 179].

1.1 Metal fuel cycle

Powders of micron-sized metal particles, so-called metal fuels, can be burned exothermally at high temperatures in oxidative atmospheres in a similar way to common fossil fuels, releasing chemically stored energy as heat. Contrary to hydrocarbons, however, upon combustion inside a metal fuel combustor, the metals are converted into oxide particles that are solid at ambient conditions. Since these main reaction products can, in principle, be

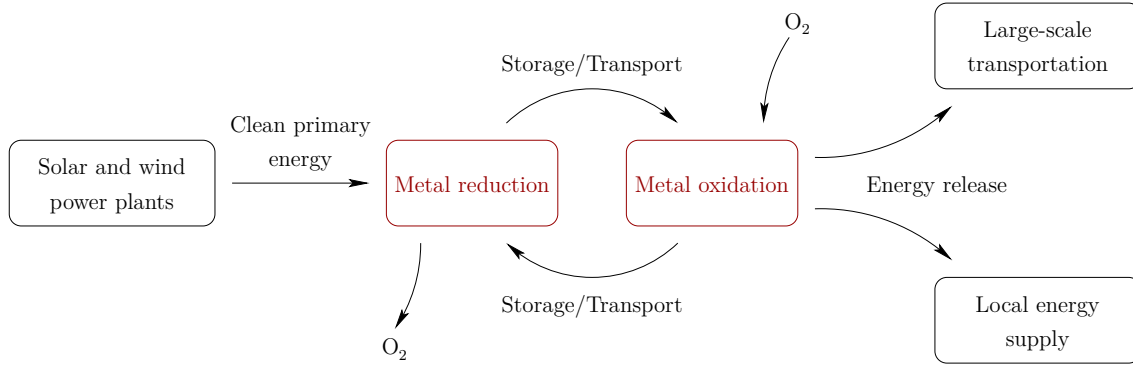


Figure 1.1 Schematic illustration of the metal fuel cycle following the delineation of Bergthorson et al. [13, Fig. 2].

separated from the exhaust fumes using existing gas-particle separation techniques, metals have recently been proposed as recyclable energy carriers. While the energy released during the combustion may drive the local energy supply (power plants) or large-scale transportation (*e.g.*, cargo ships), the ‘decharged’ oxide particles may subsequently be ‘recharged’ by reduction to pure metals with the aid of renewable energy sources [84], *e.g.*, solar and wind energy. This oxidation-reduction sequence has motivated the conceptualization of a redox-cycle [12, 13] (Fig. 1.1) in which metal powders play a similar role as high-temperature batteries. The metal fuel cycle thereby mitigates the temporal and spatial intermittency associated with green energy capture and the demand-controlled energy release. In other words, it separates, spatially and temporally, energy generation and consumption. For example, energy may be generated at solar power plants in a clean fashion during the summer, but is needed for heating in the winter, or countries that benefit from excellent geophysical and meteorological conditions produce the clean primary energy in excess, but it is needed in completely different parts of the world where the power generation is more difficult for particular reasons. Here, the concept of the metal fuel cycle comes into play to close the spatial and temporal gaps.

1.2 Characteristics of aluminum combustion

In this thesis, we specifically focus on the combustion of aluminum (Al) in air and the concomitant formation of aluminum oxide (Al_2O_3 , alumina). Aluminum, the most abundant metallic element in the Earth’s crust, is considered here not only because it has been hypothesized as a viable metal fuel [84, 179] due to its availability and suitable thermo-

dynamic properties, but also because the chemical and physical processes involved in its high-temperature oxidation [11] provide a blueprint for the combustion of other interesting metals such as magnesium or lithium [151], for instance. Additionally, our quantitative kinetic understanding of aluminum combustion in the gas phase and via heterogeneous surface reactions is very advanced [69, 143, 166] since aluminum particles have long been used as additives in solid rocket propellants [11, 65] or pyrotechnics [87, 129] and detailed kinetics for both gas phase and surface reactions have been developed [29, 68, 69, 175]. Particularly, the solid rocket propellant research conducted in the 1960s and 1970s has contributed a lot to the understanding of the fundamental combustion characteristics of aluminum [11, 22].

In an oxidizing atmosphere, the combustion of metal particles may occur via two, possibly complementary routes, each providing a distinct pathway for oxide formation. On the one hand, heterogeneous reactions can take place on the free surface of a solid or liquid metal particle that may result in the direct formation of condensed phase oxide, leading to a biphasic metal-oxide particle. In the metal fuel community, this path is referred to as combustion mode C and is thought to be dominant for metals whose flame temperature is below the boiling point [13], *e.g.*, iron. On burnout, the remnant oxide particle is called oxide residue; it is often of a similar size as the original metal fuel particle and possibly even larger. On the other hand, the liquid metal may vaporize, particularly near the boiling temperature, and incite homogeneous reactions in the gas phase to form a supersaturated vapour of volatile metal oxides or suboxides which serve as gaseous precursors for the condensation of nanometric smoke fines [11]. These oxide smoke droplets constitute a size-polydispersed aerosol that may either deposit, for example, on the fuel particles' surfaces or a reactor wall driven by diffusive, advective or thermophoretic transport phenomena, or leave the reactor with the exhaust fumes. This pathway is referred to as combustion mode A and is typically associated with aluminum combustion [13]. Although, technically, aluminum powders burn in mode A, the regeneration and migration of aluminum suboxides towards the fuel particles may lead to the heterogeneous oxidation of bulk aluminum.

Before we turn to the discussion of this work's objectives, we will have a closer look at the combustion of a single aluminum particle to provide a basic physical picture of the processes involved (Fig. 1.2). At ambient conditions, aluminum particles are typi-

1 Introduction

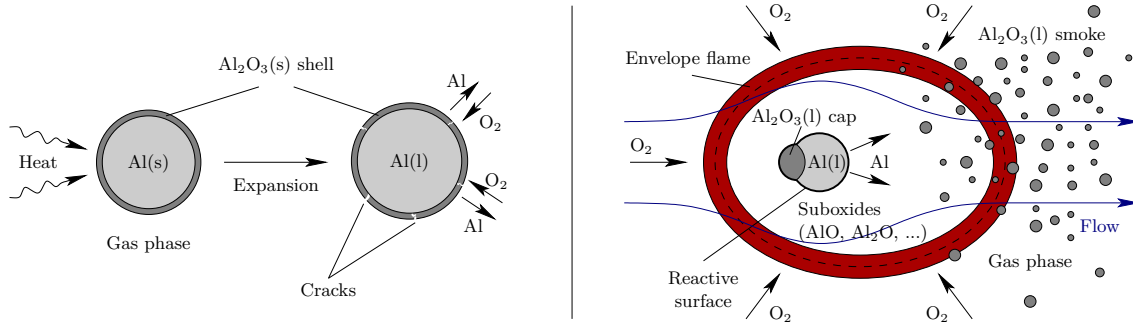


Figure 1.2 Schematic of the ignition process and the physical mechanisms involved in aluminum combustion following the delineation of Beckstead et al. [11, Fig. 1].

cally surrounded by a passivating solid oxide layer of a few nanometers thickness [24, 44, 190] that is formed upon the rapid surface oxidation of the pure Al(s) surfaces in oxygen-containing atmospheres and prevents further conversion of the bulk aluminum. As a particle is heated, either by thermal radiation from a laser beam or by thermal diffusion of heat provided by the combustion of other particles in an aluminum dust flame, the particle's core expands and, eventually, melts as soon as the particle temperature exceeds the melting point of aluminum, $T_{m,\text{Al}} = 933 \text{ K}$ [31, 172], while the oxide layer remains solid, $T_{m,\text{Al}_2\text{O}_3} = 2327 \text{ K} > T_{m,\text{Al}}$ [31]. At this point, the inner core exerts mechanical stresses on the outer shell which, upon evaporation of the bulk aluminum, cause the shell to fail and locally crack, exposing pure aluminum to the surrounding atmosphere. If the particle temperature, which is, however, typically limited by the aluminum boiling temperature $T_{b,\text{Al}} = 2791 \text{ K}$ [31] (at atmospheric pressure), is further increased, aluminum vaporizes through the cracks and fuels a reactive atmosphere surrounding the fuel particle. As soon as the melting temperature of the oxide layer is reached, the shell's fragments melt and recede into a protruding oxide cap to minimize the surface energy. In general, after a sufficiently long time period, only one oxide cap remains since internal flow structures, *e.g.*, Hill's vortex [60], cause the migration of oxide islands to a particular location. Since liquid aluminum and liquid alumina are immiscible, the cap-body configuration is maintained throughout the combustion process. Concomitantly, the volatile aluminum molecules initiate homogeneous gas phase combustion as they diffuse away from the particle's surface and are oxidized by the ambient oxidizer, spawning a micro-diffusion flame that surrounds the particle and is often referred to as envelope flame. Inside the envelope flame, a cascade of gas phase reactions involving several aluminum suboxides (AlO, Al₂O, Al₂O₂, AlO₂)

1.3 Objectives, literature review and scientific contributions

causes the formation of a supersaturated vapour phase from which nano-sized aluminum oxide smoke droplets precipitate. This condensation process in the vicinity of the micro-diffusion flame is thought to contribute a major part of the total heat released during aluminum combustion [167]. Contrary to fossil fuels, the maximum flame temperature is, however, limited due to an endothermic decomposition mechanism that causes the oxide smoke droplets to dissociate into suboxides as the temperature exceeds the Al_2O_3 boiling point ($T_{b,\text{Al}_2\text{O}_3} = 3763 \text{ K}$ for bulk Al_2O_3 at atmospheric pressure [135]).

Throughout this thesis, we reserve the term ‘droplet’ for the liquid oxide smoke fines, which, technically, may also be solid if the temperature becomes sufficiently small ($T < T_{m,\text{Al}_2\text{O}_3}$). By contrast, the possibly biphasic fuel particle is referred to as ‘particle’, although it is liquid during the combustion, to avoid confusion with the smoke droplets.

1.3 Objectives, literature review and scientific contributions

A critical challenge in the realization of the metal fuel cycle, especially based on aluminum, is the control of oxide smoke formation and the recovery of smoke droplets from the exhaust gases. While oxide smoke deposits may pollute the combustor and smoke emissions can cause health hazards, they also constitute oxide leakages that endanger the circular nature of a metal-based energy economy. Moreover, the efficient recovery of oxide smoke that remains suspended in the gas phase is immensely challenging and energy-intensive unless the smoke droplets acquire inertial sizes ($\text{St} \gg 1$). At the moment, the mere formation of smoke is considered to be detrimental to the idea of separating condensed phase metal oxides from the exhaust fumes of a combustor for green reduction and recycling. While micron-sized oxide particles may be retrieved from the exhaust gases in a very efficient manner using cyclones since these particles are inertial ($\text{St} \gg 1$) and do not longer follow the gas’ streamlines, smaller, *i.e.*, nano-sized, combustion products with small Stokes numbers ($\text{St} \ll 1$) may require the use of HEPA-type or electrostatic filters [13] to be separated from the gas stream. Consequently, the final combustion products’ sizes ultimately determine the efficacy of the whole circular process and, thus, the practicability of the metal fuel cycle based on aluminum. In order to allow for an informed assessment of possible extraction techniques and aid the design of metal combustors, we aim at predicting the size distribution of the oxide smoke, determining the fraction of smoke deposited

1 Introduction

on the fuel particle and elucidating the mechanisms that are conducive to oxide smoke deposition and droplet enlargement. A kinetically detailed and size-sensitive description of the oxide smoke is not only instrumental in informing the choices of smoke filters or gas-droplet separators by quantifying the energy penalty associated with smoke retrieval, but also enables us to identify physical mechanisms that enhance the droplets' sizes or explore operating strategies that promote droplet growth and coagulation. Furthermore, our focus on a detailed, size-resolved description of the oxide smoke is motivated by the fact that the droplets' sizes influence the diffusive and thermophoretic motion of the oxide smoke [60] and, thereby, affect any potential attraction of smoke by the fuel particles causing a redistribution of smoke mass to the residue particles. This mechanism is highly desired as the residue particle, which is typically inertial and, thus, extractable in an energetically efficient manner, acts as a smoke collector. In addition, recent investigations by Ruan et al. [142] emphasize the important role smoke migration plays in the ignition of polydispersed metal cloud flames. It is shown that spreading and deposition of hot nano-sized smoke droplets produced during the combustion of small Al-particles cause the ignition of larger fuel particles and, thus, directly influence the combustion behaviour. Concomitantly, it is our objective to predict the exhaust fume composition, including potential pollutants [98], that plays an important role in design considerations for a metal dust combustor. Due to the enormous energy release associated with aluminum combustion, we expect very high temperatures that are known to promote the formation of harmful nitrogen oxides (NO_x) that are either toxic or act as greenhouse gases [64].

While the performance of a large-scale metal dust combustor as depicted in Fig. 1.3 in terms of heat release, fuel conversion and pollutant emissions is tied to the collective behaviour of a dust cloud in an oxidizing atmosphere and its interaction with the reactor's walls, the chemical conversion mainly occurs on much smaller length scales, namely on the single particle level, either through heterogeneous surface reactions or gas phase combustion in the envelope flame. Therefore, this work mainly focuses on the combustion of single aluminum particles. Due to the high temperatures and the moderate particle sizes (micrometer range), the flow around a single burning aluminum particle is highly viscous and the particle Reynolds number is small ($\text{Re}_p \lesssim 10$) justifying the assumption of a laminar flow regime. However, in order to build a bridge to practically more meaningful configurations, we also provide first insights in the modelling of turbulent flames spawned

1.3 Objectives, literature review and scientific contributions

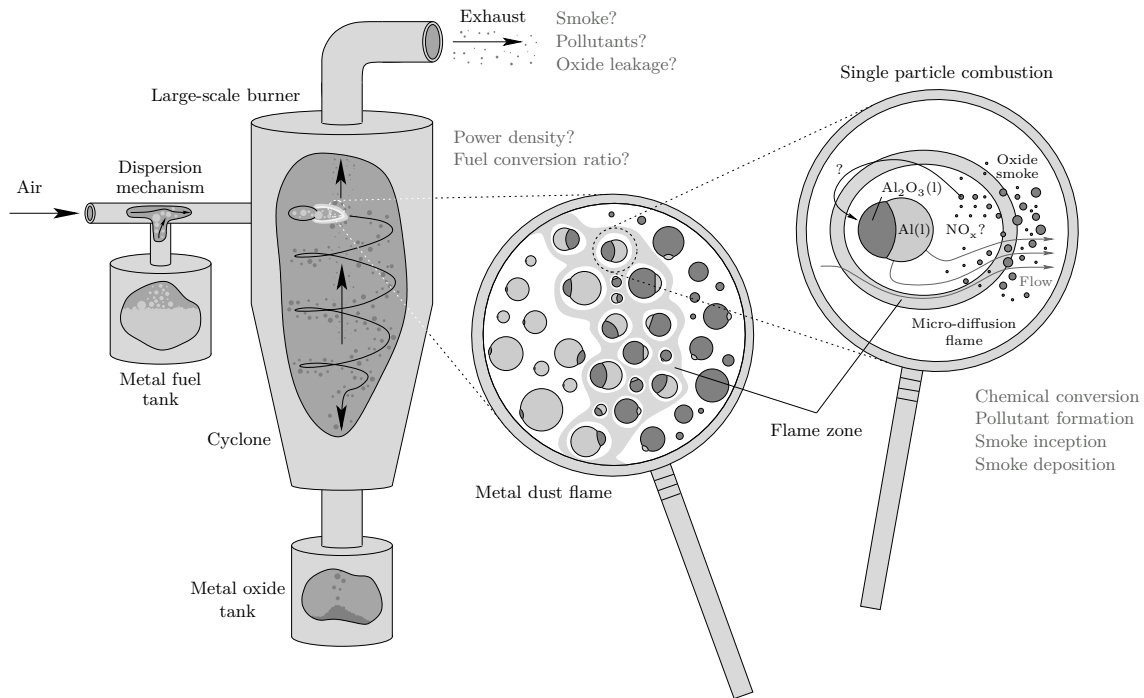


Figure 1.3 Schematic of an aluminum-fuelled large-scale burner adapted from Bergthorson et al. [13, Fig. 9] including the transition to the metal dust and single particle levels.

by aluminum dust clouds.

As a first step towards a comprehensive modelling framework that supports the design of metal dust reactors and oxide smoke separators, our objective is to develop a kinetically detailed description of a polysized oxide smoke cloud that interacts, chemically and thermally, with a carrier gas and a reactive surface. In this light, we focus here on the dynamics that drive the change in constitution and thermal state of the droplet-laden atmosphere around a burning aluminum particle, incorporating the interaction between size-polydispersed oxide smoke droplets, the carrier gas and a reactive aluminum (or biphasic aluminum/alumina) surface. Frequently, the oxide smoke that forms as a result of gas phase aluminum combustion is described in terms of a mass fraction whose value changes as liquid alumina condenses or dissociates. In spatially inhomogeneous configurations, for example, the reactive flow of an oxidizing gas about an aluminum particle, the mass fraction is then transported as a tracer [11, 19, 60, 69, 187]. Albeit conceptually compact and kinetically simple, the main disadvantage of this approach is that it does not permit the prediction of the oxide smoke size distribution or the incorporation of size-resolved droplet transport processes and droplet-droplet or droplet-gas interactions. To our awareness, the size-resolved description of oxide droplet dynamics was pioneered by Storozhev and Yer-

1 Introduction

makov [167, 169] who investigated the combustion of gaseous aluminum and aluminum nanoparticles in water vapour. Their description of a dispersed droplet phase is based on the mean size $r(\tau, t)$ of droplets nucleated at time $\tau < t$ as well as the number density $dN(\tau, t)$ at time t of droplets that were incepted during the time interval $[\tau, \tau + d\tau)$. This description may, in fact, be linked to a population balance equation (PBE) for the droplet size distribution $N(\cdot, t)$ with the aid of the method of size-characteristics. In a subsequent contribution, Storozhev and Yermakov [170] amended their submodel for condensational surface growth of oxide smoke droplets by heterogeneous reactions with aluminum sub-oxides. Focussing on an unsteady nucleation model, Starik et al. [166] showed how the formation of liquid nuclei from kinetically detailed $(\text{Al}_2\text{O}_3)_n$ cluster dynamics can be linked to a PBE for the $\text{Al}_2\text{O}_3(l)$ droplet mass distribution. Here, the PBE was solved with the aid of a reduction to the first two moments, the total droplet number density and the partial $\text{Al}_2\text{O}_3(l)$ density. In the present thesis, we complement and generalize these efforts by combining a population balance approach for the description of the oxide droplet size distribution with detailed species and enthalpy balances, accounting for droplet dissociation and radiation and incorporating a reactive surface through which the gas-droplet dispersion may interact with bulk aluminum (and possibly aluminum oxide). The kinetic rates that control droplet nucleation, growth and coagulation are evaluated based on low-level theories of phase transition and aerosol transport. Moreover, the kinetic framework is successively extended to accommodate the kinetics of spatial transport phenomena such as droplet diffusion and thermophoretic transport to permit the analysis of a spatially resolved aluminum particle combustion. In this regard, the PBE-based model formulation is augmented by spatial transport terms and embedded in a set of transport equations governing the gas species mass as well as the dispersion's mass, momentum and enthalpy that is complemented by flux-matching boundary conditions at the interface separating the fuel particle from the surrounding gas-droplet dispersion. Based on a mathematical description of the cap-body morphology [7, 60], the model is eventually enhanced by the capability of analyzing the effect of unsteady morphological changes on the combustion process and the exhaust composition.

The PBE-based framework developed here is applied within the scope of three different setups each of which is specifically designed to investigate particular aspects of the combustion process. First, the model is deployed in a perfectly stirred reactor (PSR) which

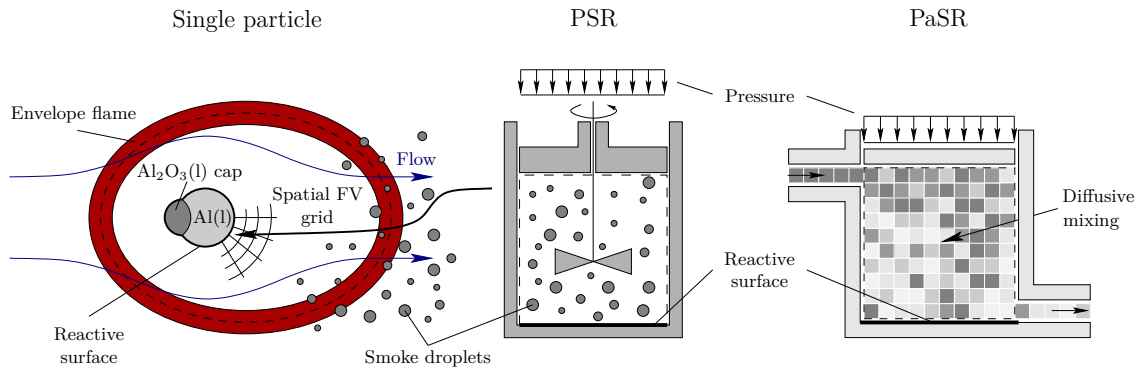


Figure 1.4 Schematic illustration of the investigated reactors. The PSR and PaSR are spatially homogeneous and representative of both the chemical and physical processes that take place in a spatial finite volume (FV) grid cell at the surface of a single particle immersed in a laminar or turbulent reactive flow, respectively.

serves as a test bed for the droplet formation kinetics and resembles a spatial grid cell at the reactive surface of a burning aluminum particle in a laminar reactive flow calculation. Second, as a preliminary and preparatory step towards modelling of turbulent droplet-laden flows, the governing balance laws and kinetics are additionally cast into the framework of a partially stirred reactor (PaSR). Lastly, the combustion of a spatially resolved single aluminum particle is investigated both in steady state disregarding the oxide cap and in an unsteady case including a temporally changing fuel particle morphology. As visual support, Fig. 1.4 depicts schematics of the three different reactor configurations investigated here and their logical link. Complementary to the single particle model, we also present the fundamentals of a PBE-based modelling framework for a turbulent aluminum dust flame in the form of an outlook towards the description of large-scale metal burners and show preliminary results.

The key scientific contributions of this thesis are summarized in the following:

- First, a complete set of spatially localized alumina condensation kinetics, including nucleation, growth, coagulation, dissociation as well as species scavenging and radiation, is presented that covers the entire droplet size range from the free molecular or kinetic regime up to the continuum regime and is based on first principles. In conjunction with detailed gas phase and surface reaction mechanisms, these kinetics drive the temporal changes in the droplet size distribution, the gas phase composition and the constitution of a reactive aluminum surface. A particular novelty is the calibration of coagulation enhancement factors accounting for droplet-droplet

1 Introduction

interactions based on low-level theories.

- Second, we provide a novel extension of the spatially homogeneous PaSR model to accommodate a reactive surface whose chemical composition features small-scale variability.
- Third, we show predictions of the alumina size distribution in a PSR and a PaSR, investigate the role of residence time and molecular mixing and analyze the competition and interaction of the different physical processes involved (nucleation, growth and coagulation). This not only provides a first indication of the droplet sizes that may be present in the oxide smoke near a burning Al-particle and the amenability to retrieval, but also constitutes an important step towards the prediction of heat release and pollutant (NO_x) formation in laminar and turbulent aluminum dust flames.
- Fourth, we present an extension of the kinetic framework by spatially inhomogeneous droplet transport phenomena that is also based on first principles and calibrate and validate our nucleation and coagulation kinetics based on a comparison with experimental data.
- Fifth, contrary to previous PBE-based descriptions of dispersed multiphase flows, we derive balance equations governing mass, momentum and enthalpy based on the notion of a gas-droplet dispersion assuming an instantaneous equilibration in terms of temperature and bulk velocity.
- Sixth, the spatially resolved single aluminum particle combustion model is enhanced by a time-varying biphasic particle morphology permitting the analysis of configurational changes in the envelope flame and their ramifications on smoke scavenging and pollutant emissions over the course of the particle conversion.
- Seventh, we investigate the influence of the operating pressure on the key quantities characterizing the combustion of aluminum in all three setups and provide predictions as to what extent it is possible to control the smoke size distribution by adjusting the pressure.
- Eighth, a preliminary modelling concept towards the description of turbulent metal dust flames is developed that is based on a probability density function (PDF) ap-

1.3 Objectives, literature review and scientific contributions

proach. The PBE-PDF framework is employed within the scope of aluminum dust combustion in a PaSR and allows for the individual assessment of two physically distinct sources of variability (turbulence and polydispersity) influencing particle-laden flows.

This thesis is structured as followed: In Chapter 2, we introduce the governing equations of a PSR, present the kinetic framework for the droplet formation and interaction kinetics and show our predictions of the smoke size distribution and chemical composition in a spatially homogeneous perfectly mixed reactor. Based on these developments, Chapter 3 is devoted to the discussion of the PaSR model including the extension to account for small-scale heterogeneity with respect to the surface composition alongside an investigation of the effect of the micro-mixing intensity on the smoke droplets' sizes and the chemical gas composition. Subsequently, in Chapter 4, the PBE-based model is extended to accommodate spatial transport phenomena and the governing transport equations for modelling the steady combustion of a spatially resolved aluminum particle are presented based upon which we obtain predictions of the smoke droplet size distribution and gas composition in the envelope flame spawned by the particle. In Chapter 5, the single particle combustion model is augmented by a time-varying cap-body morphology allowing for an unsteady analysis of the combustion process and permitting an estimation of the amount of smoke and pollutants cumulatively emitted over the course of a fuel particle's conversion. Before the thesis is concluded and an outlook is given in Chapter 7, we build a bridge from the single particle to the particle population level and provide insights into a PBE-PDF model formulation to describe turbulent metal dust flames and present tentative predictions of the interaction between polydispersity and turbulence in a PaSR.

Apart from several detailing extensions and modifications, the work reported in Chapters 2 to 5 has also recently been published in the following journal articles and conference proceedings/articles:

- J. Finke and F. Sewerin. “Combining a population balance approach with detailed chemistry to model the condensation of oxide smoke during aluminum combustion in spatially homogeneous reactors”. In: *Combustion and Flame* 248 (2023), p. 112510.
- J. Finke and F. Sewerin. “A combined PBE-CFD approach for modelling the formation and dispersion of oxide smoke in homogeneous aluminum combustors and

1 Introduction

around a burning aluminum particle”. In: *Proceedings of the 11th European Combustion Meeting (2023)*, pp. 1826–1831.

- J. Finke and F. Sewerin. “A population balance approach for predicting the size distribution of oxide smoke near a burning aluminum particle”. In: *Combustion and Flame* 265 (2024), p. 113464.
- J. Finke and F. Sewerin. “An unsteady PBE-CFD analysis of the asymmetric smoke-laden flame around a burning aluminum particle”. In: *Proceedings of the Combustion Institute* 40 (2024), p. 105564.

Moreover, this thesis extends upon preliminary developments and tentative investigations reported in the following unpublished student works:

- J. Finke. “Modelling of aluminum oxide formation using a population balance approach”. Student research project (2020), *Institute of Solid Mechanics/Institute of Mechanics and Adaptronics, Technical University Braunschweig*.
- J. Finke. “An integrative approach for investigating the precipitation of aluminum oxide near a burning aluminum particle”. Master’s thesis (2021), *Institute of Mechanics and Adaptronics, Technical University Braunschweig*.

Chapter 2

The perfectly stirred reactor

2.1 Chapter introduction

Although this work ultimately aims at the development of modelling tools that resolve the entire oxide smoke size distribution in the vicinity of an aluminum particle (see Chapters 4 and 5), it is imperative to consolidate and test the kinetic framework governing the rates of droplet formation before it is included in a reactive flow calculation. Spatially homogeneous reactor configurations constitute idealized test beds as they combine an adequate representation of the real combustion dynamics with a negligible computational effort and thus qualify to assess the kinetics. Figure 2.1 depicts a schematic of a single burning aluminum particle that is suspended in a uniform laminar flow. While the perfectly stirred reactor (PSR) discussed here involves assumptions on spatial homogeneity, it represents the chemical and physical processes that occur in a single FV cell at the particle surface during the reaction fractional step of a laminar flame calculation. The dashed lines in the left part of Fig. 2.1 delineate such a (surface) cell which we may idealize, in the laminar case and upon omission of spatial transport, as indicated on the right hand side. Thus, the PSR not only permits to test the kinetics but also allows for an investigation of the chemical interactions between the reactive particle surface, the surrounding gas and the dispersed oxide smoke droplets in the absence of spatial transport as preliminary stage to spatially resolved laminar flame calculations.

This chapter is structured as follows: After a brief summary of the main describing variables characterizing the reactive surface, the gas phase and the dispersed droplet phase in Section 2.2, the governing equations of a PSR are summarized in Section 2.3. This is followed by a detailed account of the oxide smoke condensation kinetics, the mass and

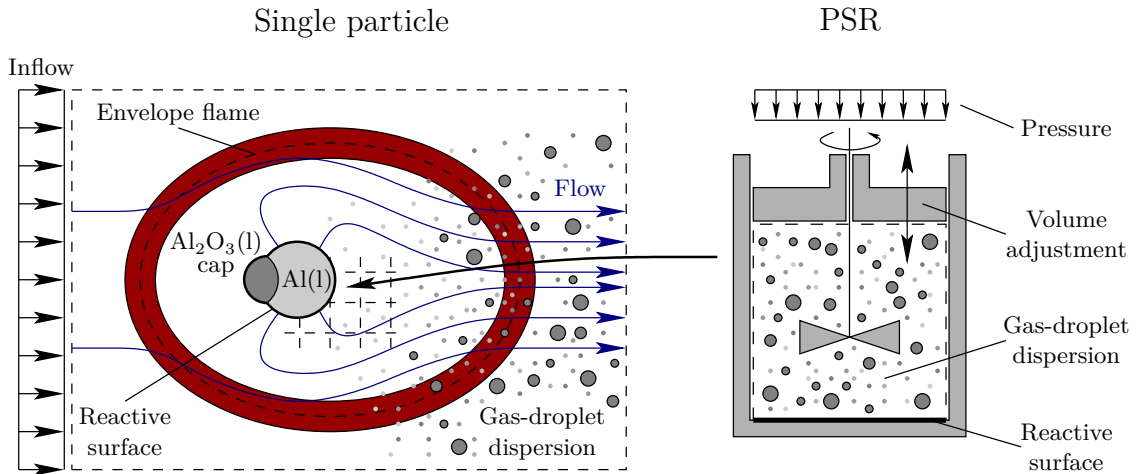


Figure 2.1 Schematic illustration of a burning aluminum particle in a laminar flow of an oxidizing gas mixture (left). In the absence of spatial transport, the chemical and physical processes inside a single FV grid cell at the particle surface (dashed box) are akin to those in a simplified PSR (right). Although the walls are adiabatic, energy may leave the reactor in the form of thermal radiation. Here and throughout this thesis, the oxide smoke droplets are represented by filled circles, while the multicomponent gas phase is illustrated as differently shaded dots.

enthalpy transfer rates and radiative heat losses in Section 2.4. With the aid of the numerical schemes of Section 2.5, we obtain predictions of the temporal changes in the gas phase, surface composition and smoke size distribution in a PSR at atmospheric pressure (Section 2.6). As the investigations reported up until this point only relate to a PSR operated at atmospheric pressure, in Section 2.7, the effect of a varying operating pressure on the key observables is analyzed. Finally, conclusions are drawn in Section 2.8. Appendix A contains explanatory background information on the low-level theories underlying the droplet formation and interaction rates as well as a summary of key assumptions in the presented kinetic framework.

2.2 Physical description of the interacting phases and thermochemistry

The physical model we present in this chapter encompasses the dynamics of three distinct phases that interact through mass and enthalpy exchanges along chemical routes (reaction, cluster formation, dissociation) or by physical processes (nucleation/condensation, coagulation, temperature assimilation and radiation). The schematic illustration in Fig. 2.2 serves us as a guiding frame whose contents are addressed in detail here and in Section 2.4

2.2 Physical description of the interacting phases and thermochemistry

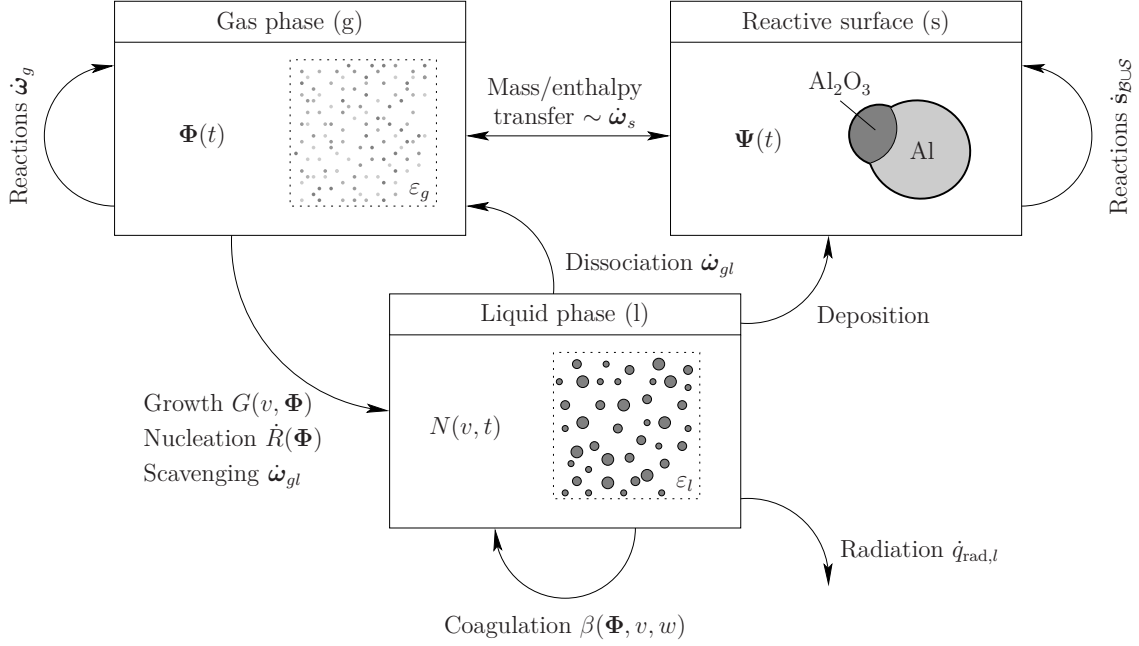


Figure 2.2 Schematic overview of the interacting phases and their kinetic interdependencies. While we are aware of the fact that gas phase radiation may play a role in aluminum combustion, this pathway is not included in our kinetic framework due to a lack of data (Section 2.4.4). Note that the effect of droplet deposition turned out to be insignificant at atmospheric pressure and is, thus, omitted in the discussion in Section 2.6 but investigated within the scope of Section 2.7.

(apart from deposition which is first discussed within the scope Section 2.7).

2.2.1 Gas phase chemistry

The chemical composition of a carrier gas phase is frequently described in terms of species mass fractions $Y_k \in [0, 1]$ [kg_k/kg(g)] which we assemble into a vector \mathbf{Y} for conciseness,

$$\mathbf{Y} = \left(Y_{\text{Al}}, \dots, Y_k, \dots, Y_{\text{N}_2} \right)^T. \quad (2.1)$$

Here, $k \in \mathcal{G}$ denotes the label of a particular gas species and $\mathcal{G} = \{\text{Al}, \dots, \text{N}_2\}$ represents the set of all gas species labels. At constant thermodynamic pressure p , the chemical and sensible energy contents are commonly measured in terms of the mass-specific gas enthalpy h_g [J/kg(g)] which can be linked to the gas temperature T according to

$$h_g(T, \mathbf{Y}) = \sum_{k \in \mathcal{G}} Y_k h_k(T), \quad (2.2)$$

2 The perfectly stirred reactor

where the species-specific enthalpies $h_k(T)$ [J/kg_k] are computed according to

$$h_k(T) = \Delta h_{f,k}^0 + \int_{T_0}^T C_{p,k}(\tilde{\tau}) d\tilde{\tau}. \quad (2.3)$$

Equation (2.3) indicates that h_k consists of the enthalpy of formation $\Delta h_{f,k}^0$ evaluated at the reference temperature T_0 , representing chemical storage, and the sensible enthalpy due to thermal storage that is expressed in terms of the specific heat capacity at constant pressure $C_{p,k}$ [J/(kg_kK)]. In pure gas phase combustion, the gas enthalpy remains unchanged and the heat of reaction is liberated as sensible enthalpy, resulting in a temperature rise. For a given chemical composition \mathbf{Y} , we may solve Eq. (2.2) for the gas phase temperature, yielding the functional dependency

$$T = \hat{T}(\mathbf{Y}, h_g). \quad (2.4)$$

Considering a multicomponent ideal gas, the gas density ρ_g may be similarly expressed in terms of \mathbf{Y} and h_g by the ideal gas law and Eq. (2.4),

$$\rho_g = \hat{\rho}_g(\mathbf{Y}, h_g) = \frac{p}{R\hat{T}(\mathbf{Y}, h_g) \sum_{k \in \mathcal{G}} \frac{Y_k}{W_k}}, \quad (2.5)$$

where R [J/(molK)] represents the universal gas constant and W_k [kg_k/mol_k] is the molecular weight of species k .

Since \mathbf{Y} and h_g jointly define the chemical and thermal state of the gaseous mixture if p remains constant, they are frequently aggregated into a vector of reactive scalars Φ ,

$$\Phi = \begin{pmatrix} \mathbf{Y} \\ h_g \end{pmatrix}. \quad (2.6)$$

To promote a consistent and simple notation, we use the index label set $\mathcal{G} \cup \{h_g\}$ to access any of the components of Φ .

For the description of the chemical reactions that occur in the gas phase, we employ the detailed reaction mechanism of Catoire et al. [29] and Swihart et al. [175] as summarized by Glorian et al. [69, Appendices A and B]. Since our focus lies on the combustion of aluminum in dry air, all species and chemical reactions involving elements other than Al, O

2.2 Physical description of the interacting phases and thermochemistry

or N are removed from the original mechanism. Additionally, the condensed phase species $\text{Al}_2\text{O}_3(\text{l})$ is replaced by the notion of an oxide droplet number density (Section 2.2.3), whence the chemical reactions adopted by Glorian et al. [69] to represent the condensation of $\text{Al}_2\text{O}_3(\text{l})$ do not apply. The reaction rates for the formation of nitrogen oxides (NO_x), moreover, are taken from the mechanism of Glarborg et al. [64]. Specifically, we adopt all chemical reactions from the supplementary material of Reference [64] that involve only species made from the elements N or O. The thermodynamic properties of the $\text{Al}_2\text{O}_3(\text{l})$ droplets are obtained from the database of Reference [27] which are in line with the data tabulated in the NIST-JANAF tables [31].

2.2.2 Reactive surfaces and heterogeneous surface reactions

Glorian et al. [69] investigated the combustion of a single aluminum particle in different oxidizing atmospheres and concluded that surface chemistry is particularly important for the combustion of small particles ($\lesssim 100\ \mu\text{m}$) at low pressures. Apart from these observations, our knowledge on the extent to which surface reactions affect the overall aluminum conversion for combustion in air at ambient pressure is limited. For this reason, we incorporate here the detailed mechanism for heterogeneous surface reactions developed by Glorian et al. [68, 69] as a gateway for the chemical and thermal interaction of a condensed-phase aluminum bulk with an oxidizing atmosphere. The surface mechanism is based on the theoretical framework proposed by Coltrin et al. [34] which underlies the SURFACE CHEMKIN-III library (also see Reference [90]). This framework is based on the notion of surface sites at which chemical reactions between gas phase (species labels without suffix), surface (suffix ‘(S)’) or bulk species (suffix ‘(B)’) may take place (Fig. 2.3). In our present case, the surface site density remains constant at $\Gamma = 4.42 \times 10^{-9}\ \text{mol}/\text{cm}^2$ and all reactions comply with the principle of surface site conservation.¹ Surface species form the top layer of molecules on the surface sites and may vaporize or adsorb/desorb by interaction with gas phase molecules above. If the surface molecule on a site is liberated,

¹Strictly, Glorian [67] determined this value of the surface site density for a neat Al(1 1 1) surface. Yet, at the temperatures investigated by Glorian et al. [69] and us, the aluminum particle is liquid and the crystalline structure of solid aluminum does not persist. As we are not aware of relevant data on site densities on molten aluminum surfaces or the validity of the concept of surface sites on liquid surfaces, we adopt the Al(1 1 1) site density value proposed by Glorian et al. [69] also for the liquid case.

2 The perfectly stirred reactor

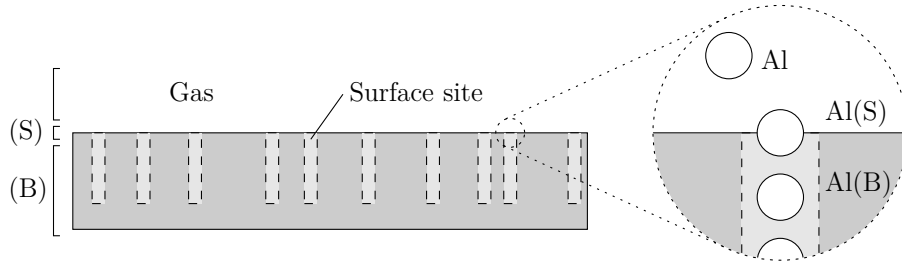


Figure 2.3 Illustration of the gas-surface interface and a particular site based on the atomic site convention [90].

then the bulk molecule underneath turns into the new surface molecule. Conversely, the deposition of a molecule on a surface site results in a reclassification of the original surface molecule as a bulk molecule. In this context, one feature of the surface mechanism of Glorian et al. [69] is that the condensation and vaporization of aluminum (illustrated in Fig. 2.3) are treated in a purely kinetic way as adsorption/desorption reactions,



Like the gas phase, the reactive surface is characterized in terms of scalars that are aggregated in the vector Ψ . In particular, the surface composition Ψ encompasses the surface site fractions $\theta_k [-]$, $k \in \mathcal{S}$, as well as specific transmitted bulk masses $B_k [\text{kg}_k/\text{m}^2]$, $k \in \mathcal{B}$,

$$\Psi = \left(\theta_{\text{Al(S)}}, \dots, \theta_{\text{Al}_2\text{O(S)}}, B_{\text{Al(B)}}, B_{\text{Al}_2\text{O}_3(\text{B})} \right)^T, \quad (2.8)$$

where the subscripted species labels are taken from the set of surface species labels \mathcal{S} or the bulk species label set \mathcal{B} , respectively. The mass of surface, bulk or gas phase species k that is consumed or released by heterogeneous surface reactions per unit of surface area is quantified by the rate $\dot{s}_k(\Phi, \Psi) [\text{kg}_k/(\text{m}^2\text{s})]$ obtained from the reaction mechanism of Glorian et al. [68, 69]. In the evaluation of $\dot{\mathbf{s}}$, the activities of all bulk species $k \in \mathcal{B}$ are set to zero apart from Al(B) for which we adopt a unity activity. This approach was previously used by Glorian et al. [69] and is based on the idea that, in the liquid state, bulk alumina ($\text{Al}_2\text{O}_3(\text{B})$) forms islands or recedes into a segregated phase that does not interfere with the surface chemistry on a liquid Al(B) substrate. For efficiency, the reaction rates $\dot{\mathbf{s}}$ are hard-coded and the implementation was verified by comparison with the SURFACE CHEMKIN-III output.

2.2.3 Dispersed oxide droplets

Besides the multicomponent gas phase and the reactive surface, liquid aluminum oxide droplets formed from gaseous precursors constitute the third phase in our physical model (Fig. 2.2). Since the droplets may differ from each other in terms of volume v , they are said to be polydispersed with respect to v . If the number of droplets is very large, then the dispersed phase can be described in terms of a number density $N(v)$ [$1/(\text{m}^3(1)\text{m}^3)$], where

$$N(v) dv = \frac{|\{i \in \mathbb{N}; v_i \in [v, v + dv)\}|}{V} \quad (2.9)$$

is the number of droplets whose volumes lie in an infinitesimal range about v per unit of volume V in physical space. The function $N(\cdot)$ is also termed the droplet volume (or size²) distribution and provides a quantitative measure of the population heterogeneity in terms of droplet volume. For brevity, we denote the entire droplet volume space by $\Omega_v = [0, \infty)$.

The k th moment of the droplet size distribution $N(\cdot)$ is defined according to

$$M_k(N(\cdot)) = \int_{\Omega_v} v^k N(v) dv, \quad (2.10)$$

where the augmented argument $N(\cdot)$ is used to indicate that M_k is a functional of the distribution $N(\cdot)$. The moments are particular statistics of the droplet size distribution and typically bear a special physical significance. For example, the zeroth moment M_0 is associated with the total number of droplets per unit of physical volume, while the first moment M_1 yields the droplet volume fraction ε_l [$\text{m}^3(1)/\text{m}^3$]. Its complement $\varepsilon_g = 1 - \varepsilon_l$ [$\text{m}^3(\text{g})/\text{m}^3$] corresponds to the gas phase volume fraction. For spherical droplets, the surface area of a droplet is given by $\sqrt[3]{36\pi v^2}$, whence the surface density ξ_l [$\text{m}^2(1)/\text{m}^3$] of the entire particulate phase can be obtained from $M_{2/3}$ as

$$\xi_l = \sqrt[3]{36\pi} M_{2/3}. \quad (2.11)$$

In practice, the droplet volume space Ω_v is restricted to the interval $[v_1, v_r]$, where v_r is a large, albeit finite value beyond which the droplet number density vanishes identically.

²In this thesis, the terms ‘volume’ and ‘size’ are used interchangeably when referring to the droplet property.

Commensurate with the capillarity approximation (Section 2.4.1), moreover, v_1 is taken as the volume of a single $\text{Al}_2\text{O}_3(l)$ molecule with bulk liquid properties.³

Both the numerical solution of the PBE and the formulation of the PaSR model we present in the following chapter rely on a v -discrete representation of the droplet size distribution $N(\cdot)$. In this regard, $N(\cdot)$ is parameterized in terms of a finite number of unknowns \mathbf{H} . Since the entries of \mathbf{H} describe the behaviour of the dispersed droplet phase in a similar way as the gas phase scalars Φ determine the state of the carrier gas, they are termed droplet phase scalars. Depending on the prediction objectives, the droplet phase scalars may be defined in different ways; in moment methods, for example, the scalars \mathbf{H} are chosen as key low-order statistics of $N(\cdot)$ [82, 115], while direct discretization methods involve a representation of $N(\cdot)$ in terms of nodal values [141] or cell averages [132], permitting a resolution of the entire droplet size distribution. Although this fidelity comes at the expense of a large number of droplet phase scalars, techniques have recently been advanced for the economical compression of the droplet size distribution into fewer scalars than traditional discretization schemes require. As examples, we mention the adoption of v -grid adaptivity [41, 159] or the incorporation of a reduced-order representation [155].

2.2.4 Dispersion characteristics

Because dispersed alumina droplets are very small and possess a low thermal inertia, we assume that heat is instantaneously exchanged between the ambient gas and the dispersed oxide smoke droplets such that both phases exist at a common temperature T . As for a homogeneous gas phase, this temperature can be related to the chemical composition of the gas-droplet dispersion (\mathbf{Y} and $N(\cdot)$) and its specific enthalpy h [J/kg] according to

$$h(T, \mathbf{Y}, N(\cdot)) = \left(\sum_{k \in \mathcal{G}} h_k(T) Y_k \right) \frac{\rho_g(T) (1 - \varepsilon_l)}{\rho(T)} + h_l(T) \varepsilon_l \frac{\rho_l}{\rho(T)} + \xi_l \frac{\sigma_l(T)}{\rho(T)}. \quad (2.12)$$

Here, the first term accounts for the enthalpy contributed by the gas phase, the second term represents the contribution of the droplets' bulk liquid and the final term indicates the energy penalty associated with a gas-liquid interface. The dispersion density ρ [kg/m³]

³According to the capillarity approximation [85, Chapter 3] of the underlying nucleation theory, even the smallest molecular clusters are assumed to possess bulk liquid properties (Section 2.4.1).

2.2 Physical description of the interacting phases and thermochemistry

in Eq. (2.12) is obtained as a weighted average of the gas phase density ρ_g and the density ρ_l of liquid aluminum oxide,

$$\rho = \rho_g(1 - \varepsilon_l) + \rho_l \varepsilon_l. \quad (2.13)$$

Similar to $\rho_g = \hat{\rho}_g(\Phi)$ in Eq. (2.5), we define $\hat{\rho}(\Phi, \mathbf{H})$ as a function that returns the dispersion density ρ for given gas and droplet phase scalars Φ and \mathbf{H} .

Since, in the capillarity approximation of Section 2.4.1, liquid phase clusters of molecules are assumed to inherit the bulk properties of liquid alumina, the volume of a cluster with k molecules is computed as km_1/ρ_l , where $m_1 = 1.6931 \times 10^{-25}$ kg is the mass of a single Al_2O_3 molecule. Similarly, a single-molecule droplet possesses the volume $v_1 = m_1/\rho_l$ corresponding to the left boundary of Ω_v in our description. Drawing on the experimental measurements of Glorieux et al. [70], we take ρ_l as the mean density of $\text{Al}_2\text{O}_3(l)$ over the temperature interval $[T_{m,\text{Al}_2\text{O}_3}, T_{b,\text{Al}_2\text{O}_3}]$, where $T_{m,\text{Al}_2\text{O}_3} = 2327$ K is the melting point of alumina and $T_{b,\text{Al}_2\text{O}_3} = 3763$ K denotes its boiling temperature, yielding $\rho_l = 2728.9 \text{ kg}(l)/\text{m}^3(l)$. Strictly, using a temperature-dependent expression for droplet density is also possible, but causes the left boundary of the droplet size space to vary in time as the temperature changes. In order to apply the numerical methods reported in Section 2.5 without modifications to account for temporally changing domain boundaries, we use a constant value here.

The interface contribution to the dispersion enthalpy is determined by the droplet surface density ξ_l (Eq. (2.11)) as well as the temperature-dependent surface tension $\sigma_l(T)$ [$\text{J}/\text{m}^2(l)$]. Savel'ev and Starik [148] reviewed several experimental measurements of $\sigma_l(T)$ [45, 71, 121, 161], reflecting a rather wide scatter at temperatures well above the melting point. Out of these measurements, the expression by Glorieux et al. [71] was calibrated for the widest temperature range, $T \in [T_{m,\text{Al}_2\text{O}_3}, 3200 \text{ K}]$, which is why we adopt their relation here,

$$\sigma_l(T) = 0.65 \text{ J}/\text{m}^2 - \left(3.9 \times 10^{-5} \text{ J}/(\text{m}^2\text{K})\right) \times (T - 2500 \text{ K}). \quad (2.14)$$

In the context of aerosol condensation in a turbulent jet, Garmory and Mastorakos [62] found the temperature-dependency of the surface tension to have a much more pronounced influence on the magnitude and spatial distribution of the total number density than potential segregation on the unresolved scales. In this light, we quantitatively assessed

2 The perfectly stirred reactor

the sensitivity of the key properties of the gas-droplet dispersion, such as the droplet size distribution and temperature, to the expression for $\sigma_l(T)$ in a PSR and could not confirm a strong influence.

2.3 Governing equations

In a PSR, spatial transport is absent and the dynamics of the gas phase scalars $\Phi = \Phi(t)$ and the surface composition $\Psi = \Psi(t)$ are governed by the mass and enthalpy balances

$$\frac{d\Phi_k(t)}{dt} = \dot{r}_k(\Phi(t), \Psi(t), N(\cdot, t), \gamma(t)), \quad k \in \mathcal{G} \cup \{h_g\}, \quad (2.15)$$

$$\frac{d\Psi_k(t)}{dt} = \dot{r}_k(\Phi(t), \Psi(t), \gamma(t)), \quad k \in \mathcal{S} \cup \mathcal{B}, \quad (2.16)$$

with

$$\dot{r}_k = \frac{\dot{\omega}_{g,k}}{\rho_g} + \dot{\omega}_{gl,k} + \dot{\omega}_{s,k}, \quad k \in \mathcal{G}, \quad (2.17)$$

$$\dot{r}_k = \dot{\omega}_{\text{rad},k} + \dot{\omega}_{gl,k} + \dot{\omega}_{s,k}, \quad k = h_g, \quad (2.18)$$

$$\dot{r}_k = \dot{s}_k \frac{\zeta_k}{W_k \gamma}, \quad k \in \mathcal{S}, \quad (2.19)$$

$$\dot{r}_k = \dot{s}_k, \quad k \in \mathcal{B}. \quad (2.20)$$

Here, $\dot{\omega}_g(\Phi)$ and $\dot{s}(\Phi, \Psi)$ represent, respectively, the source terms due to homogeneous gas phase (Section 2.2.1) and heterogeneous surface reactions (Section 2.2.2), while $\dot{\omega}_{\text{rad},h_g}(\Phi, N(\cdot, t))$ indicates radiative heat losses (Section 2.4.4). Furthermore, $\dot{\omega}_{gl}(\Phi, N(\cdot, t))$ accounts for the gas-liquid mass and enthalpy exchanges (Section 2.4.2) and $\dot{\omega}_s(\Phi, \Psi, N(\cdot, t))$ represents the transfer of mass and enthalpy from the reactive surface to the gas-droplet dispersion (Section 2.4.3). Lastly, $\zeta_k [-]$ is the number of reaction sites occupied by one molecule of surface species k and $\gamma(t) [\text{m}^2/\text{m}^3]$ denotes the density of the reactive surface.

One important property of the PSR we consider here is that the surface area A of the reactive surface remains constant, whereas the reactor volume $V(t)$ may adjust to accommodate density changes at a constant thermodynamic pressure p . Consequently,

the surface-to-volume ratio $\gamma(t) = A/V(t)$ changes in time according to

$$\frac{d\gamma(t)}{dt} = \frac{\gamma(t)}{\rho(t)} \left(\frac{d\rho(t)}{dt} - \gamma(t) \sum_{k \in \mathcal{G}} \dot{s}_k \right), \quad (2.21)$$

where $\rho(t)$ is the dispersion density defined in Eq. (2.13).

Complementary to Eqs. (2.15) and (2.16), the droplet number density $N = N(v, t)$ evolves according to the population balance equation (PBE) [82]

$$\begin{aligned} \frac{\partial N(v, t)}{\partial t} + \frac{\partial(G(v, \Phi(t))N(v, t))}{\partial v} &= \dot{R}(\Phi(t))\delta(v - v_0) - \frac{N(v, t)}{V(t)} \frac{dV(t)}{dt} \\ &+ \frac{1}{2} \int_{v_1}^v \beta(\Phi(t), v - w, w) N(v - w, t) N(w, t) dw \\ &- \int_{\Omega_v} \beta(\Phi(t), v, w) N(v, t) N(w, t) dw. \end{aligned} \quad (2.22)$$

The PBE encompasses processes due to both gas-liquid conversion and droplet-droplet interaction and is kinetically driven by the nucleation rate $\dot{R}(\Phi)$ [$1/(\text{m}^3\text{s})$], the droplet growth/shrinkage rate $G(v, \Phi)$ [$\text{m}^3(\text{l})/\text{s}$] and the coagulation kernel $\beta(\Phi, v, w)$ [m^3/s] (Section 2.4.1). Droplet nucleation is controlled by the difference in chemical potentials of vapour phase and condensed phase alumina (modulo an interface penalty) as measured by the supersaturation (Section 2.4.1). The Dirac δ -distribution $\delta(v - v_0)$ in Eq. (2.22) indicates that all nuclei share the same nominal size v_0 , an assumption we relax in Section 2.5 for reasons of finite v -resolution. The integral terms on the right hand side of Eq. (2.22) constitute the v -continuous counterpart of the Smoluchowski equation [163, 164] and represent the binary coagulation of two droplets with sizes w and $v - w$ to form a single droplet of size v as well as the removal of droplets of size v that are presently coagulating. Since the droplet number density $N(v, t)$ is defined based on the current reactor volume $V(t)$ (Eq. (2.9)), $N(v, t)$ changes as the reactor expands or contracts ($dV(t)/dt \neq 0$). This is accounted for by the second term on the right hand side of Eq. (2.22). With the aid of the mass balance

$$\frac{d(\rho(t)V(t))}{dt} = V(t) \frac{d\rho(t)}{dt} + \rho(t) \frac{dV(t)}{dt} = \gamma(t)V(t) \sum_{k \in \mathcal{G}} \dot{s}_k \quad (2.23)$$

and Eqs. (2.5) and (2.13), the rate $(dV(t)/dt)/V(t)$ on the right hand side of Eq. (2.22)

2 The perfectly stirred reactor

may be recast in terms of the temporal changes in $\mathbf{Y}(t)$, $T(t)$ and $\varepsilon_l(t)$ as

$$\frac{1}{V} \frac{dV}{dt} = \frac{\rho_g \varepsilon_g}{\rho} \left(\frac{1}{T} \frac{dT}{dt} + W \sum_{k \in \mathcal{G}} \frac{1}{W_k} \frac{dY_k}{dt} \right) - \frac{\rho_l - \rho_g}{\rho} \frac{d\varepsilon_l}{dt} + \frac{\gamma}{\rho} \sum_{k \in \mathcal{G}} \dot{s}_k, \quad (2.24)$$

where $W = (\sum_{k \in \mathcal{G}} Y_k / W_k)^{-1}$ denotes the mean molecular weight of the gas phase. By Eq. (2.10) with $k = 1$, $d\varepsilon_l/dt$ is related to the change in the droplet size distribution $\partial N/\partial t$. Similarly, the temperature rate-of-change dT/dt can be expressed in terms of dh_g/dt by combining Eq. (2.12) with the enthalpy balance we discuss in Eqs. (2.79) and (2.81) below. The PBE is complemented by the following homogeneous Dirichlet boundary condition

$$N(v_r, t) = 0, \quad t \geq 0 \quad \text{if } G(v_r) < 0. \quad (2.25)$$

Note that, at the left boundary of v -space, no boundary condition is required because $G(v_1) \leq 0$ by the nature of condensational droplet growth (see Section 2.4.1).

Progressing to a v -discrete formulation of the PBE and against the background of the considerations in Chapter 3, we leave the particular definition of the scalars $\mathbf{H}(t)$ in terms of $N(\cdot, t)$ unspecified and assume, with negligible loss of generality, that the dynamics of $\mathbf{H}(t)$ as obtained from a projection of Eq. (2.22) may be cast into the form

$$\frac{d\mathbf{H}(t)}{dt} = \dot{\mathbf{g}}(\mathbf{H}(t), \Phi(t), \Psi(t), \gamma(t)). \quad (2.26)$$

2.4 Kinetic framework

In this section, we present a detailed kinetic framework for the combustion of aluminum and the concomitant formation of polysized aluminum oxide droplets. The framework includes droplet nucleation, growth/shrinkage, coagulation and dissociation alongside mass and heat transfer due to surface reactions and phase transition as well as thermal radiation (see Fig. 2.2). Although our kinetic framework is tailored here to the combustion of aluminum, the underlying physical principles are independent of the particular metal fuel and the kinetic rates we present may be adapted also to other metals if the requisite material data are available. The key kinetic quantities that control the dynamics of the droplet formation and their interdependencies are schematically illustrated in Fig. 2.4.

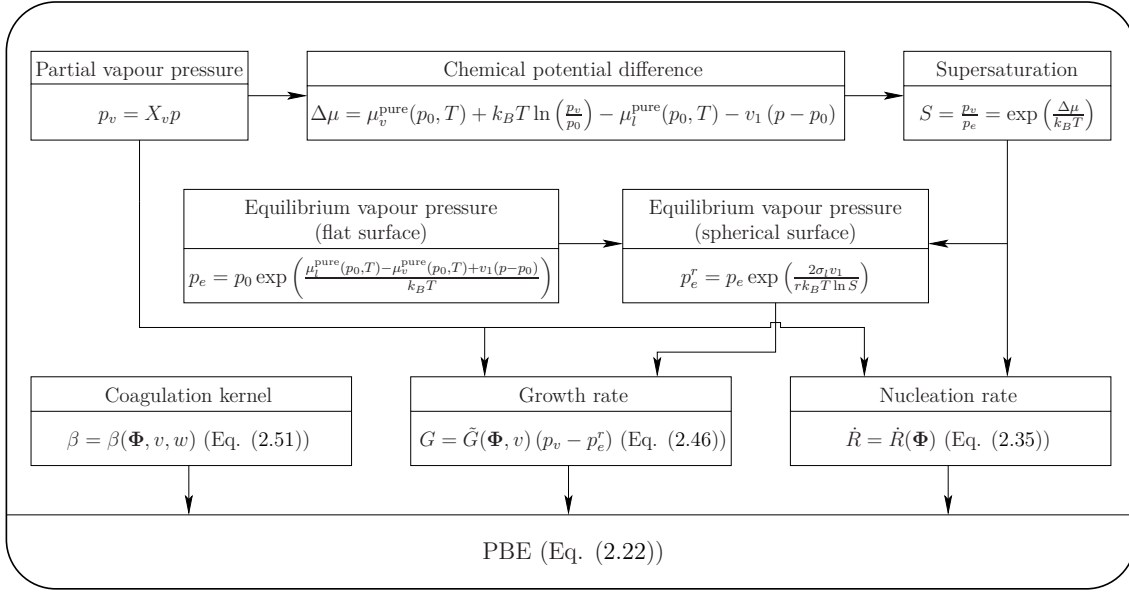


Figure 2.4 Schematic overview of the kinetic variables determining the condensation of polysized $\text{Al}_2\text{O}_3(\text{l})$ droplets and their interrelations. In order to systematically track all connections, we recommend to start from the $\text{Al}_2\text{O}_3/\text{c}$ partial vapour pressure p_v in the top left part of the diagram and follow the arrows. (Chemical reactions as well as gas-droplet and surface-dispersion interactions are omitted here.)

2.4.1 Droplet formation and interaction kinetics

Liquid alumina droplets condense from a supersaturated Al_2O_3 vapour by nucleation and may, subsequently, grow by molecular surface condensation, shrink due to evaporation or dissociation or coagulate on collision with other droplets. Jointly, these processes shape the droplet size distribution $N(\cdot, t)$ through the kinematics inherent in the PBE (Eq. (2.22)) and are, potentially, modified by molecular mixing (Eq. (3.6)). Before the rate expressions are presented, we briefly discuss the concept of supersaturation in the context of Al_2O_3 condensation.

Supersaturation

Presently, our understanding of the physical pathways by which alumina droplets form during the gas phase combustion of aluminum is incomplete because experimental observations are challenging and scarce or bound to specific thermal conditions. Against this backdrop, three rather different notions of $\text{Al}_2\text{O}_3(\text{l})$ droplet formation from gaseous precursors have been developed in the past. Henderson [79] first hypothesized that $\text{Al}_2\text{O}_3(\text{l})$ nuclei form at the end of a chain of $(\text{AlO})_n$ cluster polymerization reactions in the gas

phase. Alternatively, $\text{Al}_2\text{O}_3(\text{l})$ droplets could form as heterogeneous clusters of gaseous aluminum suboxides that mature subsequently until the bulk composition $\text{Al} : \text{O} = 2 : 3$ is attained [94]. Here, by contrast, we follow a third, frequently adopted approach [11, 69, 143, 148, 166, 167, 169, 170] and consider gaseous Al_2O_3 molecules (alongside the molecules of its isomer $\text{Al}_2\text{O}_3\text{c}$) as precursors that combine, through clusterization, into $\text{Al}_2\text{O}_3(\text{l})$ droplets. Beckstead et al. [11] was the first to put forward this two-stage condensation process in which the formation of aluminum oxide droplets from gaseous suboxides (AlO , Al_2O , AlO_2) proceeds through the intermediate gas species Al_2O_3 . Even if the role of gaseous alumina in the condensation of $\text{Al}_2\text{O}_3(\text{l})$ at the conditions of aluminum combustion is contentious and this physical picture may not truly correspond to reality, it may be viewed as a practical simplification in which gaseous Al_2O_3 serves as a (possibly even surrogate and) short-lived gateway species for gas-droplet transition.

Phase changes are driven by the difference in chemical potentials of a substance in distinct aggregate states. Frequently, this difference is measured in terms of the supersaturation S , where $S = 1$ indicates saturation and $S > 1$ characterizes a supersaturated vapour. Strictly, S merely quantifies the propensity of phase change because the initiation of a phase transition is energetically hindered by an energy barrier associated with the formation of an interface. In practice, passage of the energy barrier is effected by perturbations, for example, in the density or pressure [136, 137].

In aerosol science, the supersaturation is commonly defined as [11, 58, 147]

$$S = \frac{p_v}{p_e}, \quad (2.27)$$

where

$$p_v = p_{\text{Al}_2\text{O}_3} + p_{\text{Al}_2\text{O}_3\text{c}} = \left(X_{\text{Al}_2\text{O}_3} + X_{\text{Al}_2\text{O}_3\text{c}} \right) p \quad (2.28)$$

is the joint partial pressure of gaseous Al_2O_3 and its isomer $\text{Al}_2\text{O}_3\text{c}$ and p_e is the equilibrium vapour pressure over a flat surface.⁴ X_k , moreover, represents the mole fraction of species k [$\text{kmol}_k/\text{kmol}(\text{g})$]. The approach we employ here to evaluate S is rooted in the difference in chemical potentials as driving force of phase change and employs stan-

⁴For brevity, throughout this thesis, we employ the label $\text{Al}_2\text{O}_3/\text{c}$ to refer to gaseous alumina in both of its isomeric forms, *i.e.*, Al_2O_3 and $\text{Al}_2\text{O}_3/\text{c}$.

standard thermodynamic data such as those from the JANAF database [31] or the database of Burcat and Ruscic [27]. Following the developments in Section A.1 of Appendix A on the change in chemical potential of a single Al_2O_3 (or $\text{Al}_2\text{O}_3\text{c}$) molecule during transition from the gaseous to the liquid state, the supersaturation S of an $\text{Al}_2\text{O}_3/\text{c}$ -laden gas at pressure p and temperature T can be evaluated according to

$$S = \frac{p_v}{p_0} \exp \left(\frac{\mu_v^{\text{pure}}(p_0, T) - \mu_l^{\text{pure}}(p_0, T) - v_1 (p - p_0)}{k_B T} \right), \quad (2.29)$$

where k_B denotes Boltzmann's constant. At the standard pressure $p_0 = 1$ atm, the chemical potentials $\mu_v^{\text{pure}}(p_0, T)$ and $\mu_l^{\text{pure}}(p_0, T)$ of the pure substances can, in turn, be expressed in terms of their thermodynamic properties (Eq. (A.9) in Section A.1 of Appendix A, JANAF polynomials).

Sometimes, it is advantageous to express the equilibrium vapour pressure over a flat surface $p_e = p_e(T)$ directly in terms of the thermodynamic properties, skipping the intermediate variable S . From Eqs. (2.27) and (2.29), it immediately follows

$$p_e = p_0 \exp \left(- \frac{\mu_v^{\text{pure}}(p_0, T) - \mu_l^{\text{pure}}(p_0, T) - v_1 (p - p_0)}{k_B T} \right). \quad (2.30)$$

Using the thermodynamic data of Glorian et al. [69] and Burcat and Ruscic [27], we validated this expression by comparing the equilibrium vapour pressure curves it delivers for Al and Al_2O_3 with those of Bojko et al. [19] and Storozhev [168], respectively. Figure 2.5 shows that the vapour pressure curve of Al_2O_3 obtained from the approach discussed above matches the data communicated by Storozhev [168] very well to within a maximum relative deviation of 14.8% for $T < 3702.7$ K. The divergence of both curves above $T = 3702.7$ K is due to different definitions of the dissociation point.

If the vapour pressure p_v above a plane liquid surface coincides with $p_e(T)$, then there is no net gas-to-liquid mass transfer and both the liquid and gaseous phases remain in phase equilibrium. If the interface is curved, however, the vapour pressure required to maintain phase equilibrium differs from $p_e(T)$ in general. For a spherical droplet that is immersed in a gas, for example, the equilibrium vapour pressure is given by

$$p_e^r \equiv p_e \underbrace{\exp \left(\frac{2\sigma_l v_1}{r k_B T} \right)}_{\geq 1}. \quad (2.31)$$

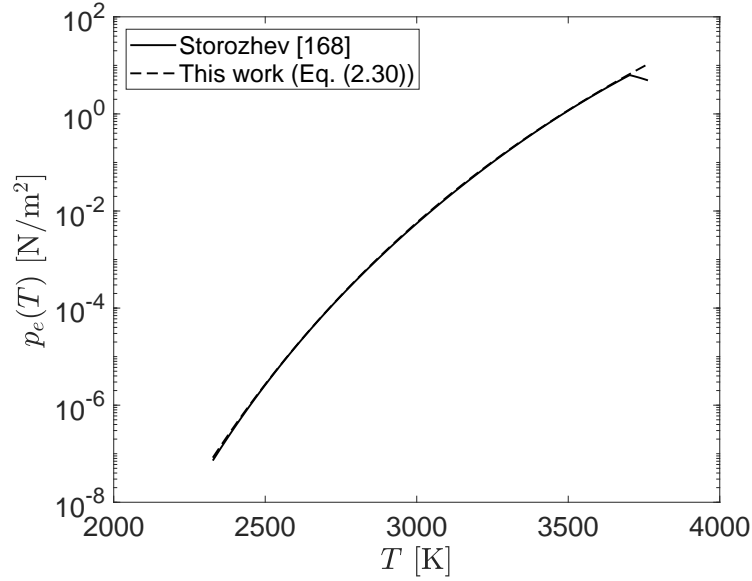


Figure 2.5 Comparison of the equilibrium vapour pressure $p_e(T)$ of gaseous Al_2O_3 computed from Eq. (2.30) with Storozhev’s data [168].

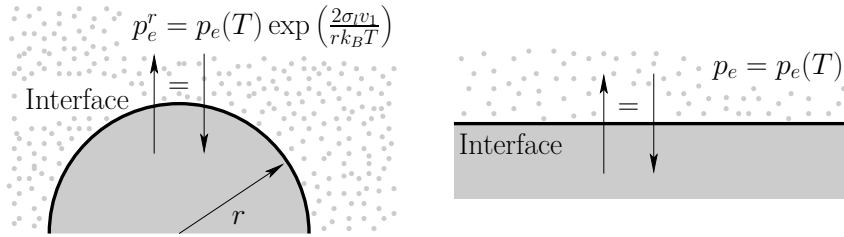


Figure 2.6 Illustration of the Kelvin effect. Curved interfaces require a higher vapour pressure to remain in phase equilibrium as indicated by the larger density of vapour molecules on the left hand side.

Equation (2.31) is also referred to as Kelvin’s equation (Kelvin effect) and shows that the vapour pressure $p_v = p_e^r$ required to ensure phase equilibrium between a liquid phase and a vapour increases with the surface’s curvature ($\sim \exp(1/r)$). Physically, this is due the fact that the attachment of molecules to neighbouring molecules on a curved surface is weaker than in a planar surface such that evaporation is facilitated [180]. The Kelvin effect is schematically illustrated in Fig. 2.6.

For $S > 1$, the Kelvin relation in Eq. (2.31) can, alternatively, be rearranged for the radius r_0 of a droplet that is in equilibrium with the vapour at pressure p_v ,

$$r_0 = \frac{2\sigma_1 v_1}{k_B T \ln S}, \quad (2.32)$$

where the definition of S in Eq. (2.27) has been applied. Combining Eqs. (2.31) and (2.32),

we obtain

$$p_e^r = p_e S^{\frac{r_0}{r}} = p_v S^{\frac{r_0-r}{r}}, \quad S > 1. \quad (2.33)$$

This equation is not only in line with our observations on the behaviour of the change in Gibbs free energy of formation $\Delta G(n)$ below, but also attains a more general significance if we consider an existing droplet with radius r that is exposed to a supersaturated vapour with $\text{Al}_2\text{O}_3/c$ partial pressure p_v . Droplets larger than the current equilibrium size (which is determined by the degree of supersaturation, $r_0 = r_0(S)$ by Eq. (2.32)) experience a vapour pressure that exceeds the one required to maintain phase equilibrium; specifically, the excess vapour pressure causes condensational surface growth. Droplets that are smaller than the critical size, by contrast, cannot be preserved and evaporate.

$$\begin{aligned} r > r_0 : \quad p_e^r < p_v &\Rightarrow \text{Growth} \\ r < r_0 : \quad p_e^r > p_v &\Rightarrow \text{Shrinkage} \end{aligned} \quad (2.34)$$

Nucleation

Nucleation describes the process which causes the formation of small liquid $\text{Al}_2\text{O}_3(l)$ droplets from a supersaturated $\text{Al}_2\text{O}_3/c$ -containing vapour and is driven by the decrease in Gibbs free energy of the bulk that accompanies the phase transition. The nucleation rate we employ in this chapter to test the droplet formation kinetics is based on the Classical Nucleation Theory (CNT, [8, 48, 57, 183]) amended by Courtney's correction and corrected for internal consistency (Internally Consistent Classical Theory (ICCT), [63, 85, 147]),

$$\dot{R}(\Phi) = \left(\frac{p_v}{k_B T}\right)^2 v_1 \sqrt{\frac{2\sigma_l(T)}{\pi m_1}} \frac{1}{S} \exp\left(-\frac{16\pi\sigma_l(T)^3 v_1^2}{3k_B^3 T^3 (\ln S)^2} + \frac{s_1\sigma_l(T)}{k_B T}\right). \quad (2.35)$$

Here, $s_1 = (36\pi)^{1/3} v_1^{2/3}$ is the surface area of a single spherical liquid phase molecule. The supersaturation S is given by Eq. (2.29). Although the nucleation rate in Eq. (2.35) is used to obtain the predictions presented in Sections 2.6 and 2.7 of this chapter, the effect of the mentioned corrections is assessed in the context of the single particle simulations in Chapter 4 where experimental reference data are available for a model calibration and validation (Sections 4.6.1 and 4.6.2). In this regard, another modification of the CNT as well as an unactivated nucleation rate are discussed and assessed.

Phase equilibrium and nuclei size Nuclei are delineated by a phase interface separating $\text{Al}_2\text{O}_3/c$ -containing vapour on the outside from bulk liquid $\text{Al}_2\text{O}_3(l)$ inside the droplet. The formation and maintenance of this interface requires energy that is supplied by independent fluctuations in the macroscopic thermal state or by external perturbations. The competition between the reduction in chemical potential due to gas-liquid conversion in the bulk and the energy penalty imposed by the formation of an interface can be quantified in terms of the Gibbs free energy. In particular, the change in Gibbs free energy associated with the formation of a liquid cluster with n molecules from a gas phase [127] is given by

$$\Delta G(n) = \underbrace{\sigma_l s_1 n^{\frac{2}{3}}}_{\text{surface}} - \underbrace{n\Delta\mu}_{\text{bulk}}. \quad (2.36)$$

For Al_2O_3 , $\Delta G(n)$ is depicted in Fig. 2.7 along with the surface and bulk contributions. If the Gibbs free energy does not respond to an infinitesimal mass transfer across the phase interface, then the liquid droplet with n molecules is in equilibrium with the surrounding vapour. Formally, this implies that, in phase equilibrium, $\Delta G(n)$ in Eq. (2.36) is independent of n to first order,

$$\frac{d\Delta G(n)}{dn} = 0. \quad (2.37)$$

This equilibrium condition particularly applies to nuclei for which we obtain on substitution of Eq. (2.36) into Eq. (2.37) with $n = n_0$

$$n_0 = \left(\frac{2\sigma_l s_1}{3\Delta\mu} \right)^3 = \left(\frac{2\sigma_l s_1}{3k_B T \ln S} \right)^3, \quad (2.38)$$

yielding the critical volume $v_0 = v_1 n_0$. At n_0 , the change in Gibbs free energy $\Delta G(n_0)$ corresponds to the energy barrier ΔG_{\max} per nucleus that withstands nucleation.

Since, in nature, phases evolve towards a minimum Gibbs free energy, the derivative $d\Delta G(n)/dn$ provides information on the directionality of phase change. For example, a cluster with $n < n_0$ molecules shrinks due to evaporation ($d\Delta G(n)/dn > 0$), whereas clusters which are larger than nuclei, $n > n_0$, grow due to continuing condensation ($d\Delta G(n)/dn < 0$, Fig. 2.7). In practice, the boundary n_0 is not sharp, however, because fluctuations in the Gibbs free energy may assist the growth of subcritical clusters or induce the evaporation of supercritical clusters. Since an independent fluctuation in

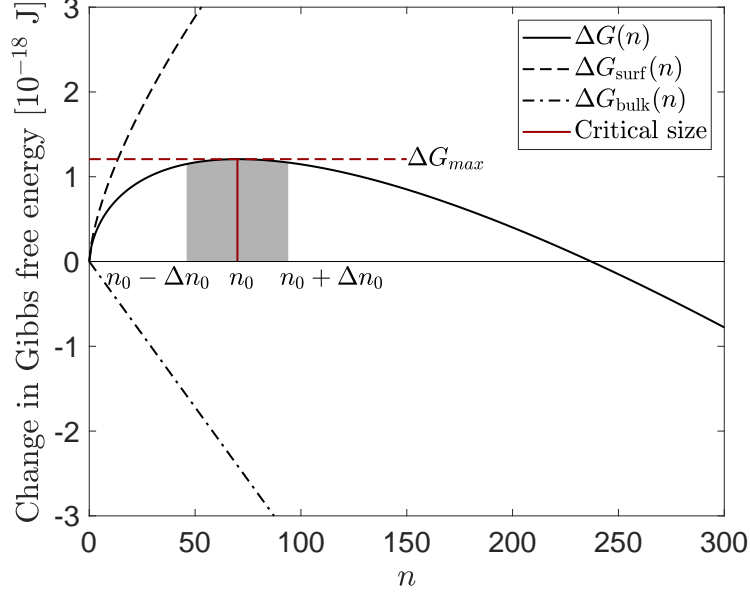


Figure 2.7 Change in Gibbs free energy ΔG during formation of a cluster with n molecules. In order to serve as stable nuclei, $(\text{Al}_2\text{O}_3/c)_n$ clusters have to surpass the energy barrier ΔG_{\max} associated with the critical size n_0 . Since the barrier is not sharp in practice, a nuclei size range $n \in [n_0 - \Delta n_0, n_0 + \Delta n_0]$ is defined.

$\Delta G(n)$ is of order $k_B T$, a nuclei size range is commonly defined as $n \in [n_0 - \Delta n_0, n_0 + \Delta n_0]$ with $\Delta G(n_0) - \Delta G(n_0 \pm \Delta n_0) = k_B T$ [85]. By expanding $\Delta G(n)$ in Eq. (2.36) about n_0 to second order in n , Δn_0 can be obtained as [85, 125]

$$\Delta n_0 = \sqrt{\frac{-2k_B T}{\left. \frac{d^2 \Delta G(n)}{dn^2} \right|_{n=n_0}}} = \frac{4\sigma_l s_1}{3(\Delta\mu)^2} \sqrt{k_B T \sigma_l s_1}. \quad (2.39)$$

Because a nucleus may not consist of less than one molecule, the condition $n_0 - \Delta n_0 \geq 1$ leads to an upper bound on the realizable supersaturation. From Eqs. (2.38) and (2.39), we obtain with $S = S_{\max}$

$$\left(\frac{2\sigma_l s_1}{3k_B T \ln S_{\max}} \right)^3 - \frac{4\sigma_l s_1}{3(k_B T \ln S_{\max})^2} \sqrt{k_B T \sigma_l s_1} = 1, \quad (2.40)$$

which is solved for S_{\max} using Cardano's formula. The maximum supersaturation we compute here is extremely sensitive to the minimum number of molecules composing a nucleus. For example, if the condition $n_0 - \Delta n_0 \geq 1$ is replaced by the requirement $n_0 \geq 1$, then the maximum admissible supersaturation may increase by a notable factor.

Limitations of the classical nucleation theory and potential extensions In the CNT, monomers (Al_2O_3 and $\text{Al}_2\text{O}_3\text{c}$ molecules) combine to yield $(\text{Al}_2\text{O}_3/\text{c})_n$ clusters which are considered stable nuclei for $n \geq n_0$. Here, the formation of an $(\text{Al}_2\text{O}_3/\text{c})_n$ cluster proceeds either through the addition of a monomer to an existing $(\text{Al}_2\text{O}_3/\text{c})_{n-1}$ cluster or the loss of one monomer by an $(\text{Al}_2\text{O}_3/\text{c})_{n+1}$ cluster. The addition of one monomer to an existing cluster is commonly termed condensation and occurs at a rate that is proportional to the collision frequency of monomers and clusters. The rate at which the reverse process, the dissociation of one molecule from a cluster, occurs is much more difficult to evaluate and has, in the past, been computed based on the constraint that the cluster size distribution assumes an equilibrium shape [57, Chapter VII]. This equilibrium shape is, in turn, controlled by the thermodynamic properties of the clusters and the thermal state of the gas. For the clusters' thermodynamic properties, the CNT relies on the so-called capillarity approximation [85, Chapter 3]:

- Clusters of molecules are homogeneous droplets of a well-defined radius with bulk liquid properties inside and bulk vapour properties outside.
- The liquid phase is incompressible ($\tilde{v}_1(p, T) = v_1$ in Eq. (A.6) in Section A.1 of Appendix A).
- The surface tension of a cluster containing n molecules (an n -mer) can be evaluated as the product of the planar interfacial tension $\sigma_l(T)$ and the surface area $s_1 n^{2/3}$ (Eq. (2.36)).

These assumptions are thought to be nearly accurate if the nuclei consist of a large number of molecules ($\gtrsim 100$), but may not hold true at very high supersaturations when the nuclei only consist of a few molecules [147, 148, 166]. The latter case also occurs in our application, casting doubt on the validity of the CNT. For the condensation of liquid $\text{Al}_2\text{O}_3(l)$ from a supersaturated vapour of gaseous Al_2O_3 , Starik et al. [166] and Savel'ev and Starik [148] pioneered an unsteady nucleation model in which the cluster dynamics are integrated into a gas phase reaction mechanism. Here, the forward rate coefficients of the monomer-addition reactions are computed from low-level collision theories, while the reverse rates of the monomer-dissociation reactions are related to the thermodynamic properties of the clusters and monomers through the equilibrium constants. The main difficulty associated with an unsteady nucleation model arises from the determination

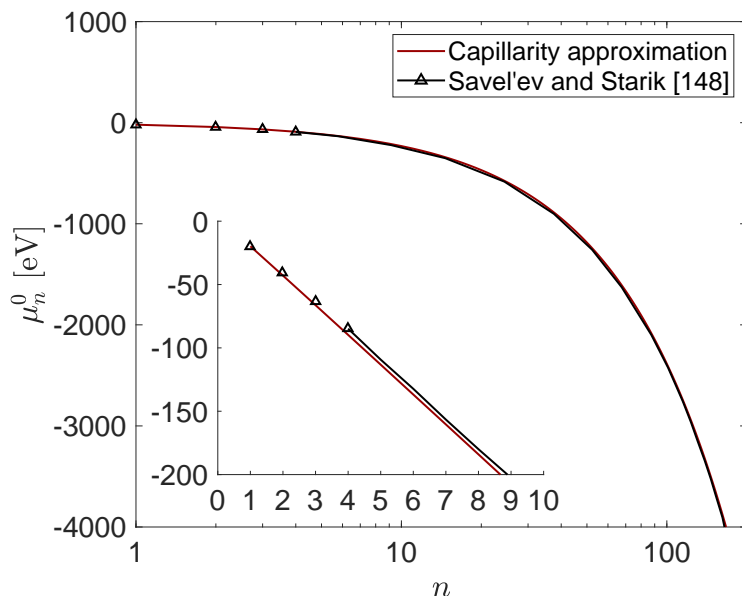


Figure 2.8 Comparison of the standard chemical potential of an n -mer $\mu_n^0 = \mu_v^0 + (n-1)\mu_l^0 + s_1\sigma_l(n^{2/3}-1)$ computed based on the capillarity approximation and the internal consistency correction with the interpolative calculations of Savel'ev and Starik [148, Fig. 2] at $T = 3000$ K.

of the thermodynamic properties of the individual clusters. Since, at present, quantum chemical calculations of thermodynamic properties are limited to small cluster sizes, Starik et al. [166] and Savel'ev and Starik [147, 148] developed an interpolation scheme by which the thermodynamic properties of intermediate-sized clusters can be approximated based on the chemical potentials of small clusters ($n \leq 4$) on the one hand and large, liquid-like clusters on the other hand ($n \gtrsim 100$).

Although the unsteady nucleation model permits a relaxation of the capillarity approximation and circumvents the constraint of an equilibrium cluster size distribution, it inherits the fundamental assumption that the formation of $\text{Al}_2\text{O}_3(l)$ droplets occurs through the clustering of gaseous Al_2O_3 . One practical drawback of unsteady nucleation models, moreover, is the large number of additional species that are introduced to capture the clusterization dynamics. Particularly in spatially inhomogeneous flow configurations, transporting about one hundred (or more) cluster mass fractions alongside the droplet phase scalars would entail a nearly prohibitive increase in the computational expense.

In order to probe the validity of the capillarity assumption, we compare, in Fig. 2.8, the standard chemical potential μ_n^0 of an n -molecule cluster evaluated based on the capillarity approximation with the expression of Savel'ev and Starik [148] at $T = 3000$ K. The correspondence is qualitatively very good, corroborating the validity of the capillarity

approximation in the present case.

Growth

Kinetically, droplet growth and coagulation can be approached very similarly since both are controlled by collisions, either of droplets with gas phase molecules or between droplets. In the collision theory, a distinction is made between three different transport regimes [58, 153]. If the radius of a droplet is small compared to the mean free path of the ambient gas, then the droplet exists in a rarefied medium and its transport properties are obtained from the kinetic theory of gases. This regime is called the free molecular or kinetic regime. Conversely, for droplets that are much larger than the mean free path of the gas, the continuum hypothesis is applicable and the associated regime is called the continuum regime. Since the transport properties of droplets in-between these limiting cases are affected by characteristics of either regime, the third regime is called the transition regime.

The ratio of the mean free path λ_{mfp} of gas molecules and the radius r of a droplet is called the Knudsen number and is commonly used to identify the transport regime experienced by a droplet,

$$\text{Kn} = \frac{\lambda_{\text{mfp}}}{r}. \quad (2.41)$$

Following Bird [14, Section 1.5], the mean free path of a gas mixture can be computed as

$$\lambda_{\text{mfp},g} = \sum_{k \in \mathcal{G}} X_k \lambda_{\text{mfp},k}, \quad (2.42)$$

where the species-specific mean free path $\lambda_{\text{mfp},k}$ is obtained as the ratio of the mean thermal speed and the average collision frequency, that is,

$$\lambda_{\text{mfp},k} = \frac{k_B T \bar{c}_k}{p \sum_{l \in \mathcal{G}} X_l \pi \sigma_{kl}^2 \bar{c}_{kl}}. \quad (2.43)$$

In Eq. (2.43), $\bar{c}_k = \sqrt{8RT/(\pi W_k)}$ denotes the mean thermal speed of molecules of species k , $\sigma_{kl} = (\sigma_k + \sigma_l)/2$ is the total collision diameter and $\bar{c}_{kl} = \sqrt{8RT(W_k + W_l)/(\pi W_k W_l)}$ represents the relative mean thermal speed of molecules of species k and l .

Kinetic regime In the kinetic regime ($\text{Kn} \gg 1$), the collision rate Z is obtained from the kinetic theory of gases [30] and the volumetric growth rate $[\text{m}^3(1)/\text{s}]$ evaluates to [153,

Sections 11.1-2 and 12.1]

$$G^{\text{kin}}(v, \Phi) = v_1 (Z_v - Z_e) = \frac{\alpha_{\text{mac}} v_1 (p_v - p_e^r) \pi \sqrt{\frac{v_1}{v} + 1} (d + d_v)^2}{\sqrt{2\pi m_1 k_B T}}, \quad (2.44)$$

where p_e^r is the equilibrium vapour pressure over a droplet with radius $r = d/2$ (or volume $v = \pi d^3/6$) (Eq. (2.31)) and d_v denotes the Lennard–Jones collision diameter of an $\text{Al}_2\text{O}_3/c$ vapour molecule. We ought to mention that, for our transport data, the collision diameter of a vapour molecule is smaller than the diameter of a single liquid molecule computed from the liquid phase density ρ_l , $d_v < d_1$. Equation (2.44) shows that the growth rate is obtained from a comparison of the collision frequency Z_v at an $\text{Al}_2\text{O}_3/c$ vapour pressure of p_v (Eq. (2.28)) with the collision frequency Z_e at the equilibrium vapour pressure p_e^r (Eq. (2.31)); the excess or defect collision frequency causes the droplets to grow by condensation ($p_v > p_e^r$) or evaporate ($p_v < p_e^r$), respectively.

The parameter $\alpha_{\text{mac}} \in [0, 1]$ in Eq. (2.44) is called mass accommodation coefficient and, physically, represents the likelihood for a colliding molecule to adhere to the droplet or for a molecule to be released on evaporation. In the absence of further information on α_{mac} for $\text{Al}_2\text{O}_3/c$ condensation, we choose $\alpha_{\text{mac}} = 1$, yielding the maximum condensation or evaporation rate [169].

Continuum regime For droplets much larger than the mean free path of the carrier gas ($\text{Kn} \ll 1$), the growth rate is based on the diffusive transport of gas molecules towards the droplet surface and can be obtained as the solution of a diffusion equation. From the diffusive flux evaluated at the droplet surface, we obtain the volumetric growth rate [58, Chapters 2 and 10]

$$G^{\text{con}}(v, \Phi) = \frac{2\pi d \mathcal{D}_{\text{Al}_2\text{O}_3/c} v_1 (p_v - p_e^r)}{k_B T}, \quad (2.45)$$

where $\mathcal{D}_{\text{Al}_2\text{O}_3/c}$ is the diffusion coefficient of $\text{Al}_2\text{O}_3/c$ into the gas mixture [126, Eq. (1.44)].

Kinetic, transition and continuum regimes The growth rate in the transition regime ($\text{Kn} \approx 1$) is commonly estimated by interpolating the growth rates in the kinetic and continuum regimes [153, Chapter 12]. Here, we specifically adopt the harmonic averaging of Pratsinis [130],

$$G(v, \Phi) = \frac{G^{\text{con}}(v, \Phi) G^{\text{kin}}(v, \Phi)}{G^{\text{con}}(v, \Phi) + G^{\text{kin}}(v, \Phi)}. \quad (2.46)$$

2 The perfectly stirred reactor

Since this interpolation approach is consistent with the limiting cases of purely kinetic ($\text{Kn} \gg 1$, $G = G^{\text{kin}}$) or continuum transport ($\text{Kn} \ll 1$, $G = G^{\text{con}}$), Eq. (2.46) is applied across the entire droplet size range Ω_v [122, 130].

Coagulation

The shape-preserving merger of two potentially differently sized droplets to form a single larger droplet is referred to as coagulation. In general, coagulation occurs as the sequence of droplet collision followed by coalescence. If coalescence is nearly instantaneous and poses a negligible energy barrier, then the coagulation of two droplets with volumes v and w , respectively, may be kinetically associated with their collision rate $\beta(\Phi, v, w)$.

Kinetic regime In the kinetic regime ($\text{Kn} \gg 1$), the coagulation kernel is evaluated based on the collision rate from the kinetic theory of gases and, apart from the constitutive differences between the collision partners, takes a similar form as Z in Eq. (2.44),

$$\beta^{\text{kin}}(\Phi, v, w) = \mathcal{W}^{\text{kin}} \sqrt{\frac{\pi k_B T}{2\rho_l}} \sqrt{\frac{1}{v} + \frac{1}{w}} (d(v) + d(w))^2 \quad (2.47)$$

with

$$d(v) = \sqrt[3]{\frac{6v}{\pi}}. \quad (2.48)$$

Here, \mathcal{W}^{kin} is an enhancement factor that accounts for field effects; we turn to its evaluation at the end of this section.

Continuum regime As for droplet growth, coagulation in the continuum regime ($\text{Kn} \ll 1$) is caused by the diffusive Brownian motion of the collision partners. Following Friedlander [58, Chapter 7], the coagulation kernel is obtained as

$$\beta^{\text{con}}(\Phi, v, w) = \mathcal{W}^{\text{con}} \frac{2k_B T}{3\mu_g} \left(\frac{C(v)}{d(v)} + \frac{C(w)}{d(w)} \right) (d(v) + d(w)), \quad (2.49)$$

where μ_g is the laminar dynamic viscosity of the gas mixture that can be evaluated with the aid of Wilke's formula [188]. The Cunningham slip correction factor C in Eq. (2.49) results from an amendment to Stokes' drag law and is designed to maintain its validity as

the droplet size decreases towards the mean free path of the gas [153, Eq. (9.34)],

$$C = 1 + \text{Kn} \left(1.257 + 0.4 \times \exp \left(-\frac{1.1}{\text{Kn}} \right) \right). \quad (2.50)$$

Kinetic, transition and continuum regimes Following along a similar rationale as in the case of droplet growth, we employ the harmonic averaging proposed by Pratsinis [130] across the entire droplet size range to evaluate the coagulation rate,

$$\beta(\Phi, v, w) = \frac{\beta^{\text{kin}}(\Phi, v, w)\beta^{\text{con}}(\Phi, v, w)}{\beta^{\text{kin}}(\Phi, v, w) + \beta^{\text{con}}(\Phi, v, w)}. \quad (2.51)$$

Enhancement factors The coagulation kernels summarized above are based on droplet-droplet collision frequencies due solely to Brownian motion, neglecting potential attractive or repulsive interactions mediated by the interstitial gas or electro-magnetic fields. These interactions may promote or impede collisions and can be accounted for using the enhancement factors \mathcal{W}^{kin} and \mathcal{W}^{con} in Eqs. (2.47) and (2.49), respectively. Based on the theories for retardation by viscous forces and London–van der Waals attraction outlined in Section A.2 of Appendix A, we calibrated enhancement factors for either regime in terms of the temperature T and the radii r_1 and r_2 of the approaching/colliding droplets,

$$\mathcal{W}(r_1, r_2, T) = 1 + (a_1 + a_2 T) \exp \left(a_3 \ln \left(\frac{r_1}{r_2} \right)^2 \right) \times (a_4 (r_1 + r_2) + 1)^{a_5}. \quad (2.52)$$

The fit coefficients a_i , $i = 1, \dots, 5$, are listed in Table 2.1. The mean relative errors in Eq. (2.52) compared to the exact expressions in Eqs. (A.19) and (A.20) over the considered ranges of r_1 , r_2 and T amount to 5% and 4% in the continuum and the kinetic regimes, respectively, an error margin we deem adequate in view of the physical assumptions in Section A.2 in Appendix A. The maximum norms of the relative errors in \mathcal{W}^{con} and \mathcal{W}^{kin} , on the other hand, are 17% and 14%, respectively. When choosing the functional form of Eq. (2.52) before parameter optimization, we attempted to minimize the number of real powers for computational efficiency, constraining, for example, $a_5^{\text{kin}} = -0.5$.

Viscous retardation is particular to the continuum regime and associated with the eviction of gas from the space in-between two approaching droplets [153]. The small-scale, interstitial gas flow features velocity gradients that impede the approach of the two droplets through viscous forces [4]. For $\mathcal{W}^{\text{con}} = 1$, Eq. (2.49) is based on the relative Stokes–

| Coefficients | Kinetic regime | Continuum regime |
|--------------|------------------------|------------------------|
| a_1 | 1.44 | -2.85×10^{-1} |
| a_2 | -1.26×10^{-4} | -1.57×10^{-5} |
| a_3 | -1.29×10^{-1} | -1.21×10^{-1} |
| a_4 | 4.84×10^5 | 3.54×10^6 |
| a_5 | -0.5 | 7.81×10^{-2} |

Table 2.1 Coefficients for the non-linear fits of the coagulation enhancement factors in Eq. (2.52).

Einstein diffusion coefficient $\mathcal{D}_{12} = \mathcal{D}_1 + \mathcal{D}_2$ which is, strictly, only valid if the droplets are sufficiently far apart such that viscous interactions can be neglected. In order to account for the near-field action of viscous forces, Spielman [165] introduced a correction factor $\mathcal{W}^{\text{con}} \neq 1$ into Eq. (2.49) and evaluated it based on series solutions. Later, Alam [4] obtained a closed expression for the ratio of the relative diffusion coefficients with and without viscous interaction which we employ here (Eq. (A.11) in Section A.2 of Appendix A).

The attractive London–van der Waals forces between globally uncharged droplets, on the other hand, result from the spontaneous formation of dipoles due to fluctuations in the electron clouds of their molecules [58]. The potential energy associated with London–van der Waals attraction depends on the material constitution of the colliding droplets and their distance. For details about the formulation of the London–van der Waals potential and its relation to the enhancement factors, we refer to Section A.2 of Appendix A.

2.4.2 Heat and mass exchange within the dispersion

In a gas-droplet dispersion, mass and enthalpy are exchanged between the gas and the dispersed droplets due to phase transitions and temperature assimilation. In our case of an oxide smoke dispersion, the phase transitions are caused by condensation or evaporation and dissociation. Implicitly, droplet coagulation also influences the gas enthalpy as the area of the interface separating gas and liquid decreases in size. In this section, we present a unified formulation for the rates at which the gas phase composition $\Phi(t)$ and the droplet size distribution $N(\cdot, t)$ change as a result of mass and enthalpy exchanges between the dispersed droplets and the carrier gas phase. While this formulation is independent of the particular physical effect causing the exchange, it is particularized to condensation/evaporation and dissociation subsequently.

For clarity, we consider a single material element of a gas-droplet dispersion in isolation

from its surroundings. The material element presently occupies the volume $V(t)$ and possesses a total mass of $m = m_g(t) + m_l(t)$ containing the droplet mass $m_l(t)$ and the gas mass $m_g(t)$ with

$$m_g(t) = \sum_{k \in \mathcal{G}} m_k(t). \quad (2.53)$$

By the conservation of mass, m remains constant in time, while the mass shares $m_k(t)$ of the gas species, $k \in \mathcal{G}$, and $m_l(t)$ of the dispersed droplets may change. Both are interrelated according to

$$\frac{dm_k(t)}{dt} = \frac{dm_g(t)Y_k(t)}{dt} = -\delta_k \frac{dm_l(t)}{dt}, \quad \sum_{k \in \mathcal{G}} \delta_k = 1, \quad (2.54)$$

where $\delta_k = \delta'_k W_k / W_l$ involves the stoichiometric coefficients δ'_k of the gas-to-liquid conversion reactions as well as the molecular weight $W_l = W_{\text{Al}_2\text{O}_3(1)}$ of the condensed phase species $\text{Al}_2\text{O}_3(1)$. Summation of Eq. (2.54) over all species $k \in \mathcal{G}$ shows $dm_g(t)/dt = -dm_l(t)/dt$. With the aid of this result and the product rule, we obtain from Eq. (2.54) upon division by the reactor volume $V(t)$

$$\rho_g(t)\varepsilon_g(t) \frac{dY_k(t)}{dt} = (Y_k(t) - \delta_k) \frac{1}{V(t)} \frac{dm_l(t)}{dt}. \quad (2.55)$$

The term $(dm_l(t)/dt)/V(t)$ on the right hand side of Eq. (2.55) corresponds to the change in liquid mass per unit of volume at the current volume $V(t)$ and can be referred to the droplet size distribution $N(\cdot, t)$ according to

$$\frac{1}{V(t)} \frac{dm_l(t)}{dt} = \rho_l \frac{d\varepsilon_l(t)}{dt} = \rho_l \frac{d}{dt} \int_{\Omega_v} v N(v, t) dv. \quad (2.56)$$

On substitution of Eq. (2.56) into Eq. (2.55), we arrive at the result

$$\rho_g(t)\varepsilon_g(t) \frac{dY_k(t)}{dt} = (Y_k(t) - \delta_k) \rho_l \frac{d\varepsilon_l(t)}{dt}, \quad k \in \mathcal{G}. \quad (2.57)$$

If the material element is adiabatic and isobaric (Section 2.2.1), it exerts only pressure/volume work and, by the first law of thermodynamics, maintains the enthalpy content $H = m_g h_g + m_l h_l + \sigma_l A_l$ [J], where A_l is the surface area of the liquid droplets. This implies $dH/dt = 0$ or, on application of the product rule and division by the current

2 The perfectly stirred reactor

reactor volume $V(t)$,

$$\rho_g \varepsilon_g \frac{dh_g}{dt} + \rho_l \varepsilon_l \frac{dh_l}{dt} + (h_l - h_g) \frac{1}{V(t)} \frac{dm_l}{dt} + \xi_l \frac{d\sigma_l}{dt} + \sigma_l \frac{1}{V} \frac{dA_l}{dt} = 0. \quad (2.58)$$

The final term in Eq. (2.58) represents the change in the stored enthalpy associated with the gas-droplet interface due to a changing droplet surface area. Similar to the liquid mass change in Eq. (2.56), this term can be related to the droplet size distribution $N(\cdot, t)$ according to

$$\frac{1}{V(t)} \frac{dA_l(t)}{dt} = \frac{d\xi_l(t)}{dt} = (36\pi)^{\frac{1}{3}} \frac{d}{dt} \int_{\Omega_v} v^{\frac{2}{3}} N(v, t) dv. \quad (2.59)$$

Introducing Eqs. (2.56) and (2.59) into Eq. (2.58) and expressing the time derivatives of h_g , h_l and σ_l in terms of the rate-of-change of the common temperature T and the species mass fractions Y_k , $k \in \mathcal{G}$, ultimately yields

$$\rho_g \varepsilon_g \sum_{k \in \mathcal{G}} h_k \frac{dY_k}{dt} + \rho C_p \frac{dT}{dt} = \rho_l (h_g - h_l) \frac{d\varepsilon_l}{dt} - \sigma_l \frac{d\xi_l}{dt} \quad (2.60)$$

with

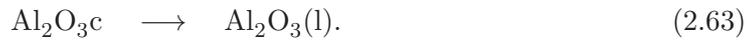
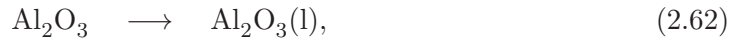
$$\rho C_p = \rho_g \varepsilon_g C_{p,g} + \rho_l \varepsilon_l C_{p,l} + \xi_l \tilde{\sigma}_l. \quad (2.61)$$

Here, $C_{p,g} = \sum_{k \in \mathcal{G}} C_{p,k} Y_k$ and $C_{p,l} = dh_l/dT$ represent the mean heat capacities of the gas and the bulk liquid, respectively, at constant pressure and $\tilde{\sigma}_l = d\sigma_l/dT$ accounts for the change in surface tension with temperature (Eq. (2.14)).

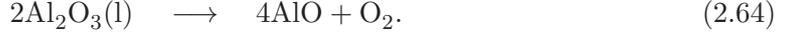
Jointly, Eqs. (2.57) and (2.60) constitute a system of equations relating changes in the droplet volume and surface densities ($d\varepsilon_l/dt$, $d\xi_l/dt$) to changes in the gas phase composition (dT/dt , dY_k/dt , $k \in \mathcal{G}$).

Aluminum oxide condensation, evaporation and coagulation

For $d\varepsilon_l/dt > 0$, gaseous Al_2O_3 and $\text{Al}_2\text{O}_3\text{c}$ transition into the dispersed liquid phase according to the conversion reactions



Conversely, for $d\varepsilon_l/dt < 0$, droplet evaporation occurs, proceeding along the reaction pathway [11, Eq. (R10)]



Frequently, changes in ε_l are accompanied by a change in the droplet surface density ξ_l at the rate $d\xi_l/dt$. Yet, even in the absence of phase transitions, $d\varepsilon_l/dt = 0$, the surface density may change due to coagulation, with ramifications in the dispersion temperature (Eq. (2.60)). In the case of condensation, the contributions δ_k , $k \in \mathcal{A} = \{\text{Al}_2\text{O}_3, \text{Al}_2\text{O}_3c\}$, of either pathway in Eqs. (2.62) and (2.63) to the overall mass transfer rate $dm_l(t)/dt$ in Eq. (2.54) are determined based on the mole fractions of the isomers,

$$\delta_k = \frac{1}{\sum_{i \in \mathcal{A}} X_i} \begin{cases} X_k, & k \in \mathcal{A} \\ 0, & \text{otherwise} \end{cases}. \quad (2.65)$$

For evaporation, by contrast, the stoichiometric coefficients δ'_k are those of Eq. (2.64), that is, $\delta'_{\text{AlO}} = 2$, $\delta'_{\text{O}_2} = 1/2$ and $\delta'_k = 0$ for the remaining gas species.

For a pure phase change, the solutions $dY_k(t)/dt$ of Eq. (2.57) coincide with the gas-liquid conversion term $\dot{\omega}_{gl,k}$ in Eq. (2.17),

$$\dot{\omega}_{gl,k} = \frac{\rho_l}{\rho_g \varepsilon_g} (Y_k - \delta_k) \frac{d\varepsilon_l}{dt}. \quad (2.66)$$

The corresponding source term for the gas phase enthalpy in Eq. (2.18), moreover, can be obtained as the time derivative of Eq. (2.2) on substitution of the temperature rate-of-change from Eq. (2.60) in conjunction with Eq. (2.57),

$$\dot{\omega}_{gl,h_g} = \frac{C_{p,g}}{\rho C_p} \left(\left(\sum_{k \in \mathcal{G}} \delta_k h_k - h_l \right) \rho_l \frac{d\varepsilon_l}{dt} - \sigma_l \frac{d\xi_l}{dt} \right) + \sum_{k \in \mathcal{G}} h_k \dot{\omega}_{gl,k}. \quad (2.67)$$

Dissociation

A special property that distinguishes aluminum dust flames from hydrocarbon-fuelled flames is that the aluminum oxide droplets dissociate into aluminum sub-oxides and oxygen-species at the boiling temperature $T_{b,\text{Al}_2\text{O}_3}$ [9, 11]. This dissociation reaction is endothermic and results in a limitation of the flame temperature T at $T_{b,\text{Al}_2\text{O}_3}$. Specifically, the sensible enthalpy associated with any excess temperature $T - T_{b,\text{Al}_2\text{O}_3} > 0$ is absorbed

2 The perfectly stirred reactor

by the dissociating $\text{Al}_2\text{O}_3(l)$. Following Beckstead et al. [11], the dissociation reaction in our model occurs commensurate with the reaction in Eq. (2.64). The boiling temperature of $\text{Al}_2\text{O}_3(l)$ is given by [65, 135]

$$T_{b,\text{Al}_2\text{O}_3} = (250.365 \times \ln p + 876.84) \text{ K}. \quad (2.68)$$

At $p = 1$ atm, Eq. (2.68) yields a boiling temperature of $T_{b,\text{Al}_2\text{O}_3} \approx 3763$ K.

Since dissociation causes the chemical composition of the gas-droplet dispersion to change such that the temperature is limited to $T_{b,\text{Al}_2\text{O}_3}$, Beckstead et al. [11] suggested to solve an equation of the type

$$f(T, \dot{\omega}_{\text{dis},\text{Al}_2\text{O}_3(l)}) - T_{b,\text{Al}_2\text{O}_3} = 0 \quad (2.69)$$

for the dissociation rate $\dot{\omega}_{\text{dis},\text{Al}_2\text{O}_3(l)}$. Strictly speaking, however, in our PBE-based model, dissociation is already included by means of a negative growth rate, *i.e.*, a possibly negative change in the droplet volume fraction associated with evaporation discussed in the preceding section. If the vapour partial pressure p_v in Eqs. (2.44) and (2.45) drops below the equilibrium vapour pressure p_e^r which relates to the dissociation temperature, the droplets of radius r dissociate at finite rate through the evaporation pathway of Eq. (2.64). Due to the inertia associated with the finite-rate dissociation, it may be possible for the droplets to exist at temperatures that exceed the Al_2O_3 boiling point (Eq. (2.68)). In order to strictly limit the flame temperature to $T_{b,\text{Al}_2\text{O}_3}$, we particularize the idea behind Eq. (2.69) here by adapting the mass and enthalpy balances in Eqs. (2.57) and (2.60) to instantaneous dissociation, thereby preventing the droplets to exist at temperatures above the alumina boiling point at any time. Assuming that dissociation indeed occurs instantaneously, all time derivatives are replaced by increments which we indicate by the prefix Δ . Contrary to condensation, the increments ΔY_k in the species mass fractions as well as the dissociating volume fraction $\Delta \varepsilon_l$ and the change in surface density $\Delta \xi_l$ are sought, while the temperature increment ΔT is given in terms of the negative excess temperature $T_{b,\text{Al}_2\text{O}_3} - T < 0$. Because the dissociating volume $\Delta \varepsilon_l$ does not uniquely determine the change in surface density $\Delta \xi_l$, the solutions of Eqs. (2.57) and (2.60) are indeterminate. For closure, a statement on how the droplet size distribution $N(\cdot, t)$ changes in response to a volume fraction increment $\Delta \varepsilon_l$ is required.

Since dissociation occurs mainly at the droplets' surfaces, we assume that the change in the number density of droplets with volume inside $[v, v + dv)$ scales with the contribution of this droplet volume class to the total surface density of the entire droplet phase,

$$\Delta N(v, t) dv = \Delta\eta \frac{v^{2/3} N(v, t) dv}{M_{2/3}(t)}. \quad (2.70)$$

Here, $\Delta\eta$ is a proportionality factor which is determined based on the condition that the first moment of $\Delta N(\cdot, t)$ coincides with $\Delta\varepsilon_l$,

$$\Delta\varepsilon_l = \int_0^\infty v \Delta N(v, t) dv = \frac{\Delta\eta M_{5/3}(t)}{M_{2/3}(t)}. \quad (2.71)$$

Upon rearranging Eq. (2.71) for $\Delta\eta$ and substitution into Eq. (2.70), we obtain for the change in surface density $\Delta\xi_l$ associated with $\Delta N(\cdot, t)$ (Eq. (2.11)),

$$\Delta\xi_l = (36\pi)^{\frac{1}{3}} \int_0^\infty v^{\frac{2}{3}} \Delta N(v, t) dv = (36\pi)^{\frac{1}{3}} \underbrace{\frac{M_{4/3}}{M_{5/3}}}_{=\nu} \Delta\varepsilon_l, \quad (2.72)$$

representing a linear relation between $\Delta\xi_l$ and $\Delta\varepsilon_l$ with proportionality constant ν . Taken together, Eqs. (2.57), (2.60) and (2.72) constitute the following linear system for ΔY_k , $k \in \mathcal{G}$, and $\Delta\varepsilon_l$ given $\Delta T = T_{b, Al_2O_3} - T$,

$$\begin{bmatrix} \rho_g \varepsilon_g & 0 & \dots & 0 & -\rho_l (Y_1 - \delta_1) \\ 0 & \ddots & & \vdots & \vdots \\ \vdots & & \ddots & 0 & \vdots \\ 0 & \dots & 0 & \rho_g \varepsilon_g & -\rho_l (Y_{n_S} - \delta_{n_S}) \\ \rho_g \varepsilon_g h_1 & \dots & \dots & \rho_g \varepsilon_g h_{n_S} & \rho_l (h_l - h_g) + \sigma_l \nu \end{bmatrix} \begin{bmatrix} \Delta Y_1 \\ \vdots \\ \vdots \\ \Delta Y_{n_S} \\ \Delta\varepsilon_l \end{bmatrix} = \begin{bmatrix} 0 \\ \vdots \\ \vdots \\ 0 \\ -\rho C_p \Delta T \end{bmatrix}, \quad (2.73)$$

supplemented by the relation $\Delta\xi_l = \nu \Delta\varepsilon_l$. For brevity, the gas phase species have been numbered from 1 to n_S in Eq. (2.73). Since the system in Eq. (2.73) is of arrowhead type, it can be solved very efficiently in a direct way, involving $n_S + 1$ steps. Specifically, by substituting the n_S leading ΔY_k -equations into the equation for $\Delta\varepsilon_l$, we obtain an equation for the single unknown $\Delta\varepsilon_l$. After solution, $\Delta\varepsilon_l$ can be used to solve for the increments ΔY_k . Note that the developments regarding dissociation detailed here, are discarded for the single particle combustion model discussed in Chapters 4 and 5 where

we solely use the finite-rate dissociation rate included in Eqs. (2.44) and (2.45) in order to omit the assumption of an instantaneous phase transition and facilitate the coupling with a reactive flow solver. Also, the effect of additionally imposing an instantaneous dissociation to limit the flame temperature at every point in time is investigated as part of our analysis in Section 2.7 and turned out to be negligible.

2.4.3 Heat and mass exchange between dispersion and reactive surface

At the reactive surface, gas phase species may be absorbed or released by heterogeneous reactions. Similarly, heat can either be supplied to the gas-droplet dispersion or withdrawn, depending on the sensible enthalpy budget of the surface reactions. In this section, kinetic expressions for the source terms $\dot{\omega}_{s,k}$ and $\dot{\omega}_{s,h_g}$ in the evolution equations for the gas phase scalars Y_k , $k \in \mathcal{G}$, and h_g are derived based on mass and enthalpy balances.

Adopting a similar rationale as in Section 2.4.2, we consider a material element of the gas-droplet dispersion with gaseous mass content $m_g(t)$ and volume $V(t)$. The rate-of-change in the mass $m_k(t)$ of species $k \in \mathcal{G}$ due to surface reactions is given by

$$\frac{dm_k(t)}{dt} = V(t)\gamma(t)\dot{s}_k. \quad (2.74)$$

Taking the time derivative of the species mass fraction's definition, $Y_k(t) = m_k(t)/m_g(t)$, and substituting Eqs. (2.53) and (2.74) yields the following relation for the time derivative of the species mass fraction $Y_k(t)$,

$$\frac{dY_k(t)}{dt} = \frac{\gamma(t)}{\rho_g(t)\varepsilon_g(t)} \left(\dot{s}_k - Y_k(t) \sum_{j \in \mathcal{G}} \dot{s}_j \right), \quad k \in \mathcal{G}, \quad (2.75)$$

corresponding to the source term $\dot{\omega}_{s,k}$ in Eq. (2.17).

The exchange of mass between a bulk phase and the gas-droplet dispersion through a reactive surface is accompanied by the enthalpy exchange schematically illustrated in Fig. 2.9. In an application, the bulk phase may represent an evaporating Al-particle, for example, as depicted in Fig. 2.1. If we assume that the reactive surface possesses no capacity to store enthalpy (or mass), then balancing of the fluxes leaving the surface (s)

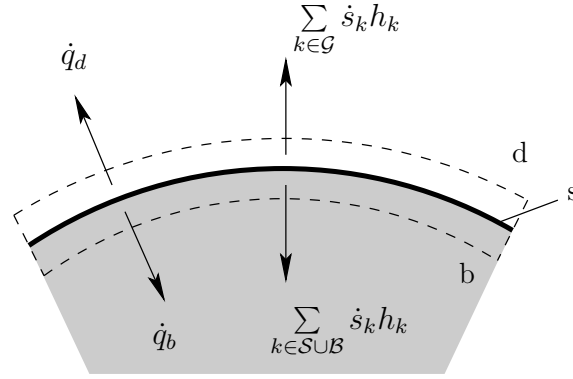


Figure 2.9 Schematic illustration of the species-bound enthalpy fluxes and the conductive heat fluxes leaving the reactive surface.

towards the dispersion above (d) or the bulk below (b) yields

$$\sum_{k \in \mathcal{G} \cup \text{SUB}} \dot{s}_k h_k + \dot{q}_d + \dot{q}_b = 0. \quad (2.76)$$

Note that the reactive surface is considered an infinitely thin sheet, covering the idealized fuel particle surface, which is distinct from the bulk material and the surface sites. Consequently, the bulk and surface species are assigned to the particle's core (b), whereas the gas species (and droplets) live on the other side (d) of this thin layer. In practice, due to a rather small Biot number ($\text{Bi} \ll 1$), it is reasonable to assume a uniform temperature across the particle volume (see also Chapters 4 and 5). Here, we choose the particle temperature to coincide with the boiling temperature of aluminum $T_{b,\text{Al}} = 2791 \text{ K}$. Consequently, by Fourier's law of heat conduction, the heat flux \dot{q}_b into the bulk vanishes in this case and Eq. (2.76) reduces to

$$\dot{q}_d = - \sum_{k \in \mathcal{G} \cup \text{SUB}} \dot{s}_k h_k. \quad (2.77)$$

Physically, Eq. (2.77) implies that all sensible enthalpy released or consumed by surface reactions is received or supplied, respectively, by the gas-droplet dispersion. In practice, the assumption $\dot{q}_b = 0$ which we maintain here may be relaxed and replaced by a constitutive law linking \dot{q}_b to the primary unknowns (Section 4.4.3).

The enthalpy fluxes crossing the dispersion-surface interface in Fig. 2.9 enter the balance

2 The perfectly stirred reactor

equation for the dispersion enthalpy $H = mh = (m_g + m_l)h$,

$$\frac{dH}{dt} = \rho V \frac{dh}{dt} + h \frac{d(m_g + m_l)}{dt} = \gamma V \left(\sum_{k \in \mathcal{G}} \dot{s}_k h_k + \dot{q}_d \right). \quad (2.78)$$

Introducing Eqs. (2.53), (2.74) and (2.77) into Eq. (2.78), we obtain with $dm_l/dt = 0$

$$\frac{dh}{dt} = -\frac{\gamma}{\rho} \left(\sum_{k \in \text{SUB}} \dot{s}_k h_k + h \sum_{k \in \mathcal{G}} \dot{s}_k \right). \quad (2.79)$$

In conjunction with Eq. (2.12) and the definition of the dispersion heat capacity C_p in Eq. (2.61), Eq. (2.79) may be recast in terms of the gas phase enthalpy according to

$$\frac{dh_g}{dt} = \frac{\gamma}{\rho_g \varepsilon_g} \sum_{k \in \mathcal{G}} (h_k - h_g) \dot{s}_k - \gamma \frac{C_{p,g}}{\rho C_p} \sum_{k \in \mathcal{G} \cup \text{SUB}} h_k \dot{s}_k, \quad (2.80)$$

corresponding to the source term $\dot{\omega}_{s,h_g}$ in Eq. (2.18).

2.4.4 Thermal radiation

In aluminum combustion, very high flame temperatures occur, causing the gaseous and condensed phase molecules to spontaneously acquire higher energy levels. Due to the instability of these excitation states, the molecules emit electromagnetic waves (photons) which appear as thermal radiation and cause radiative heat losses. Since electromagnetic waves travel at the speed of light, the associated energy is nearly instantaneously transported out of the reactor into the ambient environment. Within the scope of our kinetic model, thermal radiation is accounted for as a local sink term in the dispersion enthalpy balance that leaves the gas and droplet masses unchanged ($dm_g/dt = 0$, $dm_l/dt = 0$),

$$\frac{dh(t)}{dt} = C_p \frac{dT(t)}{dt} = \dot{q}_{\text{rad}}. \quad (2.81)$$

Here, \dot{q}_{rad} [J/(kgs)] denotes the emissive power. On substitution of Eq. (2.81) into the time derivative of Eq. (2.2), we obtain for the concomitant change in gas enthalpy

$$\frac{dh_g(t)}{dt} = \frac{C_{p,g}}{C_p} \dot{q}_{\text{rad}} \quad (2.82)$$

which coincides with the source term $\dot{\omega}_{\text{rad},h_g}$ due to radiation in Eq. (2.18). By Kirchhoff's law, the degrees of absorption and emission coincide and both mechanisms take place at the same spectral lines. Furthermore, we assume the gas-droplet dispersion to behave as an optically thin medium that does not reabsorb any emitted radiation. The radiation disappears into a background medium at the constant reference temperature $T_{\text{ref}} = 295 \text{ K}$.⁵ In this case, the Stefan–Boltzmann law [118, Chapter 1] yields the following kinetic expression for the radiative heat flux [103, 106, 160]

$$\dot{q}_{\text{rad}}(T, \mathbf{Y}, N(\cdot)) = -\frac{4\sigma_{SB}}{\rho} (\varepsilon_g \kappa_{P,g} + \varepsilon_l \kappa_{P,l}) (T^4 - T_{\text{ref}}^4). \quad (2.83)$$

Here, σ_{SB} denotes the Stefan–Boltzmann constant and κ_P is the Planck mean absorption coefficient of the gas (subscript g) or the dispersed droplet phase (subscript l), respectively. By definition, κ_P relates the emissive power of a real, grey body to that of a black body and, thus, provides a quantitative measure of the radiative quality of a body [118],

$$\kappa_P = \frac{\int_0^\infty \kappa_{P\lambda_w} E_{b\lambda_w} d\lambda_w}{\int_0^\infty E_{b\lambda_w} d\lambda_w}. \quad (2.84)$$

In Eq. (2.84), $\kappa_{P\lambda_w}$ is the spectral absorption coefficient, while

$$E_{b\lambda_w} = \frac{2\pi h_P c^2}{\lambda_w^5 \left(\exp\left(\frac{h_P c}{\lambda_w k_B T}\right) - 1 \right)} \quad (2.85)$$

represents the blackbody emissive power. Furthermore, h_P denotes Planck's constant and c is the speed of light in the ambient gas. For ordinary gases and optically thin gas-droplet dispersions, the speed of light may be approximated by its value in vacuum. In the Rayleigh scattering limit of small molecules or particles, the spectral absorption coefficient can be computed from [118]

$$\kappa_{P\lambda_w} = \frac{36\pi n_1 n_2}{\lambda_w \left((n_1^2 - n_2^2 + 2)^2 + 4n_1^2 n_2^2 \right)}, \quad (2.86)$$

⁵For the considerations in Chapters 4 and 5 this value was chosen as 298 K to coincide with the inflow conditions.

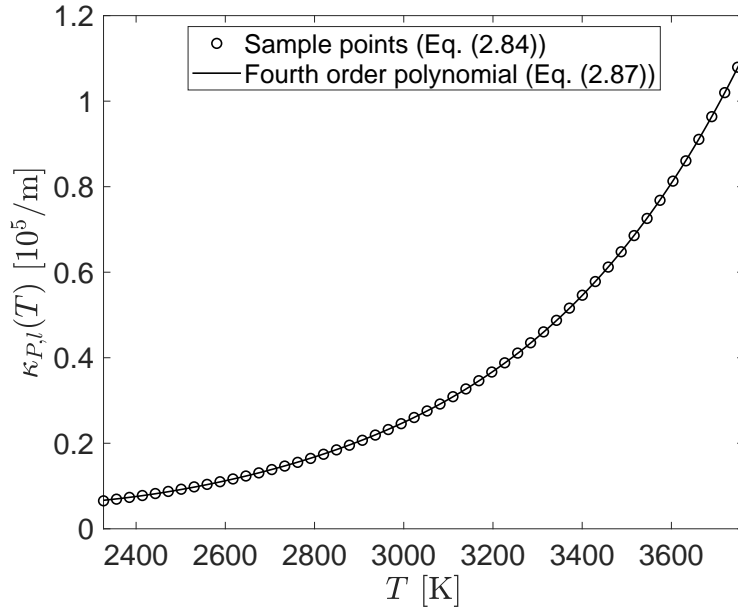


Figure 2.10 Temperature dependency of the Planck mean absorption coefficient of $\text{Al}_2\text{O}_3(1)$ droplets (Eq. (2.84)) and polynomial fit (Eq. (2.87)).

where n_1 and n_2 are the refractive and absorption indices of the complex-valued and material-dependent index of refraction, $\mathcal{N}_r = n_1 - i n_2$. Over the wavelength range $\lambda_w \in [\lambda_{w,\min}, \lambda_{w,\max}] = [0.265 \mu\text{m}, 5.58 \mu\text{m}]$ and the temperature range $T \in [2500 \text{ K}, 3500 \text{ K}]$, Duval et al. [42, Eqs. (11) and (12)] list approximations of the refractive and absorption indices of $\text{Al}_2\text{O}_3(1)$ [39, 42, 110, 135]. In the absence of alternatives, we employ these approximations across the temperature range $[T_{m,\text{Al}_2\text{O}_3}, T_{b,\text{Al}_2\text{O}_3}]$, although this slightly exceeds their range of validity. Furthermore, in the evaluation of κ_P for $\text{Al}_2\text{O}_3(1)$ ($= \kappa_{P,l}$) by Eq. (2.84), $\kappa_{P\lambda_w}$ is assumed to vanish outside the wavelength range $[\lambda_{w,\min}, \lambda_{w,\max}]$. This leads to an underestimation of the radiative heat losses as emissive contributions from wavelengths outside $[\lambda_{w,\min}, \lambda_{w,\max}]$ are omitted. Based on a numerical integration of Eq. (2.84) at different temperature sample points, we calibrated $\kappa_{P,l}$ as a fourth order polynomial in T (Fig. 2.10),

$$\kappa_{P,l}(T) = \sum_{k=0}^4 a_k T^k. \quad (2.87)$$

The coefficients a_i , $i = 0, \dots, 4$, are listed in Table 2.2. Compared to Eq. (2.84), the maximum relative error in Eq. (2.87) over the temperature range $[T_{m,\text{Al}_2\text{O}_3}, T_{b,\text{Al}_2\text{O}_3}]$ amounts to 2%. In order to verify the evaluation of $\kappa_{P,l}$ based on Eq. (2.84), we confirmed that it yields the well-known value for the Planck mean absorption coefficient of soot [103].

Besides the radiation of $\text{Al}_2\text{O}_3(1)$ droplets, there is evidence that gas phase species, for

example, AlO [134], radiate at discrete wavelengths. However, quantitative studies on gas radiation within the scope of aluminum combustion are scarce and we were not able to identify the Planck mean absorption coefficient $\kappa_{P,g}$ for any of the gaseous species in the reaction mechanism. For this reason, gas phase radiation is omitted here, $\kappa_{P,g} = 0$.

| Coefficients | Values |
|--------------|-------------------------|
| a_0 | 8.184×10^5 |
| a_1 | -1.232×10^3 |
| a_2 | 7.012×10^{-1} |
| a_3 | -1.799×10^{-4} |
| a_4 | 1.787×10^{-8} |

Table 2.2 Coefficients of the polynomial fit in Eq. (2.87) for the temperature dependency of the Planck mean absorption coefficient $\kappa_{P,l}(T)$ of $\text{Al}_2\text{O}_3(l)$ droplets.

2.4.5 Characteristic time scales of droplet formation and interaction

Chemical reactions and droplet formation/interaction processes can take place on very different time scales, posing immense challenges for numerical time integrators. However, also in physical terms, characteristic time scales play an important role. They provide insights into the mutual competition and interaction of processes and allow for the identification of dominant processes. Frequently, even dynamic simplifications are motivated by time scale analyses. In this section, the formulas for estimating the time scales of droplet nucleation, growth and coagulation are briefly reviewed.

For nucleation, the characteristic time scale can be obtained from the evolution equation for the total number density $M_0(t)$. Taking $G = 0$, $\beta = 0$, $dV/dt = 0$ and integrating the PBE (Eq. (2.22)) over v -space yields

$$\dot{M}_0^N = \int_{\Omega_v} \dot{R} \delta(v - v_0) dv = \dot{R} \quad (2.88)$$

for the temporal change of the zeroth moment due solely to nucleation. The nucleation time scale is then readily obtained as the ratio of the number of droplets and its rate-of-change at the current point in time [181],

$$\tau_N = \frac{M_0}{\dot{R}}. \quad (2.89)$$

2 The perfectly stirred reactor

Since droplet growth causes the mass of the liquid phase $m_l(t)$ to change, we define the time scale associated with growth in terms of $\dot{m}_l^G(t) = \rho_l V(t) \dot{M}_1^G(t)$ (Eq. (2.56)) according to

$$\tau_G = \frac{m_l}{|\dot{m}_l^G|} = \frac{M_1}{|\dot{M}_1^G|}. \quad (2.90)$$

Here, the absolute value ensures a positive time scale even though the mass of the liquid phase may decrease due to evaporation. From the PBE for pure growth (Eq. (2.22) with $\dot{R} = 0$, $\beta = 0$, $dV/dt = 0$), the change in the first moment due to growth is obtained as

$$\begin{aligned} \dot{M}_1^G &= \int_{\Omega_v} v \frac{\partial N(v)}{\partial t} dv = - \int_{\Omega_v} v \frac{\partial G(v) N(v)}{\partial v} dv \\ &= -v G(v) N(v) \Big|_{\partial\Omega_v} + \int_{\Omega_v} G(v) N(v) dv, \end{aligned} \quad (2.91)$$

where the final equality follows from integration by parts and $\partial\Omega_v$ denotes the boundary of v -space. Since the cancellation of droplet growth ($G > 0$) and shrinkage ($G < 0$) may lead to an overestimation of τ_G , G is replaced by the absolute value $|G|$ inside the integral on the right hand side of Eq. (2.91).

Adapting the idea used for the evaluation of the nucleation time scale, we evaluate the coagulation time scale based on the rate at which the total number density decreases, that is

$$\tau_C = -\frac{M_0}{\dot{M}_0^C}, \quad (2.92)$$

where \dot{M}_0^C is the change in the zeroth moment associated with coagulation,

$$\begin{aligned} \dot{M}_0^C &= \int_{\Omega_v} \left(\frac{1}{2} \int_{v_1}^v \beta(v-w, w) N(v-w) N(w) dw \right. \\ &\quad \left. - \int_{\Omega_v} \beta(v, w) N(v) N(w) dw \right) dv. \end{aligned} \quad (2.93)$$

2.5 Numerical methods

In order to convert the PBE into a dynamical system for droplet phase scalars $\mathbf{H}(t)$ parameterizing $N(\cdot, t)$, we employ the high resolution finite volume method of Koren [93] on a fixed exponential v -grid with 512 cells [132]. The coagulation source terms are evaluated with the aid of the conservative scheme developed by Liu and Rigopoulos [104] and O'Sullivan and Rigopoulos [119]. The Dirac δ -distribution in the nucleation term,

moreover, is approximated, in v -discrete terms, by a symmetric, hat-shaped profile on the interval $v \in [v_0 - v_1 \Delta n_0, v_0 + v_1 \Delta n_0]$ with unity integral.

The system of ordinary differential equations (ODEs) that describes the time evolution of $\Phi(t)$, $\Psi(t)$, $\mathbf{H}(t)$ and $\gamma(t)$ in the PSR is decomposed into three sequential steps for gas/surface chemistry, droplet formation/interaction and gas-droplet mass/heat exchange using a first order accurate fractional steps scheme [128, Section 6.3]. This has the advantage that any stiffness associated with potential disparities in the characteristic time scales among the fractional steps is eliminated and that the numerical time integration method can be adapted to the requirements of each fractional step. At the end of every fractional step, the droplet phase scalars $\mathbf{H}(t)$ are updated to account for changes in the reactor volume (Eqs. (2.22) and (2.24) with $G = 0$, $\dot{R} = 0$, $\beta = 0$). Similarly, the surface density $\gamma(t)$ is explicitly advanced in time, apart from the chemistry step where Eq. (2.21) is solved in a fully coupled way. In order to solve the ODE system governing the gas/surface chemistry (Eqs. (2.15) and (2.16) with $\dot{\omega}_{gl} = \mathbf{0}$), we employ the variable order implicit time integrator DVODE [21] or the fifth order accurate implicit Runge-Kutta method RADAU5 [75]. The PBE fractional step (Eq. (2.26) based on Eq. (2.22) with $dV(t)/dt = 0$), by contrast, is integrated in time using the third and fifth order accurate explicit Runge-Kutta methods RK3(2) [18, 20] and DOPRI5 [76]. Lastly, mass and heat are exchanged between the gas phase and the droplet dispersion (Eq. (2.15) with $\dot{\omega}_g = \mathbf{0}$, $\dot{\omega}_s = \mathbf{0}$, $\dot{\omega}_{\text{rad},h_g} = 0$) by invoking the explicit Euler method, followed by an algebraic solution of our dissociation relations (Eq. (2.70) to (2.73)). Since the v -discrete PBE is explicitly integrated in time, we select the leading time step of the fractional steps decomposition as $\Delta t_n = 5 \times 10^{-9}$ s; this value remains below the smallest droplet formation time scale (Section 2.4.5) for the PSR investigated in Section 2.6 (Fig. 2.14(a)). For more details on the numerical solution schemes and, particularly, the decoupling of droplet formation and gas phase chemistry, we refer to Section 4.5.

2.6 Aluminum combustion at atmospheric pressure

In the present section, we employ the kinetic framework developed in Section 2.4 to investigate the combustion of aluminum in the PSR of Section 2.3. The PSR is operated at constant atmospheric pressure, $p = 1$ atm, and fuelled by bulk aluminum through a

reactive surface. In order to avoid setting an initial bulk mass and tying the PSR to a particular length scale, we assume the amount of Al(B) underneath the reactive surface to be so large that the evaporation of aluminum is not limited by the availability of Al(B). Initially, all surface sites are occupied by Al(S) and the surface density $\gamma(t = 0)$ amounts to $0.4 \text{ m}^2/\text{m}^3$ [69]. On start-up, the reactor is filled with pure air consisting of O_2 and N_2 at a ratio of 21/79 by volume. As initial temperature, we choose the boiling temperature of liquid aluminum, $T(0) = T_{b,\text{Al}} = 2791 \text{ K}$. In the first part of this section, we analyze the combustion of aluminum in a PSR without NO_x chemistry in order to understand the key mechanisms of Al oxidation and oxide smoke inception, before we assess the effect of nitrogen oxide species on the combustion characteristics towards the end of the section.

2.6.1 Gas phase chemistry without NO_x formation

For a PSR operated without NO_x chemistry, Figs. 2.11 and 2.12 depict the time courses of key gas phase and surface/bulk species as well as the concomitant changes in temperature and supersaturation. As aluminum vaporizes from the reactive surface, the temperature decreases slightly until about $t = 10^{-5} \text{ s}$ because the heat of evaporation is extracted from the gas and because the release of fuel molecules introduces additional thermal inertia into the reactor. The evaporation is reflected in the negative accumulated bulk mass of Al(B). The gaseous aluminum reacts very rapidly with oxygen to form aluminum suboxides, particularly Al_2O , AlO and AlO_2 , which are, subsequently, converted into gaseous $\text{Al}_2\text{O}_3/c$, driving a surge in supersaturation. The exothermicity of these reactions as well as the heat release from the incipient condensation of $\text{Al}_2\text{O}_3(l)$ droplets counteract the decrease in temperature due to evaporation until, at approximately $t = 10^{-4} \text{ s}$, the temperature exceeds the initial temperature, rising up to the dissociation temperature of $\text{Al}_2\text{O}_3(l)$. At this point, almost all O_2 has been consumed and the supply of gaseous $\text{Al}_2\text{O}_3/c$ ceases. Condensation proceeds until the supersaturation vanishes and ends at about $t = 4 \times 10^{-4} \text{ s}$. All the while, the evaporation of aluminum continues, causing the temperature to decrease once the heat supply by combustion and condensation terminates. Additionally, radiation from the dispersed oxide droplets contributes a heat sink that promotes the reduction of temperature. In the absence of oxidizer, gaseous Al accumulates inside the reactor. Ultimately, evaporation also ceases as the temperature decreases below the aluminum boiling point.

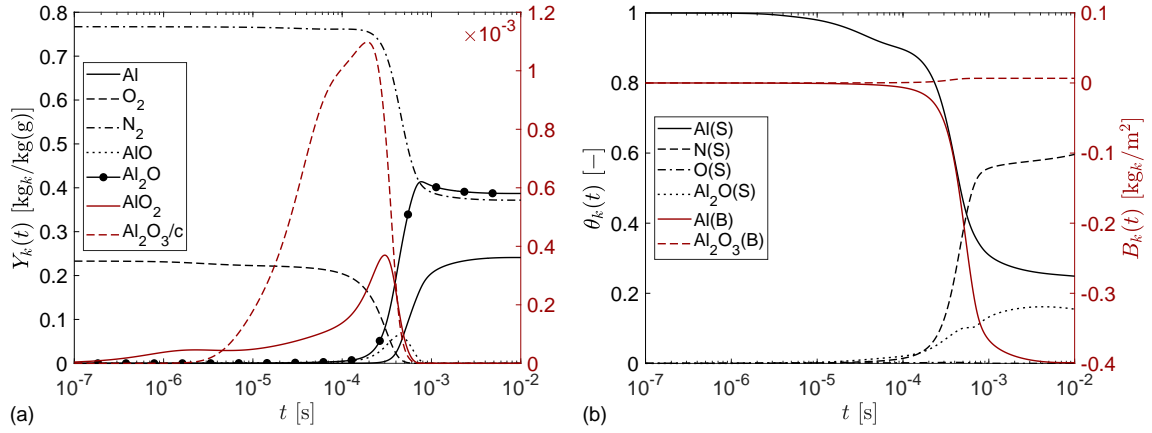


Figure 2.11 Temporal change in the chemical gas phase composition (a) and the surface composition (b) in a PSR without NO_x chemistry.

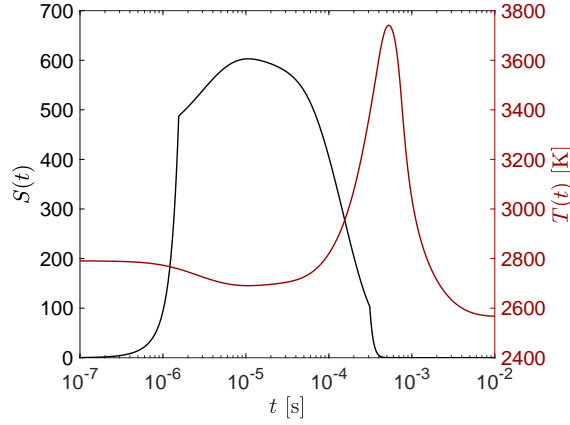


Figure 2.12 Time evolution of supersaturation and temperature in a PSR without NO_x chemistry.

Figure 2.11 indicates that the surface chemistry is heavily influenced by the presence of N_2 in the initial atmosphere. Nitrogen may adsorb onto the surface, yielding $\text{N}(\text{S})$ surface species that remain unreactive and, thus, deactivate the surface sites. Consequently, the proportion of surface sites through which $\text{Al}(\text{S})$ (or $\text{Al}(\text{B})$, respectively) may evaporate decreases, impeding the aluminum evaporation rate. Lastly, we mention that, out of all the condensed phase $\text{Al}_2\text{O}_3(\text{l})$ formed inside the reactor by the final time $t = 10^{-2}$ s, $[\text{Al}_2\text{O}_3(\text{B})]/[\text{Al}_2\text{O}_3(\text{B}) + \text{Al}_2\text{O}_3(\text{l})] = 18.8\%$ are directly formed at the reactive surface due to heterogeneous reactions, where $[\cdot]$ denotes a mass concentration ($[\text{kg}_k/\text{m}^3]$).

Complementary to Figs. 2.11 and 2.12, the change in the oxide smoke size distribution over time is shown in Fig. 2.13. In order to elucidate, concomitantly, the competition between droplet nucleation, growth and coagulation in shaping the droplet size distribution, we provide the corresponding time scales (Section 2.4.5) in Fig. 2.14(a). Typically, the

2 The perfectly stirred reactor

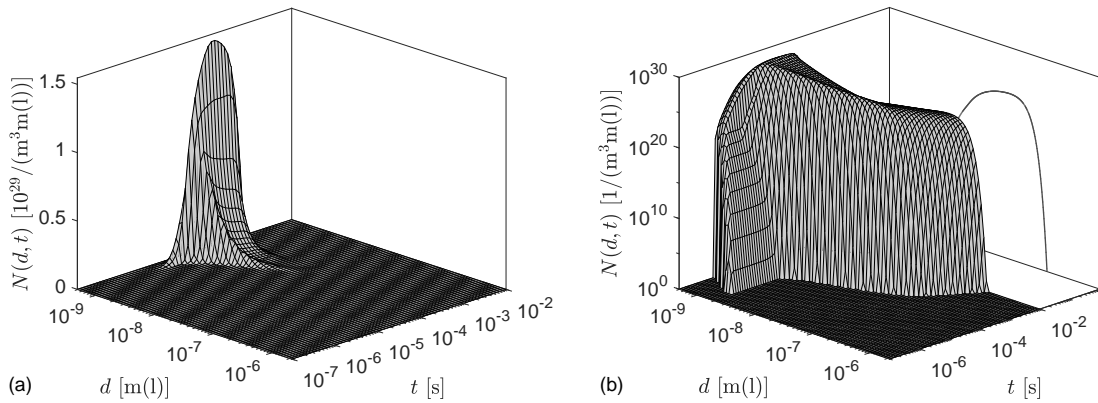


Figure 2.13 Temporal change of the $\text{Al}_2\text{O}_3(\text{l})$ droplet size distribution on linear (a) and logarithmic scales (b) in a PSR without NO_x chemistry. In figure (b), the droplet size distribution at the final time point ($t = 10^{-2}$ s) is shown in the far right N - d -plane. Note that the droplet size distribution was transformed from a volume-based to a diameter-based distribution.

process with the smallest associated time scale at a given time is the most vigorous and dominant. Figures 2.13 and 2.14(a) indicate that, until $t \approx 2 \times 10^{-5}$ s, nucleation dominates droplet formation and most droplets possess the nuclei volume. As supersaturation increases, the nuclei volume decreases up to the point where the smallest nuclei with volume $v_0 - v_1 \Delta n_0$ consist of single $\text{Al}_2\text{O}_3(\text{l})$ molecules (Section 2.4.1). This limit point is reflected by the kink in the supersaturation curve at $t = 1.5 \times 10^{-6}$ s in Fig. 2.12 (and also later at $t = 3 \times 10^{-4}$ s). At $t = 3 \times 10^{-5}$ s, growth and coagulation become competitive, in terms of time scale, with nucleation and the droplet size distribution begins to propagate and extend towards larger droplet sizes. Once the supersaturation falls below unity, nucleation ceases ($\tau_N \rightarrow \infty$), whereas condensational surface growth gives way to evaporative shrinkage ($v_0 \rightarrow \infty$). As the temperature decreases, however, evaporation rapidly slows down. At the same time, coagulation continues and remains the dominant droplet formation process in the final stages which is also reflected in the very smooth droplet size distribution at the final point in time (Fig. 2.13(b)). For an average mean free path of $\lambda_{\text{mfp,g}} = 7 \times 10^{-7}$ m, the Knudsen number associated with mean-sized droplets is very much bigger than unity (even the largest droplets with $d \approx 3 \times 10^{-7}$ m are characterized by $\text{Kn} \approx 5$) and, thus, most droplets persist in the kinetic regime.

As key statistics characterizing the droplet size distribution, Fig. 2.14(b) shows the mean and standard deviation of the droplet diameter over time. For comparison and to identify the influence of nucleation, the nuclei diameter d_0 is also included in Fig. 2.14(b). Depending on the residence time inside the reactor, the mean droplet diameter ranges

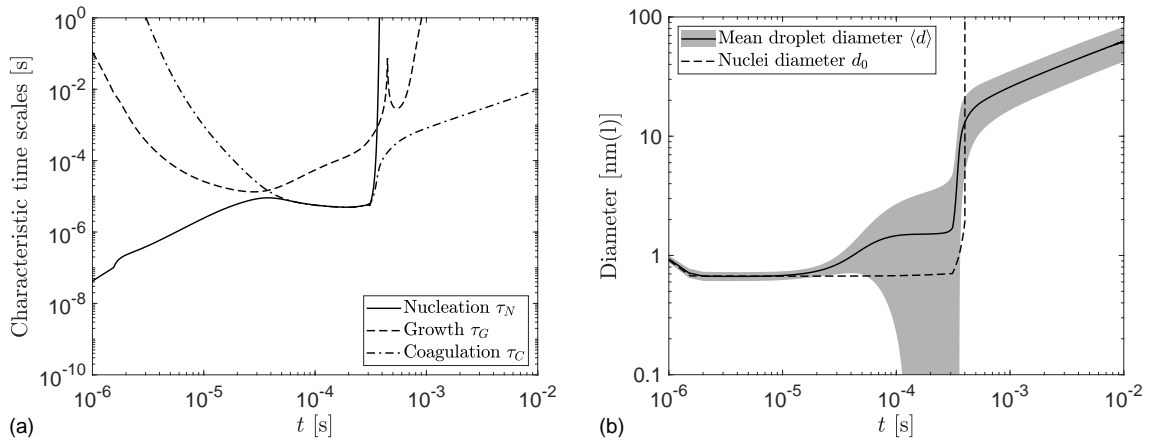


Figure 2.14 Temporal evolution of the characteristic time scales controlling droplet nucleation, growth and coagulation (a) as well as the critical nuclei size and the mean droplet diameter (b) in a PSR without NO_x formation. The shaded area indicates plus/minus one standard deviation from the mean droplet diameter.

between 10^{-9} m and 10^{-7} m. Although these sizes may be too small for an efficient separation from the gas phase without the use of filters, we emphasize that the PSR is an idealized test bed that does not include all physical effects determining the fate of oxide smoke. For example, thermophoresis and advective/diffusive transport (Chapters 4 and 5) provide natural means by which oxide smoke droplets can be removed from the carrier gas and deposited on a burning Al-fuel particle, turning into large oxide residues [60].

2.6.2 Effect of nitrogen oxide formation

Nitrogen oxides are major gaseous pollutants that form during the combustion of fuels in air [64]. Particularly at the high temperatures encountered in aluminum combustion, the thermal pathway for NO formation is thought to be strong, posing an important concern. In this section, the analyses from Section 2.6.1 are repeated for a gas phase chemistry that has been amended by the relevant NO_x reactions of Glarborg et al. [64] in order to quantitatively estimate the amount of NO_x formed and assess their influence on Al-surface chemistry.

Figure 2.15 shows the time evolution of gas phase and surface species including NO_x. During the initial stage of the combustion in the PSR (until about $t = 4 \times 10^{-4}$ s), the gas phase composition is very similar to the one without NO_x formation in Fig. 2.11. The production of NO, the most important NO_x species by mole fraction, quickly accelerates at about $t = 10^{-4}$ s. The high-temperature NO_x chemistry is accompanied by the production

2 The perfectly stirred reactor

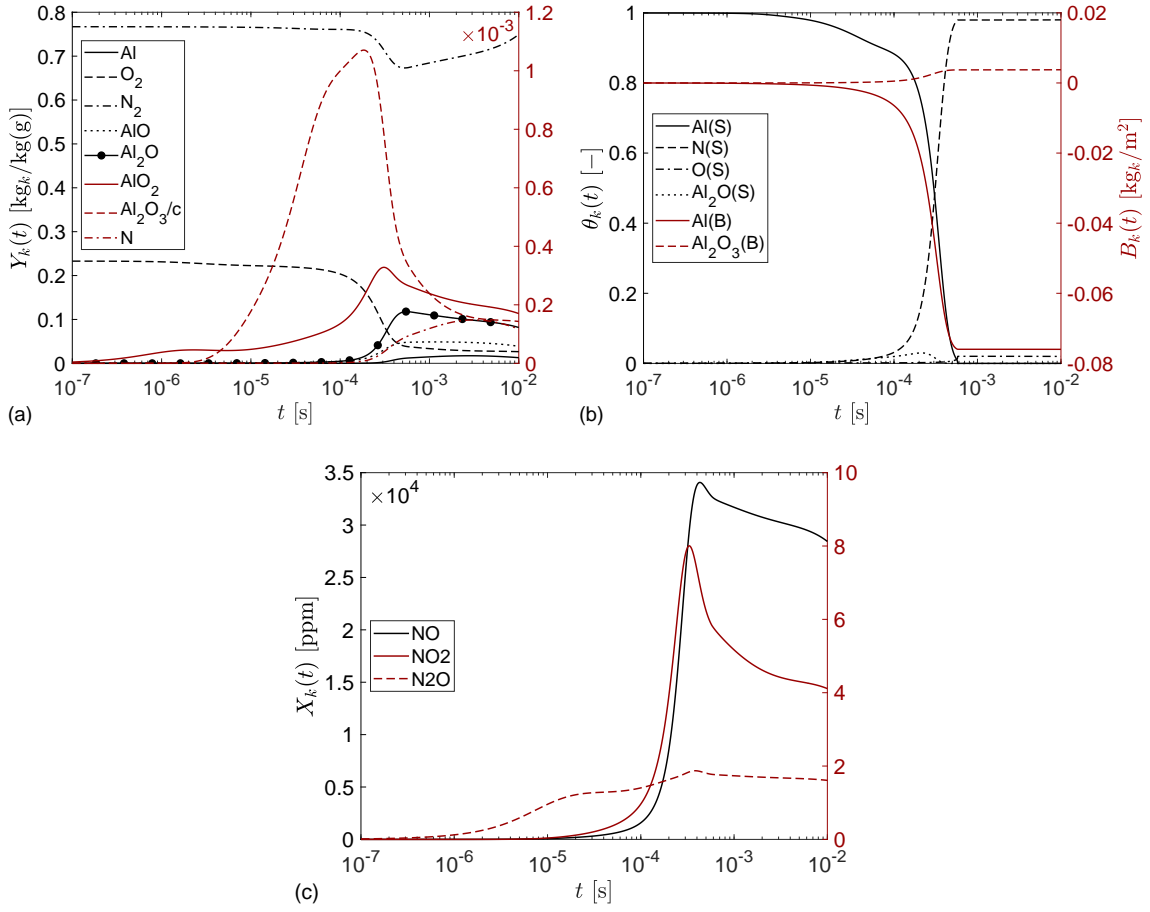


Figure 2.15 Temporal change in the chemical gas phase composition (a, c) and the surface composition (b) for a PSR with NO_x chemistry.

of atomic nitrogen N that adsorbs onto the reactive surface and deactivates the surface sites. By $t = 5 \times 10^{-4}$ s, the reactive surface has been covered almost completely by unreactive N(S), eliciting a rapid termination of all surface reactions and interrupting the Al(B)/Al fuel supply. An important consequence of the blockage of the reaction sites by N(S) is that the formation of bulk liquid aluminum oxide ($\text{Al}_2\text{O}_3(B)$) at the surface ceases. Compared to the previous case without NO_x chemistry, this results in a decrease of the $\text{Al}_2\text{O}_3(l)$ fraction formed on the reactive surface to 4.8%. The occupation of the surface sites by atomic nitrogen proceeds very fast, *i.e.*, at time scales much smaller than typical particle burning times (Chapter 5), casting doubt on the compatibility of the surface [69] and NO_x mechanisms [64]. Since, at least to our awareness, the surface mechanism was never tested with NO_x chemistry, we discard the reaction



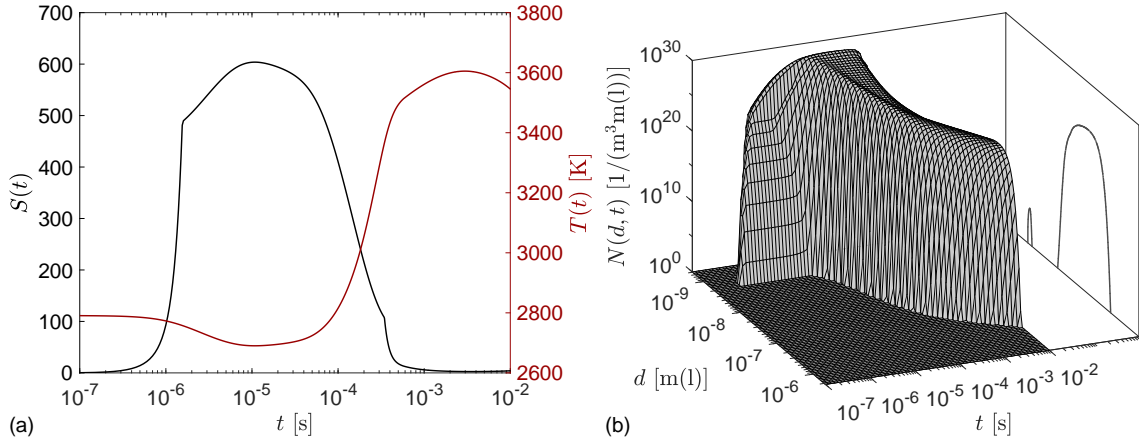


Figure 2.16 Time evolution of the supersaturation and temperature (a) and the droplet size distribution (b) in a PSR with NO_x chemistry.

leading to the deactivation of the surface sites, from the surface mechanism for the spatially resolved single particle investigations presented in Chapters 4 and 5.

Complementary to Fig. 2.15, Fig. 2.16 depicts the temporal changes in the supersaturation and temperature alongside the droplet size distribution. Here, the maximum temperature is slightly smaller than in our previous case without NO_x chemistry and remains below the dissociation temperature of alumina. Because the adsorption of $\text{N}(\text{S})$ on the surface inhibits evaporation, the heat losses from the gas to the evaporating surface subside and the temperature remains high.

In Figs. 2.15 and 2.16(a), we additionally observe that gaseous $\text{Al}_2\text{O}_3/\text{c}$ and Al remain in the gas phase alongside O_2 ($t \gtrsim 5 \times 10^{-4}$ s). The presence of $\text{Al}_2\text{O}_3/\text{c}$ is reflected in a small supersaturation of about 3 that drives the formation of nuclei with volumes v_0 and the condensational growth of droplets with $v \geq v_0$. Conversely, droplets with $v < v_0$ evaporate, thereby releasing AlO and O_2 (Eq. (2.64)) from which other suboxides and $\text{Al}_2\text{O}_3/\text{c}$ are generated. Because AlO competes with the remaining Al for O_2 , the gas phase oxidation of Al slows down and Al and O_2 exist besides one another. At the same time, O_2 and N_2 are regenerated from NO . Since the heat release from Al -combustion, droplet formation and N_2 recovery are counteracted by the endothermal O_2 regeneration, the evaporation of subcritical droplets and, more importantly, the absorption of heat by the growing droplet phase ($C_{p,l} > C_{p,g}$), the temperature begins to decrease, resulting in a slight increase in the supersaturation (Eq. (2.29)) and a concomitant reduction of v_0 . The nuclei that are formed at this stage are smaller than the droplets already present in

2 The perfectly stirred reactor

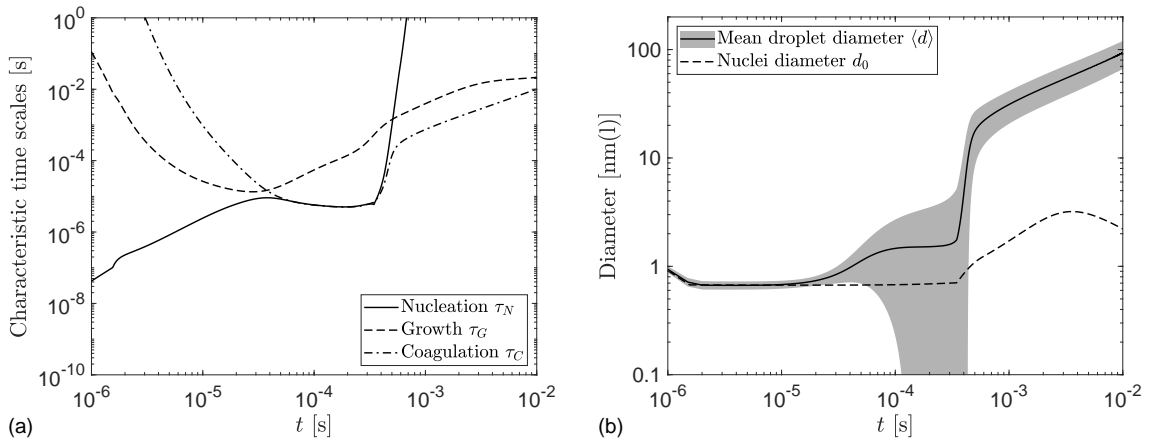


Figure 2.17 Temporal evolution of the characteristic time scales controlling droplet nucleation, growth and coagulation (a) as well as the critical nuclei size and the mean droplet diameter (b) in a PSR with NO_x formation.

the reactor, eliciting a small-size mode in the final droplet size distribution (N - d -plane in Fig. 2.16(b)). By $t = 8 \times 10^{-3}$ s, all subcritical droplets have disappeared either due to coagulation or evaporation.

Contrary to the case without NO_x formation, surface growth still competes with coagulation in shaping the droplet size distribution towards the end of our simulation (Fig. 2.17(a)). In particular, the continuing droplet growth ($S > 1$) causes the final mean droplet diameter to be larger than the one measured without NO_x chemistry by about 50% as depicted in Fig. 2.17(b).

2.7 Aluminum combustion at elevated pressures

While the operating pressure was kept at atmospheric level up until now, this section is devoted to the investigation of the influence a varying operating pressure has on the predictions obtained in a PSR. In particular, here, we report on amendments on the kinetic framework used so far and elucidate how the reactor pressure affects the temperature and smoke droplet size evolution.

2.7.1 Extensions of the kinetic framework

In this section, the kinetic framework presented in Section 2.4 is applied with two modifications. First, droplet dissociation is solely considered as a special case of droplet evaporation (Eqs. (2.44), (2.45) and (2.64)), proceeding at a finite rate as already discussed in the end

of Section 2.4.2. In this way, we are able to elucidate the impact the superimposed instantaneous dissociation mechanism of Section 2.4.2 has on our predictions of temperature and smoke size, for example. Second, we extend the kinetic framework to account for droplet deposition on the reactive surface, since the collision of droplets with the reactive surface may increase significantly at elevated pressures, possibly increasing the amount of $\text{Al}_2\text{O}_3(\text{B})$. Specifically, in the kinetic regime, the rate at which droplets with volume v impinge on a surface is given by

$$\dot{s}_{\text{dep}}(v, T) = -\sqrt{\frac{k_B T}{2\pi\rho_l v}}\gamma. \quad (2.95)$$

Including droplet deposition, kinetically driven by Eq. (2.95), in the oxide smoke dynamics yields a slightly modified version of the PBE in Eq. (2.22),

$$\begin{aligned} \frac{\partial N}{\partial t} + \frac{\partial(GN)}{\partial v} &= \dot{R}\delta(v - v_0) + \dot{s}_{\text{dep}}N - \frac{N}{V}\frac{dV}{dt} \\ &+ \frac{1}{2}\int_{v_1}^v \beta(v - w, w)N(v - w, t)N(w, t)dw \\ &- \int_{\Omega_v} \beta(v, w)N(v, t)N(w, t)dw. \end{aligned} \quad (2.96)$$

Accordingly, the change in the transmitted mass of $\text{Al}_2\text{O}_3(\text{B})$ relates to the rate-of-change in the droplet volume fraction obtained from v -weighted integration of the PBE in Eq. (2.96) while taking $G = \dot{R} = dV/dt = \beta = 0$.

2.7.2 Effect of varying operating pressures

In order to accelerate the simulation campaign including several different pressure levels ranging from 1 bar to 10 bar, we decided to reduce the v -resolution to 256 cells compared to the previous section, which was proven to be sufficiently accurate (see also Section 4.6.1). Moreover, in Section 2.6, we found the oxide smoke size distributions encountered in the PSR to feature a heavy logarithmic tail towards large droplet sizes (Figs. 2.13 and 2.16(b)), which is particularly challenging to be accurately resolved using piecewise constant reconstructions of the number density [104, 119, 156]. In order to accurately represent the large-size tail of the droplet size distribution and to assess the effect the choice of the coagulation scheme has on our results, the coagulation source terms in Eq. (2.96) are v -discretely evaluated using a recently developed conservative finite volume scheme based

2 The perfectly stirred reactor

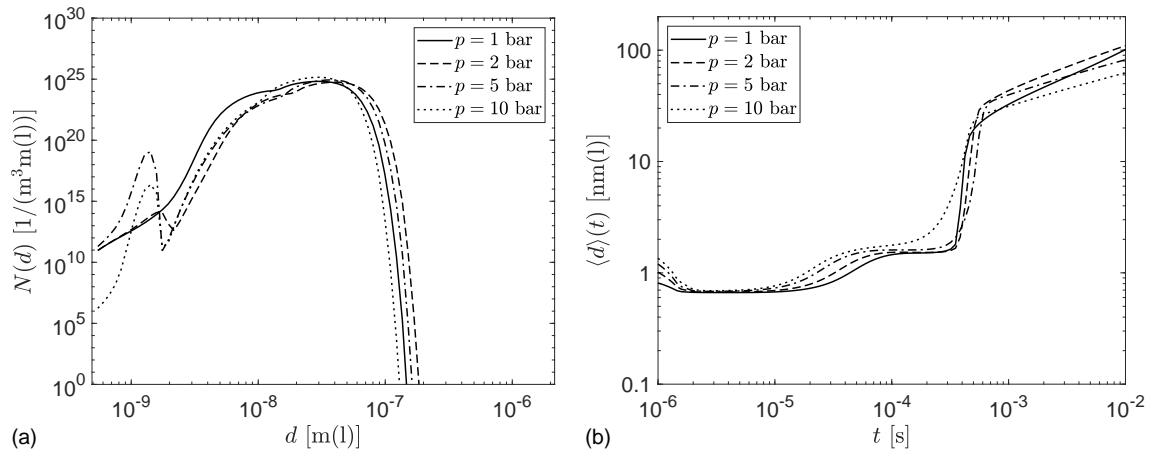


Figure 2.18 Oxide smoke droplet size distributions $N(\cdot)$ at time $t = 10^{-3}$ s (a) and time evolution of the mean droplet diameter $\langle d \rangle$ (b) for different operating pressures.

on a piecewise linear, discontinuous reconstruction of N [156].

Initially, the PSR contains pure air at the aluminum boiling temperature [9, Eq. (8)], yielding a different initial condition on T due to varying pressures, and features a reactive surface made from pure liquid aluminum. The results reported in the following are obtained with NO_x chemistry. Figure 2.18 shows the droplet size distributions $N(\cdot, t)$ at time $t = 10^{-3}$ s after start-up alongside the time course of the mean droplet diameter $\langle d \rangle$ for different reactor pressures. Complementary to Fig. 2.18, Fig. 2.19 depicts the temporal evolution of the dispersion temperature as well as the evaporated Al(B) mass. Since we imagine the PSR to initially correspond to a cell at the surface of a reactive Al-particle immersed in air (Fig. 2.1), the reactor’s initial volume and surface density are unchanged as the operating pressure is modified. Consequently, at a larger pressure, the gas mass that is initially present inside the reactor is also larger, enhancing the reactor’s thermal inertia. This increase in heat capacity limits the temperature rise accompanying the release of combustion heat to such an extent that the maximum temperature at 10 bar is about 400 K lower than at 1 bar, curtailing further evaporation (Fig. 2.19). Since the gas phase and surface reactions are enhanced by the larger species concentrations at higher pressures and since lower temperatures entail larger supersaturations, droplet condensation is promoted (Fig. 2.18(b)). At $t \approx 5 \times 10^{-4}$ s, coagulation begins to dominate the droplet dynamics. Perhaps due to the higher temperatures, coagulation appears to be more effective at lower pressures. However, the droplets still remain nano-sized on average and, at least in the PSR, the effect of pressure on the smoke size (distribution) is limited.

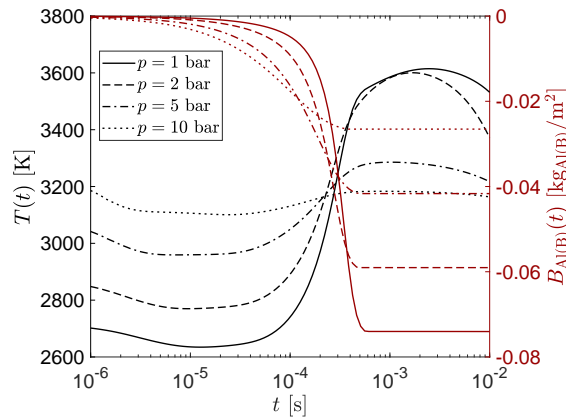


Figure 2.19 Time evolution of temperature and evaporated Al(B) mass for different reactor pressures.

Comparing the amount of bulk aluminum oxide ($\text{Al}_2\text{O}_3(\text{B})$) at the reactive surface for $p = 1$ bar calculated here including droplet deposition (Eqs. (2.95) and (2.96)) with the results reported in Section 2.6.2 (excluding deposition) reveals an insignificant effect of smoke deposition on our predictions. This observation is, moreover, confirmed by the fact that the deposition mass flux computed based on Eq. (2.95) is orders of magnitude smaller than the rate at which bulk alumina is formed upon heterogeneous surface chemistry. Hence, kinetically driven droplet deposition is negligible within the scope of the PSR. Regarding the differences between finite-rate dissociation and the additional instantaneous removal of droplet mass to strictly maintain the flame temperature at the alumina boiling point, we found no discernible changes in our key observables if the time step size is sufficiently small, suggesting that the finite-rate dissociation included in the droplet growth rates (Eqs. (2.44) and (2.45)) is already sufficiently fast.

2.8 Chapter conclusions

In the present chapter, we combined balance laws for mass and enthalpy with a population balance approach to describe the size-resolved condensation of oxide smoke during aluminum combustion above a reactive aluminum surface. The changes in the gas phase composition, the surface composition and the oxide size distribution are kinetically driven by chemical reactions and surface-gas-transitions as well as droplet nucleation, condensation/dissociation, coagulation and radiation for which we supplied detailed expressions informed by low-level theories. With the exception of the gas and surface chemistry, a

2 The perfectly stirred reactor

particular feature of our kinetic framework is that it can be adapted also to other metals by replacing the relevant material properties.

The dynamics of the gas composition, the surface composition and the droplet size distribution were formulated in the context of a perfectly stirred reactor. The PSR is an important test bed that permits the analysis of localized gas, surface and droplet interactions in a single finite volume cell of a laminar flow simulation independent of spatial transport.

In the absence of NO_x chemistry, we observed that the combustion and concomitant oxide smoke condensation in the PSR terminate when all oxygen has been consumed and the temperature has decreased below the aluminum boiling point. By contrast, NO_x chemistry promotes the formation of atomic nitrogen that adsorbs onto the reactive aluminum surface, causing its deactivation. In this case, the droplet size distribution ultimately acquires a bimodal shape as small nuclei form in a remnant, slightly supersaturated vapour while the existing large droplets grow and progressively shift towards larger sizes. The oxide smoke droplets remained nano-sized on average, rendering their potential separation from exhaust fumes challenging. An increase in reactor pressure, however, results in a faster formation of larger droplets at early times, an effect that may be outrun at lower pressures by subsequent vigorous high-temperature coagulation.

Despite its reliance on fundamental low-level theories, our kinetic framework involves assumptions and kinetic uncertainties or limitations. For example, gas phase radiation is omitted as we are not aware of data on the relevant Planck mean absorption coefficients. To aid enhancements and refinements, the main assumptions are summarized in Section A.3 of Appendix A. While all investigations in this chapter were limited to the spatially homogeneous case, our modelling efforts in Chapters 4 and 5 target the spatially resolved description of a burning aluminum particle, augmenting the kinetic processes considered here by advective, diffusive and thermophoretic transport to elucidate oxide smoke migration and deposition.

Chapter 3

The partially stirred reactor

3.1 Chapter introduction

Similar to its perfectly mixed counterpart discussed in the preceding chapter, the partially stirred reactor (PaSR) represents a spatially homogeneous test bed that resembles the dynamics in a single finite volume cell at the particle surface in a turbulent flame simulation (Fig. 1.4) based on the probability density function (PDF) approach [128, 140]. The PaSR is a simplified flow model in which the constituent phases are imperfectly mixed on the smallest length scales, but appear homogeneous on scales comparable to the reactor size. Frequently, the small-scale heterogeneity is caused by a distribution in residence time or age of the fluid elements inside the reactor, but may be also caused by heterogeneity on part of the reactive surface the fluid elements are in contact with.

Although the focus of this thesis is the analysis of laminar aluminum-fuelled flames on the single particle level, the developments presented in this chapter are indicative of how molecular mixing introduced by turbulence may affect the gas-phase composition and oxide smoke size distribution in the vicinity of a burning aluminum particle in a turbulent flame which is frequently encountered in practical metal dust burners.

The current chapter is structured as follows: In Section 3.2, the governing equations of a PaSR are presented along with the amendments required to account for the presence of a reactive surface with locally varying constitution and a temporal decorrelation of gas phase and surface compositions. This is followed by a brief discussion of the numerical methods applied to solve the governing transport equation (Section 3.3). The effect of residence time and molecular mixing on the temporal evolution of the gas phase and surface composition as well as the smoke droplet size distribution in a PaSR operated

3 The partially stirred reactor

at atmospheric pressure is then investigated in Section 3.4. Subsequently, in Section 3.5, we briefly assess the influence of increased reactor pressures on the temperature and the smoke droplets' sizes, before we conclude this chapter (Section 3.6). An overview of the stochastic solution scheme we employ to solve the model equation of the PaSR is contained in Appendix B.

3.2 Governing equations

3.2.1 A partially stirred reactor model

In line with Section 2.2, every fluid (or dispersion) element is described in terms of a vector of gas phase scalars $\Phi(t)$ and the local droplet size distribution $N(\cdot, t)$ at time t after the reactor was set into operation. Following the developments at the end of Section 2.2.3, the droplet size distribution $N(\cdot, t)$ is assumed to be uniquely parameterized in terms of the droplet phase scalars $\mathbf{H}(t)$. As $\Phi(t)$ and $\mathbf{H}(t)$ vary from one fluid element to another, we may consider $(\Phi(t), \mathbf{H}(t))$ as a random variable whose statistics contain information on all fluid elements inside the reactor. Formally, any statistical information on the variability of $\Phi(t)$ and $\mathbf{H}(t)$ over the fluid elements can be retrieved from the probability density function (*pdf*) $f_{\Phi, \mathbf{H}}(\phi, \mathbf{h}; t)$. In particular, $f_{\Phi, \mathbf{H}}(\phi, \mathbf{h}; t) d\phi d\mathbf{h}$ provides the likelihood for selecting out of all fluid elements inside the reactor an element with gas phase composition $\Phi(t) \in [\phi, \phi + d\phi]$ and droplet phase scalars $\mathbf{H}(t) \in [\mathbf{h}, \mathbf{h} + d\mathbf{h}]$. The variables ϕ and \mathbf{h} are termed sample space variables and range over the spaces on which $\Phi(t)$ and $\mathbf{H}(t)$ are defined. In order to aid our exposition of the PaSR, the interaction of the dispersion with a reactive surface is omitted in this section and all surfaces with which the fluid elements may be in contact are assumed to be inert.

In view of the formulations by Chen [32] and Rigopoulos [140] and in the absence of surface chemistry, we adopt as model for $f_{\Phi, \mathbf{H}}(\phi, \mathbf{h}; t)$ the evolution equation

$$\begin{aligned} \frac{\partial f_{\Phi, \mathbf{H}}}{\partial t} = & - \sum_{k \in \mathcal{G} \cup \{h_g\}} \frac{\partial}{\partial \phi_k} (f_{\Phi, \mathbf{H}} \dot{r}_k(\phi, \mathbf{h})) - \sum_i \frac{\partial}{\partial h_i} (f_{\Phi, \mathbf{H}} \dot{g}_i(\mathbf{h}, \phi)) \\ & + \mathcal{M} f_{\Phi, \mathbf{H}} + \frac{1}{\tau_{\text{res}}} (f_{\Phi, \mathbf{H}}^{\text{in}} - f_{\Phi, \mathbf{H}}), \end{aligned} \quad (3.1)$$

where $\mathcal{M} f_{\Phi, \mathbf{H}}$ represents the influence by diffusion-induced molecular mixing on the temporal change in $f_{\Phi, \mathbf{H}}$, τ_{res} is the mean residence time of fluid elements inside the reac-

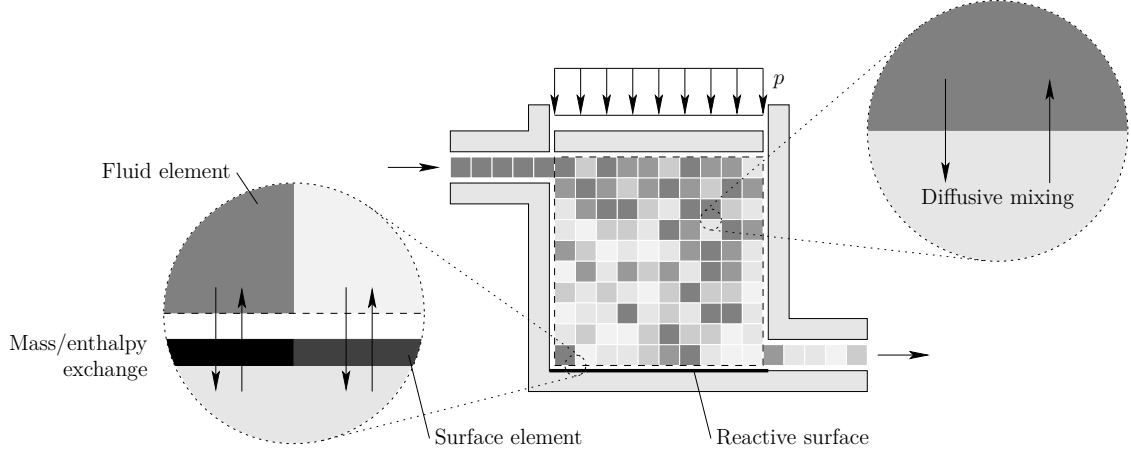


Figure 3.1 Schematic illustration of the micro-scale heterogeneity in a partially stirred reactor. Here, the grey-shaded squares correspond to fluid elements that may differ in terms of chemical composition, thermal state and droplet size distribution. Note that every fluid element is in contact with a distinct surface element and that the fluid elements can possess different volumes, although this is not visually represented in the figure.

tor and $f_{\Phi, \mathbf{H}}^{\text{in}}(\phi, \mathbf{h}) = \delta(\phi - \Phi^{\text{in}})\delta(\mathbf{h} - \mathbf{H}^{\text{in}})$ denotes the *pdf* associated with the composition Φ^{in} and droplet charge \mathbf{H}^{in} of inflowing gas. In the absence of micro-mixing ($\mathcal{M}f_{\Phi, \mathbf{H}} = 0$) and for $\tau_{\text{res}} \rightarrow \infty$, Eq. (3.1) corresponds to the *pdf* evolution equation associated with the composition $(\Phi(t), \mathbf{H}(t))$ of an isolated fluid element and may be obtained from Eqs. (2.15) and (2.26) using Lundgren’s rationale [107], for instance. By the final term on the right hand side of Eq. (3.1), the likelihood for a fluid element to leave the reactor within the time interval Δt_n and for a fluid element with composition $(\Phi^{\text{in}}, \mathbf{H}^{\text{in}})$ to enter the reactor amounts to $\Delta t_n / \tau_{\text{res}}$.

One physical effect that reduces the difference in constitution $(\Phi(t), \mathbf{H}(t))$ among different fluid elements is the diffusive heat and mass exchange schematically illustrated in Fig. 3.1. This micro-mixing process is represented here using the interaction-by-exchange-with-the-mean (IEM) model [32, 144],

$$\mathcal{M}f_{\Phi, \mathbf{H}} = \frac{C_{\text{mix}}}{2\tau_{\text{mix}}} \left(\sum_{k \in \mathcal{G} \cup \{h_g\}} \frac{\partial}{\partial \phi_k} ((\phi_k - \langle \Phi_k \rangle) f_{\Phi, \mathbf{H}}) + \sum_i \frac{\partial}{\partial h_i} ((h_i - \langle H_i \rangle) f_{\Phi, \mathbf{H}}) \right). \quad (3.2)$$

C_{mix} is termed the micro-mixing constant [83, 128] and τ_{mix} denotes the micro-mixing time scale. The angled brackets in Eq. (3.2), moreover, indicate the expectation with respect to $f_{\Phi, \mathbf{H}}(\phi, \mathbf{h}; t)$; for example, the mean gas composition $\langle \Phi(t) \rangle$ is obtained from the first

3 The partially stirred reactor

moment of $f_{\Phi, \mathbf{H}}(\phi, \mathbf{h}; t)$ as

$$\langle \Phi(t) \rangle = \int \int \phi f_{\Phi, \mathbf{H}}(\phi, \mathbf{h}; t) d\phi d\mathbf{h} = \int \phi f_{\Phi}(\phi; t) d\phi. \quad (3.3)$$

3.2.2 A partially stirred reactor model including a reactive surface

In this section, the PaSR model summarized above is extended to account for the presence of a reactive surface with which the individual fluid elements may exchange mass or enthalpy. In our case, the fuel is introduced into the reactor via evaporation from the surface, while heterogeneous oxidation reactions may also directly take place at the surface. The physical picture we propose is that, at any time instant t after start-up, every fluid element is in contact with one distinct surface element whose chemical composition is described in terms of $\Psi(t)$. In the same way as $\Phi(t)$ and $\mathbf{H}(t)$ differ from one fluid element of the gas-droplet dispersion to another, $\Psi(t)$ may also vary among distinct surface elements. Across the entire set of surface elements, the composition $\Psi(t)$ is, hence, a random vector whose variability characterizes the small-scale heterogeneity of the surface. Concomitantly, the entire state of the reactor is described in terms of the joint scalar *pdf* $f_{\Phi, \Psi, \mathbf{H}}(\phi, \psi, \mathbf{h}; t)$. If we imagine the flow through the reactor to drive advective mixing, then the motion of the individual fluid elements may cause the surface elements with which they are presently in contact to change. Since the time scale associated with this change in reaction partner is caused by advective transport, it is termed τ_{adv} .

Based on $f_{\Phi, \Psi, \mathbf{H}}(\phi, \psi, \mathbf{h}; t)$, the marginal *pdf* $f_{\Phi, \mathbf{H}}(\phi, \mathbf{h}; t)$ of the dispersion constitution ($\Phi(t), \mathbf{H}(t)$) inside a fluid element can be obtained by integration over the sample space variable ψ associated with the surface composition $\Psi(t)$,

$$f_{\Phi, \mathbf{H}}(\phi, \mathbf{h}; t) = \int f_{\Phi, \Psi, \mathbf{H}}(\phi, \psi, \mathbf{h}; t) d\psi, \quad (3.4)$$

where the integration domain is taken to coincide with the entire space on which $\Psi(t)$ is defined. Conversely, integration of $f_{\Phi, \Psi, \mathbf{H}}(\phi, \psi, \mathbf{h}; t)$ over all of (ϕ, \mathbf{h}) -space yields the marginal *pdf* associated with $\Psi(t)$,

$$f_{\Psi}(\psi; t) = \int f_{\Phi, \Psi, \mathbf{H}}(\phi, \psi, \mathbf{h}; t) d\phi d\mathbf{h}. \quad (3.5)$$

In light of the physical considerations summarized above, we propose, as an amendment

to the formulation in Eq. (3.1), the *pdf* evolution equation

$$\begin{aligned}
 \frac{\partial f_{\Phi, \Psi, \mathbf{H}}}{\partial t} = & - \sum_{k \in \mathcal{G} \cup \{h_g\}} \frac{\partial}{\partial \phi_k} (f_{\Phi, \Psi, \mathbf{H}} \dot{r}_k(\phi, \psi, \mathbf{h}, \gamma)) \\
 & - \sum_{k \in \mathcal{SUB}} \frac{\partial}{\partial \psi_k} (f_{\Phi, \Psi, \mathbf{H}} \dot{r}_k(\phi, \psi, \mathbf{h}, \gamma)) \\
 & - \sum_i \frac{\partial}{\partial h_i} (f_{\Phi, \Psi, \mathbf{H}} \dot{g}_i(\mathbf{h}, \phi, \psi, \gamma)) + \mathcal{M} f_{\Phi, \Psi, \mathbf{H}} \\
 & + \frac{1}{\tau_{\text{res}}} (f_{\Phi, \mathbf{H}}^{\text{in}} f_{\Psi} - f_{\Phi, \Psi, \mathbf{H}}) + \frac{1}{\tau_{\text{adv}}} (f_{\Phi, \mathbf{H}} f_{\Psi} - f_{\Phi, \Psi, \mathbf{H}}).
 \end{aligned} \tag{3.6}$$

Whereas heterogeneous surface reactions induce a correlation between $(\Phi(t), \mathbf{H}(t))$ and $\Psi(t)$, the final term in Eq. (3.6) acts in a decorrelating way and reduces the interdependencies of the gas-droplet constitution and the composition of the surface. Moreover, note that, contrary to Eq. (3.1), the molecular mixing term $\mathcal{M} f_{\Phi, \Psi, \mathbf{H}}$ in Eq. (3.6) is formulated in terms of $f_{\Phi, \Psi, \mathbf{H}}(\phi, \psi, \mathbf{h}; t)$ instead of $f_{\Phi, \mathbf{H}}(\phi, \mathbf{h}; t)$. Concomitantly, the IEM-based mixing model is given by Eq. (3.2) with $f_{\Phi, \mathbf{H}}(\phi, \mathbf{h}; t)$ replaced by $f_{\Phi, \Psi, \mathbf{H}}(\phi, \psi, \mathbf{h}; t)$. This formulation ensures that, while mixing occurs within the gas-droplet dispersion, the marginal *pdf* $f_{\Psi}(\psi; t)$ of the surface scalars remains unchanged. The penultimate term on the right hand side of Eq. (3.6) describes the change in the gas phase composition and droplet phase scalars due to inflow and outflow and, compared to Eq. (3.1), also includes an amendment due to the presence of a reactive surface. As fluid elements are flushed out of the PaSR, they are replaced by inflowing medium, causing a decorrelation of $(\Phi(t), \mathbf{H}(t))$ and $\Psi(t)$ in a formally similar manner as the advective decoupling of dispersion and surface elements in the last term, albeit on a different time scale.

The surface density $\gamma(t)$ of the reactive surface inside the reactor changes in a similar way as in the PSR, although the driving density change and mass influx are obtained as expectations with respect to the randomness in $(\Phi(t), \Psi(t), \mathbf{H}(t))$,

$$\frac{d\gamma(t)}{dt} = \frac{\gamma(t)}{\langle \rho(t) \rangle} \left(\frac{d\langle \rho(t) \rangle}{dt} - \gamma(t) \sum_{k \in \mathcal{G}} \langle \dot{s}_k(\Phi(t), \Psi(t)) \rangle \right). \tag{3.7}$$

Here,

$$\langle \rho(t) \rangle = \langle \hat{\rho}(\Phi(t), \mathbf{H}(t)) \rangle = \int \hat{\rho}(\phi, \mathbf{h}) f_{\Phi, \mathbf{H}}(\phi, \mathbf{h}; t) d\phi d\mathbf{h} \tag{3.8}$$

is the expected (or mean) dispersion density inside the reactor, while $\langle \dot{s}_k(\Phi(t), \Psi(t)) \rangle$

3 The partially stirred reactor

represents the mean release rate of gas phase species $k \in \mathcal{G}$ from the reactive surface. Note that Eq. (3.7) is based on the notion that every fluid element inside the reactor is exposed to the same surface density $\gamma(t)$. In principle, the PaSR model may also be formulated for other hypotheses on the surface exposure of the fluid elements; for example, $\gamma(t)$ could be assumed to vary from fluid element to fluid element as every element sees the same share of the total reactive surface. Here, we do not consider such amendments, however.

3.3 Numerical methods

Within the scope of the PaSR, the governing *pdf* equation (Eq. (3.6)) is also split into a sequence of fractional steps using a first order scheme (Section 2.5). Upon introduction of a stochastic particle representation [128], each fractional step can either be converted into a system of ODEs or a system of stochastic differential equations (SDEs) driven by compound Poisson processes. For the ODEs, we employ the same numerical time integrators as in the case of the PSR (Section 2.5), while the time integrals of the SDEs are implemented using bespoke sampling procedures. The evolution equation for the surface density (Eq. (3.7)) is integrated with respect to time using the midpoint rule in conjunction with temporally linear reconstructions of the density and the gas mass liberated from the reactive surface. The algorithmic details for the numerical solution of Eqs. (3.6) and (3.7) are summarized in Appendix B. For the analyses in Section 3.4, we choose a constant fractional time step of $\Delta t_n = 10^{-7}$ s. As for the PSR (Section 2.5), in the PaSR, the PBE is also converted into an ODE system governing the droplet phase scalars $\mathbf{H}(t)$ using the high resolution finite volume method of Koren [93] on a fixed exponential v -grid but with 256 cells in order to reduce the computational cost, while maintaining a reasonable level of accuracy (see also Section 4.6.1).

3.4 Aluminum combustion at atmospheric pressure

The PaSR model we introduced in Sections 3.2.1 and 3.2.2 permits an analysis of the influence of micro-scale heterogeneity and mixing on our key observables, particularly, the expected gas composition, the mean droplet size distribution and the expected ratio of dispersed and surface-bound $\text{Al}_2\text{O}_3(l)$, delivering insights that are relevant to the conden-

3.4 Aluminum combustion at atmospheric pressure

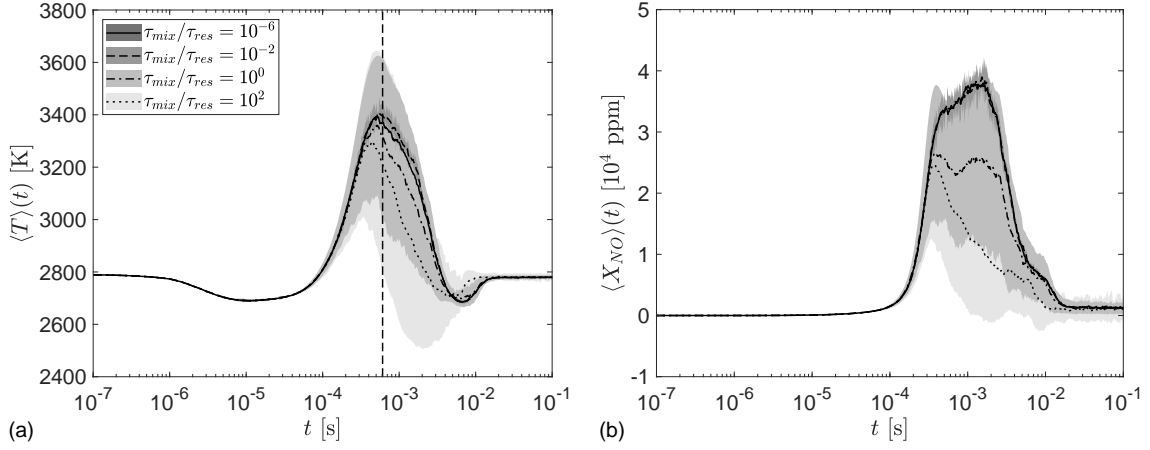


Figure 3.2 Influence of the micro-mixing intensity $(\tau_{mix}/\tau_{res})^{-1}$ on the mean dispersion temperature (a) and the mean mole fraction of NO (b) in a PaSR with NO_x chemistry. Here, the shaded areas correspond to the standard deviations from the means and are indicative of the fluid element-to-fluid element variability. The standard deviation for $\tau_{mix}/\tau_{res} = 10^{-6}$ is very small and not visible in the graphs. The dashed vertical line in figure (a) indicates the time point by which all surface elements have been occupied by N(S) and $\langle \theta_{N(S)} \rangle > 0.97$.

sation of oxide smoke in turbulent aluminum flames. The PaSR encompasses an ensemble of fluid elements (or realizations), each carrying a distinct constitution $(\Phi(t), \mathbf{H}(t))$, that interact with surface samples bearing the composition $\Psi(t)$. The fluid elements exchange mass and enthalpy through molecular mixing (micro-mixing constant $C_{mix} = 2$, time scale τ_{mix}) and swap surface reaction partners on the time scale $\tau_{adv} = 10^{-8} \text{ s} \ll \tau_{res}$. The residence time of the fluid elements inside the reactor is exponentially distributed with mean $\tau_{res} = 10^{-3} \text{ s}$ [32]. The initial and inflow compositions correspond to pure air at $T = 2791 \text{ K}$ without any droplet charge and the gas phase chemistry includes NO_x formation. As for the PSR, the reactive surface is initially covered by Al(S) throughout and the supply of bulk Al(B) underneath the surface does not limit the aluminum evaporation. Considering an ensemble of 240 fluid elements, the PaSR is operated at atmospheric pressure, $p = 1 \text{ atm}$, for a duration of $t_{end} = 10^{-1} \text{ s}$.

Figure 3.2 shows how the mean temperature and the mean NO mole fraction inside the PaSR change over time for different ratios τ_{mix}/τ_{res} . While the rise in temperature that indicates ignition is almost independent of the micro-mixing rate, we observe a reduction in the maximum mean temperature and the maximum NO charge with decreasing mixing intensity. Concomitantly, the micro-scale variability among the fluid elements increases as indicated by the shaded patches of standard deviation. By $t = 6 \times 10^{-4} \text{ s}$, almost all sites on the surface elements of the PaSR have been occupied by N(S), causing the

3 The partially stirred reactor

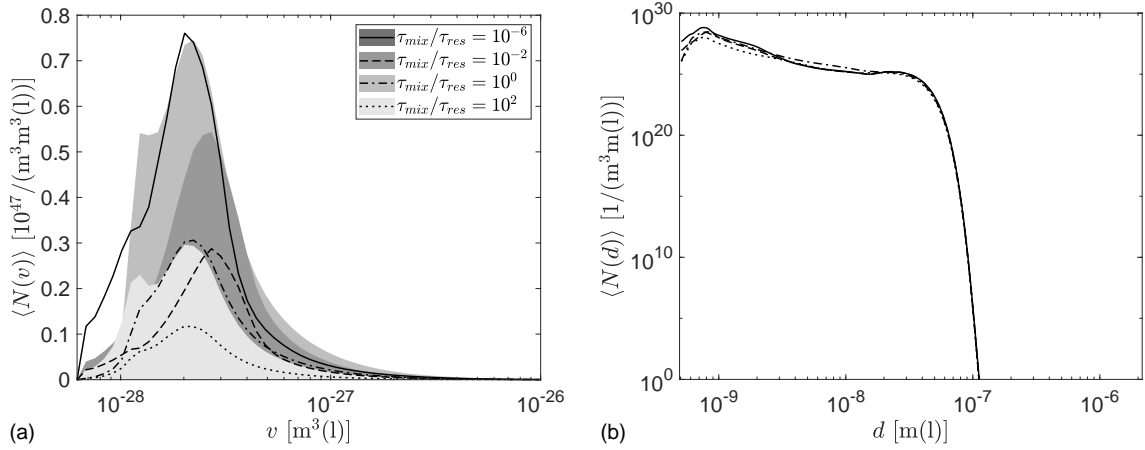


Figure 3.3 Influence of the micro-mixing intensity $(\tau_{\text{mix}}/\tau_{\text{res}})^{-1}$ on the mean smoke size distribution at time $t = 6 \times 10^{-4}$ s. As in Fig. 3.2, the shaded areas indicate plus/minus one standard deviation. Since the standard deviation for $\tau_{\text{mix}}/\tau_{\text{res}} = 10^{-6}$ is very small, it is not visible. Note that both panels show the same size distributions. On the left, the size distribution is plotted on a linear scale and in terms of the droplet volume as the statistics are obtained based on a volume-based distribution, whereas, on the right, the scale is logarithmic and the size distribution is transformed from a volume- to a diameter-based distribution for better perception.

surface chemistry and the release of gaseous Al to cease in a similar way as for the PSR in Section 2.6.2. At this point in time, Fig. 3.3 shows the $\text{Al}_2\text{O}_3(\text{l})$ droplet size distribution for the same ratios of $\tau_{\text{mix}}/\tau_{\text{res}}$ as in Fig. 3.2. Besides inhibiting bimodality in the mean droplet size distribution, we observe that a decrease in the micro-mixing rate also causes a reduction in the number density by about one order of magnitude. Factoring in the decrease in reactor volume $V(t)$ with the micro-mixing rate, this reduction is related to the lower dispersion temperature and a smaller mean evaporative Al-influx.

After the reactive surface has been deactivated by N(S) adsorption ($t \gtrsim 6 \times 10^{-4}$ s), the reactive, droplet-laden samples are successively flushed out of the reactor and the reactor's memory, that controls, for example, the capacity for incoming fluid elements to be ignited by existing ones, solely relies on molecular mixing. Specifically, slow micro-mixing entails a short-term memory, whence the reactor composition quickly converges to the inflow conditions. This is reflected in the rapid decay of the mean temperature and the mean NO mole fraction for the long mixing times in Fig. 3.2.

Figure 3.4(a) shows that slow micro-mixing entails an increase in the maximum mean droplet diameter and the diameter variability. In view of Fig. 3.2, this may be explained in terms of the lower dispersion temperatures inside the fluid elements that are accompanied by a larger nuclei size (Eq. (2.38)) and a larger growth rate (Eqs. (2.44) and (2.45)). Con-

3.4 Aluminum combustion at atmospheric pressure

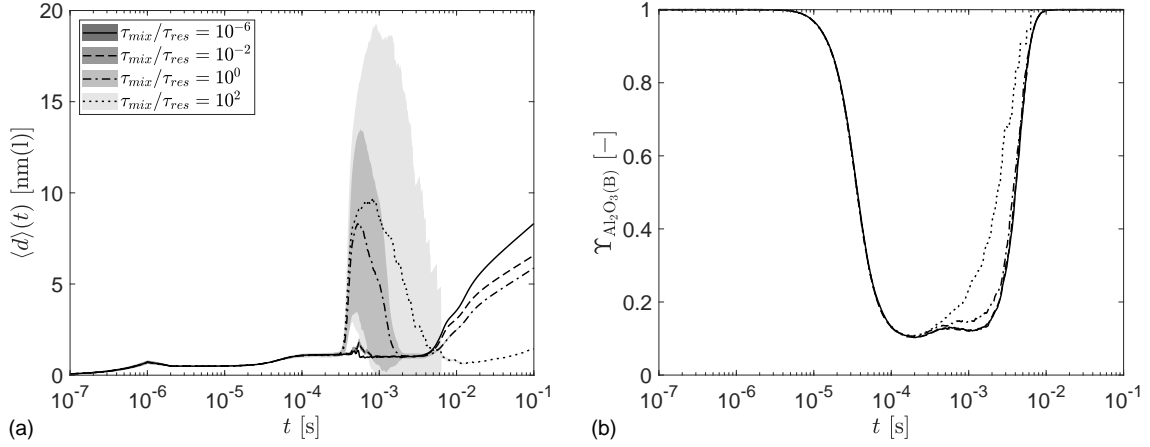


Figure 3.4 The mean droplet diameter (a) and the mean share of $Al_2O_3(B)$ on the reactive surface (b) for different time scale ratios τ_{mix}/τ_{res} in a PaSR. On the left, the small-scale variability is indicated by the size of the shaded areas, representing plus/minus one standard deviation. For $\tau_{mix}/\tau_{res} = 10^{-6}$, the standard deviation is very small and not discernible. Note that figure (a) shows the average of the mean droplet diameter over all fluid elements.

sequently, less intense mixing promotes the formation of fewer, larger droplets. Towards the end of the PaSR run ($t \gtrsim 5 \times 10^{-3}$ s), the droplet population inside the reactor consists of droplets that are passed, through micro-mixing, from fluid elements with long residence times to younger fluid elements before the former leave the reactor. Concomitantly, coagulation may lead to an increase of the droplets' sizes, eliciting a rise in the mean size of the remnant droplet phase as indicated on the far right of Fig. 3.4(a). Yet, since the expected number density after $t \approx 5 \times 10^{-3}$ s becomes extremely small, we caution that it may be affected by temporal discretization and round-off errors.

Besides the droplet size characteristics, we are particularly interested in the share of liquid aluminum oxide that is formed on the reactive surface,

$$\Upsilon_{Al_2O_3(B)} = \frac{\gamma \langle B_{Al_2O_3(B)}(\Psi) \rangle}{\rho_l \langle \varepsilon_l(\mathbf{H}) \rangle + \gamma \langle B_{Al_2O_3(B)}(\Psi) \rangle}, \quad (3.9)$$

and in how it is influenced by the strength of molecular mixing. Figure 3.4(b) indicates that the minimum share of surface-bound $Al_2O_3(l)$ is hardly affected by the intensity of molecular mixing and amounts to less than 20% for all mixing time scales. Both in the beginning and towards the end of the PaSR simulation, the share tends to unity because the inflowing gas is droplet-free and almost all droplets formed inside the reactor are, ultimately, flushed out. The quicker recovery of the surface share of $Al_2O_3(l)$ for $\tau_{mix}/\tau_{res} = 10^2$ is related to the smaller amount of dispersed $Al_2O_3(l)$ that is formed in

this case and the lower dispersion temperatures.

3.5 Aluminum combustion at elevated pressures

Like for the PSR, in this section, the influence of the thermodynamic pressure on the combustion dynamics in a PaSR is investigated. For the analysis below, the initial/inflow conditions are chosen identical to the initial condition of the PSR (Section 2.7) and, like for the PaSR operated at atmospheric pressure, the advective mixing time scale is set to $\tau_{\text{adv}} = 10^{-8}$ s, while the micro-mixing time scale is varied from $\tau_{\text{mix}} = 10^{-9}$ s to 10^{-1} s. Although Eq. (3.6) is solved numerically using the same Monte Carlo method as in the atmospheric pressure case, the number of samples is slightly reduced to 192 in order to accelerate the simulation campaign without curtailing accuracy too much. Moreover, the same extensions of the kinetic framework and amendments of the numerical solution schemes reported in Sections 2.7.1 and 2.7.2 apply here.

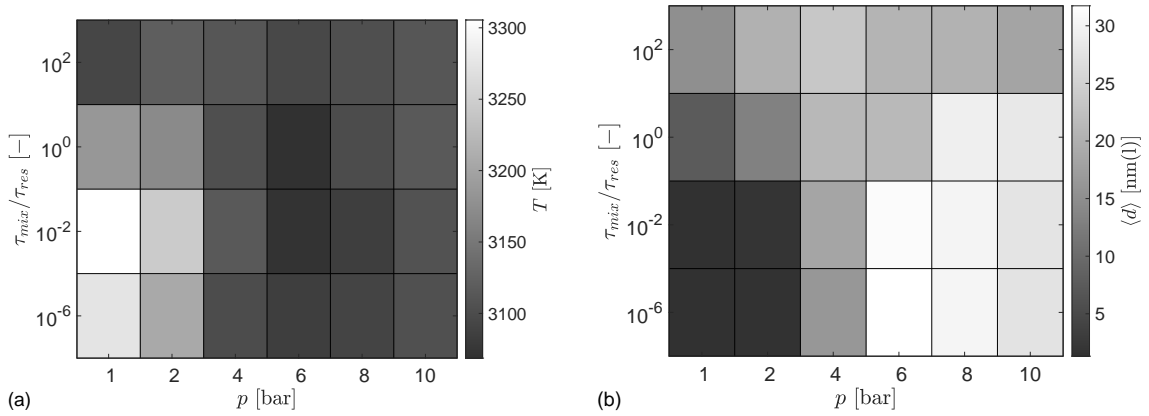


Figure 3.5 Change in temperature T (a) and mean droplet diameter $\langle d \rangle$ (b) with pressure and mixing intensity at $t = 10^{-3}$ s.

Figure 3.5 shows heat maps of the temperature $T(t)$ and the mean droplet diameter $\langle d \rangle(t)$ as a function of the mixing intensity at time $t = 10^{-3}$ s after start-up. If micro-mixing is fast, then the mean droplet size attains a maximum near a pressure of about 7 bar. In terms of temporal changes, the PaSR echoes our findings from the PSR analysis that an increase in pressure causes the maximum mean temperature to decrease (not shown).

3.6 Chapter conclusions

Based on the kinetic framework developed in the previous chapter, in this chapter, we investigated how small-scale heterogeneity on part of the gas-droplet dispersion and the reactive surface influences the combustion characteristics in an aluminum-fuelled partially stirred reactor. A particular novelty of this chapter is the amendment of the PaSR concept by the presence of a reactive surface, including a decorrelation of dispersion and surface compositions that mimics small-scale advective motions. As turbulent counterpart of the perfectly stirred reactor, the PaSR permits the analysis of localized gas, surface and droplet interactions in a single FV cell of a transported PDF calculation.

Analyzing a PaSR with NO_x chemistry, we found that slow micro-mixing inhibits the temperature rise on ignition, resulting in less NO as well as fewer, notably larger oxide smoke droplets. However, as in the PSR, these oxide smoke droplets remained nano-sized on average, rendering their potential separation from exhaust fumes challenging. The investigation of a PaSR operating at elevated pressures suggests that the average droplet size peaks around 7 bar, while, similar to the PSR, the maximum mean temperature decreases with the thermodynamic pressure.

Chapter 4

A steadily burning aluminum particle

4.1 Chapter introduction

Extending upon the developments of the previous chapters, in the present chapter, we report on a detailed modelling framework that permits the spatially resolved prediction of the gas phase composition and oxide smoke size distribution in the vicinity of a spatially resolved metal dust particle. In order to compare our model predictions with existing experimental measurements of single aluminum particle combustion [23–26], the model is instrumented to reproduce the specific setup investigated in the experiments. First comparisons revealed a significant influence of both the nucleation and coagulation rates on the predictions and their quality with respect to the measurements. Based on this observation, we decided to conduct a detailed sensitivity analysis including not only additional enhancements or modifications of the nucleation theory presented and reviewed in Section 2.4.1 but also different surface and gas phase kinetics. In particular, the droplet nucleation and coagulation rates are calibrated by comparison with the experimental data of Bucher et al. [24] for an isolated aluminum particle burning in an O₂/Ar gas mixture. Based on the consolidated droplet formation kinetics, predictions of the envelope flame and smoke halo are subsequently validated for combustion in air [24, 25].

Physical approaches for describing the combustion of individual spatially resolved aluminum particles were pioneered by Beckstead et al. [11] who idealized the oxide lobe as a spherical cap and focused on the condensation of aluminum oxide and the deposition of smoke on the reactive particle surface. Subsequently, Bucher et al. [24] adapted a one-dimensional particle combustion model [33] to a pure Al-particle, invoking equilibrium surface and gas phase chemistry. For a decreasing particle size, the transition

from a diffusion-controlled to a kinetic combustion regime was investigated by Bojko et al. [19] who additionally explored two different reduced descriptions as basis for modelling the combustion of aluminum dusts. Shortly afterwards, Glorian et al. [69] amended the combustion chemistry by a detailed mechanism for heterogeneous surface reactions, demonstrating that surface chemistry is particularly relevant to the combustion of small particles ($\lesssim 100 \mu\text{m}$) at low pressures as well as for CO_2 and H_2O containing atmospheres. Accounting for the non-spherical shape of a biphasic $\text{Al}/\text{Al}_2\text{O}_3$ -particle, Gallier et al. [60] subsequently extended the model developed by Glorian et al. [69] to investigate the importance of thermo- and diffusiophoresis on the deposition of oxide smoke on a steadily burning aluminum particle in the absence of surface chemistry. They found that, at least in Ar containing atmospheres, thermophoresis is instrumental in transporting oxide smoke towards the particle surface, highlighting the role of the oxide cap as a smoke collector, while diffusiophoresis is negligible.

A common trait of the previous modelling efforts is that the dispersed oxide smoke droplets were described in terms of a single mass fraction without regard of the size-polydispersity of the oxide smoke. This polydispersity is not only relevant for design considerations of metal dust combustors and exhaust fume treatment devices, but also influences the transport properties of the smoke, the gas-droplet thermodynamics and droplet-droplet interactions. Recently, a first step towards the incorporation of smoke polydispersity was taken by Thijs et al. [177] who investigated the formation of oxide smoke during the combustion of an iron particle, restricting the consideration to instantaneous nucleation and Brownian coagulation. Both the heat release due to condensation and surface growth/shrinkage as well as radiative heat losses from the dispersed phase appear to have been omitted here. In the present thesis, we proceed further and amend the existing models for aluminum surface and gas phase chemistry by a detailed population balance description of the oxide smoke size distribution that is linked to the carrier gas through channels for two-way mass and heat exchanges. To our awareness and in the context of aluminum combustion, this constitutes the first approach targeting a complete description of the size-resolved oxide smoke dynamics inside the laminar envelope flame spawned by a single particle.

Besides a comprehensive kinetic framework (Section 2.4) covering not only the droplet formation rates (nucleation, growth/dissociation and coagulation) but also the rates of

heat and mass exchange between a multicomponent carrier gas and a dispersed droplet population as well as radiation, the prediction of the oxide smoke dynamics based on the PBE requires parameters controlling spatial transport phenomena. In this chapter, we extend the kinetic framework of Section 2.4 by including the rates governing thermophoresis and droplet diffusion.

The present chapter is structured as follows: In Section 4.2, the kinetic framework for the localized gas, surface and droplet interactions of Section 2.4 is briefly reviewed and four different expressions for the nucleation rate are discussed. In the following Section 4.3, the balance equations governing the droplet-laden flow, the chemical gas composition and the oxide smoke size distribution are presented. Here, a special focus lies on the instantaneous gas-droplet equilibration in terms of temperature and bulk velocity. Subsequently, the mass and enthalpy conserving exchange of gas species and oxide droplets between the particle surface and the gas-smoke dispersion is discussed in Section 4.4. After a brief overview of the most important numerical aspects of our in-house solver in Section 4.5, we employ the developed model to predict the gas phase composition and oxide smoke size distribution in the vicinity of an aluminum particle burning in an O_2/Ar atmosphere at atmospheric pressure and analyze the influence of different gas/surface kinetics and droplet formation rates on the shape of the envelope flame and its temperature profile (Section 4.6). Based on a comparison with the experimental measurements of Bucher et al. [24], droplet formation rates are identified which we subsequently deploy in an attempt to validate the modelling framework for combustion in air. Using the consolidated kinetics, in the following Section 4.7, we allude to the characteristics that come along with a steadily burning aluminum particle at elevated pressures and investigate the differences to single particle combustion at atmospheric pressure. Finally, the chapter's conclusion is presented in Section 4.8.

4.2 Gas phase, surface and droplet formation kinetics

In this section, we briefly summarize the previously developed kinetic framework (Section 2.4) containing the kinetic rates that govern the spatially localized chemical and physical interactions of the gas phase, the reactive particle surface and the dispersed droplets (Fig. 4.1) and detail modifications. Since both the aluminum particle and the

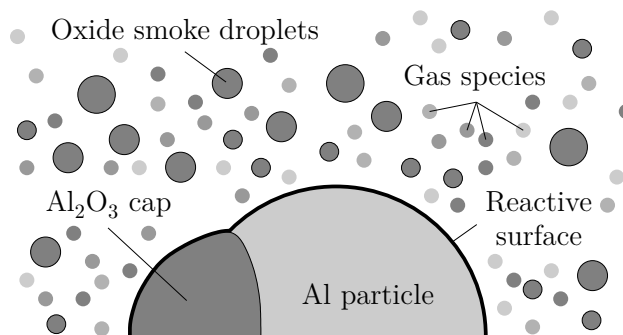


Figure 4.1 Schematic illustration of the interacting phases involved in the combustion of an aluminum particle. The reactive surface is delineated by the thick solid line covering the aluminum particle. Both surface reactions and the deposition of oxide smoke result in an Al_2O_3 cap adjoining the aluminum particle which is not taken into account in this chapter but subject of Chapter 5.

boundary layer flow in its vicinity are spatially resolved, the kinetic framework is subsequently amended by the rates controlling differential diffusion of gas phase species and droplets as well as thermophoresis (Section 4.3.2).

4.2.1 Gas and surface chemistry

In this chapter, we consider the steady combustion of a single aluminum particle in an oxidizing gas stream at constant thermodynamic pressure p . The gas phase constitutes a multicomponent ideal gas and includes, besides elemental species, the oxidizer O_2 , a diluent (Ar or N_2), aluminum suboxides (AlO , Al_2O , AlO_2 and Al_2O_2), the condensing species $\text{Al}_2\text{O}_3/c$ as well as possible pollutants (NO_x). In particular, we consider two alternatives for the gas chemistry here. On the one hand, a detailed gas phase reaction mechanism [29, 69, 175] for Al-O-N/Ar chemistry is combined with a mechanism for the formation of NO_x [64] as outlined in Chapter 2. On the other hand, the gas phase composition can also be obtained from equilibrium computations minimizing the Gibbs free energy [73, 74]. Equilibrium calculations are frequently used if the reaction rates proceed much faster than spatial transport. Complementary to the gas chemistry, the surface chemistry may either be described by a kinetic mechanism [67, 69] or an equilibrium assumption. The latter is based on the notion of a phase equilibrium between the bulk liquid aluminum constituting the fuel particle and the aluminum vapour in its vicinity (Section 4.4). Note that the equilibrium formulation is limited to the evaporation of aluminum and the adsorption of $\text{Al}_2\text{O}_3/c$, whereas the surface mechanism additionally includes the adsorption of oxygen species and the condensed phase oxidation of aluminum. Compared to the PSR and PaSR

analyses, the adsorption of atomic N at the reactive surface is omitted here because it results in a rapid deactivation of the surface sites and a consequent inhibition of surface chemistry and Al-evaporation (Sections 2.6.2 and 3.4). At present, the natural occurrence of this deactivation is unclear, in particular as it prevents the attainment of a steady particle combustion state for a particle burning in a uniform flow ($Re_p > 0$). Consequently, we eliminated the reaction describing the direct adsorption of N radicals (Eq. (2.94)) from the reaction mechanism of Glorian et al. [69] for the spatially resolved calculations reported in this and the following chapter. All four combinations of gas and surface chemistry are applied in the context of the single particle model and their effect on our predictions is assessed in Section 4.6. The thermodynamic properties of the aluminized species are still taken from Glorian et al. [69], whereas the properties of species involved in the NO_x chemistry are taken from Glarborg et al. [64]. While Glorian et al. [69] approximated the properties of $Al_2O_3(l)$ by extrapolating the thermodynamic data of solid Al_2O_3 to temperatures above its melting point, we use the thermodynamic data of liquid Al_2O_3 from Reference [27]. For our droplet size-resolved simulations (CFD-PBE), the reactions leading to the formation of $Al_2O_3(l)$ are removed from the gas phase mechanism and replaced by droplet formation kinetics detailed in Section 2.4 and modified/extended in the following.

4.2.2 Droplet formation kinetics

In the beginning of this section, we briefly recap our understanding of aluminum oxide nucleation to support the following discussion of different nucleation theories, leaving details to Section 2.4.1. Following a common approach [11, 19, 69, 166, 169], we assume that the condensation of $Al_2O_3(l)$ droplets proceeds from a supersaturated vapour of gaseous Al_2O_3/c ,



as detailed in Section 2.4.2. Although the existence of gaseous Al_2O_3/c at the conditions of atmospheric Al- O_2 combustion is contentious [169, 174] and both laser ablation experiments and equilibrium calculations suggest that incipient oxide smoke droplets are chemically heterogeneous, turning into bulk $Al_2O_3(l)$ only after a maturation process [94], Al_2O_3/c may here be thought of as a short-lived, perhaps artificial intermediate species

whose reaction dynamics constitute a replica of the true droplet nucleation and maturation process. This idea is supported by the unsteady nucleation analysis of Savel'ev and Starik [148] who showed that the clusterization of gaseous Al_2O_3 molecules may indeed lead to the inception of $\text{Al}_2\text{O}_3(\text{l})$ nuclei and concluded that Al_2O_3 is a viable precursor for condensed phase smoke. In a similar vein, Saba et al. [143] considered clusters of Al_2O_3 molecules as incipient $\text{Al}_2\text{O}_3(\text{l})$ droplets.

Conversely, droplets whose volume v is smaller than the critical nuclei size v_0 decompose upon evaporation into suboxides. This endothermic dissociation process extends over all droplets as soon as the dispersion temperature T reaches the $\text{Al}_2\text{O}_3(\text{l})$ dissociation temperature $T_{b,\text{Al}_2\text{O}_3}$ and the critical size v_0 becomes very large. Based on the observations within the scope of the spatially homogeneous reactor in Section 2.7.2, we assume here that dissociation proceeds at a finite rate through evaporation (Eqs. (2.44) and (2.45)). Moreover, contrary to the chemical reaction in Eq. (2.64), here, we assume that droplets dissociate via the reverse chemical pathway of Eq. (4.1). In this way, the released $\text{Al}_2\text{O}_3/\text{c}$ is, subsequently, reconverted into suboxides by the gas phase chemistry. The equilibrium vapour pressure of $\text{Al}_2\text{O}_3/\text{c}$ is related to the gas temperature through the difference in chemical potentials of gaseous and liquid Al_2O_3 (Eqs. (2.30) and (2.31)). This leads to a boiling point that differs from the one delivered by the expressions of Reed and Calia [135] and Beckstead et al. [11], but is consistent with the thermodynamic properties of $\text{Al}_2\text{O}_3/\text{c}$ included in the gas phase mechanism.

The propensity of an $\text{Al}_2\text{O}_3/\text{c}$ vapour to change phase is typically measured in terms of the supersaturation S which we evaluate in terms of the difference in chemical potentials of single $\text{Al}_2\text{O}_3/\text{c}$ and $\text{Al}_2\text{O}_3(\text{l})$ molecules (Eq. (2.29)) at the current thermal state (p, ρ_g, T) [57, p. 397]. By the Classical Nucleation Theory (CNT) [8, 57], the rate at which $\text{Al}_2\text{O}_3(\text{l})$ nuclei with critical volume

$$v_0 = \left(\frac{2\theta_\sigma}{3 \ln S} \right)^3 v_1 \quad (4.2)$$

form can be computed in terms of S according to

$$\dot{R}_{\text{CNT}} = \left(\frac{p_v}{k_B T} \right)^2 v_1 \sqrt{\frac{2\sigma_l}{\pi m_1}} \exp \left(-\frac{16\pi\sigma_l^3 v_1^2}{3k_B^3 T^3 (\ln S)^2} \right). \quad (4.3)$$

Here, $\theta_\sigma = s_1\sigma_l/(k_B T)$ is the reduced surface tension.

Owing to severe assumptions on the gas-droplet thermodynamics and on the rates at which clusterization and nucleation occur, the CNT may mispredict the actual nucleation rate. Seeing as many extensions and modifications of the CNT have been developed in an effort to rectify its shortcomings or eliminate inherent assumptions, we investigate, in Section 4.6, the influence of two of these modifications on the prediction of the smoke halo about an isolated burning aluminum particle in relation to the experimental measurements of Bucher et al. [24]. On the one hand, the Internally Consistent Classical Theory (ICCT) [63, 85] provides an equilibrium cluster distribution that is self-consistent even down to the smallest clusters and is based on a stable equilibrium between vapour and condensed phase [89]. Compared to the CNT, the ICCT results in a slightly modified nucleation rate,

$$\dot{R}_{\text{ICCT}} = \dot{R}_{\text{CNT}} \frac{1}{S} \exp(\theta_\sigma), \quad (4.4)$$

and also includes Courtney's correction [16, 35]. Note that the rate in Eq. (4.4) has already been introduced in the context of the spatially homogeneous reactors (Eq. (2.35)). On the other hand, Reiss et al. [138, 139] (RKK) incorporated the effect of a fluctuation in the center of mass of a liquid nucleus based on the notion of the replacement free energy, yielding the nucleation rate

$$\begin{aligned} \dot{R}_{\text{RKK}} = & \frac{s_1 p_v \left(1 + n_0^{\frac{1}{3}}\right)^2}{2\pi k_B T \sqrt{m_1 \kappa_T v_1}} \sqrt{1 + \frac{1}{n_0}} \sqrt{\frac{1}{2n_0^2} + \frac{2\theta_\sigma}{9n_0^{\frac{4}{3}}}} \\ & \times \exp\left(-\frac{1}{2} \ln n_0 + n_0 \ln S - \theta_\sigma n_0^{\frac{2}{3}}\right). \end{aligned} \quad (4.5)$$

Here, the number of molecules in a critically-sized nucleus n_0 is computed by minimizing the term inside the exponential on the right hand side of Eq. (4.5) using Cardano's formula. Furthermore, $\kappa_T = 1/(\rho_l c_s^2) + \alpha_V^2 T/(\rho_l C_{p,l})$ denotes the isothermal compressibility of the $\text{Al}_2\text{O}_3(l)$ droplets and is evaluated using a thermodynamic relation including the density $\rho_l = 2728.9 \text{ kg}(l)/\text{m}^3(l)$ (Section 2.2.4), the speed of sound $c_s(T)$ [162], the volumetric coefficient of thermal expansion α_V [70] and the specific heat capacity $C_{p,l}(T)$ of $\text{Al}_2\text{O}_3(l)$. Equation (4.5) was derived following the considerations detailed in References [88, 120] using the exact expression for the molecular collision rate [153, Eq. (11.19)]. Like Eqs. (4.3), (4.4) and (4.5), the fourth rate expression that we include in the comparisons of Section 4.6 is of the Arrhenius-type, but features a vanishing activation

4 A steadily burning aluminum particle

energy (EA0),

$$\dot{R}_{\text{EA0}} = k_f \frac{\rho_g \varepsilon_g}{\rho_l v_0} Y_{\text{Al}_2\text{O}_3/c}. \quad (4.6)$$

Commensurate with the rate of the reaction $\text{Al}_2\text{O}_3/c \rightarrow \text{Al}_2\text{O}_3(l)$ in the gas phase mechanism of Glorian et al. [69], the forward rate k_f in Eq. (4.6) is chosen as $10^{15}/\text{s}$. In the absence of dissociation and condensational surface growth, this choice ensures that the droplet mass formation rate is consistent with the rate of Glorian et al. [69] for a size-agnostic formulation in which the smoke is described in terms of a mass fraction and allows us to explicitly investigate the ramifications of a size-sensitive description of the oxide smoke dynamics on envelope flame predictions. Since the rate in Eq. (4.6) is not based on the CNT and since there is, consequently, no physically motivated expression for the critical nucleus volume v_0 , we set $v_0 = 2v_1$ here.

Depending on their size and the gas' rarefaction, the droplets either feel the molecular nature of the surrounding gas or experience the carrier medium as a continuum. The theories we invoke to determine the droplet growth ($G(v)$) and coagulation rates ($\beta(v, w)$) in either of these limiting cases are smoothly blended to yield expressions that are valid over the entire droplet size range. For computational efficiency and contrary to Eq. (2.42), moreover, the gas' mean free path is approximated by the mean free path of a pure species with concentration-weighted average collision diameter $\bar{\sigma}$, $\lambda_{\text{mfp},g} = k_B T / (\sqrt{2} p \bar{\sigma}^2)$ [30, Chapter 5] (relative error $\lesssim 1\%$). For more details on the kinetic rates of droplet growth and coagulation, the gas-droplet heat and mass exchange and thermal radiation of the oxide droplets, we refer to Section 2.4.

Contrary to the spatially homogeneous reactors discussed in Chapters 2 and 3, which have been initialized with temperatures well above the alumina melting point, spatial transport phenomena may cause the migration of smoke droplets in regions with temperatures below the melting point controlled by the boundary conditions of the spatially resolved simulations. Since our droplet description is based on the hypothesis of a spherical shape and, thus, inapplicable to non-spherical aggregates that may form upon collision of solidified droplets, coagulation is limited to temperatures above the melting point of Al_2O_3 , $T_{m,\text{Al}_2\text{O}_3} = 2327 \text{ K}$. Although the notion of a gas-liquid interface ceases to be valid at temperatures below the melting point, we use the liquid phase properties also to evaluate the nucleation and growth rates for temperatures $T < T_{m,\text{Al}_2\text{O}_3}$, where the respective rates are expected to be very small. The release of the enthalpy of fusion during

solidification of the oxide smoke droplets is taken into account by smoothly blending the thermodynamic properties of liquid and solid Al_2O_3 [157].

4.3 Governing equations

The atmosphere above the reactive surface of an aluminum fuel particle consists of a multicomponent gas that is laden with dispersed, polysized oxide smoke droplets (Fig. C.1 in Appendix C). In the present section, the governing equations of this gas-droplet dispersion are established, including sources due to homogeneous gas phase reactions and phase transitions. In Sections 4.3.1 and 4.3.2, we specifically recall the evolution equations governing the gas species and droplet transport before the equations governing the dispersion mass, momentum and enthalpy are detailed in Section 4.3.3. The set of governing equations is completed by an enthalpy balance inside the burning fuel particle introduced in Section 4.3.4. Although some of the variables introduced below have already been defined (Chapter 2), we redefine them here in order to emphasize their spatial dependency, possibly mediated by a dependence on the primary unknowns, which are now a function of the spatial location around the burning fuel particle.

4.3.1 Species transport and chemical reactions

At any location $\mathbf{x} \in \Omega_{\mathbf{x}}$ and point in time t , the thermochemical state of the reactive atmosphere above the aluminum particle is described in terms of species mass fractions $Y_k(\mathbf{x}, t)$, $k \in \mathcal{G}$, accumulated in the vector $\mathbf{Y}(\mathbf{x}, t)$, and the temperature $T(\mathbf{x}, t)$.¹ The latter is linked to the gas composition by the gas enthalpy (Eq. (2.2)). Moreover, we still assume a small Mach number, a constant thermodynamic pressure and the multicomponent gas to behave ideal.

By the Hirschfelder–Curtiss approximation of the species diffusion velocity, which is frequently used to avoid solving for the exact diffusion velocities [189, Appendix E.2], and upon introduction of a correction velocity \mathbf{u}_c [126, Chapter 1], the transport velocity of

¹In contrast to the considerations in Chapter 2, here, we replace the gas enthalpy by the temperature as primary variable characterizing the gas phase’s state. Although both quantities are linked through \mathbf{Y} , it is advantageous to use the temperature as primary variable for reasons discussed in Section 4.3.3.

4 A steadily burning aluminum particle

gas species k reads

$$\mathbf{u}_k(\mathbf{u}, \mathbf{Y}, T) = \mathbf{u} + \mathbf{u}_{d,k} = \mathbf{u} + \mathbf{u}_c - \mathcal{D}_k \frac{\nabla X_k}{X_k}, \quad k \in \mathcal{G}, \quad (4.7)$$

where $\mathbf{u}(\mathbf{x}, t)$ represents the bulk velocity, $\mathbf{u}_{d,k}(\mathbf{Y}, T)$ denotes the species' diffusion velocity and \mathcal{D}_k is the diffusion coefficient of species k into the rest of the mixture,

$$\mathcal{D}_k(\mathbf{Y}, T) = \frac{1 - Y_k}{\sum_{l \in \mathcal{G} \setminus \{k\}} \frac{X_l}{\mathcal{D}_{kl}}}. \quad (4.8)$$

Additionally, $\mathcal{D}_{kl}(T)$ represents the binary diffusion coefficient of species k into l and vice versa [90, Chapter 2],

$$\mathcal{D}_{kl} = \frac{16}{3} \frac{\sqrt{2\pi R^3 T^3}}{N_A p \pi \sigma_{kl}^2 \Omega_{kl}^{(1,1)*}} \sqrt{\frac{(W_k + W_l)}{W_k W_l}}, \quad (4.9)$$

where N_A is Avogadro's constant, σ_{kl} denotes the reduced collision diameter of species k and l and $\Omega_{kl}^{(1,1)*}$ is the diffusion collision integral. The correction velocity \mathbf{u}_c in Eq. (4.7) is determined based on the condition that diffusion does not induce a net bulk flow, $\sum_{k \in \mathcal{G}} Y_k \mathbf{u}_{d,k} = \mathbf{0}$, and evaluates to

$$\mathbf{u}_c(\mathbf{Y}, T) = \sum_{k \in \mathcal{G}} \mathcal{D}_k \frac{W_k}{W} \nabla X_k. \quad (4.10)$$

Discounting the part of the flow domain that is occupied by smoke droplets, the localized balance law for the partial density $\rho_k(\mathbf{Y}, T) = \rho_g Y_k$ of species $k \in \mathcal{G}$ is obtained as

$$\frac{\partial \rho_g \varepsilon_g Y_k}{\partial t} + \nabla \cdot (\rho_g \varepsilon_g Y_k (\mathbf{u} + \mathbf{u}_c)) = \nabla \cdot \left(\rho_g \varepsilon_g \mathcal{D}_k \frac{W_k}{W} \nabla X_k \right) + \varepsilon_g \dot{\omega}_{g,k} + \dot{\omega}_{gl,k}. \quad (4.11)$$

The gas phase volume fraction $\varepsilon_g(N(\cdot)) = 1 - \varepsilon_l$ that appears here is related to the droplet size distribution $N(\cdot)$ through the droplet volume fraction $\varepsilon_l(N(\cdot))$ (Section 4.3.2 below). The last two terms on the right hand side of Eq. (4.11) account for the change in the species' mass density due to homogeneous gas phase reactions ($\dot{\omega}_{g,k}(\mathbf{Y}, T)$, Section 4.2.1) and gas-droplet phase transitions ($\dot{\omega}_{gl,k}(\mathbf{Y}, T, N(\cdot))$, Section 4.3.2), respectively.

4.3.2 Droplet transport and phase transition

In order to formally describe the oxide smoke droplets, that form upon clusterization of gaseous Al_2O_3 and $\text{Al}_2\text{O}_3\text{c}$ molecules [166] and constitute a polysized aerosol, in a Eulerian framework, we introduce $N(v, \mathbf{x}, t)$ as the number density of droplets inside an infinitesimal control volume $\omega_{\tilde{\delta} \rightarrow 0}(v, \mathbf{x})$ in the state space $\Omega_v \times \Omega_{\mathbf{x}}$,

$$N(v, \mathbf{x}, t) = \lim_{\tilde{\delta} \rightarrow 0} \frac{|\{i \in \mathbb{N} | (v_i, \mathbf{x}_i)^T \in \omega_{\tilde{\delta}}(v, \mathbf{x})\}|}{\text{vol} \omega_{\tilde{\delta}}(v, \mathbf{x})}, \quad (4.12)$$

where $\tilde{\delta} > 0$ denotes the size of the control volume, the index i refers to a particular droplet and $\Omega_v = [0, \infty)$ represents the droplet volume/size-space. In particular, $N(v, \mathbf{x}, t) dv d\mathbf{x}$ is the number of droplets with volume in $[v, v + dv)$ which are located, at time t , inside the physical volume element $[\mathbf{x}, \mathbf{x} + d\mathbf{x})$ [82]. Although the smoke droplets are not inertial, both thermophoresis and size-sensitive droplet diffusion may cause the droplets' trajectories to deviate from the pathlines of the bulk gas velocity \mathbf{u} . Correspondingly, the velocity $\mathbf{u}_l(v)$ of a droplet with size v is decomposed as

$$\mathbf{u}_l(v, \mathbf{u}, \mathbf{Y}, T, N(\cdot)) = \mathbf{u} + \mathbf{u}_t + \mathbf{u}_{d,l}(v) = \mathbf{u} + \mathbf{u}_t - \mathcal{D}_l(v) \frac{\nabla N(v)}{N(v)}, \quad (4.13)$$

where \mathbf{u}_t denotes the thermophoretic velocity defined below, $\mathbf{u}_{d,l}(v, \mathbf{Y}, T, N(\cdot))$ represents the droplet diffusion velocity and $\mathcal{D}_l(v)$ is the droplet diffusivity (see below). Like the mechanical inertia, the thermal inertia of the smoke droplets is sufficiently small such that we may assume the temperatures of the droplets and the carrier gas to locally equilibrate instantaneously and both phases to be present at the common dispersion temperature T .

The evolution of the droplet number density is governed by the spatially inhomogeneous PBE which can be obtained, for example, by matching all (v, \mathbf{x}) -statistics of $N(v, \mathbf{x}, t)$ with those of the discrete droplet population [133, Section 2.10],

$$\frac{\partial N(v)}{\partial t} + \nabla \cdot (N(v) (\mathbf{u} + \mathbf{u}_t)) = \nabla \cdot (\mathcal{D}_l(v) \nabla N(v)) + \dot{s}_N(v). \quad (4.14)$$

For notational conciseness, the source and sink terms that are associated with spatially

localized changes of $N(\cdot)$ were aggregated into the single rate

$$\begin{aligned} \dot{s}_N(v, \mathbf{Y}, T, N(\cdot)) = & - \frac{\partial G(v)N(v)}{\partial v} + \dot{R}\delta(v - v_0) \\ & + \frac{1}{2} \int_0^v \beta(v-w, w)N(v-w)N(w) dw \\ & - \int_{\Omega_v} \beta(v, w)N(v)N(w) dw. \end{aligned} \quad (4.15)$$

Compared to the PBE governing the dynamics in the spatially homogeneous reactors (Eq. (2.22)), Eq. (4.15) does not contain a term for volume expansion which is instead driven by the local flow field governed by the mass and momentum balances introduced below. Note that the droplet velocity $\mathbf{u}_l(v)$ in Eq. (4.13) follows from Eq. (4.14) by reinterpreting the diffusion term on the right hand side in terms of an advection velocity.

The PBE in Eq. (4.14) is kinetically driven not only by spatially localized processes, covering droplet nucleation, growth/dissociation and coagulation at the rates $\dot{R}(\mathbf{Y}, T, N(\cdot))$ (at $v = v_0(\mathbf{Y}, T)$), $G(v, \mathbf{Y}, T)$ and $\beta(v, w, \mathbf{Y}, T, N(\cdot))$, respectively, but also by spatial transport due to advection, thermophoresis and diffusion. In the following, we briefly discuss the transport parameters \mathbf{u}_t and $D_l(v)$ that were not included in the kinetic framework of Section 4.2.2 and Section 2.4.

Thermophoresis

In the kinetic transport regime, the thermophoretic velocity is size-independent and given by [58]

$$\mathbf{u}_t(\mathbf{Y}, T, N(\cdot)) = - \frac{3\mu}{4\rho(1 + 0.9\frac{\pi}{8})T} \nabla T, \quad (4.16)$$

where ρ is the dispersion density defined in Section 4.3.3 below. For sufficiently dilute dispersions, the dispersion viscosity μ can be linked to ε_l and the gas viscosity μ_g by Einstein's formula [43]

$$\mu(\mathbf{Y}, T, N(\cdot)) = \mu_g \left(1 + \frac{5}{2}\varepsilon_l \right). \quad (4.17)$$

The gas viscosity is computed from Wilke's formula [90, 188],

$$\mu_g(\mathbf{Y}, T) = \sum_{k \in \mathcal{G}} \frac{X_k \mu_k}{\sum_{l \in \mathcal{G}} X_l \Phi_{kl}} \quad (4.18)$$

with

$$\Phi_{kl}(T) = \frac{1}{\sqrt{8}} \sqrt{\frac{W_l}{W_l + W_k}} \left(1 + \sqrt{\frac{\mu_k}{\mu_l}} \sqrt{\frac{W_l}{W_k}} \right)^2, \quad (4.19)$$

while the viscosities $\mu_k(T)$ of the individual species $k \in \mathcal{G}$ are obtained from the kinetic theory of gases [30, 90],

$$\mu_k = \frac{5}{16} \frac{\sqrt{\pi W_k R T}}{N_A \pi \sigma_{kk}^2 \Omega_{kk}^{(2,2)*}}, \quad (4.20)$$

where $\Omega_{kk}^{(2,2)*}$ is the viscosity collision integral. In our current model, Eq. (4.16) is applied across the entire droplet volume range. Although this constitutes a simplifying assumption, an *a posteriori* justification is provided in Section 4.6. Consequently, we defer the extension of our model to accommodate size-dependent expressions for the thermophoretic velocity in the transition regime [38, 105, 173, 176] to future work.

Droplet diffusion

Droplet diffusion is a strongly size-dependent transport process that may cause the droplets to disperse spatially even though they are not inertial. Based on the Stokes–Einstein diffusion theory [58], the size-dependent droplet diffusion coefficient is obtained as

$$\mathcal{D}_l(v, \mathbf{Y}, T, N(\cdot)) = \frac{k_B T C}{3\mu\pi d}, \quad (4.21)$$

where $d(v) = (6v/\pi)^{1/3}$ is the droplet diameter and the Cunningham slip correction factor $C(v, \mathbf{Y}, T)$ accommodates non-continuum effects [153, Eq. (9.34)].

Moment evolution equations

At (\mathbf{x}, t) , $N(\cdot, \mathbf{x}, t)$ corresponds to the droplet size distribution, one of our major prediction objectives. The statistics of $N(\cdot, \mathbf{x}, t)$ describe droplet-averaged characteristics of the entire droplet population at (\mathbf{x}, t) and include the size-moments M_k (Eq. (2.10)).

The evolution equations of the moments indicate how particular characteristics of the dispersed phase change in space and time and may be obtained from the PBE by weighted v -integration. For example, multiplying Eq. (4.14) by v and integrating over Ω_v yields the

following law for the droplet volume fraction

$$\frac{\partial \varepsilon_l}{\partial t} + \nabla \cdot (\varepsilon_l(\mathbf{u} + \mathbf{u}_l)) = \nabla \cdot \left(\int_{\Omega_v} v \mathcal{D}_l(v) \nabla N(v) dv \right) + \underbrace{\int_{\Omega_v} v \dot{s}_N(v) dv}_{\dot{s}_{\varepsilon_l}}. \quad (4.22)$$

Note that the contribution of the coagulation birth and death terms to the volume-weighted integral \dot{s}_{ε_l} on the right hand side of Eq. (4.22) vanishes since coagulation is volume conserving. The source term \dot{s}_{ε_l} plays a special role in gas-liquid phase transitions and may be linked to the rate $\dot{\omega}_{gl,k}$, $k \in \mathcal{G}$, in Eq. (4.11). Since gas-liquid phase transitions maintain the dispersion mass, we specifically have

$$\dot{\omega}_{gl,k} = -\rho_l \delta_k \dot{s}_{\varepsilon_l}, \quad (4.23)$$

where δ_k represents the fraction of the produced or consumed droplet mass that species k either receives or provides and is obtained from the stoichiometry of the condensation/dissociation reaction in Eq. (4.1).

Similarly, an evolution equation for the droplet surface density ξ_l can be obtained as

$$\begin{aligned} \frac{\partial \xi_l}{\partial t} + \nabla \cdot (\xi_l(\mathbf{u} + \mathbf{u}_l)) = & \nabla \cdot \left(\sqrt[3]{36\pi} \int_{\Omega_v} v^{\frac{2}{3}} \mathcal{D}_l(v) \nabla N(v) dv \right) \\ & + \underbrace{\sqrt[3]{36\pi} \int_{\Omega_v} v^{\frac{2}{3}} \dot{s}_N(v) dv}_{\dot{s}_{\xi_l}}, \end{aligned} \quad (4.24)$$

where \dot{s}_{ξ_l} accounts for changes in ξ_l due to droplet formation or v -transport.

For future reference, we define the diffusion-induced velocities by which the droplet volume fraction and surface density are advected as

$$\varepsilon_l \mathbf{u}_{d,l}^{\varepsilon_l}(\mathbf{Y}, T, N(\cdot)) = \int_{\Omega_v} v N(v) \mathbf{u}_{d,l}(v) dv = - \int_{\Omega_v} v \mathcal{D}_l(v) \nabla N(v) dv, \quad (4.25)$$

$$\xi_l \mathbf{u}_{d,l}^{\xi_l}(\mathbf{Y}, T, N(\cdot)) = -\sqrt[3]{36\pi} \int_{\Omega_v} v^{\frac{2}{3}} \mathcal{D}_l(v) \nabla N(v) dv. \quad (4.26)$$

4.3.3 Dispersion mass, momentum and enthalpy balances

Commensurate with the characterization of the oxide smoke droplets in terms of a number density, the carrier gas and the smoke constitute interpenetrating continua that may, conceptually, be unified into a gas-droplet dispersion with homogenized properties. Con-

sequently, both the droplets and the gas contribute to the mass, momentum and enthalpy content of the dispersion. In Sections 4.3.1 and 4.3.2 above, the transport velocities of the droplets and the gas' individual species were synthesized with spatially localized conversion and interaction rates to establish phase-specific mass (or number) balances. Drawing on the transport processes identified in this context, we present combined-phase evolution laws for the mass, momentum and enthalpy of the gas-droplet dispersion here. Since the gas species and the oxide droplets diffuse differently and since the droplets experience thermophoresis, the balances for the dispersion mass, momentum and enthalpy differ from their single phase counterparts. For this reason, outlines of the physical arguments leading to Eqs. (4.28), (4.29) and (4.31) below are included in Appendix C.

Mass

If the carrier gas and the dispersed smoke droplets are considered as interpenetrating continua, then the gas-droplet dispersion may be characterized in terms of a dispersion mass density

$$\rho(\mathbf{Y}, T, N(\cdot)) = \rho_g \varepsilon_g + \rho_l \varepsilon_l. \quad (4.27)$$

With the aid of Eq. (4.27), we obtain for the continuity equation pertaining to both phases

$$\frac{\partial \rho}{\partial t} + \nabla \cdot (\rho \mathbf{u}) = -\nabla \cdot \left(\rho_l \varepsilon_l \left(\mathbf{u}_t + \mathbf{u}_{d,l}^{\varepsilon_l} \right) \right). \quad (4.28)$$

Momentum

If the inertia associated with droplet diffusion and thermophoresis is negligible and if the gas momentum is assumed to be advected by the bulk velocity, then the spatially localized momentum balance of the gas-droplet dispersion reads

$$\rho \frac{\partial \mathbf{u}}{\partial t} + \left(\left(\rho \mathbf{u} + \rho_l \varepsilon_l \left(\mathbf{u}_t + \mathbf{u}_{d,l}^{\varepsilon_l} \right) \right) \cdot \nabla \right) \mathbf{u} = -\nabla P + \nabla \cdot \left(\mu \left(\nabla \mathbf{u} + (\nabla \mathbf{u})^T \right) \right). \quad (4.29)$$

Note that the dispersion is assumed to be sufficiently dilute such that Eq. (4.17) for the dispersion viscosity μ remains valid and the viscous stresses may be evaluated based on the bulk velocity field only. As is common, moreover, the dilatational part $2\mu/3(\nabla \cdot \mathbf{u})$ of the viscous stress tensor has been absorbed into the mechanical pressure $P(\mathbf{x}, t)$. Unlike the thermodynamic pressure p , P may vary in space and time and is, conceptually, akin

to a multiplier that enforces the continuity equation (Eq. (4.28)).

Enthalpy

In order to complete the description of the dispersion dynamics, we formulate an evolution equation for the dispersion enthalpy based on the premise that both the gas and the dispersed droplets share the common temperature $T(\mathbf{x}, t)$ at (\mathbf{x}, t) . In particular, any potential temperature differences between both phases are instantaneously eliminated by a heat exchange that conserves the dispersion enthalpy. The specific dispersion enthalpy h is defined as

$$\rho h(\mathbf{Y}, T, N(\cdot)) = \rho_g \varepsilon_g h_g + \rho_l \varepsilon_l h_l + \xi_l \sigma_l, \quad (4.30)$$

where $h_l(T)$ is the specific enthalpy of $\text{Al}_2\text{O}_3(\text{l})$. The third term in Eq. (4.30) represents the energy that is stored by an interface separating bulk $\text{Al}_2\text{O}_3(\text{l})$ from the surrounding gas.

Neglecting viscous heating, the dispersion enthalpy density ρh obeys the following evolution equation

$$\begin{aligned} \frac{\partial \rho h}{\partial t} + \nabla \cdot (\rho h \mathbf{u}) &= \nabla \cdot (\lambda \nabla T) + \dot{\omega}_{\text{rad},h} \\ &- \nabla \cdot \left(\rho_g \varepsilon_g \left(h_g \mathbf{u}_c - \sum_{k \in \mathcal{G}} Y_k h_k \mathcal{D}_k \frac{\nabla X_k}{X_k} \right) \right. \\ &\quad \left. + \rho_l \varepsilon_l h_l \left(\mathbf{u}_t + \mathbf{u}_{d,l}^{\varepsilon_l} \right) + \xi_l \sigma_l \left(\mathbf{u}_t + \mathbf{u}_{d,l}^{\xi_l} \right) \right), \end{aligned} \quad (4.31)$$

where $\dot{\omega}_{\text{rad},h}(\mathbf{Y}, T, N(\cdot)) = \rho \dot{q}_{\text{rad}}$ represents the heat emission rate due to thermal radiation (Section 2.4.4). By Maxwell's relation, the thermal conductivity of the gas-droplet dispersion λ can be expressed in terms of the gas conductivity, the droplet conductivity and the droplet volume fraction [47, Chapter 11] according to

$$\lambda(\mathbf{Y}, T, N(\cdot)) = \lambda_g \frac{\lambda_l + 2\lambda_g + 2\varepsilon_l (\lambda_l - \lambda_g)}{\lambda_l + 2\lambda_g - \varepsilon_l (\lambda_l - \lambda_g)}. \quad (4.32)$$

The thermal conductivity of liquid aluminum oxide is taken to be $\lambda_l = 1.5 \text{ W}/(\text{mK})$. However, this value is not only subject to rather large experimental uncertainties, but has also been obtained at a temperature close to the Al_2O_3 melting point and may not apply to the much larger temperatures encountered during combustion [15]. The thermal gas

conductivity λ_g [28, 90, 114], on the other hand,

$$\lambda_g(\mathbf{Y}, T) = \frac{1}{2} \left(\sum_{k \in \mathcal{G}} X_k \lambda_k + \left(\sum_{k \in \mathcal{G}} \frac{X_k}{\lambda_k} \right)^{-1} \right), \quad (4.33)$$

is computed in terms of the species-specific conductivities $\lambda_k(T)$ which are, in turn, obtained from the species viscosities μ_k [90, 186].

The first term on the right hand side of Eq. (4.31) may be expressed in terms of h by computing the gradient of Eq. (4.30) and solving the resulting expression for ∇T . In practice, however, we found a finite volume solver for Eq. (4.31) to frequently fail since the independently interpolated values of \mathbf{Y} , T and $N(\cdot)$ at a cell face and the interpolated face enthalpy h may not jointly satisfy Eq. (4.30). Phrased slightly differently, the reconstruction scheme of the finite volume method may lead to thermochemical state variables \mathbf{Y} , h and $N(\cdot)$ at a cell face for which a dispersion temperature T cannot be found and Eq. (4.30) is not honoured. In order to eliminate this robustness problem, we reformulate the enthalpy balance in terms of the dispersion temperature, obtaining after substitution of Eqs. (4.11), (4.22) and (4.24)

$$\begin{aligned} \rho C_p \left(\frac{\partial T}{\partial t} + \mathbf{u} \cdot \nabla T \right) &= \nabla \cdot (\lambda \nabla T) + \dot{\omega}_{\text{rad},h} \\ &\quad - \sum_{k \in \mathcal{G}} h_k (\varepsilon_g \dot{\omega}_{g,k} + \dot{\omega}_{gl,k}) - \rho_l h_l \dot{s}_{\varepsilon_l} - \sigma_l \dot{s}_{\xi_l} \\ &\quad - \left(\sum_{k \in \mathcal{G}} \rho_g \varepsilon_g Y_k \mathbf{u}_{d,k} C_{p,k} + \rho_l \varepsilon_l (\mathbf{u}_t + \mathbf{u}_{d,l}^{\varepsilon_l}) C_{p,l} \right. \\ &\quad \left. + \xi_l (\mathbf{u}_t + \mathbf{u}_{d,l}^{\xi_l}) \frac{d\sigma_l}{dT} \right) \cdot \nabla T. \end{aligned} \quad (4.34)$$

4.3.4 Enthalpy balance inside the fuel particle

After ignition and the formation of an envelope flame, the aluminum fuel particle remains liquid throughout the combustion process and may, strictly, develop internal flow structures such as Hill's vortex [60]. Here, however, we idealize the liquid particle as a thermally thick fixed rigid body, hence reducing the set of equations governing the internal particle dynamics to a single heat conduction equation,

$$\rho_p C_{p,p} \frac{\partial T}{\partial t} = \nabla \cdot (\lambda_p \nabla T), \quad (4.35)$$

4 A steadily burning aluminum particle

| Coefficients | Solid | Liquid |
|--------------|------------------------|------------------------|
| a_0 | 1.96×10^2 | 5.79×10^1 |
| a_1 | 2.50×10^{-1} | 4.53×10^{-2} |
| a_2 | -4.33×10^{-4} | -8.84×10^{-6} |
| a_3 | 1.96×10^{-7} | 0 |

Table 4.1 Coefficients of the polynomial fit in Eq. (4.36) for the temperature dependency of the thermal conductivity in the solid and liquid state.

where $\rho_p(T)$, $C_{p,p}(T)$ and $\lambda_p(T)$ denote, respectively, the bulk density [80, 146], the heat capacity [27, 69] and the thermal conductivity of the aluminum fuel particle. The thermal conductivity of Al is evaluated based on polynomial fits of the conductivities taken from Touloukian et al. [178] which are in line with more recently obtained data of Leitner et al. [100], but cover a wider temperature range. The solid and liquid phase heat conductivities as a function of the temperature are thus obtained as

$$\lambda_{p,\text{solid/liquid}}(T) = \sum_{i=0}^3 a_{i,\text{solid/liquid}} T^i, \quad (4.36)$$

where the coefficients $a_{i,\text{solid/liquid}}$, $i = 0, \dots, 3$, are listed in Table 4.1. The polynomials are then smoothly blended [157] to yield the particle conductivity as a function of T ,

$$\lambda_p(T) = s_b(T)\lambda_{p,\text{liquid}} + (1 - s_b(T))\lambda_{p,\text{solid}} \quad (4.37)$$

with

$$s_b(T) = \frac{1}{2} \left(1 + \tanh \left(\frac{T - T_{m,\text{Al}}}{\Delta T_m} \right) \right), \quad (4.38)$$

where we choose $\Delta T_m = 10$ K and used $T_{m,\text{Al}} = 933.61$ K as melting point of aluminum. Figure 4.2 depicts the data of the thermal conductivity of aluminum as a function of the temperature [100, 178] along with the polynomial fits and the blended function. A similar blending procedure is applied to obtain smooth transitions between the liquid and solid phase density and heat capacity of Al. Note that the steady-state solutions obtained in Sections 4.6 and 4.7 do not require a blending of the solid and liquid phase properties since the particle temperature remains well above $T_{m,\text{Al}}$ throughout the simulation. However, in view of the transition to an unsteady analysis in Chapter 5, we take the opportunity to discuss this technical aspect here.

Equations (4.34) and (4.35) governing, respectively, the dispersion temperature and the

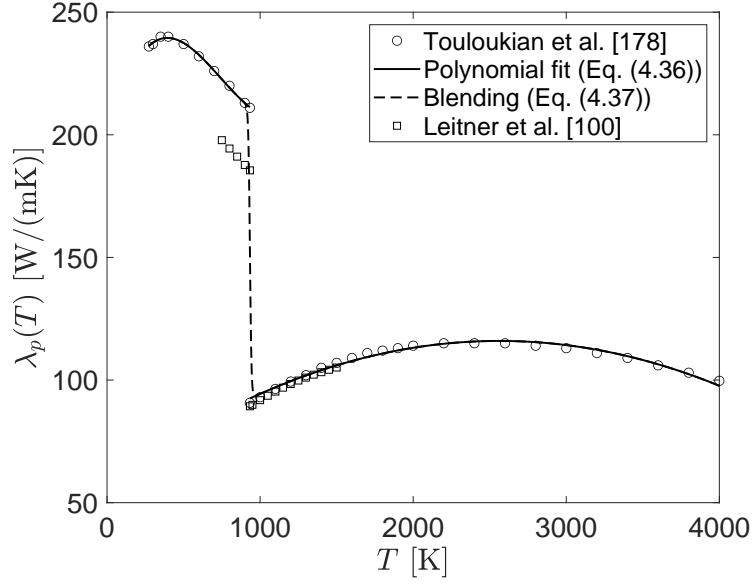


Figure 4.2 Temperature dependency of the thermal conductivity of aluminum. The plot includes the polynomial fits to the data of Reference [178] along with a smooth blending of the solid and liquid state properties as a function of the temperature and more recently obtained data [100].

internal particle temperature are linked through the flux-matching condition in Eq. (4.46) below.

4.4 Flux-matching interface conditions

At the interface separating the gas-droplet dispersion from the bulk aluminum particle (thick solid line in Fig. 4.3), the gas composition $Y_{k,s}$, $k \in \mathcal{G}$, temperature T_s and droplet charge $N_s(v)$, $v \in \Omega_v$, can be related to surface mass and heat fluxes through interfacial mass and enthalpy balances which are often referred to as flux-matching conditions [90, Section 16.9]. Here and below, the subscript s indicates evaluation at the particle surface. The surface values of \mathbf{Y} , T and $N(v)$ are imposed as Dirichlet boundary conditions and complement Eqs. (4.11), (4.34), (4.35) and (4.14).

Regarding droplet deposition, we assume that the rate at which the droplets are adsorbed at the particle surface is much larger than the rate at which the droplets are supplied by transport from the bulk dispersion. Consequently, the droplet number density at the surface vanishes, $N_s(v) = 0$ for $v \in \Omega_v$.

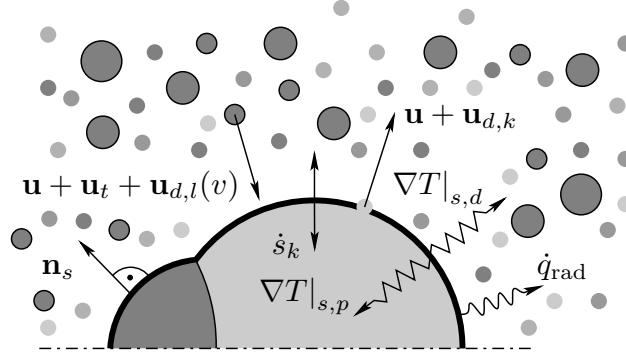


Figure 4.3 Illustration of the interface (thick solid line) separating the gas-droplet dispersion from the bulk fuel particle. At the interface, flux-matching conditions apply, ensuring a mass and enthalpy conserving exchange due to advective and diffusive transport, heterogeneous surface reactions and thermal radiation. Since the oxide droplets are assumed to be instantaneously incorporated into the particle upon collision, the droplet concentration vanishes at the surface as indicated by the absence of droplets close to the surface. Although the oxide cap is not considered in this chapter and excluded from the boundary treatment, in reality, it significantly affects the boundary conditions at the particle's surface and, thus, the structure of the envelope flame as discussed in Chapter 5.

4.4.1 Species mass fluxes

In the surface normal direction, the mass flux $\rho_g Y_k \mathbf{u}_k$ of species $k \in \mathcal{G}$ across the surface is balanced by its production rate \dot{s}_k due to heterogeneous surface reactions,

$$(\rho_g \mathbf{u}_k Y_k)|_s \cdot \mathbf{n}_s = \dot{s}_k, \quad k \in \mathcal{G}, \quad (4.39)$$

where $\mathbf{n}_s(\mathbf{x}, t)$ represents the outward-pointing surface unit normal vector. Upon summation of Eq. (4.39) over all species $k \in \mathcal{G}$ and substitution of Eq. (4.7), we obtain the following expression relating the Stefan flow velocity \mathbf{u}_s to the cumulative released or adsorbed mass

$$\rho_{g,s} \mathbf{u}_s \cdot \mathbf{n}_s = \sum_{k \in \mathcal{G}} \dot{s}_k = \dot{s}_G. \quad (4.40)$$

Introducing this result alongside Eq. (4.7) into Eq. (4.39), the species mass balance at the reactive particle surface reads

$$\dot{s}_G Y_{k,s} + \left(\rho_g Y_k \sum_{i \in \mathcal{G}} \mathcal{D}_i \frac{W_i}{W} \nabla X_i \right) \Big|_s \cdot \mathbf{n}_s - \left(\rho_g \mathcal{D}_k \frac{W_k}{W} \nabla X_k \right) \Big|_s \cdot \mathbf{n}_s = \dot{s}_k, \quad k \in \mathcal{G}. \quad (4.41)$$

The Stefan flow velocity $\mathbf{u}_s \cdot \mathbf{n}_s$ normal to the particle surface is imposed as Dirichlet boundary condition on the bulk velocity field (Eq. (4.29)).

4.4.2 Droplet mass fluxes

Although the droplet number density $N(v)$ is assumed to vanish at the reactive surface, droplets may still deposit on the reactive surface. Similar to Eq. (4.39), the balance of the droplet number density at the reactive surface reads

$$(N(v)\mathbf{u}_l(v))|_s \cdot \mathbf{n}_s = \dot{s}_v, \quad v \in \Omega_v, \quad (4.42)$$

where $\mathbf{u}_{l,s}(v)$ and $\dot{s}_v(v, \mathbf{Y}, T, N(\cdot))$ are, respectively, the velocity and the deposition rate of droplets with volume v . With the aid of the definition of $\mathbf{u}_l(v)$ in Eq. (4.13), Eq. (4.42) may be reformulated as

$$(N(v)(\mathbf{u} + \mathbf{u}_t))|_s \cdot \mathbf{n}_s - (\mathcal{D}_l(v)\nabla N(v))|_s \cdot \mathbf{n}_s = \dot{s}_v, \quad v \in \Omega_v. \quad (4.43)$$

If the thermophoretic and Stefan velocities $\mathbf{u}_{t,s}$ and \mathbf{u}_s jointly cause a droplet flux towards the particle surface ($(\mathbf{u} + \mathbf{u}_t)|_s \cdot \mathbf{n}_s < 0$), then the surface boundary condition $N_s(v) = 0$ does not apply to the advective flux in Eq. (4.43) [101, Chapter 2]. In spatially discrete terms, this implies that thermophoretic or flow-induced deposition may occur despite the condition $N_s(v) = 0$. Conversely, for outward-pointing advective transport ($(\mathbf{u} + \mathbf{u}_t)|_s \cdot \mathbf{n}_s \geq 0$), the boundary condition $N_s(v) = 0$ is active and the advective flux in Eq. (4.43) vanishes. The diffusive flux in Eq. (4.43), on the other hand, feels the boundary condition $N_s(v) = 0$ irrespective of the direction of the bulk and thermophoretic velocities. The deposition fluxes associated with particular moments of the droplet size distribution, for example, the volume fraction ($a = 1, k = 1$) or the surface density ($a = \sqrt[3]{36\pi}, k = 2/3$), can be obtained by av^k -weighted integration of Eq. (4.43) over the droplet size range Ω_v . Consequently, the mass flux associated with droplet deposition becomes

$$\begin{aligned} \dot{s}_l(\mathbf{u}, \mathbf{Y}, T, N(\cdot)) &= \rho_l \int_{\Omega_v} v(N(v)(\mathbf{u} + \mathbf{u}_t) - \mathcal{D}_l(v)\nabla N(v))|_s \cdot \mathbf{n}_s \, dv \\ &= \rho_l \left(\varepsilon_l \left(\mathbf{u} + \mathbf{u}_t + \mathbf{u}_{d,l}^{\varepsilon_l} \right) \right) \Big|_s \cdot \mathbf{n}_s. \end{aligned} \quad (4.44)$$

4.4.3 Enthalpy flux

Similarly, the conductive heat flux into the gas-droplet dispersion as well as the species- and droplet-bound enthalpy fluxes emitted from the surface are balanced by conductive

4 A steadily burning aluminum particle

heat fluxes into the particle, radiative heat losses to the surroundings and the heat released or consumed by the surface chemistry,

$$\begin{aligned}
& -\lambda_{g,s} \nabla T|_{s,d} \cdot \mathbf{n}_s + \sum_{k \in \mathcal{G}} (\rho_g \mathbf{u}_k Y_k h_k(T))|_s \cdot \mathbf{n}_s \\
& + \int_{\Omega_v} \left((\rho_l h_l v + \sigma_l \sqrt[3]{36\pi v^{\frac{2}{3}}}) N(v) \mathbf{u}_l(v) \right) \Big|_s \cdot \mathbf{n}_s dv \\
& = -\lambda_{p,s} \nabla T|_{s,p} \cdot \mathbf{n}_s - \sigma_{SB} \epsilon \left(T_s^4 - T_{\text{ref}}^4 \right) - \sum_{k \in \mathcal{S} \cup \mathcal{B}} \dot{s}_k h_k(T_s).
\end{aligned} \tag{4.45}$$

In Eq. (4.45), the reference background temperature is chosen as $T_{\text{ref}} = 298$ K and the additional subscripts d or p indicate the evaluation of the one-sided temperature gradients at the surface on part of the dispersion or the particle, respectively. The thermal emissivity of the particle amounts to $\epsilon = 0.1$ [78]. Note that the conductive heat flux into the bulk matter of the particle is expected to be minor for two reasons. First, we consider a steady combustion state in which all intra-particle temperature gradients vanish if the temperature T_s is uniform along the surface. Second, because the thermal conductivity of liquid aluminum is much higher than that of the gas [100, 178], the particle Biot number becomes rather small ($\text{Bi} \ll 1$). Consequently, heat diffuses much faster than it is supplied from the environment, rendering the temperature across the particle approximately constant. The third term in Eq. (4.45) represents the enthalpy deposition flux associated with the transport of droplet bulk enthalpy (h_l) and surface energy (σ_l). With the aid of Eq. (4.39), Eq. (4.45) can be simplified as

$$\begin{aligned}
& -\lambda_{g,s} \nabla T|_{s,d} \cdot \mathbf{n}_s + \int_{\Omega_v} \left((\rho_l h_l v + \sigma_l \sqrt[3]{36\pi v^{\frac{2}{3}}}) N(v) \mathbf{u}_l(v) \right) \Big|_s \cdot \mathbf{n}_s dv \\
& = -\lambda_{p,s} \nabla T|_{s,p} \cdot \mathbf{n}_s - \sigma_{SB} \epsilon \left(T_s^4 - T_{\text{ref}}^4 \right) - \sum_{k \in \mathcal{G} \cup \mathcal{S} \cup \mathcal{B}} \dot{s}_k h_k(T_s).
\end{aligned} \tag{4.46}$$

Since the depositing droplets carry the same bulk enthalpy h_l as the particle bulk species $\text{Al}_2\text{O}_3(\text{B})$ they are converted into, these terms cancel from Eq. (4.46).

4.4.4 Solution procedure

At every surface point, Eqs. (4.41) and (4.46) constitute a system of non-linear equations, $\mathbf{f}(\mathbf{y}_s) = \mathbf{0}$, for $|\mathcal{G}| + 1$ independent variables \mathbf{y}_s . The system is solved using a Newton–Raphson scheme based on a semi-analytical Jacobian. Since we employ two different

surface reaction mechanisms (Section 4.2.1), the physical variables included in \mathbf{y}_s depend on the thermodynamic and chemical assumptions accompanying either mechanism. If the surface production rates $\dot{s}_k(\mathbf{Y}_s, T_s, \Psi)$, $k \in \mathcal{G} \cup \mathcal{S} \cup \mathcal{B}$, where Ψ denotes the surface composition (Section 2.2.2), are computed from the detailed reaction mechanism of Glorian et al. [69], then \mathbf{y}_s encompasses the surface mass fractions \mathbf{Y}_s as well as the surface temperature T_s . On the other hand, if vapour-liquid phase equilibrium holds at the interface, that is, the partial pressure $p_{\text{Al},s}(\mathbf{Y}_s) = X_{\text{Al},s}p$ of the aluminum vapour at the surface coincides with the equilibrium vapour pressure $p_e^{R_p}(T_s)$ over the curved particle surface with radius R_p , $p_{\text{Al},s} = p_e^{R_p}(T_s)$, then $X_{\text{Al},s} = p_e^{R_p}(T_s)/p$ is prescribed as a function of the surface temperature T_s . Consequently, the unknowns \mathbf{y}_s include the aluminum evaporation rate \dot{s}_{Al} , the mass fractions $Y_{k,s}$ of the remaining species $k \in \mathcal{G} \setminus \{\text{Al}\}$ and the surface temperature T_s . The equilibrium vapour pressure $p_e^{R_p}(T)$ includes the Kelvin effect and can be obtained from the difference in the chemical potentials of gaseous and liquid aluminum (Eqs. (2.30) and (2.31) adapted to Al). With the phase equilibrium-based surface chemistry, the production rates \dot{s}_k , $k \in \mathcal{G} \setminus \{\text{Al}\}$, of species other than Al can be prescribed either using a detailed mechanism or based on additional phase equilibrium conditions. Here, we specifically set $\dot{s}_k = 0$ for $k \in \mathcal{G} \setminus \{\text{Al}, \text{Al}_2\text{O}_3/\text{c}\}$ and determine the adsorption rate of gaseous $\text{Al}_2\text{O}_3/\text{c}$ based on the kinetic theory of gases [30],

$$\dot{s}_{\text{Al}_2\text{O}_3/\text{c}} = -X_{\text{Al}_2\text{O}_3/\text{c},s}p\sqrt{\frac{W_{\text{Al}_2\text{O}_3/\text{c}}}{2\pi RT_s}}, \quad (4.47)$$

with unity sticking coefficient. The kinetic rate in Eq. (4.47) embodies the direct heterogeneous conversion of gaseous to bulk liquid aluminum oxide on the particle surface following the reaction in Eq. (4.1). The chemical reaction in Eq. (4.1) is also part of the surface mechanism of Glorian et al. [69], but kinetically described in a way that slightly differs from Eq. (4.47). Although surface chemistry and smoke deposition may cause the formation of bulk $\text{Al}_2\text{O}_3(\text{l})$ at the particle surface, rendering the aluminum particle biphasic, for the sake of steadiness, we neglect any influence of the change in bulk composition on the shape of the particle and maintain a spherical, pure aluminum particle with constant radius R_p throughout this chapter. We ought to emphasize that this assumption is relaxed in the context of the unsteady analysis in the following chapter, where a varying particle morphology is explicitly accounted for.

Strictly, the non-linear system of equations based on Eqs. (4.41) and (4.46) is singular since the species mass fractions obey the constraint

$$\sum_{k \in \mathcal{G}} Y_{k,s} = 1 \quad (4.48)$$

by definition. The singularity can be eliminated by replacing one of the species equations (Eq. (4.41)) by Eq. (4.48). Additionally, it is advantageous to switch from species mass to mole fractions $X_{k,s} = W_s Y_{k,s} / W_k$, $k \in \mathcal{G}$, since the diffusion velocities are formulated in terms of mole fractions and since, in the case of aluminum phase equilibrium, the Al mole fraction is prescribed.

4.5 Numerical methods

4.5.1 General aspects

The governing equations of Section 4.3 are solved using our finite volume-based in-house research software BOFFIN [83]. For computational efficiency, the equations governing the species mass fractions and droplet number density as well as the dispersion mass, momentum and temperature are decoupled and solved sequentially.

The PBE in Eq. (4.14) is discretized along the v -coordinate using the same flux-limited high-resolution finite volume method [3, 93, 132] as used for the spatially homogeneous reactors discussed before. Similarly, the coagulation birth and death terms are evaluated using a volume-conserving finite volume formulation [104, 119] based on a piecewise linear, discontinuous reconstruction of the droplet size distribution [156] (Section 2.7.2).

Within a global time step, the gas species (Eq. (4.11)), discrete number densities (Eq. (4.14)) and temperature (Eqs. (4.34) and (4.35)) are first independently evolved in space and time. Here, a first order accurate fractional time stepping [128, Section 6.3] is applied in order to separate spatial transport from spatially localized processes, particularly chemical reactions, gas-droplet mass and heat exchange and droplet v -transport. This ameliorates the disparity in time scales between different physical and chemical processes and allows for the application of tailored time integrators. Specifically, the spatial transport step is integrated using the forward Euler scheme, while the variable order implicit integrator DVODE [21] or, as fallback, the fifth-order accurate implicit Runge-Kutta

scheme RADAU5 [75] are used for the stiff gas phase reaction step. The PBE step is, in turn, split into one ODE system for droplet nucleation and growth and one for droplet coagulation that are integrated with the fifth order accurate explicit Runge-Kutta method DOPRI5 [76] and the third-order Runge-Kutta scheme RK3(2) [18, 20], respectively. In the event that either explicit integrator fails, RADAU5 is called as fallback. Both the chemical reaction and PBE steps are parallelized using a bespoke load-balancing scheme [158]. For the spatial transport, the advective fluxes are computed from a total variation diminishing (TVD) linear combination of upwind, central and downwind differences using a weight related to van Leer’s limiter [81, 99], whereas the diffusive fluxes are evaluated based on central differences.

For computational economy, the reaction step is only executed for spatial cells in which the dispersion temperature T exceeds the threshold of 400 K and both the gas phase and surface reaction rates from the detailed reaction mechanisms of Glorian et al. [69] are hard-coded. In the droplet formation kinetics, we further replaced, in many instances, the cubic root by an approximation that is based on an adaptation of the fast inverse square root algorithm [17], incurring an error of less than 0.3%.

After the scalars characterizing the gas and dispersed phase have been advanced in time, the variable-density continuity and momentum equations (Eqs. (4.28) and (4.29)) are solved over the global time step. The pressure-velocity coupling is achieved with the aid of the SIMPLEC scheme on a staggered grid [49] and central differences are used for all spatial derivatives. The time integration is based on the midpoint rule and the linear systems of equations are solved using conjugate gradient methods [116, 184]. The interface separating the aluminum fuel particle from the dispersion is represented by a simple cell-blocking scheme [123, Section 7.3-2], rendering the particle’s surface stair-stepped as visualized in Fig. 4.4. Although the particle’s volume associated with this discrete representation of the interface converges to the actual volume of a spherical particle as the grid is refined, the surface area remains constant. For this reason, the advective and diffusive fluxes are evaluated based on the actual surface density computed from the intersection of the spherical surface with the FV cells rather than the surface-to-volume ratio of the cells, permitting an exact recovery of the particle’s true surface area. Since, in general, most of the cells contain two faces which are associated with the reactive surface, the surface density in these particular cells needs to be distributed between the two faces. Here, we

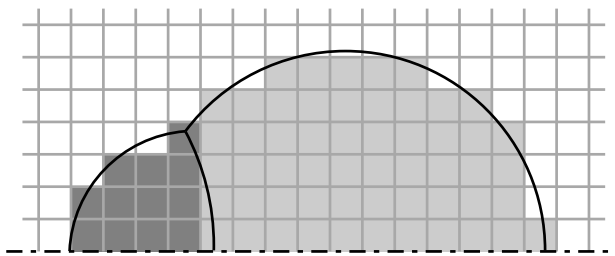


Figure 4.4 Schematic illustration of the cell blocking scheme. The grey shaded cells (light: Al-body, dark: Al_2O_3 -cap) correspond to blocked cells representing the fuel particle. Note that the cap is disregarded in the considerations of this chapter but included in the following unsteady analysis (Chapter 5).

introduce a splitting factor which is computed in terms of the position of a particular cell center with respect to the center point of the spherical surface, *i.e.*, aluminum body or oxide cap, the cell is associated with. For instance, the factor becomes small if the cell is located close to the centerline in Fig. 4.4 and the surface density is predominantly redistributed to the vertical cell face, whereas the factor tends to unity for cells that are located close to the horizontal center of the particle and the surface density is to a greater extent associated with the horizontal face. In this way, we can continuously distribute the surface density between two orthogonal cell faces.

4.5.2 Decoupling of droplet formation and gas phase chemistry

Prior to the analysis of the effect of different nucleation kinetics (Section 4.2.2) on our spatially resolved predictions reported in Section 4.6.1, we took a step back and assessed the different nucleation theories within the scope of the perfectly stirred reactor model (Chapter 2) to get a first impression of the impact of different nucleation rates at reasonable computational runtime. In this regard, moreover, we found the fully sequential numerical scheme employed for solving the PBE and the ODE for the gas phase chemistry to produce erroneous solutions given a reasonable time step size and a high enough nucleation rate. In order to investigate this behaviour in conjunction with different nucleation rates, we compared four different strategies to decouple the PBE (Eq. (2.26) as semi-discrete counterpart of Eq. (2.22)) and the ODE system governing the reactive gas-phase scalars (Eq. (2.15)).²

²Although surface chemistry is taken into account in the developments presented in this section, it does not affect the gas-droplet interactions and is omitted in the discussion.

In order to omit the integration of large and possibly stiff ODE systems, the reaction fractional step of PBE-based formulations is frequently integrated in time using a decoupling strategy that allows for the separation of particular processes and reduces the computational effort drastically. In our standard scheme (strategy 1), for instance, we successively integrate the gas phase chemistry (Eq. (2.15) with $\dot{\omega}_{gl} = \mathbf{0}$) while keeping the discrete droplet number densities \mathbf{H} fixed, the PBE (Eq. (2.22) with $dV/dt = 0$) with fixed Φ and finally the gas-droplet interaction and reactor expansion (Eq. (2.15) with $\dot{\omega}_g = \dot{\omega}_s = \mathbf{0}$ and $\dot{\omega}_{\text{rad},h_g} = 0$ and Eq. (2.26) following from Eq. (2.22) with $G = \dot{R} = \beta = 0$) using an explicit Euler scheme. An alternative solution strategy (strategy 2) is based on the idea to solve the semi-discrete PBE (Eq. (2.26)) and the ODE system governing species scavenging (Eq. (2.15) with $\dot{\omega}_g = \dot{\omega}_s = \mathbf{0}$ and $\dot{\omega}_{\text{rad},h_g} = 0$) in a coupled fashion in order to achieve a regulation of the nucleation process by reduction of the supersaturation during the integration. Lastly, a fully coupled scheme (strategy 3) is considered where we solve the semi-discrete PBE (Eq. (2.26) based on Eq. (2.22)) and the complete ODE system governing the reactive scalars (Eq. (2.15)) concomitantly. Note that the concomitant evolution of PBE and gas phase chemistry is not only prohibitive due to the stiffness of the overall ODE system caused by the disparities in time scales but is also computationally very expensive due to the increasing complexity; a fact that also applies to the previous strategy. In order to account for the reduction in supersaturation during droplet nucleation and to establish a direct feedback from the nucleation process to the gas composition without a prohibitive increase in computational cost, we developed a fourth coupling strategy (strategy 4), in which the gas phase reaction step is augmented by balance equations that describe the consumption of gas phase species due solely to nucleation (Eq. (2.15) with $\dot{\omega}_{gl}$ based on changes in the droplet population caused by nucleation). Specifically, in order to ensure exact mass exchange between gas and droplets by the nucleation process, the change in the droplet volume fraction and surface density caused by nucleation are solved analytically using the piecewise linear parameterization of the regularized δ -distribution (Section 2.5). Subsequently, based on the time-integral of the nucleation rate during the reaction step, an effective nucleation rate is computed for application during the PBE step (Eq. (2.26) based on Eq. (2.22)). Finally, the release of heat due to coagulation and the consumption or release of $\text{Al}_2\text{O}_3/c$ by condensational surface growth and dissociation are accounted for by repeating the reaction step, albeit restricted to gas-droplet mass and heat exchange,

4 A steadily burning aluminum particle

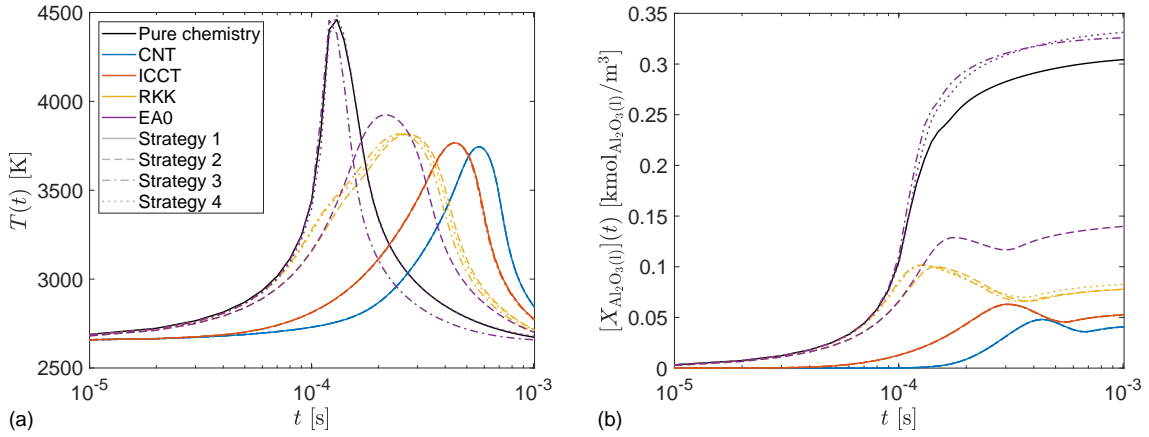


Figure 4.5 Time evolution of temperature (a) and $\text{Al}_2\text{O}_3(\text{l})$ concentration (b) in a PSR at atmospheric pressure obtained with different combinations of nucleation kinetics and coupling strategies. In the figure, the different colors correspond to different nucleation kinetics, while the line style indicates the coupling scheme. The black solid line represents a size-agnostic simulation with pure chemistry that serves as baseline for the comparison.

after the PBE step (Eq. (2.15) with $\dot{\omega}_{gl}$ based on the change in the droplet volume fraction and surface density caused by processes other than nucleation).

Figure 4.5 depicts the time evolutions of the temperature and $\text{Al}_2\text{O}_3(\text{l})$ concentration in a PSR at atmospheric pressure obtained with the different combinations of nucleation kinetics (distinguished by line color) and coupling strategies (distinguished by line style). Besides information on the quality of different coupling schemes, Fig. 4.5 reveals that the nucleation based on the unactivated rate (EA0, Eq. (4.6)) proceeds on the smallest time scale, *i.e.*, at the highest rate, since droplet inception commences about an order of magnitude earlier and the smoke concentration is higher compared to the other kinetics. This is followed by the RKK (Eq. (4.5)) and the ICCT (Eq. (4.4)) nucleation rate, while the CNT nucleation kinetics (Eq. (4.3)) are the slowest among the theories under consideration. Given the disparities in nucleation time scales, we can indeed acknowledge a major influence of different nucleation models on our predictions. As baseline for our comparison of the different coupling strategies, we use a pure chemistry simulation without dissociation (black line) in which the smoke is described in terms of a mass fraction and the nucleation is considered part of the gas phase chemistry [69]. Since the unactivated nucleation rate of Eq. (4.6) is specifically constructed to resemble the nucleation kinetics in a size-agnostic description, we expect this nucleation rate to yield the best agreement. In fact, this is only the case given a particular coupling strategy is used (see purple lines). While the standard scheme used so far (strategy 1) completely fails for the

EA0 and the RKK nucleation kinetics (not shown), since, in these cases, nucleation is so fast that more nuclei are produced than gaseous Al_2O_3 is available, it seems to work fine for the slower nucleation processes driven by the rates originating from ICCT and CNT. Here, the coupling strategy has no significant influence on the temperature and smoke concentration. However, as nucleation becomes more intense (RKK), the solutions drift apart, causing a significant deviation of the solution obtained using coupling strategy 2 for the EA0 kinetics. Compared to the baseline (pure chemistry), only the fully coupled (strategy 3) and the time-integrated (strategy 4) approaches yield reasonable accuracy. Besides being numerically infeasible, the fully coupled strategy introduces high-frequency oscillations in the oxide smoke size distribution (not shown) caused by the disparities in the order of magnitude between species mass fractions and temperature on the one hand and the discrete droplet number densities on the other hand.

The investigations reported here lead to two important conclusions. First, the nucleation kinetics have a major impact on the combustion characteristic by affecting not only the maximum flame temperature and smoke concentration but also the time scale of smoke inception. Second, given reasonable time step sizes, an intensification of the nucleation rate causes standard decoupling strategies to fail and more sophisticated approaches are required. In order to ensure an accurate solution, we employ the coupling strategy 4 (time-integral nucleation rate) to obtain the predictions discussed in the following Sections 4.6 and 4.7 and Chapter 5.

4.5.3 Performance of the transport fractional step

Besides the reaction fractional step, also for the spatial transport step a number of numerical schemes is used to meet our requirements of an accurate but numerically feasible solution of the transport equations presented in Section 4.3. Since the implementation of the transport step and the discretization scheme has changed substantially compared to the original version of the research code [83], the developments are briefly presented here before turning to the discussion.

Adaptive time stepping

Typically, the high diffusivity of some gas species results in specific CFL numbers that exceed the CFL number associated with other processes such as droplet and momentum

transport significantly. Consequently, in the original implementation, the global leading time step size was adjusted to satisfy a certain constraint on the maximum CFL number over all reactive and droplet phase scalars although the time integration of the reaction fractional step and the integration of the mass and momentum equations could deal with much larger time step sizes. In this way, the total simulation time is substantially increased by computing more time steps than necessary or, more precisely, by computing more flow and reaction steps than necessary. In order to avoid these additional expenses, we developed an explicit time integration scheme for the scalar transport step (Eqs. (4.11), (4.14), (4.34) and (4.35)) with adaptive time stepping.

The global leading time step size Δt is chosen to keep the CFL number associated with momentum transport,

$$\text{CFL}_{\mathbf{L}} = \frac{u\Delta t}{\Delta x} + \frac{2\mu\Delta t}{\rho(\Delta x)^2}, \quad (4.49)$$

below 0.4 across all FV cells and all directions, mitigating the additional computational cost in the flow and reaction fractional step. In Eq. (4.49), u and Δx represent, respectively, the flow velocity and the FV-cell width in a particular direction. Using the current global time step and the transport properties obtained from the thermochemical state at the end of the previous time step, the hypothetical CFL numbers of all scalars are then computed which, in general, exceed $\text{CFL}_{\mathbf{L}}$. Based on the largest scalar CFL number, the number of transport substeps is determined in a way that the same target CFL number as in the momentum transport step is maintained. In this way, we are able to attenuate the computational cost while preserving the solution's accuracy.

Evaluation of transport properties

The kinetically detailed description of a droplet-laden reactive flow developed in this thesis comes at the expense of a computationally extremely challenging evaluation of the transport properties. In particular, the species (Eqs. (4.8) and (4.9)) and droplet (Eq. (4.21)) diffusivities are the most expensive parameters to evaluate. In a FV-based discretization scheme, all transport properties and primary unknowns need to be interpolated onto or calculated at the control volume's face in order to compute the fluxes across the interfaces that ultimately control the change of the cell center values. The first of two alternatives to achieve this is the interpolation of the primary unknowns \mathbf{Y} , T and $N(v)$ onto the cell faces. In this way, we keep the notions of primary and derived quantities clear and

distinct. Although this approach seems straightforward, in practice, it is met by severe drawbacks on part of the computational time. Interpolating the primary unknowns on the cell face requires the evaluation of the transport parameters multiple times per grid cell depending on the dimensionality of the problem under consideration. In an alternative and more practical approach, we compute the transport properties only once per cell at the centroids and interpolate their value on the cell face, hence significantly reducing the computational cost. However, at cell faces that correspond to a reactive surface, we still compute the transport properties from the primary unknowns which are governed by the flux-matching boundary conditions of Section 4.4.

In order to further reduce the computational cost of the sequential solution scheme, the transport properties may be calculated *a priori* and stored for reuse. Because of the correction velocity introduced in Eq. (4.10) and the reappearance of the species and droplet diffusivities in the temperature evolution equation (Eq. (4.34)), these properties are needed at several instances during the transport step. Albeit memory-intensive, the pre-computation and storage of the species and droplet diffusivities at the cell centers is advantageous, since the computational cost associated with the repeated computation as part of the time step adaption scheme is prohibitive.

Artificial diffusion

The appearance of sharp gradients in the solution of the spatial transport equations requires the application of high-resolution schemes to avoid high-frequency modes in the solution. Here, we apply a TVD flux-limiting scheme to all scalars (\mathbf{Y} , $N(v)$ and T) that is based on van Leer's limiter adapted to non-uniform grids [81, 99] and implements a smooth transition between second and first order spatial accuracy wherever needed. In general, the cell face value Φ_f of a scalar quantity Φ is computed according to

$$\Phi_f = \Phi_u + \Psi_{\text{TVD}}(r_\Phi)w_{\text{int}}(\Phi_d - \Phi_u), \quad (4.50)$$

where the subscripts u and d correspond to the grid nodes on the upwind or downwind side of the cell face, respectively, w_{int} denotes the interpolation weight and $\Psi_{\text{TVD}}(r_\Phi)$ is the flux limiter. In particular, informed by the ratio r_Φ of the two upwind gradients of Φ , the scheme switches continuously between an upwind ($\Psi_{\text{TVD}} = 0$), linear ($\Psi_{\text{TVD}} = 1$) and

4 A steadily burning aluminum particle

downwind ($\Psi_{\text{TVD}} = 1/w_{\text{int}}$) interpolation of the primary unknown onto the cell face. Every deviation from the linearly interpolated value is tantamount to an additional (positive or negative) artificial diffusion term on the right hand side of the respective transport equation. In the current code, the TVD scheme is implemented by means of a modified diffusion coefficient,

$$\mathcal{D} \leftarrow \max(\mathcal{D} + \mathcal{D}_{\text{art}}, 0), \quad (4.51)$$

which includes the physical diffusivity \mathcal{D} as well as an artificial component

$$\mathcal{D}_{\text{art}} = w_{\text{int}} |u| (1 - \Psi_{\text{TVD}}) \Delta x. \quad (4.52)$$

Since the flux limiter at a particular interface varies from one scalar to another, for the gas species mass fractions ($\Phi = Y_k, k \in \mathcal{G}$), the diffusion term violates mass conservation (see also Section 4.3.1) since we have

$$\sum_{k \in \mathcal{G}} w_{\text{int}} |u| (1 - \Psi_{\text{TVD},k}) \Delta x \nabla Y_k \neq 0, \quad (4.53)$$

in general. In order to correct for this mass violation, we add the artificial diffusion term in Eq. (4.53) to our definition of the correction velocity in Eq. (4.10), which has been specifically constructed to balance the net bulk flow induced by the Hirschfelder–Curtiss approximation of the diffusion velocity. The artificial diffusivity, moreover, depends on the advective velocity u at the cell face under consideration which defines the up- and downstream nodes and, strictly, also involves the correction velocity u_c at the cell face, rendering the definition of u_c recursive. Here, we neglect the contribution of the correction velocity to the advecting velocity at the cell face based on which the artificial diffusivity is evaluated to close the equation. This is tantamount to the assumption that the TVD interpolation scheme is only applied to the advective fluxes associated with the bulk flow velocity u , while the mass fluxes related to the correction velocity are discretized using central differences.

4.6 Combustion characteristics at atmospheric pressure

In order to validate the presented model formulation, we consider the single Al-particle combustion case experimentally investigated by Bucher et al. [23–26]. An aluminum par-

4.6 Combustion characteristics at atmospheric pressure

ticle with diameter $D_p = 2R_p = 210 \mu\text{m}$ falls under the influence of gravity in a column of different oxidizing gas mixtures (79 % N_2 , 21 % O_2 and 79 % Ar , 21 % O_2 by volume) at an ambient temperature of $T = 298 \text{K}$. The particle is ignited by a laser and accelerates during free fall in a coflowing gas with velocity 0.13cm/s . Bucher et al. [24, 26] pointed out that a quasi-steady, spherically symmetrical combustion mode is established after an induction period of about 10 ms. The spatial distributions of AlO and temperature are measured significantly later such that the steadiness of the profiles is guaranteed. Bucher et al. [23, 24] measured the smoke profile by quenching the particle and its smoke envelope on a silicon wafer 3 mm below the point of ignition which, according to them, is equivalent to a burning time of 12 – 17 ms, yielding an average particle velocity of approximately 0.2m/s . Since the particle’s actual velocity just before quenching is thought to be higher than its average velocity and since the terminal settling velocity of a particle with an unreactive boundary layer in the Stokes regime is approximately 0.5m/s , we consider a resting particle that is subjected to an undisturbed flow of pure gas at an incident uniform velocity of $u_{\text{in}} = 0.5 \text{m/s}$. This value of the inflow velocity was also considered by Glorian et al. [69].

The experimental measurements of AlO and $\text{Al}_2\text{O}_3(\text{l})$ concentrations acquired by Bucher et al. [24, 25] were reported in the form of normalized radial profiles. By consequence, the comparison of these measurements with our predictions is limited to a qualitative kind and the conclusions drawn in Sections 4.6.1 and 4.6.2 are subject to the caveat that the predicted AlO and $\text{Al}_2\text{O}_3(\text{l})$ levels may be quantitatively inaccurate.

Taking advantage of the problem’s symmetry, the governing equations are solved in cylindrical coordinates $(x, r)^T \in \Omega_{\mathbf{x}}$ on a two-dimensional, wedge-shaped physical domain with axial and radial extents of $30D_p$ and $15D_p$, respectively (Fig. 4.8). At the stream-wise outlet, homogeneous Neumann boundary conditions are applied to all fields. At the lateral boundary, homogeneous Neumann conditions similarly apply to the reactive scalars and the droplet number density, while the bulk velocity obeys far-field Dirichlet conditions. For a structured 192×96 grid that contracts towards the particle, the particle surface is discretized by 36 finite volume cells in physical space with a minimum spacing of $\Delta x_{\text{min}} = 7.93 \mu\text{m}$. Commensurate with the detailed convergence analysis of Section 4.6.1, the PBE in Eq. (4.14) is discretized in v -space using a logarithmic grid with 64 cells. The droplet size space extends from the volume of a single aluminum oxide molecule up to a

4 A steadily burning aluminum particle

value that corresponds to a droplet with a diameter of approximately $2\ \mu\text{m}$. The time step is adapted during the simulation in order to maintain a CFL number below 0.4. In order to permit the establishment of a steady state necessary for a reasonable comparison with the experimentally obtained data, the size and morphology of the burning particle remain unchanged; an assumption that is relaxed within the scope of the unsteady investigations in Chapter 5. Physically, this implies that evaporated liquid aluminum is continuously replaced and any liquid aluminum oxide that has been deposited on the surface or formed through heterogeneous surface oxidation is instantaneously removed, preventing the formation of an oxide cap. A steady particle combustion state is reached after a physical time of approximately 4 to 5 ms.

In order to be able to separately analyze the changes induced in the envelope flame and smoke halo by reactions involving nitrogen (Section 4.6.2), we first investigate the influence of gas and surface chemistry and the impact of a size-resolved droplet description including dissociation and coagulation on the predictive accuracy for the Al-O₂/Ar case (Section 4.6.1). While the combustion in O₂/N₂ is relevant to the idea of a cyclic metal fuel economy, the Al-O₂/Ar case has been extensively examined in the past [11, 19, 24, 60, 69, 148], permitting us to include comparisons with previously reported predictions in which the smoke was aggregated into a mass fraction. For brevity, the droplet formation and interaction kinetics considered in the following are identified by a list of slash-separated letters, ‘N/G/C’. Here, ‘N’ indicates the nucleation rate expression and may be either CNT (Eq. (4.3)), ICCT (Eq. (4.4)), RKK (Eq. (4.5)) or EA0 (Eq. (4.6)). If ‘G’ or ‘C’ are included in the list, then surface growth/dissociation or coagulation, respectively, are included. Conversely, the absence of ‘G’ or ‘C’ indicates that the corresponding process has been deactivated.

4.6.1 Aluminum particle combustion in an O₂/Ar mixture

Resolution and computational expense

The nominal spatial and size resolutions we listed above and employ for the following analysis campaign were determined as part of a convergence analysis using the CNT nucleation rate and the surface/gas phase kinetics of Glorian et al. [69]. In the context of the perfectly stirred reactor of Chapter 2, 64 exponentially spaced v -cells were found to be sufficient for the maximum relative error in the droplet volume fraction, the total number

4.6 Combustion characteristics at atmospheric pressure

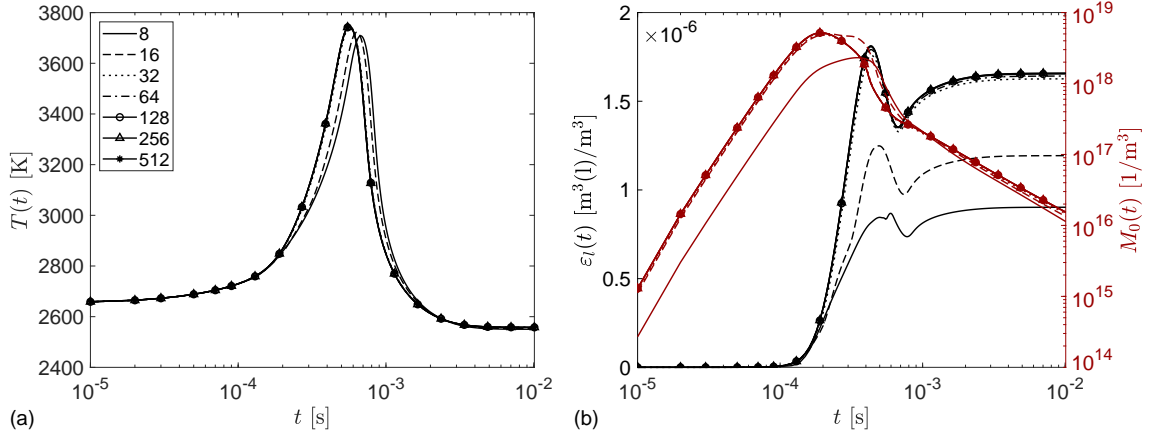


Figure 4.6 Time evolutions of temperature (a) as well as droplet volume fraction and total droplet number density (b) in a PSR at atmospheric pressure for different v -grid resolutions.

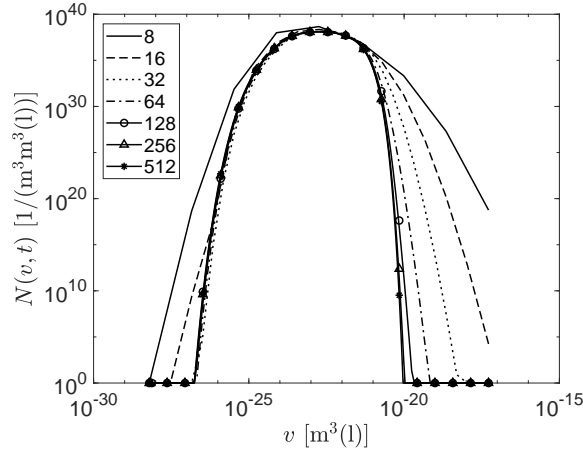


Figure 4.7 Droplet size distribution in a PSR at atmospheric pressure at $t = 10$ ms for different v -grid resolutions.

density and the dispersion temperature to remain within 2% (or less) of the solution obtained on a 512-cells grid over the entire course of combustion. Figures 4.6 and 4.7 depict, respectively, the time evolutions of temperature T , droplet volume fraction ε_l and total droplet number density M_0 as well as the droplet size distribution $N(\cdot)$ at $t = 10$ ms in a PSR at atmospheric pressure obtained on v -grids with 8, 16, 32, 64, 128, 256 and 512 cells.

For 64 v -cells, Table 4.2 shows the results of a spatial convergence analysis that includes three different grids with 120×60 , 192×96 and 240×120 finite volume cells, respectively. Besides geometrical data on the spatial resolution, Table 4.2 shows the relative deviations in the maximum values of the droplet volume fraction, total number density, flame temperature and flow velocity across the flow domain from the corresponding values computed

on the finest grid. The final column in Table 4.2, moreover, lists the spatially averaged particle temperature. On the 192×96 grid, the relative error in the droplet volume fraction decreases below 5%, while the remaining variables are accurate to within 2%. In light of the variability in the experimental data, we deemed this accuracy sufficient.

In order to quantify the additional computational expense incurred by a size-sensitive description of the oxide smoke dynamics, we compare in Table 4.3 the average runtimes of the PBE-based model for each fractional step with the runtimes of a reference CFD simulation in which the oxide smoke is described in terms of a mass fraction. The runtime measurements were acquired on 24 cores of an AMD Ryzen Threadripper 3960X processor and averaged over 100 time steps in steady state. Since we found that the droplet formation rates have a profound influence on the stiffness of the reaction step, the CFD-PBE model is operated with two different sets of kinetics; the nucleation rate EA0 without surface growth, but with coagulation and the CNT amended by Reiss' modification (RKK) including growth and coagulation. Apart from coagulation and size-dependent transport, the first case is designed to recover the formation kinetics of a size-agnostic CFD calculation without dissociation.

If the PBE is combined with the nucleation rate EA0, then the total runtime increases by a factor of 3.9 compared to the reference CFD run. About 70% of this runtime increase arises in the PBE step and is mainly incurred by the evaluation of the coagulation kernel. Although the solution of the PBE based on 64 v -cells is tantamount to an increase in the number of scalars from 11 to 75, the scalar transport step is computationally rather cheap, displaying a runtime increase by a factor of only 1.9. The runtime of the flow solver increases by a similar factor because of the more expensive evaluation of the dispersion's transport parameters as well as the computation of the additional source terms and advection velocities in Eqs. (4.28), (4.29) and (4.34). With the RKK nucleation rate and surface growth or dissociation, moreover, the total runtime of the CFD-PBE simulation doubles, indicating that the computational expense strongly depends on the droplet formation kinetics. This runtime increase is almost exclusively caused by the reaction step which turns very stiff following the evaporative release of $\text{Al}_2\text{O}_3/c$ during the preceding PBE step. Physically, we observe here a kinetically rapid condensation-evaporation cycle spanning the reaction and PBE steps. In summary, the numerical solution of the PBE appears to be computationally efficient, incurring an expense that stems mainly from

| Grid | #Cells [-] | #Cells/ D_p [-] | Δx_{\min} [μm] | $\varepsilon_{l,\max}$ [$10^{-5} \text{ m}^3(1)/\text{m}^3$] | $M_{0,\max}$ [$10^{18}/\text{m}^3$] | T_{\max} [K] | $\ \mathbf{u}\ _{\max}$ [m/s] | $T_{p,\text{avg}}$ [K] |
|------------------|---------------|----------------------|--|---|--|-------------------|----------------------------------|---------------------------|
| 120×60 | 7200 | 13 | 16.15 | 6.35 (21.0%) | 4.83 (6.8%) | 3626.90 (1.0%) | 4.21 (11.0%) | 2530.64 (0.4%) |
| 192×96 | 18432 | 27 | 7.93 | 7.65 (4.9%) | 5.09 (1.7%) | 3595.75 (0.2%) | 4.77 (0.8%) | 2522.31 (0.1%) |
| 240×120 | 28800 | 37 | 5.75 | 8.04 | 5.18 | 3590.29 | 4.73 | 2520.95 |

Table 4.2 Spatial convergence analysis for the Al-O₂/Ar case. Besides the total number of grid cells, the resolution across the particle’s diameter D_p and the minimum cell width Δx_{\min} , the table lists the maximum values across the flow domain of some of our key observables alongside the mean particle temperature $T_{p,\text{avg}}$ for three different grids. The parentheses include the relative deviations of the computed variables from those determined on the finest grid (240×120).

| Step | CFD | Runtime [ms] | |
|------------------|------|--------------------|----------------------|
| | | CFD-PBE (EA0/C) | CFD-PBE (RKK/G/C) |
| Chemistry | 17.3 | 23.7 | 204.4 |
| PBE | – | 95.1 | 124.3 |
| Flow solver | 9.0 | 17.1 | 16.6 |
| Scalar transport | 19.5 | 37.5 | 39.5 |
| Total | 47.1 | 184.8 | 394.5 |

Table 4.3 Comparison of the average runtimes per time step for a CFD simulation and two CFD-PBE simulations (EA0/C and RKK/G/C) using the gas and surface reaction mechanisms of Glorian et al. [69] in the Al-O₂/Ar case. Note that the total runtime per time step also includes post-processing operations and, hence, does not correspond to the sum of the three fractional steps.

the coagulation kinetics, but may be accompanied by the generation of fast and costly gas-droplet interaction time scales.

Influence of chemistry

Before analyzing predictions obtained with a PBE-based size-sensitive description of the oxide smoke, we assess, in this section, the influence of the surface and gas phase kinetics on the simulation results for a simplified, size-agnostic representation of the smoke in terms of a mass fraction. To this end, CFD simulations in which the oxide smoke is idealized as a gas phase species are performed for different combinations of surface and gas phase kinetics. Besides the geometry of the single particle configuration, Fig. 4.8 shows contour plots of the magnitude of the bulk flow field $\|\mathbf{u}\|$ including stream lines, the AlO and Al₂O₃(l) mass fractions Y_k , $k \in \{\text{AlO}, \text{Al}_2\text{O}_3(\text{l})\}$, and the temperature field T in steady state for the gas phase and surface kinetics of Glorian et al. [69] including Al₂O₃(l) dissociation.³ Close to the particle surface, the flow field is governed by a strong outward-pointing Stefan flow mediated by intense aluminum evaporation that causes a stagnation point on the centerline upstream of the particle. As indicated by the AlO peak, the gas flame front is located rather close to the surface where the temperature is high and reaches almost 3800 K. Following a cascade of gas phase reactions, Al₂O₃(l) condenses out and forms a wide smoke envelope that wraps around the gas flame front. Since Al₂O₃(l) condensation is accompanied by a significant heat release, the temperature

³The dissociation of Al₂O₃(l) is enabled by activating the reverse pathways of Reactions 50 and 51 in Table B1 of Reference [69].

4.6 Combustion characteristics at atmospheric pressure

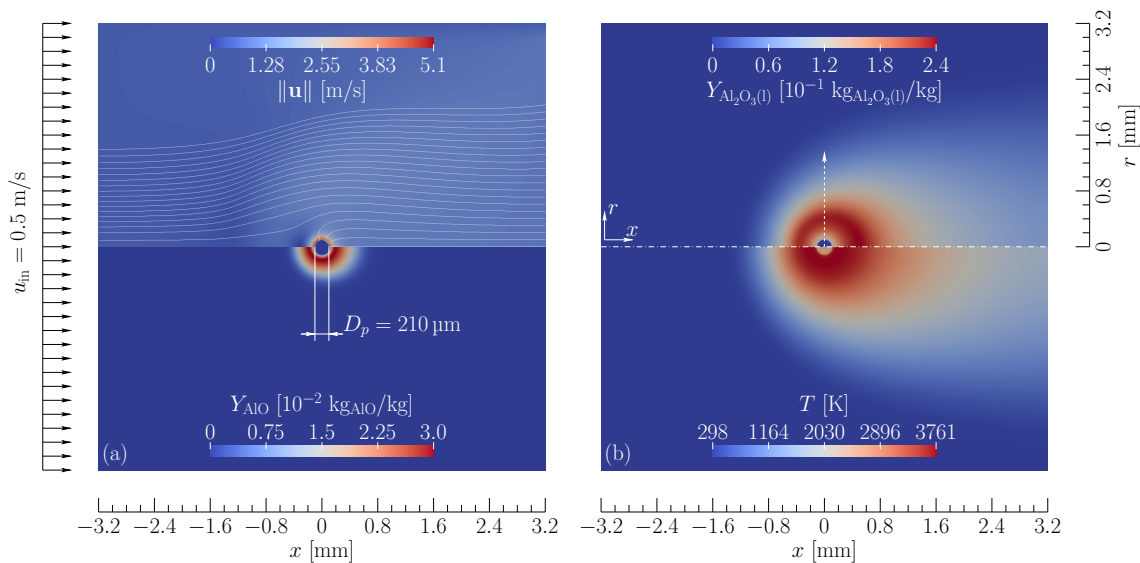


Figure 4.8 Geometry and inflow boundary conditions for the flow of an O_2/Ar gas mixture around a spherical burning aluminum particle with diameter $D_p = 210 \mu\text{m}$. The contour plots in figure (a) show the magnitude of the flow field $\|\mathbf{u}\|$ along with streamlines (top) and the distribution of the AlO mass fraction Y_{AlO} (bottom). Figure (b) depicts the distributions of the $\text{Al}_2\text{O}_3(l)$ mass fraction $Y_{\text{Al}_2\text{O}_3(l)}$ (top) and the temperature T (bottom). The results were obtained in a pure CFD simulation with gas phase and surface kinetics [69] including $\text{Al}_2\text{O}_3(l)$ dissociation.

is also high across the smoke halo, decreasing further outwards due to heat conduction towards the cold free-stream. Downstream of the particle, the combustion products are flushed out of the computational domain, while spreading diffusively in all directions.

For the surface kinetics of Glorian et al. [69] and either equilibrium gas phase chemistry [73] or the detailed kinetics of Glorian et al. [69], Fig. 4.9 shows profiles of the normalized mole fractions \bar{X}_k of $k = \text{AlO}$ and $k = \text{Al}_2\text{O}_3(l)$ and the temperature T (red lines) along the white dashed ray in Fig. 4.8(b). Since the differences between equilibrium surface chemistry and the surface kinetics of Glorian et al. [69] are minor, we decided to invoke the surface kinetics throughout and excluded, for conciseness, the results obtained with equilibrium surface chemistry from Fig. 4.9. Contrary to the red dashed line, the red dash-dotted line indicates predictions obtained with dissociation. For comparison, we also include in Fig. 4.9 the experimental data of Bucher et al. [24] (blue line with markers) and the predictions of Glorian et al. [69] and Bucher et al. [24] (black lines).

Figure 4.9 indicates that predictions obtained with equilibrium gas phase chemistry (solid lines) or gas phase kinetics including endothermic dissociation (red dash-dotted line) fit the experimental data much better than the gas phase kinetics without dissociation (dashed lines). If dissociation is absent, then the experimentally measured maximum

4 A steadily burning aluminum particle

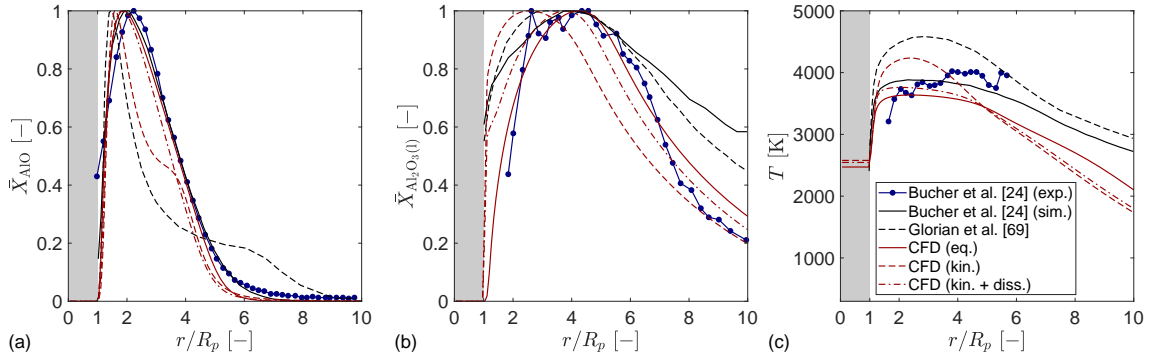


Figure 4.9 Comparison of the radial AlO (a), $\text{Al}_2\text{O}_3(l)$ (b) and temperature (c) profiles for the $\text{Al-O}_2/\text{Ar}$ case obtained in our CFD predictions (red lines) using surface kinetics and equilibrium gas chemistry (solid line), gas phase kinetics (dashed line) and gas phase kinetics including oxide dissociation (dash-dotted line) with experimental data obtained by Bucher et al. [24] (blue line with markers) and the simulation results of Bucher et al. [24] and Glorian et al. [69] (black lines).

flame temperature is significantly exceeded and the AlO profile is not only shifted towards the particle surface but also acquires a characteristic kink. Since the predictions obtained with equilibrium chemistry agree well with those computed from the detailed reaction mechanism of Glorian et al. [69] and dissociation, we conclude that the reaction rates in the mechanism are sufficiently rapid for chemical equilibrium to be attained. Inside the flame zone, the small differences between both results are caused by the thermodynamically consistent treatment of droplet incompressibility in the equilibrium calculation. Furthermore, the differences between our results with gas phase kinetics and those obtained by Glorian et al. [69] are mainly due to differences in the thermodynamic properties of $\text{Al}_2\text{O}_3(l)$ (Section 4.2.1). Similarly, the slight deviations of the equilibrium calculations by Bucher et al. [24] from ours may also be due to differences in the species' thermodynamic properties as well as the fact that Bucher et al. [24] considered a pure diffusion problem without inflow. This last point explains the faster radial decay of both the $\text{Al}_2\text{O}_3(l)$ mole fraction and the temperature at large distances from the surface in our equilibrium simulation. In comparison to the experimental measurements, the major deficiency that all predictions have in common is too sharp a temperature gradient at the surface; except for the equilibrium chemistry, moreover, oxide smoke persists too close to the particle surface.

Influence of size-sensitive droplet dynamics

In a CFD-PBE description of oxide smoke, dissociation is not included in the gas phase reaction mechanism, but instead accounted for through negative surface growth. Since

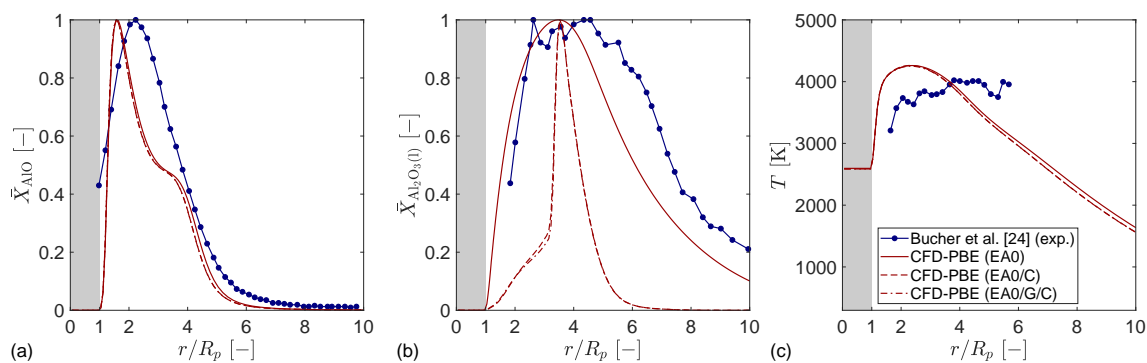


Figure 4.10 Comparison of the radial AlO (a), $\text{Al}_2\text{O}_3(\text{l})$ (b) and temperature (c) profiles for the $\text{Al-O}_2/\text{Ar}$ case obtained in our CFD-PBE predictions (red lines) using the unactivated Arrhenius nucleation rate without coagulation and growth (EA0, solid line), with coagulation but without growth (EA0/C, dashed line) and with both coagulation and growth (EA0/G/C, dash-dotted line) with the experimental data obtained by Bucher et al. [24] (blue line with markers).

the analysis of the preceding section showed that equilibrium chemistry and the detailed gas phase mechanism of Glorian et al. [69] lead to similar predictions if dissociation is included, we proceed with the gas phase kinetics of Glorian et al. [69] in the following. In order to obtain kinetic similarity in terms of droplet nucleation with the preceding CFD results (Fig. 4.9, red lines), the EA0 nucleation rate is chosen. In Fig. 4.10, the radial AlO, $\text{Al}_2\text{O}_3(\text{l})$ and temperature profiles obtained with our size-resolved CFD-PBE formulation for pure nucleation (EA0, red solid line), nucleation and coagulation (EA0/C, red dashed line) and nucleation, growth and coagulation (EA0/G/C, red dash-dotted line) are compared with the experimental data of Bucher et al. [24] (blue line with markers). In the pure nucleation case, the AlO and temperature profiles resemble the results obtained in the CFD simulation without dissociation (Fig. 4.9, red dashed line), indicating that energy storage in the gas-droplet interface has a minor effect. Notwithstanding, the oxide smoke distribution matches the experimental profile much better as it is slightly narrower and shifted away from the particle surface. This change is induced by thermophoretic droplet transport and a slight decrease in the droplet diffusivity (Eq. (4.21)) compared to the diffusivity of the $\text{Al}_2\text{O}_3(\text{l})$ species whose transport properties were previously taken as those of gaseous Al_2O_3 . While the AlO and temperature profiles remain almost unchanged if coagulation is activated, the $\text{Al}_2\text{O}_3(\text{l})$ profile is contracted to a very sharp, narrow peak that reflects the tremendous increase in the droplets' sizes and an associated reduction in the droplet diffusivities. Specifically, in the kinetic gas-droplet interaction regime, the slip-corrected Stokes–Einstein diffusion coefficient decreases approximately according to

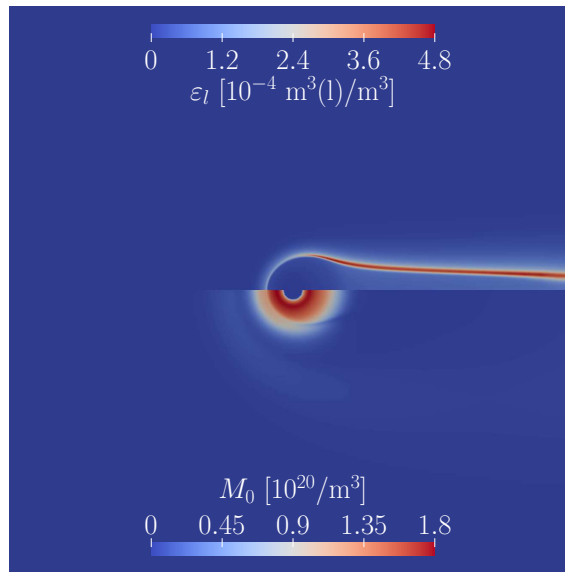


Figure 4.11 Spatial distributions of the droplet volume fraction ε_l (top) and the total droplet number density M_0 (bottom) obtained from a CFD-PBE calculation of the Al-O₂/Ar case with an unactivated nucleation rate, growth and coagulation (EA0/G/C).

$1/d^2$ as the droplet diameter d increases (Eq. (4.21)). Physically, small droplets nucleate near $r/R_p \approx 2$, and migrate both due to diffusion and Stefan advection to larger radial locations. Concomitantly, they experience rapid coagulation with an attendant reduction in diffusional mobility, finally entering a thin smoke trail (Fig. 4.11, top). Here, coagulation has been effective at reducing the total droplet number density (Fig. 4.11, bottom) whose peak correlates well with the maximum nucleation rate (not shown).

A curious implication of Fig. 4.10 is that droplet growth has hardly any effect on the radial profiles. In conjunction with the observations that the kink in the AlO profile as indicator of absent dissociation reappears and that the temperature is overpredicted, this suggests that the dissociation of Al₂O₃(l) is too weak and that the chemical equilibrium in Eq. (4.1) tends too far towards Al₂O₃(l). In order to identify potential inadequacies in the thermodynamic properties of Al₂O₃, we repeated the EA0/G/C calculation using the Al₂O₃ vapour pressure curve of Beckstead et al. [11, Eq. (2)] instead of the one obtained from the chemical potentials of Al₂O₃ and Al₂O₃(l) and found that dissociation is too fast, decreasing the flame temperature to about 3000 K (not shown). On the minus side, it remains doubtful, in this case, whether, for so large a dissociation rate, the reaction and PBE fractional steps can still be solved in a segregated fashion (Section 4.5.2).

4.6 Combustion characteristics at atmospheric pressure

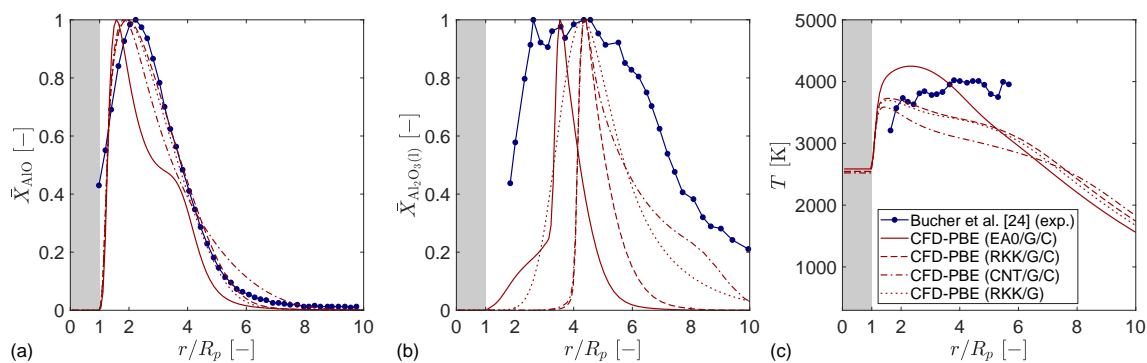


Figure 4.12 Comparison of the radial AlO (a), $\text{Al}_2\text{O}_3(\text{l})$ (b) and temperature (c) profiles obtained in our CFD-PBE calculations of the Al- O_2 /Ar case for three different nucleation rates (red lines) with experimental data obtained by Bucher et al. [24] (blue line with markers). Apart from the red dotted line, all simulations include nucleation, growth and coagulation.

| Case | $\varepsilon_{l,\max}$ [$10^{-4} \text{ m}^3(\text{l})/\text{m}^3$] | $M_{0,\max}$ [$1/\text{m}^3$] |
|-------------------|--|------------------------------------|
| CFD-PBE (EA0/G/C) | 2.02 | 1.81×10^{21} |
| CFD-PBE (RKK/G/C) | 1.36 | 2.44×10^{20} |
| CFD-PBE (CNT/G/C) | 0.39 | 4.35×10^{18} |
| CFD-PBE (RKK/G) | 0.41 | 3.08×10^{22} |

Table 4.4 Maximum droplet volume fraction $\varepsilon_{l,\max}$ and total droplet number density $M_{0,\max}$ along the radial coordinate for the CFD-PBE simulations of Fig. 4.12 in the Al- O_2 /Ar case.

Influence of the nucleation rate

In the previous section, we found that droplet diffusion is a main determinant of the smoke halo's shape, but that the unactivated nucleation rate EA0 is too fast, shifting the chemical equilibrium between aluminum suboxides and $\text{Al}_2\text{O}_3(\text{l})$ towards $\text{Al}_2\text{O}_3(\text{l})$. Since the rate EA0 was designed to mimic the forward $\text{Al}_2\text{O}_3(\text{l})$ formation rate in the reaction mechanism of Glorian et al. [69], alternative nucleation rates that are based on the CNT or modifications of the CNT are investigated here. Figure 4.12 depicts the radial AlO, $\text{Al}_2\text{O}_3(\text{l})$ and temperature profiles obtained from CFD-PBE simulations with growth and coagulation for three different nucleation rates (EA0, RKK, CNT) in comparison with the experimental measurements. Since predictions obtained with the ICCT differed insignificantly from those of the CNT, we excluded the ICCT results from Fig. 4.12. Complementary to Fig. 4.12, Table 4.4 lists the maxima of the droplet volume fraction and total droplet number density along the radial coordinate (white dashed ray in Fig. 4.8(b)).

Compared to the unactivated rate EA0, the RKK and CNT nucleation rates are sub-

4 A steadily burning aluminum particle

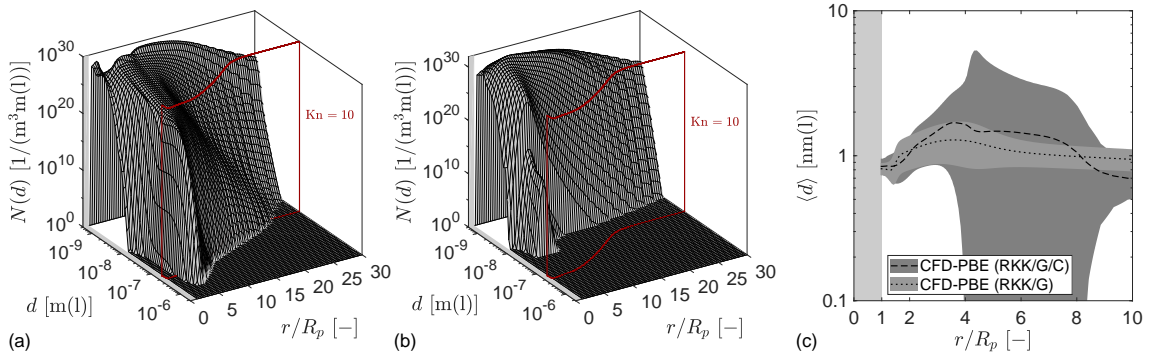


Figure 4.13 Comparison of the radial oxide smoke size distribution and the mean droplet diameter obtained in CFD-PBE calculations using the RKK nucleation rate with (a) and without (b) coagulation in the Al-O₂/Ar case. The red frames indicate a Knudsen number of 10 and approximate the boundary of the kinetic gas-droplet interaction regime. The grey patches in figure (c) represent a plus/minus one standard deviation range about the mean droplet diameter. Note that the droplet size distributions were transformed from volume-based to diameter-based distributions.

stantially smaller, leading to a decrease in the maximum total number density by one and three orders of magnitude, respectively. Likewise, the droplet volume fraction is reduced substantially. As a result of the slower nucleation and the reduction in condensational heat release, the chemical equilibrium is shifted from Al₂O₃(l) towards the aluminum suboxides and both the AlO-kink and the temperature overprediction disappear. As in Fig. 4.10, the narrow Al₂O₃(l) profiles obtained with the RKK and CNT rates originate from intense coagulation and an accompanying reduction in the droplets' diffusional mobility.

Since the narrow, coagulation-induced smoke profile is at variance with the experimental observations, we repeated the RKK calculation without coagulation. The corresponding exploratory predictions are shown as red dotted lines in Fig. 4.12. While the absence of coagulation leaves the AlO and temperature profiles nearly unchanged, the smoke halo becomes stretched and more diffuse, leading to an improved, albeit still imperfect, agreement with the measurements.

In addition to Fig. 4.12, Fig. 4.13 shows the oxide smoke size distributions obtained in a CFD-PBE simulation based on the RKK nucleation rate with (a) and without (b) coagulation as well as the respective mean droplet diameters (c) over the radial coordinate r/R_p at $x = 0$ m. The red frames represent a Knudsen number of 10 and indicate that the droplets live predominantly in the kinetic regime. Coagulation endows the size distribution with a wide exponential tail and leads to an increase in the size variance, particularly near $r/R_p \approx 5$ where the Al₂O₃(l) concentration peaks (Fig. 4.12). At this location, some droplets even prevail in the transition regime ($1 \lesssim \text{Kn} \lesssim 10$). Although the droplets

remain nano-sized, the average droplet size is increased by up to 36 % due to coagulation.

Interim summary

Based on the assumption that the experimental measurements of Bucher et al. [24] represent a ground truth, our analyses in the preceding sections led to four important conclusions. First, droplet nucleation and dissociation are decisive for the temperature and AlO predictions to be accurate as these are strongly tied to the chemical equilibrium between gaseous aluminum suboxides and the oxide smoke. If nucleation is too fast and dissociation too slow or excluded, then the temperature is overpredicted and the AlO-profile features a kink that is not observed in the experiments. Second, the shape of the smoke halo is mainly controlled by the diffusional mobility of the droplets and, hence, by the droplets' sizes. Third, coagulation seems to be either absent or far less effective at increasing the droplets' sizes than suggested by our present enhanced coagulation kernel (Section 2.4.1). A potential explanation is that the smoke droplets acquire charges due to thermionic emissions and the capture of ions and electrons from the carrier gas [86, 150], leading to electrostatic repulsion that impedes droplet collisions. In the context of magnesium combustion, this behaviour has also been observed and investigated by Vishnyakov et al. [182]. Fourth, despite the size-resolved smoke dynamics, the CFD-PBE predictions exhibit much sharper a temperature gradient near the fuel particle's surface than indicated by the experimental measurements. Savel'ev and Starik [148] surmised that the near-surface temperature observed in the experiments may be low because the smoke halo impedes the diffusion of oxygen towards the surface; on the other hand, they also pointed out possible reasons for inaccuracies in the available temperature measurements.

Possibly, the assumption that the smoke condensation proceeds through the precursor species $\text{Al}_2\text{O}_3/c$ could also be accountable for the near-surface misprediction of the temperature. If the droplets formed, instead, from a heterogeneous pool of aluminum suboxides and, subsequently, matured into the bulk Al:O ratio of 2:3 [94], then the heat release due to gas chemistry might weaken compared to the condensation-induced heat release and the rise of the dispersion temperature might be stronger tied to the presence of smoke droplets. On the other hand, we observed in CFD simulations with equilibrium gas phase chemistry that the inclusion or absence of gaseous $\text{Al}_2\text{O}_3/c$ has hardly any influence on the aluminum suboxide, smoke and temperature distributions (not shown). This finding is

corroborated by spatially homogeneous equilibrium calculations for a stoichiometric Al-O₂ mixture where a negligibly small amount of gaseous Al₂O₃/c was present. Consequently, the choice of Al₂O₃/c as intermediate and perhaps artificial condensing species does not seem to be the reason for the sharp near-surface temperature rise.

Bucher et al. [24] recovered the radial AlO, Al₂O₃(l) and temperature profiles from an inverse Abel transformation by assuming spherical symmetry. While this assumption is corroborated by our AlO and temperature predictions (Fig. 4.8), the relative gas-particle flow entails a distortion of the Al₂O₃(l) halo into a smoke trail that is not spherically symmetrical, casting doubt on the validity of the Al₂O₃(l) profile reconstruction. In order to discount the absence of spherical symmetry in our predictions from the comparison in Fig. 4.12(b), we show in Fig. 4.14 the corresponding smoke profiles after a line-of-sight integration in the streamwise direction, $\bar{X}_{\text{los,Al}_2\text{O}_3(l)}$. The line-of-sight integration corresponds to an orthogonal projection of the smoke halo onto the outflow boundary, that is, the plane on which the particle impacted in the experiments. Although the finite domain size may cause part of the smoke trail to be omitted from the line-of-sight integration, Fig. 4.14 shows that the agreement of the RKK/G predictions with the experimental measurements improves considerably. This implies that part of the remnant deviations in Fig. 4.12(b) is related to the asymmetry of the predicted smoke halo rather than a shortcoming of the droplet formation kinetics. By contrast, the dashed line in Fig. 4.14 shows that the lack in spherical symmetry of the smoke halo is not accountable for the large discrepancies we previously observed in the presence of coagulation (RKK/G/C).

In the following analysis of the steady envelope flame about an isolated Al-particle in an O₂/N₂ atmosphere, we operate the CFD-PBE formulation with the RKK nucleation rate and surface growth/dissociation, excluding coagulation. Strictly, this selection is tantamount to a calibration of the nucleation and coagulation rates based on the Al-O₂/Ar experimental data. For the consolidated droplet formation kinetics, the comparison with the Al-O₂/N₂ measurements may then be considered a validation attempt. Although coagulation as feature of a size-resolved smoke description is excluded here, the size-sensitive CFD-PBE approach allows not only for an accurate account of diffusional droplet migration, but also permits the transition from empirical droplet formation rates [69] to nucleation, dissociation and condensational growth rates derived from first principles.

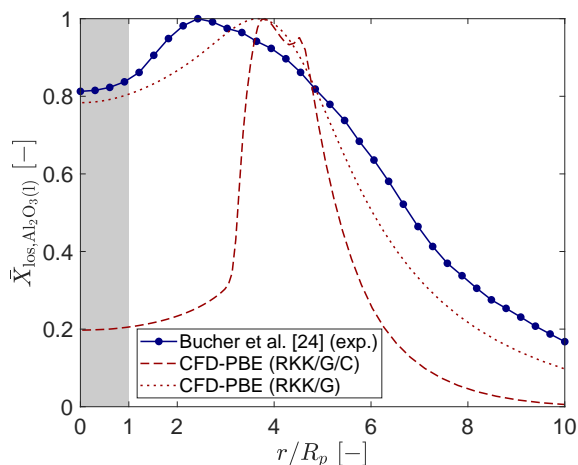


Figure 4.14 Comparison of the line-of-sight integrated $\text{Al}_2\text{O}_3(l)$ profiles obtained in our CFD-PBE calculation of the Al- O_2 /Ar case using the RKK nucleation rate with (red dashed line) and without coagulation (red dotted line) with experimental data obtained by Bucher et al. [24] (blue line with markers).

4.6.2 Aluminum particle combustion in air

Contrary to the Al- O_2 /Ar case, the combustion of aluminum particles in air is relevant to the idea of a metal-fuelled energy economy and the retro-fitting of existing solid fuel-fired power plants for operation with metals [12, 13, 36]. Following a qualitative analysis of the flame structure and smoke halo about an aluminum fuel particle burning in air, we compare, in the present section, CFD-PBE predictions obtained with the calibrated droplet formation kinetics (RKK/G) and the surface and gas phase kinetics of Glorian et al. [69] with available experimental measurements of radial AlO, $\text{Al}_2\text{O}_3(l)$ and temperature profiles [24, 25]. Subsequently, smoke size statistics are presented and the competition of droplet nucleation, dissociation and condensational surface growth is analyzed.

Spatial distributions

Figure 4.15 depicts contour plots of the advective droplet velocity $\|\mathbf{u} + \mathbf{u}_t\|$ (a, top), the temperature T (a, bottom) and the mass and mole fractions of Al_2O (b, top) and NO (b, bottom), respectively, in the vicinity of the burning particle. Near the particle surface, the Stefan flow induced by the evaporation of aluminum is opposed by a strong thermophoretic velocity that impedes the advection of the condensed oxide smoke away

4 A steadily burning aluminum particle

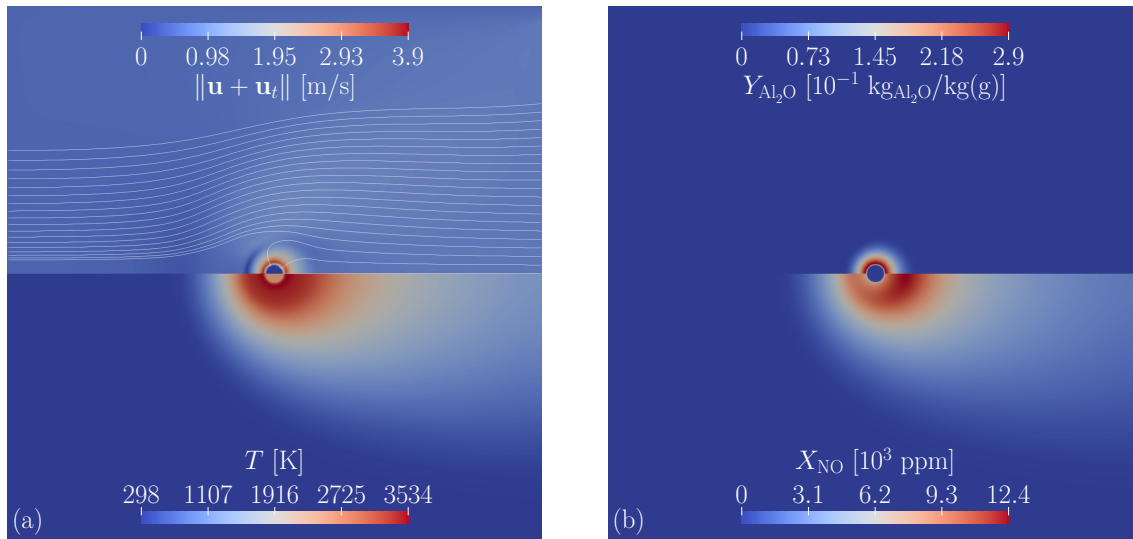


Figure 4.15 Contour plots of the magnitude of the advective droplet velocity $\|\mathbf{u} + \mathbf{u}_t\|$ along with streamlines (a, top), the temperature field T (a, bottom), the mass fraction of Al_2O , $Y_{\text{Al}_2\text{O}}$, as dominant suboxide (b, top) and the mole fraction X_{NO} of the pollutant NO (b, bottom) obtained in the $\text{Al}-\text{O}_2/\text{N}_2$ case.

from the particle [60].⁴ The maximum temperature of 3534 K is attained close to the particle surface near the location of the maximum mass fraction of Al_2O (Fig. 4.15(b, top)), the most abundant suboxide and a major precursor of $\text{Al}_2\text{O}_3/c$. The large temperatures within the envelope flame also drive the formation of NO through the thermal pathway [64], yielding an NO concentration that varies from a maximum of 12 000 ppm to 2500 ppm near the outlet. While the prediction of the overall NO_x -emissions is challenging in the context of a steady combustion mode, the amount of harmful nitrogen oxide species emitted during the conversion of single aluminum fuel particles is discussed in detail in Chapter 5.

Complementary to Fig. 4.15, Fig. 4.16 shows the spatial distributions of the droplet volume fraction ε_l (a, top) and the total droplet number density M_0 (a, bottom) as well as their rates-of-change (b) due to droplet formation. Although droplets are primarily formed upstream of the particle, the total number density forms a nearly spherically symmetrical halo about the particle that turns into a diffuse oxide trail further downstream. Contrary to the total droplet number density, the droplet volume fraction is characterized by an asymmetrical halo that is more pronounced in the wake of the particle. Near the particle surface where diffusive transport promotes deposition and the temperature exceeds 3500 K,

⁴The surface-averaged mass flux of Al due to evaporation amounts to $\dot{m}_{\text{Al},s}'' = 0.78 \text{ kg}/(\text{m}^2\text{s})$.

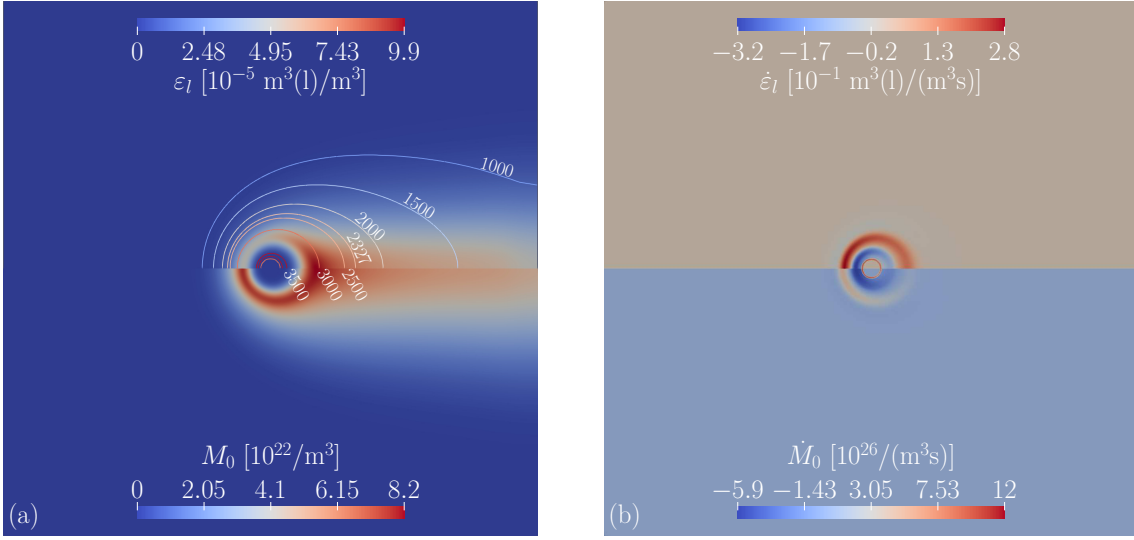


Figure 4.16 Spatial distribution of the droplet volume fraction ϵ_l (a, top) and the total droplet number density M_0 (a, bottom) obtained as statistics of the droplet size distribution $N(\cdot)$ as well as their rates-of-change (b) due to droplet formation in the Al-O₂/N₂ case. The temperature isolines in the top panel of figure (a) are coloured according to the colour scheme used in the bottom panel of Fig. 4.15(a).

the total droplet number density and volume fraction are very small as dissociation causes the droplets to dissociate endothermically. This is also reflected by the negative rates-of-changes $\dot{\epsilon}_l$ and \dot{M}_0 close to the surface in Fig. 4.16(b). The red ring at the particle surface in Fig. 4.16(b), however, indicates that there is a very narrow band where the temperature is sufficiently small for droplets to form and diffusively deposit on the burning particle.

In order to assess the influence of the heat released by droplet formation compared to gas phase chemistry, we provide, in Fig. 4.17, a scatter plot of both heat release rates at radial distances \tilde{r}/R_p measured from the origin $(x, r) = (0, 0)$ in all directions. Except at the particle surface, the heat release near the particle is almost exclusively driven by the exothermic formation of Al₂O from Al and AlO. Here, the dispersion temperature rises to such an extent that the smoke droplets begin to dissociate (filled red circles). In consequence, the gas phase is replenished with the gaseous intermediate species Al₂O₃/c and a strongly endothermic (filled black circles) regeneration of suboxides is triggered, thus completing the dissociation process and limiting the flame temperature. At the radial location where the heat release and heat consumption are balanced, the maximum temperature is reached. Further outwards, the heat contributed by droplet condensation is consumed by the endothermic formation of NO_x, leading to a temperature plateau (Fig. 4.15(a, bottom)). Beyond $\tilde{r} = 4R_p$, the exothermic recombination of O into O₂

4 A steadily burning aluminum particle

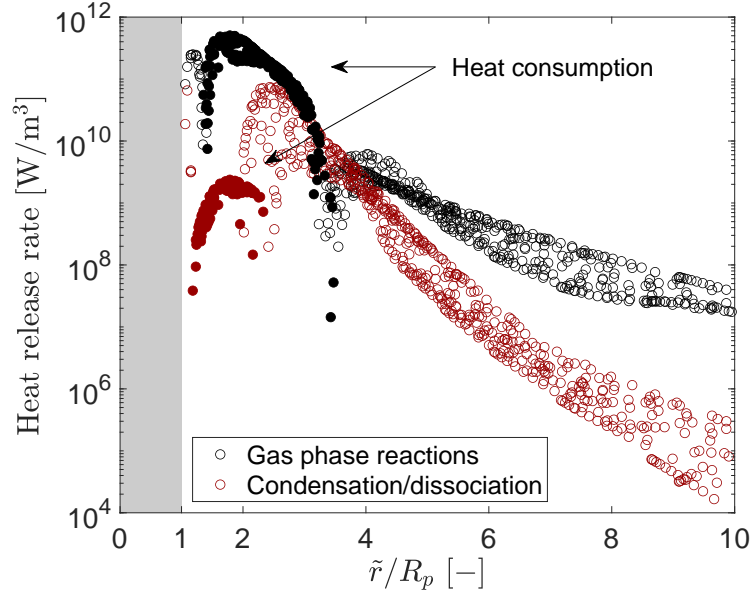


Figure 4.17 Scatter plot of the heat release by chemical gas phase reactions (black circles) and droplet formation (red circles) over the non-dimensional radial distance \tilde{r}/R_p from the center of the aluminum particle $((x, r) = (0, 0))$ in the $\text{Al-O}_2/\text{N}_2$ case. Note that net negative heat releases are indicated by filled circles and projected onto the positive ordinate because of the logarithmic scale.

commences, accompanying a decaying heat release from $\text{Al}_2\text{O}_3/c$ formation and subsequent droplet condensation. Here, advection and heat conduction towards the free-stream dominate and elicit a drop in temperature down to ambient conditions.

Comparison with experimental data

In Fig. 4.18, we qualitatively compare the normalized experimental data with CFD-PBE predictions along the radial coordinate r/R_p at $x = 0$ m, taking the differences in the two depicted measurements as estimates of the measurement uncertainties. Particularly for the more recently obtained measurements [24], the accuracy of the normalized AlO mole fractions in Fig. 4.18(a) is very good in terms of peak location and profile width. Conversely, the oxide smoke profile in Fig. 4.18(b) matches the earlier measurements [25] almost perfectly. Unfortunately, the temperature profile in Fig. 4.18(c) is poorly predicted, displaying a maximum that is located almost at the particle surface and a very steep gradient towards the surface. A similar deviation, albeit less sharp, also afflicts the model predictions reported by Beckstead et al. [11]. Because the results for an O_2/Ar atmosphere obtained in our simulations and in References [19, 24, 69, 148] (Section 4.6.1), too, display a sharp temperature gradient very close to the surface, we surmise that the deviation of

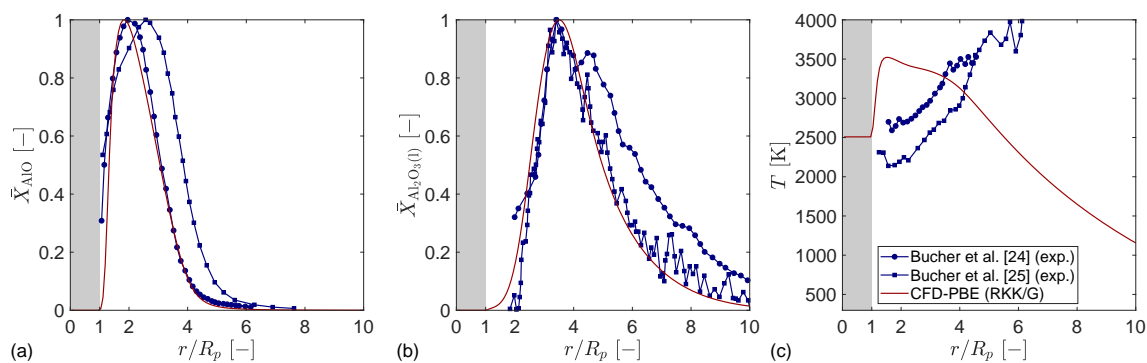


Figure 4.18 Comparison of the radial AlO (a), $\text{Al}_2\text{O}_3(\text{l})$ (b) and temperature (c) profiles obtained in our CFD-PBE predictions (red line) using the RKK nucleation rate (Eq. (4.5)) without coagulation with the experimental data obtained by Bucher et al. [24, 25] (blue lines with markers) in the Al- O_2/N_2 case.

the temperature profile is either due to an inherent drawback that our model formulation shares with these previous approaches and that is more critical if N_2 is present as diluent or related to measurement inaccuracies. Prentice and Nelson [131] suspected that nitrogen reacts with aluminum species. This conjecture is supported by the measurements of Bucher et al. [26] who detected condensed phase Al/N/O species of undetermined stoichiometry close to the surface ($r/R_P \in [1, 3]$). Since the temperature is sufficiently high here and the gas is fuel-rich, they surmised the endothermic formation of gaseous AlN through the chemical pathway $\text{Al} + 1/2\text{N}_2 \rightarrow \text{AlN}$ to locally decrease the flame temperature, a feature that is particular to N_2 containing atmospheres. Since the detailed reaction mechanism of Glorian et al. [69] does not contain AlN, any potential heat sink due to the formation of aluminum nitride is absent from our predictions, possibly promoting the large temperature near the particle surface. However, in equilibrium CFD simulations of the Al- O_2/N_2 case we found that the presence of AlN had no discernible effect on the predictions (not shown). Additionally, the fact that the $\text{Al}_2\text{O}_3(\text{l})$ profile in Fig. 4.18(b) is well predicted casts doubt on the validity of the experimental temperature data since the inward temperature gradient would drive a thermophoretic shift of the oxide smoke profile towards the burning particle. On the positive side, the surface temperature is around 2500 K and matches both the measurements and the simulation conducted by Bucher et al. [24], thus corroborating the validity of our heat flux boundary condition (Section 4.4).

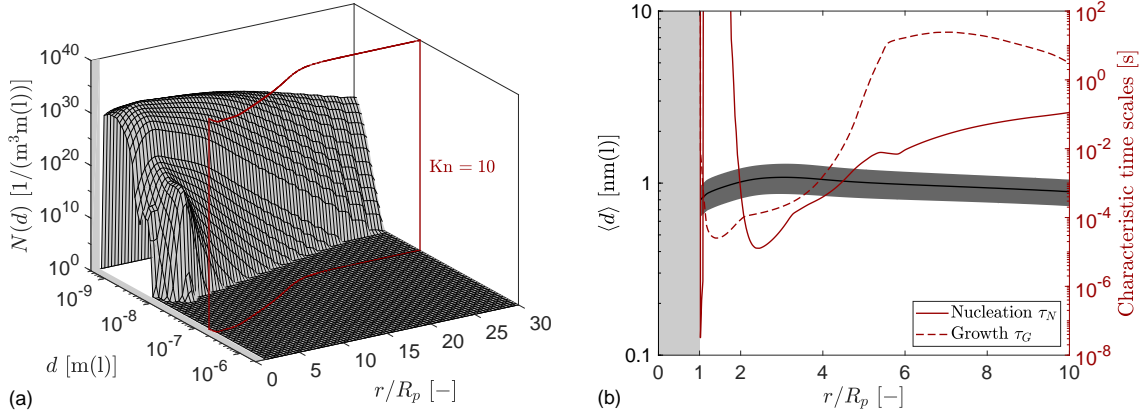


Figure 4.19 Droplet size distribution $N(\cdot)$ (a) and mean droplet diameter $\langle d \rangle$ as well as characteristic time scales τ of nucleation and growth (b) along the radial coordinate for the $\text{Al-O}_2/\text{N}_2$ case. The red frame in figure (a) corresponds to $\text{Kn} = 10$ and indicates the boundary between the kinetic and transition regime. Furthermore, the shaded patch in figure (b) represents plus/minus one standard deviation about the mean diameter. Note that the droplet size distribution was transformed from a volume-based to a diameter-based distribution.

Statistics and time scales

Compared to previous modelling efforts, the novelty in our approach lies with the incorporation of size-resolved oxide smoke dynamics, permitting a direct prediction of the oxide smoke size distribution. To illustrate the fidelity supplied by the model solutions, Fig. 4.19(a) depicts the change in the droplet size distribution along the radial coordinate r/R_p at $x = 0$ m. Since coagulation is excluded (Section 4.6.1), the droplet size distribution is shaped only by nucleation and growth. In particular, the formation of small nuclei consisting of very few molecules results in a number density peak at small droplet volumes, whereas droplet growth is reflected by a shift of the size distribution towards larger sizes and dissociation leads to the sharp number density drop at $d = \sqrt[3]{6v_1/\pi} = 4.9 \times 10^{-10}$ m. As indicated by the red frame in Fig. 4.19(a), all droplets persist in the kinetic regime ($\text{Kn} \gg 1$), justifying *a posteriori* our use of Eq. (4.16) for the thermophoretic velocity. The droplet size distribution is characterized by a small gradient towards the surface that drives a diffusive deposition flux. Yet, out of the entire droplet mass (in terms of flow rate) that leaves the computational flow domain, only 1% deposits on the reactive surface. This weak deposition is partly caused by the near-surface dissociation of smoke and partly due to the strong outward-pointing Stefan flow that renders any thermophoretic attraction ineffective. However, the presence of other aluminum particles, as in a metal dust, or the existence of an oxide cap can enhance the amount of oxide smoke deposited on parti-

cles [60]. While the former aspect has been addressed within the scope of Reference [157], the latter is subject to the investigations of Chapter 5.

In order to elucidate the competition of nucleation and growth in shaping the droplet size distribution, the respective characteristic time scales are compared in Fig. 4.19(b). Very near the particle surface where the temperature profile rapidly increases from the particle temperature to the maximum flame temperature (Fig. 4.18(c)), nucleation is dominant, causing the formation of small oxide droplets. These droplets either diffuse inwards and deposit on the particle or migrate outwards and dissociate upon intense droplet evaporation. Beyond $r/R_p \approx 2$, the droplet size distribution is mainly influenced by nucleation and, to a notably lesser extent, by droplet growth. As the temperature decreases for $r/R_p \gtrsim 4$, both time scales increase rapidly and the droplet formation kinetics slow down substantially. Further outwards, the size distribution changes only slightly due to diffusive and advective mixing (Fig. 4.19(a)). Figure 4.19(b) also contains a radial profile of the mean droplet diameter and standard deviation. On average, the oxide droplets are nanometric, suggesting that any separation from the exhaust gas is very difficult and energy-intensive (if not impossible). However, the investigations in Section 4.7 show evidence that an increasing operating pressure promotes the formation of larger oxide droplets.

4.7 Combustion characteristics at elevated pressures

In this section, the developed steady-state single particle combustion model is instrumented to investigate the changes in the reactive boundary layer and the oxide smoke halo about a burning aluminum particle as the thermodynamic pressure increases. Although most of the target applications, such as the combustion of metals as surrogate fuel in retro-fitted coal power plants, are currently operated at atmospheric conditions, pressure seems to be an intuitive parameter that may be varied in order to control the combustion process and, possibly, the exhaust composition. Most recently, for instance, it was found that an increase in pressure significantly increases the temperature in the vicinity of the fuel particle [66]; a parameter that controls not only the surface reaction rates and, thus, the aluminum evaporation but also our smoke droplet formation kinetics. To this end, we run the simulation of Section 4.6.2 again but with the thermodynamic pressure fixed at $p = 5$ bar and $p = 10$ bar. Although coagulation is excluded in the consol-

idated kinetics of Section 4.6.2, we also show predictions obtained with coagulation here in order to elucidate the sensitivity of the coagulation rate to a varying ambient pressure.

From a numerical point of view, the methods and schemes employed to solve the governing equations reported in Section 4.5 do not change. However, at high pressure, the chemical and droplet formation kinetics typically become faster than at atmospheric conditions. This has a particular influence on the mechanism limiting the time step size. While the time step size at atmospheric pressure is controlled by the transport step due to a limitation of the CFL number at fixed spatial resolution, at higher pressures, by contrast, the kinetics determine the global time step size. Moreover, compared to the combustion at atmospheric pressure, the transient phase of the combustion process is longer and the flame requires approximately twice as long ($t \approx 10$ ms) to stabilize and attain a steady mode inside our computational domain.

The predictions summarized in Figs. 4.20 and 4.21 constitute the counterpart of Fig. 4.15 and correspond to a single steadily burning aluminum particle with a diameter $d_p = 210 \mu\text{m}$ that is initially immersed in a uniform air flow at a temperature of $T = 298$ K and a pressure of $p = 5$ bar or 10 bar, respectively. Figures 4.20 and 4.21 show spatial distributions of the magnitude of the advective droplet velocity $\|\mathbf{u} + \mathbf{u}_t\|$ (a, top), the temperature T (a, bottom), the mass fraction $Y_{\text{Al}_2\text{O}}$ (b, top) and the mole fraction X_{NO} of (b, bottom) obtained with the consolidated kinetics of Section 4.6.2.

Compared to our findings at atmospheric pressure (Section 4.6.2), the maximum flame temperature increases significantly from about 3500 K at atmospheric pressure to approximately 4000 K and 4100 K at $p = 5$ bar and $p = 10$ bar, respectively, which is in good agreement with recent experimental investigations and equilibrium calculations [66, Fig. 11]. This temperature rise is related to the increase with pressure of the aluminum boiling point up to 3196 K and 3413 K⁵, respectively, and is promoted by faster gas phase chemistry and heat release. Since the particle temperatures increase to 2825 K and 2976 K as the thermodynamic pressure is raised to, respectively, $p = 5$ bar and $p = 10$ bar, the surface kinetics are accelerated causing an increasing Al-evaporation rate of $\dot{m}''_{\text{Al},s} = 0.97$ kg/(m²s) and $\dot{m}''_{\text{Al},s} = 1.04$ kg/(m²s), while the Stefan flow velocity, however, decreases due to an almost five and ten times larger gas density (Eq. (2.5)), respectively. Concomitantly, the

⁵The values are calculated using Eq. (2.30) adapted to Al while excluding the Kelvin effect.

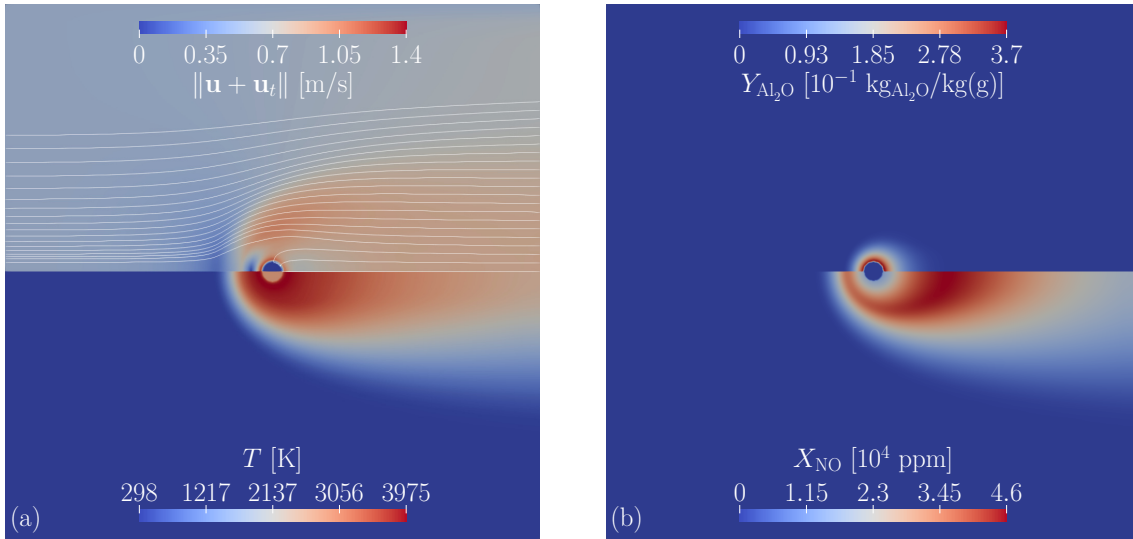


Figure 4.20 Contour plots of the magnitude of the advective droplet velocity $\|\mathbf{u} + \mathbf{u}_t\|$ along with streamlines (a, top), the temperature field T (a, bottom), the Al_2O mass fraction $Y_{\text{Al}_2\text{O}}$ (b, top) and the mole fraction X_{NO} of NO (b, bottom) obtained in the $\text{Al-O}_2/\text{N}_2$ case at $p = 5$ bar.

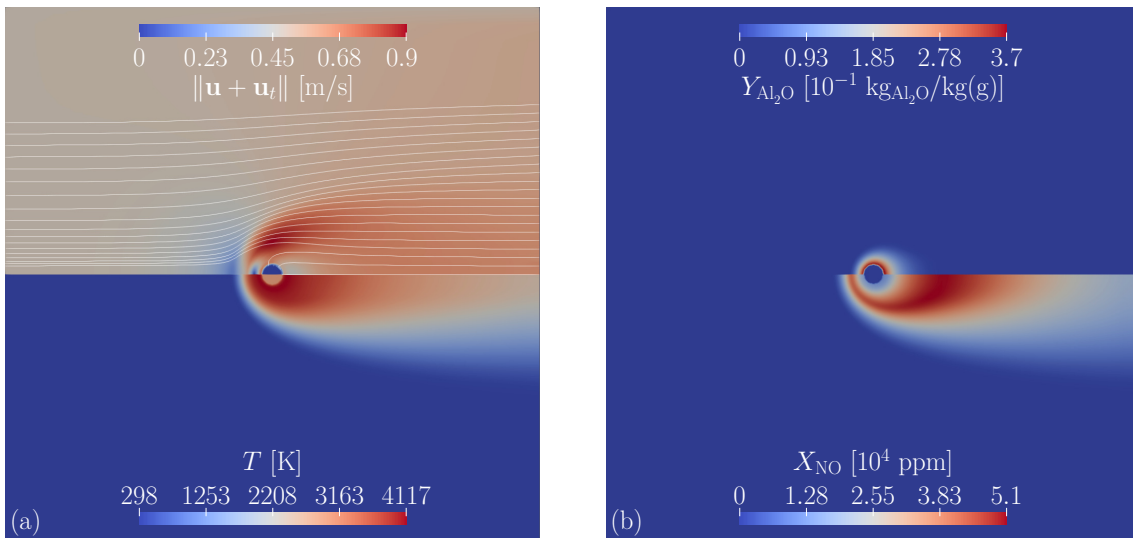


Figure 4.21 Contour plots of the magnitude of the advective droplet velocity $\|\mathbf{u} + \mathbf{u}_t\|$ along with streamlines (a, top), the temperature field T (a, bottom), the Al_2O mass fraction $Y_{\text{Al}_2\text{O}}$ (b, top) and the mole fraction X_{NO} of NO (b, bottom) obtained in the $\text{Al-O}_2/\text{N}_2$ case at $p = 10$ bar.

thermophoretic velocity is significantly reduced as it scales inversely proportional with the density (Eq. (4.16)), thus, eliminating any potential for droplet deposition and causing the fraction of deposited smoke to decrease to virtually 0%. Compared to the predictions shown in Fig. 4.15, close to the particle's surface, the flow field is still dominated by the outward-pointing Stefan flow associated with the bulk transport away from the evaporating surface, but the second velocity front further upstream forms at a smaller

axial distance and is more pronounced; here, the gas expands due to changes in the temperature and density caused by the exothermicity of the gas phase reactions, droplet condensation and heat conduction. While the maximum mass fraction of Al_2O , the most abundant gaseous suboxide, only slightly increases from $0.29 \text{ kg}_{\text{Al}_2\text{O}}/\text{kg}(\text{g})$ for $p = 1 \text{ atm}$ to $0.37 \text{ kg}_{\text{Al}_2\text{O}}/\text{kg}(\text{g})$ at $p = 5 \text{ bar}$ and remains constant for higher p , the predictions suggest that an increase in pressure is accompanied by an intensification of the NO emissions by a factor of approximately 4. In general, it stands out that, with increasing pressure, the envelope flame becomes narrower and much less diffusive, since the species diffusivities ($\sim 1/p$, Eq. (4.9)) as well as the thermal conductivity are reduced, causing the flame to stretch in the horizontal direction.

Complementary to Fig. 4.16(a), Fig. 4.22 shows contour plots of the droplet volume fraction ε_l (top) and the total droplet number density M_0 (bottom) at the two thermodynamic pressure levels (a, b). In line with the observation of a more confined and less diffusive envelope flame, the smoke halo, represented by the droplet volume fraction, for example, is also more compact and substantially more focused compared to the halo at atmospheric pressure conditions. While the droplet volume fraction scales almost proportionally with p , the total number density is reduced by a factor of almost two as the pressure rises from 1 atm to 5 bar and then increases moderately. In terms of ε_l , the smoke halos obtained at elevated thermodynamic pressures and depicted in Fig. 4.22 resemble the predictions obtained in the Al-O₂/Ar case including coagulation (Fig. 4.11), albeit based on a different nucleation rate, in terms of shape and sharpness, suggesting that an increasing thermodynamic pressure affects the smoke droplet's size and, hence, their diffusional mobility in a similar way as coagulation does. In fact, considering the smoke droplet size distributions and the profiles of the mean droplet diameters along the radial coordinate at $x = 0 \text{ m}$ for $p = 5 \text{ bar}$ and $p = 10 \text{ bar}$ depicted in Fig. 4.23 and comparing these with the respective predictions in Fig. 4.19 at $p = 1 \text{ atm}$, this observation is confirmed since the mean droplet size is significantly increased and the associated diffusivity reduced. Moreover, due to the increased gas density, the mean free path of the gas molecules becomes much smaller causing the limit separating transition and kinetic regime ($\text{Kn} \gg 1$, red frames in Fig. 4.23) to be shifted towards smaller droplet sizes. Consequently, the continuum growth rate (Eq. (2.45)) which increases with the droplet diameter contributes more to the harmonic average in Eq. (2.46) promoting the condensational growth of the smoke droplets. Since

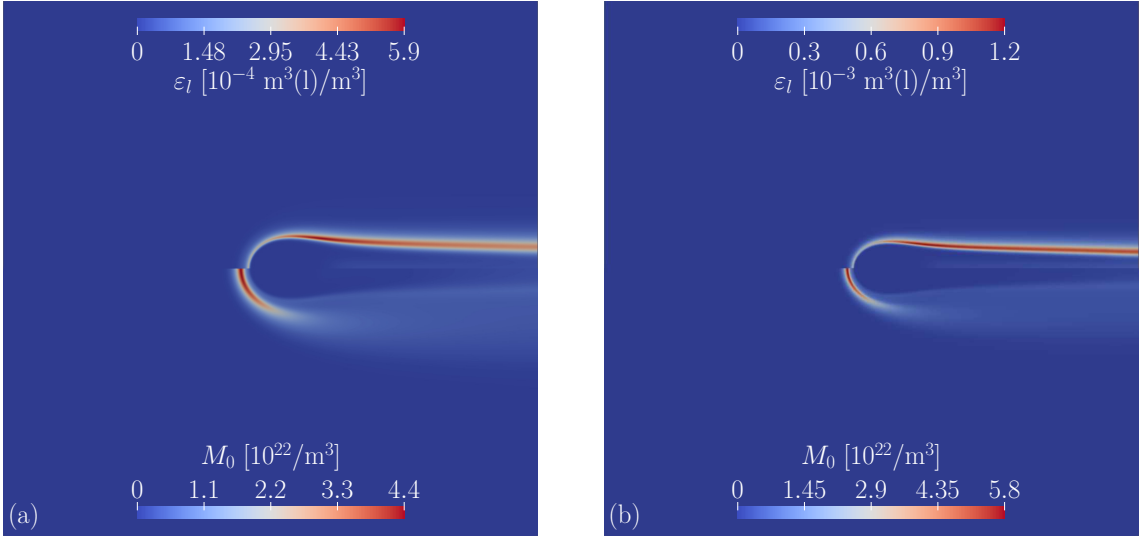


Figure 4.22 Spatial distribution of the droplet volume fraction ε_l (top) and the total droplet number density M_0 (bottom) for aluminum particle combustion in air at $p = 5$ bar (a) and $p = 10$ bar (b).

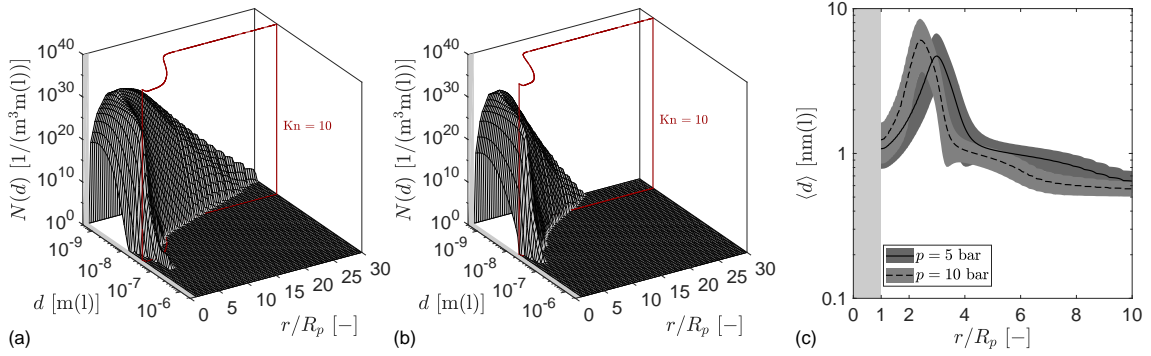


Figure 4.23 Droplet size distribution $N(\cdot)$ for $p = 5$ bar (a) and $p = 10$ bar (b) and mean droplet diameter $\langle d \rangle$ (c) along the radial coordinate for the Al- O_2/N_2 case. For details, we refer to the caption of Fig. 4.19.

nucleation is, concomitantly, slightly impeded by the high pressures, as indicated by the increase in the characteristic time scale in Fig 4.26(a) below compared to Fig. 4.19(b), the gas-liquid phase transition proceeds predominantly through condensational growth leading to the formation of less but larger and continuously growing droplets.

While the consolidated droplet formation kinetics do not include coagulation, it is still interesting to investigate the coagulation rate's sensitivity to pressure changes. As complement of Figs. 4.22 and 4.23, Figs. 4.24 and 4.25 show the predictions of the droplets' volume fraction, total number density, size distribution and mean diameter including coagulation. As expected from the nature of coagulation, the spatial distribution of the droplet volume fraction becomes slightly narrower due to coagulation, since the smoke droplets become

4 A steadily burning aluminum particle

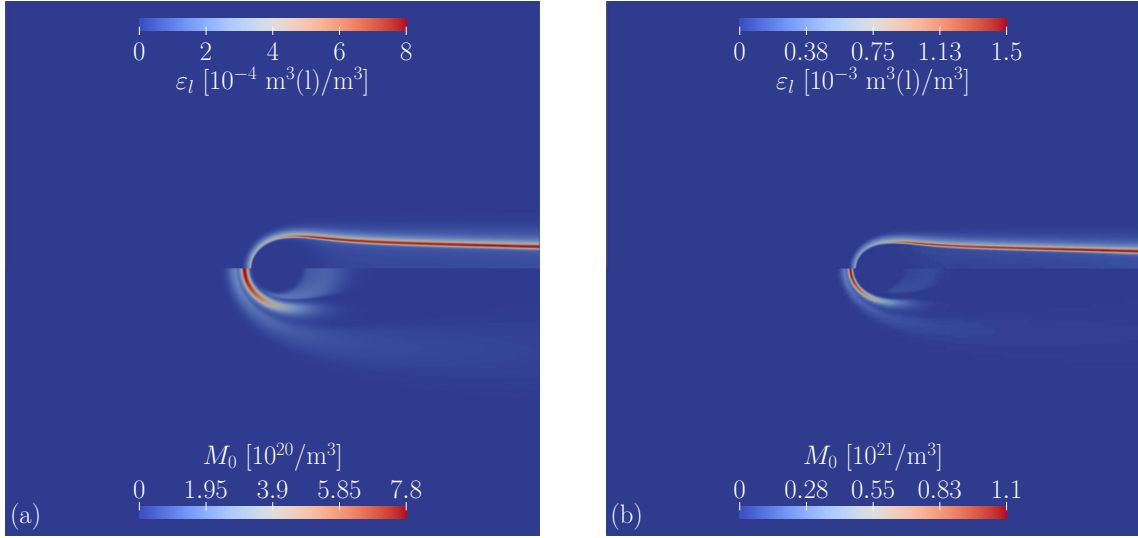


Figure 4.24 Spatial distribution of the droplet volume fraction ε_l (top) and the total droplet number density M_0 (bottom) for aluminum particle combustion in air at $p = 5$ bar (a) and $p = 10$ bar (b) including coagulation.

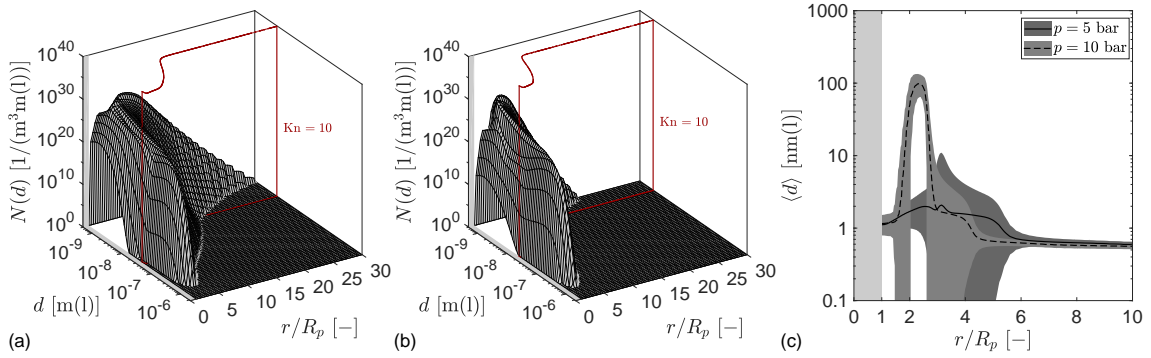


Figure 4.25 Droplet size distribution $N(\cdot)$ for $p = 5$ bar (a) and $p = 10$ bar (b) and mean droplet diameter $\langle d \rangle$ (c) along the radial coordinate for the Al-O₂/N₂ case including coagulation. For details, we refer to the caption of Fig. 4.19.

even larger, but the overall shape remains unchanged, whereas the total droplet number density reduces by a factor of roughly 50. Coagulation augments the size-enlargement of the droplets caused by the higher pressure and contributes to the formation of very large smoke droplets that reach Knudsen numbers of less than unity (continuum regime) and attain average sizes of up to $\langle d \rangle = 100$ nm for $p = 10$ bar. Curiously, however, for $p = 5$ bar, coagulation leads to an average droplet diameter that is substantially smaller than the one predicted excluding coagulation, while the standard deviation increases notably. Taking into account the radial profiles of the droplet formation mechanisms' characteristic time scales (nucleation, growth/dissociation and coagulation) plotted in Fig. 4.26 without (a) and with (b) coagulation, this may be explained by the fact that accounting for coagula-

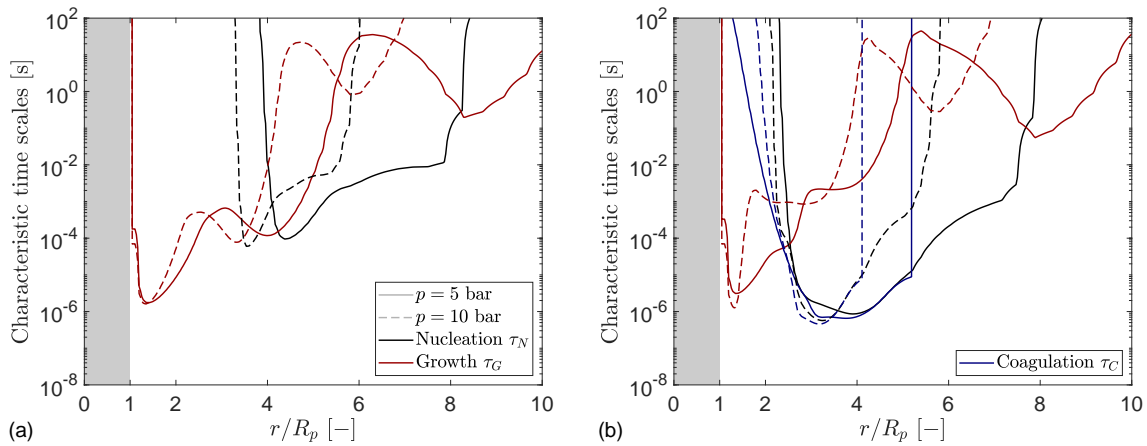


Figure 4.26 Characteristic time scales of the droplet formation mechanisms for simulations excluding (a) and including (b) coagulation along the radial coordinate for the Al-O₂/N₂ case at $p = 5$ bar and $p = 10$ bar.

tion causes the characteristic time scale of nucleation to decrease and become comparable with the time scale of growth, which remains unchanged under the influence of coagulation, suggesting that both mechanisms compete for the consumption of gaseous precursors. Consequently, small droplets precipitate and grow rapidly causing a heavy tail in the size distribution and, thus, explaining the large standard deviation and reduced mean size. The pressure level, apparently, determines whether and at which locations around the fuel particle coagulation is effective. An analysis of the coagulation rate's course across the flame (not shown) reveals that, for $p = 10$ bar, there is a thin region around the particle at $r \approx 2.5R_p$ where the coagulation rate is very high causing the peak in the profile of the mean droplet diameter.

In addition to Fig. 4.25, Fig. 4.27 depicts the smoke size distributions and profiles of the mean droplet diameter along the outflow boundary of our computational domain. Apparently, for $p = 5$ bar, the droplets' sizes increase significantly downstream of the particle due to intense coagulation, while the maximum mean droplet diameter remains almost unchanged for $p = 10$ bar. Moreover, at both pressure levels, the size distributions become much wider and feature a distinct bimodality due to coagulation, causing an increase in the standard deviation associated with the mean size. While the large droplets are formed close to the particle's surface at low radial distance and are flushed away by the inflow due to their low diffusivity, the smaller droplets migrate outwards driven by their high diffusional mobility smoothing the size distribution also in radial direction. In summary, coagulation in combination with high-pressure combustion as mechanism for

4 A steadily burning aluminum particle

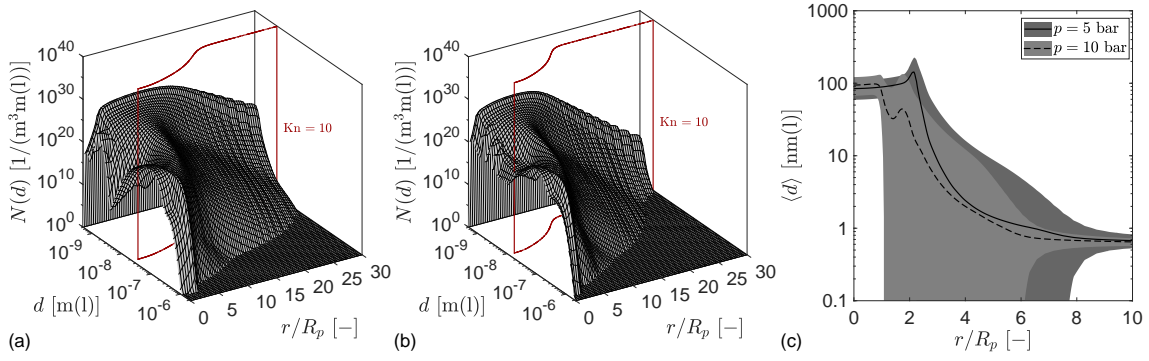


Figure 4.27 Droplet size distribution $N(\cdot)$ for $p = 5$ bar (a) and $p = 10$ bar (b) and mean droplet diameter $\langle d \rangle$ (c) along the outflow boundary at $x = 3.2$ mm for the Al-O₂/N₂ case including coagulation. For details, we refer to the caption of Fig. 4.19.

droplet size-enlargement is effective but may take place in different locations depending on the pressure level.

4.8 Chapter conclusions

In this chapter, we presented a population balance model for predicting the size-resolved formation and migration of oxide smoke droplets condensing in the vicinity of a steadily burning metal particle. The PBE is incorporated into a Eulerian modelling framework encompassing the chemical gas phase composition, the dispersion temperature and the bulk flow field and informed by kinetic rates for droplet nucleation, growth and coagulation as well as diffusion and thermophoresis. A particular feature of the balance equations for the dispersion's mass, momentum and enthalpy is that the instantaneous equilibration of gas and droplets in terms of bulk velocity and temperature is consistently accounted for. Besides accommodating droplet size-dependent phenomena, our approach permits a direct computation of the smoke size distribution at any location and point in time, thus shedding light on the physical mechanisms conducive to smoke deposition, emission and size-enlargement.

The PBE-based model formulation was applied to the combustion of a steadily burning aluminum particle settling in O₂/Ar and O₂/N₂ gas mixtures at atmospheric pressure and predictions of radial AlO, Al₂O₃(l) and temperature profiles were qualitatively compared with measurements by Bucher et al. [24, 25]. For the O₂/Ar case, we manually calibrated the droplet formation and interaction rates based on the available experimental data. The corresponding analyses showed that droplet nucleation and dissociation control the

chemical equilibrium between gaseous aluminum suboxides and condensed phase oxide smoke and that the shape of the smoke halo is strongly tied to the diffusional mobility of the droplets. This last point led to serious doubts on the occurrence of droplet coagulation within the envelope flame. Potentially, thermionic emissions and ionization reactions render the smoke droplets charged and inhibit the coagulation of similarly sized droplets in the flame zone. Our consolidated droplet formation kinetics encompass a nucleation rate from the Classical Nucleation Theory with amendments by Reiss et al. [138, 139] as well as condensational surface growth and dissociation, but exclude coagulation. In an application to an aluminum particle burning in air, the qualitative agreement of the AlO and Al₂O₃(l) profiles with measurements by Bucher et al. [24, 25] was very good, while the temperature was severely mispredicted. This deviation pertains to a very sharp near-surface gradient of the predicted temperature profile which similarly occurred in previous modelling efforts and whose physical validity remains unclear. Omitting post-flame smoke aggregation, we finally concluded that the smoke droplets are nano-sized on average, rendering their direct separation from the carrier gas challenging.

In an attempt to identify operating conditions that promote the formation of larger smoke droplets, we varied the thermodynamic pressure of the oxidizing environment and found that an increase in pressure is accompanied by an increasing flame temperature and particle evaporation rate as both the gas phase and surface kinetics are accelerated. Moreover, excluding coagulation, the mean size of the smoke droplets in the particle's vicinity also increases by a factor of about six when transitioning from atmospheric conditions to $p = 10$ bar, since droplet growth is facilitated and becomes competitive with nucleation in reducing the gas phase's supersaturation. However, this size-enlargement comes at the expense of a four times larger NO concentration intensifying the emission of pollutants from the flame. Regardless of the practicability, we identified the increase in operating pressure of metal-based burners as a key mechanism to promote droplet size-enlargement. On average, the droplets remain nano-sized, however, rendering the oxide smoke separation still challenging and energy-intensive. Although it is not conclusive whether or not coagulation takes place within the flame, an investigation of the coagulation rate's sensitivity to pressure variations revealed that coagulation further enhances the enlarging effect an elevated thermodynamic pressure has on the emitted oxide smoke droplets. In particular, at $p = 10$ bar, we observed average smoke droplet diameters of up to $\langle d \rangle = 100$ nm.

Chapter 5

Unsteady morphological changes of a burning aluminum particle

5.1 Chapter introduction

In the analysis of homogeneous combustors for bulk Al (Chapters 2 and 3), we identified nucleation and coagulation as the main processes shaping the smoke size distribution, but found the smoke droplets to remain nano-sized for residence times that are comparable to the burning times of micron-sized Al-particles. As part of a subsequent calibration of the droplet nucleation and coagulation rates based on experimental observations of the smoke halo around an Al-particle burning in O₂/Ar [24, 26] in Chapter 4, however, we concluded that droplet coagulation may be ineffective, possibly owing to electrostatic droplet repulsion induced by thermionic emissions and ionization reactions [150]. Although the reactor pressure turned out to be a key operating parameter to directly influence the smoke droplet's sizes, in this chapter, we focus on another mechanism to promote the formation of larger oxide compounds. In Al-dust flames, for example, a major part of the smoke formed appears to deposit on the reacting or burnt-out particles, rendering the fraction of oxide emitted as smoke small compared to the residue-bound oxide [157]. Here, the existence of an Al₂O₃-cap is of paramount importance for smoke migration towards the fuel particle as it enables a corridor with vanishing Stefan flow. Generally speaking, the capture of the smoke droplets by the fuel particle constitutes a natural mechanism that promotes the formation of larger oxide particles which can be separated from the exhaust gases more efficiently than the smoke fines. In this chapter, we present an unsteady analysis extending from ignition, subsequent surface oxidation and Al-evaporation to particle

burnout and infer cumulative estimates of the emitted gaseous pollutants, smoke charge and smoke size distribution alongside the size of the remaining particle residue. Focusing on the precise morphology of a biphasic Al/Al₂O₃-particle [7], Gallier et al. [60] recently investigated thermo- and diffusiophoretic deposition of oxide smoke on the particle surface in steady state, highlighting the role of the oxide cap as a smoke collector. In order to permit the analysis of configurational changes in the envelope flame and their ramifications on smoke scavenging and pollutant emissions, our model formulation (Chapter 4) is augmented by a time-varying biphasic particle morphology. While the proposed modelling approach is instrumented here to elucidate both the amount of gaseous pollutants (NO_x) as well as the smoke charge and size distribution emitted from a burning Al-particle in the presence of unsteady changes in the particle morphology and surface composition, it can similarly be used to calibrate mass and heat transfer rates in terms of the conversion degree for point-particle descriptions and assess the assumptions underlying semi-analytical gas-particle boundary layer models.

This chapter is organized as follows: Following a detailed description of the fuel particle's morphology including the quantities governing its shape in Section 5.2, Section 5.3 is devoted to the discussion of extensions and amendments of the previously developed single particle model (Chapter 4) that are required to accommodate a varying particle morphology. Using the numerical tools reported in Section 5.4, we present predictions of particle burning times, residue sizes and the exhaust stream composition as a function of the initial particle diameter alongside a detailed analysis of the combustion process (Section 5.5) before we conclude the chapter in Section 5.6.

5.2 Fuel particle properties and morphology

If an Al-particle is heated above the Al₂O₃ melting temperature $T_{m,\text{Al}_2\text{O}_3} = 2327\text{ K}$, then the oxide skin that passivates the Al-surface at ambient conditions recedes into a protruding cap [11], exposing liquid Al to the ambient gas. Correspondingly, we initialize the burning Al-particle with a cap-body morphology and an oxide fraction that matches a passivating oxide shell thickness of 4 nm [24, 44, 190]. After ignition, the mass of the Al-body decreases due to Al-evaporation and surface oxidation, while the oxide cap absorbs the heterogeneous reaction products and grows upon deposition of oxide smoke formed

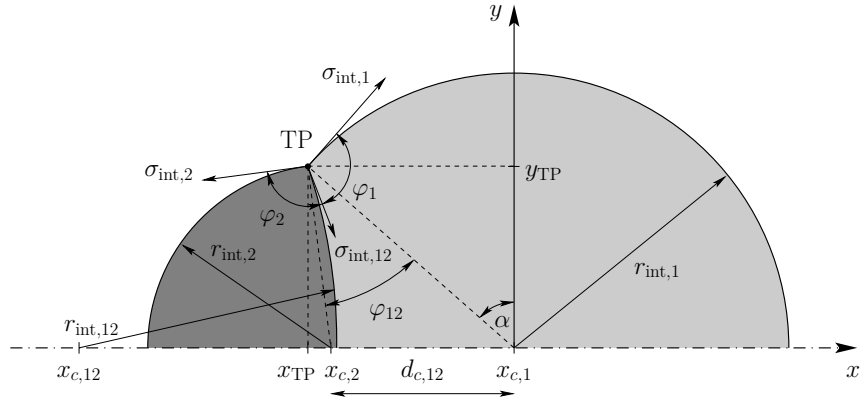


Figure 5.1 Geometrical description of the cap-body morphology adapted from Gallier et al. [60].

in the surrounding envelope flame [60]. Concomitantly, both the smoke deposited on the Al-body and the oxide islands formed heterogeneously are assumed to be instantly transported towards the cap by Hill's vortex and incorporated [60].

In the literature, various models with different levels of detail are frequently used to approximate the cap-body geometry [11, 46, 92, 185]. The precise shape of an Al-particle with an oxide lobe was, however, first determined by Babuk and Vasilyev [7] and later revisited by Gallier et al. [60]. Apart from minor constitutive changes, we employ the morphology as presented in Reference [60], but continuously adjust the particle's shape as the particle mass and conversion degree change in time.

Figure 5.1 depicts a two-dimensional cut through a biphasic axisymmetric fuel particle, including the describing geometrical parameters. The subscripts 1, 2 and 12 refer, respectively, to the free surface of the Al-body, the surface of the Al_2O_3 -cap and the Al- Al_2O_3 interface. Each of these interfaces is a spherical cap with radius $r_{\text{int},i}$ and axial center position $x_{c,i}$, $i \in \{1, 2, 12\}$. At the triple point TP, static force equilibrium holds if the inertia associated with the triple point movement is negligible. Indeed, the simulations of Section 5.5 showed that the morphology changes on time scales which are much smaller than the burning time, corroborating *a posteriori* the assumption of a quasi-static force equilibrium. The axial and radial force balances at TP yield the expressions

$$\begin{aligned} \varphi_1 &= \arccos \left(\frac{\sigma_{\text{int},2}^2 - \sigma_{\text{int},12}^2 - \sigma_{\text{int},1}^2}{2\sigma_{\text{int},12}\sigma_{\text{int},1}} \right), \\ \varphi_2 &= \arccos \left(\frac{\sigma_{\text{int},1}^2 - \sigma_{\text{int},12}^2 - \sigma_{\text{int},2}^2}{2\sigma_{\text{int},12}\sigma_{\text{int},2}} \right) \end{aligned} \quad (5.1)$$

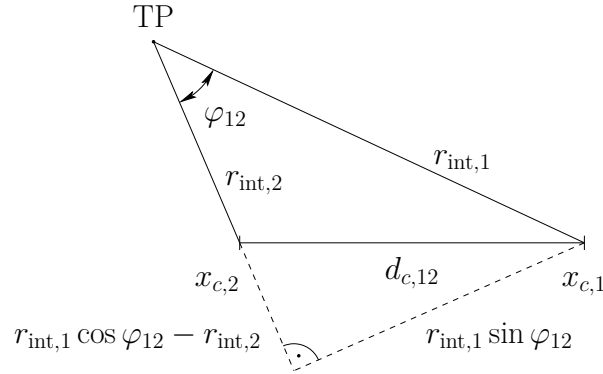


Figure 5.2 Schematic of the law of cosines applied to the cap-body morphology.

for the wetting angles φ_1 and φ_2 [60, Eqs. (9) and (10)] in terms of the surface tensions $\sigma_{\text{int},1}$, $\sigma_{\text{int},2}$ and $\sigma_{\text{int},12}$ associated with an Al-gas, an Al_2O_3 -gas and an Al- Al_2O_3 interface, respectively, which we take from Refs. [7, 71, 146]. In particular, the wetting angles turn out to be independent of the cap/body volume ratio and only depend on the temperature through the surface tensions. By geometry and the definition of an auxiliary angle $\varphi_{12} = \varphi_1 + \varphi_2 - \pi$, the three radii $r_{\text{int},1}$, $r_{\text{int},2}$ and $r_{\text{int},12}$ can be related to the wetting angles φ_1 , φ_2 and the triple point angle α ,

$$r_{\text{int},1} \cos \alpha = r_{\text{int},2} \cos(\alpha - \varphi_{12}) = r_{\text{int},12} \cos(\varphi_1 - \alpha). \quad (5.2)$$

Following the law of cosines (Fig. 5.2), the distance between the centers of body and cap reads

$$d_{c,12} = |x_{c,1} - x_{c,2}| = \sqrt{r_{\text{int},1}^2 + r_{\text{int},2}^2 - 2r_{\text{int},1}r_{\text{int},2} \cos \varphi_{12}}, \quad (5.3)$$

while the center point associated with the contact radius is determined by

$$x_{c,12} = x_{\text{TP}} - r_{\text{int},12} \sin(\varphi_1 - \alpha) \quad (5.4)$$

with

$$\begin{aligned} x_{\text{TP}} &= x_{c,1} - r_{\text{int},1} \sin \alpha, \\ y_{\text{TP}} &= r_{\text{int},1} \cos \alpha \end{aligned} \quad (5.5)$$

being the triple point coordinates.

The triple point angle completes the geometry and is determined by the current volume

ratio of the oxide cap and the Al-body. Geometrically, the body's volume is obtained by subtracting the volumes of the planar spherical cap's associated with $r_{\text{int},1}$ and $r_{\text{int},12}$ from the complete sphere with radius $r_{\text{int},1}$,

$$V_1 = \frac{\pi}{3} r_{\text{int},1}^3 \left((1 + \sin \alpha)^2 (2 - \sin \alpha) - \frac{\cos^3 \alpha}{\cos^3(\varphi_1 - \alpha)} (2 + \sin(\varphi_1 - \alpha))(1 - \sin(\varphi_1 - \alpha))^2 \right), \quad (5.6)$$

whereas the Al_2O_3 -cap's volume is obtained by adding the planar spherical cap volumes associated with $r_{\text{int},2}$ and $r_{\text{int},12}$,

$$V_2 = \frac{\pi}{3} r_{\text{int},1}^3 \left(\frac{\cos^3 \alpha}{\cos^3(\alpha - \varphi_{12})} (1 - \sin(\alpha - \varphi_{12}))^2 (2 + \sin(\alpha - \varphi_{12})) + \frac{\cos^3 \alpha}{\cos^3(\varphi_1 - \alpha)} (2 + \sin(\varphi_1 - \alpha))(1 - \sin(\varphi_1 - \alpha))^2 \right). \quad (5.7)$$

Comparing the geometrical representation of the volume ratio V_2/V_1 (Eqs. (5.6) and (5.7)) with the one obtained from balancing the cap's and body's masses, $V_{p,\text{Al}_2\text{O}_3}(t)/V_{p,\text{Al}}(t)$, yields a non-linear equation governing the triple point angle α ,

$$\begin{aligned} \mathcal{R}(\alpha) = & \left(\frac{\cos^3 \alpha}{\cos^3(\alpha - \varphi_{12})} (1 - \sin(\alpha - \varphi_{12}))^2 (2 + \sin(\alpha - \varphi_{12})) \right. \\ & \left. + \frac{\cos^3 \alpha}{\cos^3(\varphi_1 - \alpha)} (2 + \sin(\varphi_1 - \alpha))(1 - \sin(\varphi_1 - \alpha))^2 \right) \\ & \times \left((1 + \sin \alpha)^2 (2 - \sin \alpha) \right. \\ & \left. - \frac{\cos^3 \alpha}{\cos^3(\varphi_1 - \alpha)} (2 + \sin(\varphi_1 - \alpha))(1 - \sin(\varphi_1 - \alpha))^2 \right)^{-1} \\ & - \frac{V_{p,\text{Al}_2\text{O}_3}(t)}{V_{p,\text{Al}}(t)} = 0. \end{aligned} \quad (5.8)$$

Equation (5.8) is solved using a Newton method with the Jacobian given in Eq. (D.2) in Appendix D which also provides some details about the implementation.

Since the Biot number is very small, the volumes of the Al-body and Al_2O_3 -cap are evaluated in terms of the corresponding masses $m_{p,\text{Al}}(t)$ and $m_{p,\text{Al}_2\text{O}_3}(t)$ using the Al and Al_2O_3 densities at the mean temperatures $T_{p,\text{Al}}(t)$ and $T_{p,\text{Al}_2\text{O}_3}(t)$, respectively. The temperature-dependent densities of Al and Al_2O_3 are, in turn, obtained by a smooth blending (Section 4.3.4) of the solid and liquid state properties listed in Ref. [157, Table 2].

5 Unsteady morphological changes of a burning aluminum particle

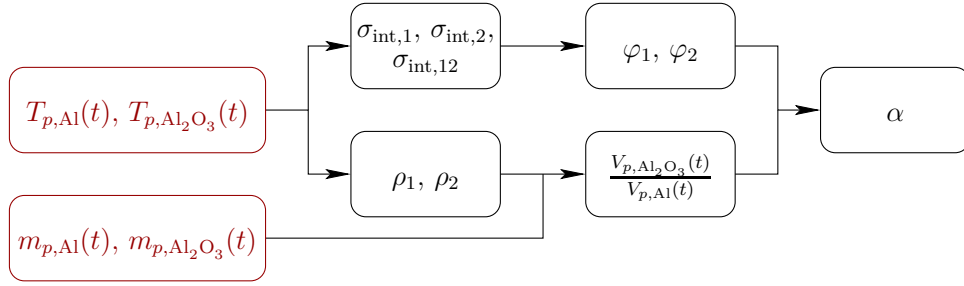


Figure 5.3 Schematic of the physical pathway to the particle geometry.

Figure 5.3 shows a schematic that summarizes the physical path from the masses and average temperatures of body and cap, serving as input variables, through a constitutive layer, including the material properties of the bulk phases as well as the interface in-between, to the geometrical quantities governing the particle's shape.

5.3 Modifications and extensions of the single particle combustion model

Physically, the combustion of an Al-particle involves the mutual interaction of three phases as detailed in Chapter 4; the biphasic Al/Al₂O₃ fuel particle (Fig. 5.1), a multicomponent carrier gas and polysized oxide smoke droplets that are dispersed throughout the gas. In this section, we allude to the modifications and extensions of our physical model that are necessary to accommodate a biphasic fuel particle including a temporally varying morphology.

5.3.1 Biphasic fuel particle

The fuel particle is idealized as a rigid body whose internal temperature field $T(\mathbf{x}, t)$ obeys the unsteady heat conduction equation in Eq. (4.35). While the heat capacity and thermal conductivity of Al are chosen as in Section 4.3.4, the existence of an oxide cap now requires the thermal properties of Al₂O₃ which are taken from Refs. [15, 27]. In order to account for a potential solidification during cooling of the burnt-out particle, the solid and liquid phase properties are smoothly blended (Section 4.3.4). Lastly, the masses $m_{p,Al}(t)$ and $m_{p,Al_2O_3}(t)$ of the Al-body and the Al₂O₃-cap, respectively, are computed from phase-specific mass balances that include the surface reaction fluxes $\dot{s}_{Al(B)}$ and $\dot{s}_{Al_2O_3(B)}$ [69] and the droplet deposition flux \dot{s}_l of Eq. (4.44).

5.3.2 Flux-matching interface conditions

The existence of the oxide cap causes a disruption in the otherwise almost uniformly distributed chemical composition at the reactive surface both in terms of the gas phase and surface scalars (Chapter 4). On both the Al-body and the Al_2O_3 -cap, the surface reaction rates \dot{s} are determined from the surface reaction mechanism of Glorian et al. [69]. In particular, due to the occupation of the surface sites by the artificial species $\text{Al}_2\text{O}_3(\text{S})$ on the part of the surface associated with the oxide cap, the cap's reactivity is limited to the direct heterogeneous adsorption of gaseous $\text{Al}_2\text{O}_3/\text{c}$ and the deposition of smoke droplets resulting in a small but inward-pointing Stefan flow above the cap. As confirmed by the discussion in Section 5.5, it is this very physical mechanism that mitigates the barrier for droplet migration towards the particle surface and is, thus, responsible for the enhanced thermophoretic droplet deposition fluxes on the cap's surface [60]. In order to account for thermal radiation of the oxide lobe in the enthalpy balance of Eq. (4.46), we take its thermal emissivity equal to that of the Al-body, *i.e.*, $\epsilon = 0.1$.

5.4 Numerical methods

As for the steadily burning aluminum particle (Chapter 4), the numerical simulations are performed using our finite volume based in-house research software BOFFIN [83]. If not stated otherwise, the same numerical schemes and parameters are employed as in Section 4.5. A single fuel particle with initial diameter $D_{p,0}$ is placed into the center of a two-dimensional computational domain that extends by $30D_{p,0}$ and $15D_{p,0}$ in the axial and radial directions, respectively. The domain is discretized using 144×72 spatial cells that contract towards the particle, resulting in a particle resolution of 22 cells per diameter. While this grid is slightly coarser than the nominal grid of Section 4.6.1, the larger grid stretching results in a similar resolution of the gas-particle boundary layer. The PBE is discretized along the v -coordinate using a high-resolution finite volume scheme [132] with 40 cells.

In line with the treatment of the Al-body in Section 4.5, the cells occupied by the oxide lobe are also blocked-off [123, Section 7.3-2] by applying the Dirichlet boundary conditions of Section 4.4 evaluated on the part of the reactive surface that is assigned to the Al_2O_3 -cap. After every tenth time step ($\text{CFL} \leq 0.45$), the shape of the interface

separating the particle from the surrounding gas-droplet dispersion is recomputed and the blocking pattern as well as the surface density is updated accordingly. As cells are blocked or unblocked, the boundary conditions on the dispersion's state variables change discontinuously, eliciting a disruption of the boundary layer flow. In practice, however, we observed these disruptions to rapidly yield to a quasi-steady state on time scales negligible compared to the particle's burning time.

At the interface separating bulk Al_2O_3 and bulk Al, moreover, the thermal conductivity of the fuel particle changes discontinuously due to an abrupt change of the material, which is why a harmonic interpolation [123, Section 4.2-3] is used to obtain the cell face conductivity required during the discretization of Eq. (4.35).

5.5 Aluminum particle combustion including a varying particle morphology

The predictions we present in this section serve two main objectives. First, the products resulting from the combustion of a single Al-particle, including nitrogen oxides and the size-resolved smoke charge, are analyzed (Sections 5.5.1 and 5.5.2). Second, the modelling approach is validated by comparing predicted burning times and residue sizes with available experimental data and empirical correlations (Section 5.5.3). The time course of particle combustion is simulated for initial particle diameters $D_{p,0}$ ranging from $20\ \mu\text{m}$ to $250\ \mu\text{m}$. Even for the smallest particle and residue sizes, the continuum hypothesis remains valid [157, Fig. 3(a)]. Since our previous calibration in Section 4.6 cast doubt on the occurrence of droplet coagulation but confirmation is pending, the predictions are presented both with and without coagulation. At the beginning of a simulation, the particle is immersed in a cold uniform air stream ($[\text{O}_2]/[\text{N}_2] = 21/79$, $T_{\text{in}} = 298\ \text{K}$) with an inflow velocity of $u_{\text{in}} = 0.5\ \text{m/s}$ at a constant thermodynamic pressure of $p = 1\ \text{atm}$. Starting from a uniform particle temperature of $T_{m,\text{Al}_2\text{O}_3}$, the particle is ignited by rapid heating up to $2550\ \text{K}$.

5.5.1 Combustion process

Figure 5.4 depicts the boundary layer flow around a single burning particle and shows spatial distributions of the advective part of the particle velocity, the dispersion temperature,

5.5 Aluminum particle combustion including a varying particle morphology

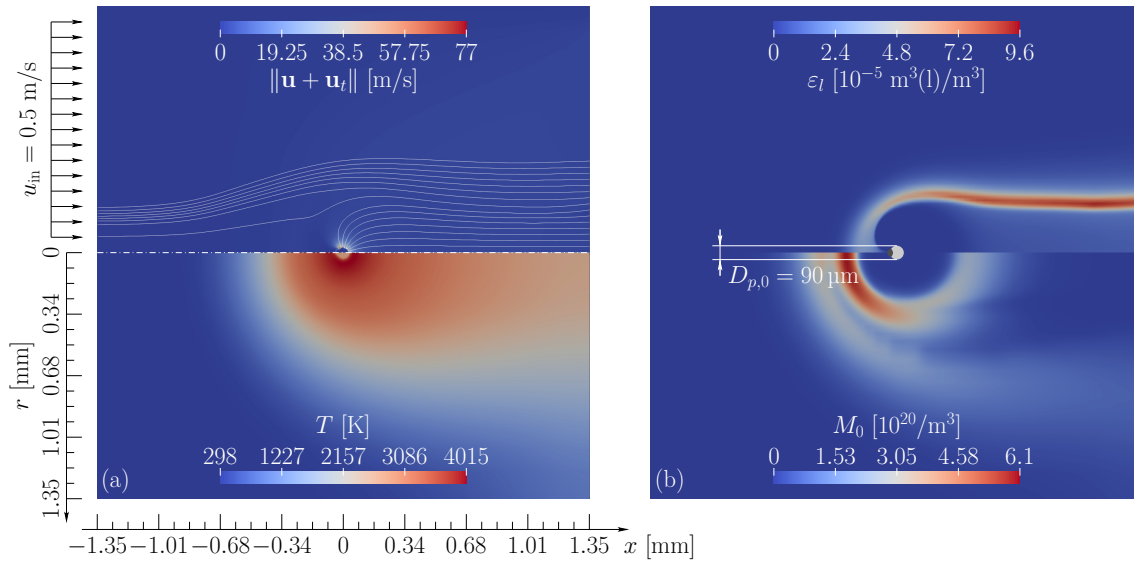


Figure 5.4 Spatial distributions of the temperature T and advective droplet velocity $\|\mathbf{u} + \mathbf{u}_t\|$ (a) as well as the droplets' volume fraction ε_l and total number density M_0 (b) approximately $t = 11$ ms after ignition for a particle with an initial diameter of $D_{p,0} = 90 \mu\text{m}$. Here, the coagulation of droplets in the envelope flame is included.

the droplet volume fraction and the total droplet number density approximately 11 ms after ignition of a fuel particle with an initial diameter of $90 \mu\text{m}$. Above the particle's Al-body, an outward-pointing Stefan flow is induced by Al-evaporation. This flow also advects the condensing and coagulating smoke droplets, but is counteracted by thermophoresis close to the surface as mediated by a sharp temperature gradient that originates from the interplay of the endothermic Al-evaporation and the exothermic formation of suboxides, particularly Al_2O . The maximum flame temperature attained over the course of the combustion amounts to 4000 K. Since the cap's reactivity is limited to $\text{Al}_2\text{O}_3/c$ -adsorption and smoke deposition, the surface velocity, albeit small, points inward here, providing a corridor for smoke deposition by thermophoresis and diffusion (Fig. 5.4(b)). Indeed, ε_l increases close to the cap's surface and circles away from the fuel particle into a concentrated trail that is advected downstream. By contrast, most of the smoke fines accumulate in front of the particle, while some of the smallest droplets also prevail in the particle's wake where the envelope flame rests unimpaired by the passive cap. Further downstream, however, M_0 reduces significantly by coagulation. The weak shield-like ridge of M_0 ahead of the particle is an artifact of restricting droplet coagulation to $T \geq T_{m,\text{Al}_2\text{O}_3}$ (Section 4.2.2).

Complementary to Fig. 5.4, Fig. 5.5 shows the time evolution of the particle-bound Al- and Al_2O_3 -masses, the mean cap and body temperatures as well as the mass flow rates

5 Unsteady morphological changes of a burning aluminum particle

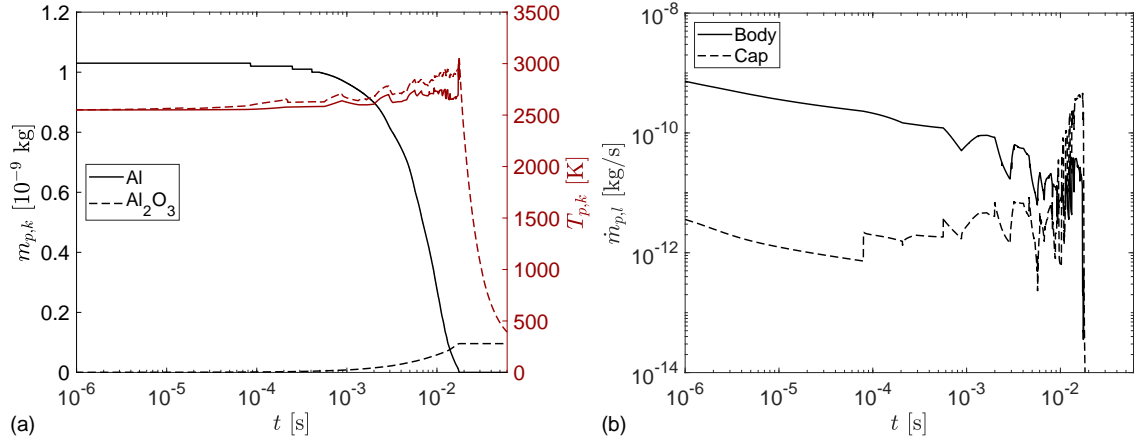


Figure 5.5 Change in time of the particle's Al- and Al_2O_3 -masses $m_{p,\text{Al}}$ and $m_{p,\text{Al}_2\text{O}_3}$ and the mean body and cap temperatures $T_{p,\text{Al}}$ and $T_{p,\text{Al}_2\text{O}_3}$ (a) as well as the smoke deposition rates $\dot{m}_{p,l}$ (b) for an initial particle size of $D_{p,0} = 90 \mu\text{m}$. As in Fig. 5.4, droplet coagulation is included here.

of oxide smoke depositing on the Al-body and the oxide cap. After particle ignition, the envelope flame develops over a brief time horizon of a few microseconds with constant particle temperature. During the first combustion stage, bulk Al is consumed and most of the droplet mass deposits on the fuel particle's body. As the surface area of the Al-body decreases, the heat sink associated with evaporation gives way to conductive heating of the cap by the flame, causing mainly $T_{p,\text{Al}_2\text{O}_3}$ but also $T_{p,\text{Al}}$ to increase and accelerating both the consumption of Al and the cap growth. Concomitantly, the widening low-velocity corridor above the cap turns into the main route for smoke deposition (Fig. 5.5(b)). While the Al-body's temperature increases moderately, the cap's temperature exceeds 3000 K just before the envelope flame extinguishes. On burnout at $t_b \approx 18$ ms, the supply of vaporized Al to the envelope flame ceases and the particle temperature peaks before it begins to decrease on account of conductive and radiative losses to the cool ambience. The remaining residue has a diameter of about $36 \mu\text{m}$ and consists mainly of heterogeneously oxidized Al.

Since droplet charging and consequent electrostatic repulsion may impede droplet collisions [150] (Section 4.6.1), we provide the counterpart of Fig. 5.4(b) for a vanishing coagulation rate ($\beta = 0$ in Eq. (4.15)) in Fig. 5.6. Compared to Fig. 5.4(b), the smoke halo is much thicker here and the total droplet number density is larger by two orders of magnitude, while the corridor through which smoke is attracted to the oxide cap remains. The similarity of the spatial ε_l and M_0 distributions, moreover, suggests that the droplet size distribution is narrower than in the case with coagulation. For completeness, Fig. 5.7

5.5 Aluminum particle combustion including a varying particle morphology

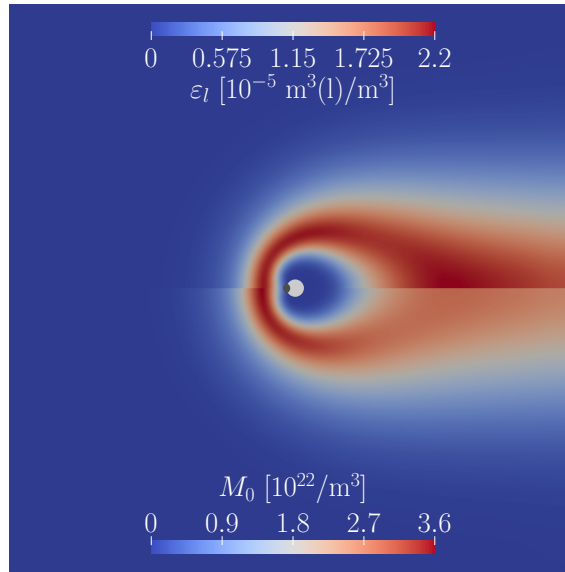


Figure 5.6 Spatial smoke distribution about $t = 11$ ms after ignition of a particle with $D_{p,0} = 90 \mu\text{m}$ for the case without droplet coagulation.

depicts the total droplet number density M_0 and the droplet volume fraction ε_l over the radial distance from the fuel particle's center at the axial location $x = 0$ (see Fig. 5.4(a)) for two time points and, thus, different oxidation degrees. The initial diameter $D_{p,0}$ of the aluminum fuel particle amounts to $90 \mu\text{m}$. In Fig. 5.7, the abscissa is normalized by the initial particle radius $R_{p,0} = D_{p,0}/2$ and the predictions are shown both in the presence and absence of droplet coagulation. If coagulation is active, then the volume fraction profile turns very narrow as the coagulating droplets are diffusively immobilized, while the total number density decreases by up to two orders of magnitude.

While the cap/body masses and mean temperatures in Fig. 5.5(a) are not influenced by droplet coagulation, the larger total number density and enhanced droplet mobility that occur in the absence of coagulation cause the deposition flow rates in Fig. 5.5(b) to increase by about 20 %.

As dynamic counterpart of Fig. 5.4 both with and without coagulation, accompanying videos can be found in the Supplementary material of Reference [54] that show how the structures of the envelope flame and smoke halo surrounding a reactive fuel particle with an initial diameter of $90 \mu\text{m}$ change as the particle ignites, burns and extinguishes.

5 Unsteady morphological changes of a burning aluminum particle

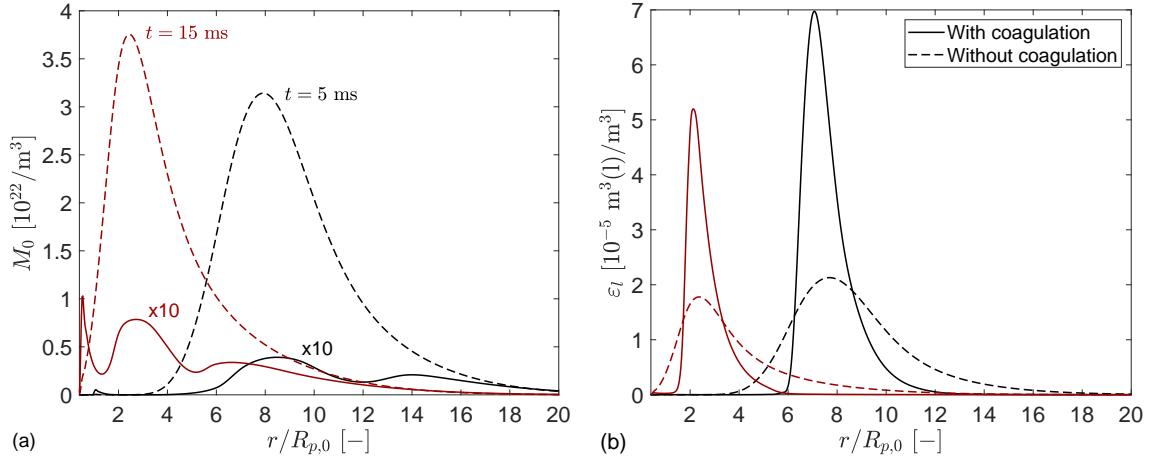


Figure 5.7 Radial profiles of the total droplet number density M_0 (a) and the droplet volume fraction ε_l (b) at $x = 0$ (Fig. 5.4(a)) both with and without droplet coagulation. The black lines correspond to the time point $t = 5$ ms and the conversion degree $1 - m_{p,Al}(t)/m_{p,Al}(0) = 35\%$, while the red lines are obtained at $t = 15$ ms with $1 - m_{p,Al}(t)/m_{p,Al}(0) = 95\%$. Note that the profiles of M_0 obtained with coagulation in figure (a) are scaled by a factor of 10.

5.5.2 Composition of emitted exhaust fumes

At the large flame temperatures we observed in the previous section, both Al-evaporation, leading to gas phase combustion and smoke formation, and nitrogen oxidation are major chemical conversion routes. Nitrogen oxides are toxic precursors of acid rain (NO , NO_2) or greenhouse gases (N_2O) [64], while the aerosolized smoke poses a major challenge to an energetically efficient oxide recovery. Figure 5.8 depicts the cumulative size distribution of all oxide smoke droplets collected beyond the outflow boundary of our computational domain for a fuel particle with $D_{p,0} = 90 \mu\text{m}$. If coagulation is active, then the terminal size distribution is shaped by intense coagulation and features a mean diameter of 0.8 nm and a standard deviation of 1.6 nm. In the absence of coagulation, the final size distribution of the emitted droplets becomes much narrower but, curiously, features a mean diameter of 1 nm that is slightly larger than in the case with coagulation. Possibly, this is caused by the intensification of condensational growth due to the larger droplet surface density and the enhanced migration of droplets into supersaturated gas regions.

Further to the size-characterization of the emitted oxide smoke, the bar plot in Fig. 5.9(a) illustrates the relative mass shares of the main Al-containing products resulting from the combustion of particles with $D_{p,0} = 20 \mu\text{m}$, $90 \mu\text{m}$ and $250 \mu\text{m}$. Here, smaller particles yield a smaller oxide smoke fraction and a larger share of remaining residue, while the volatile Al-containing species are negligible. Similarly, the emissions of NO and NO_2 per

5.5 Aluminum particle combustion including a varying particle morphology

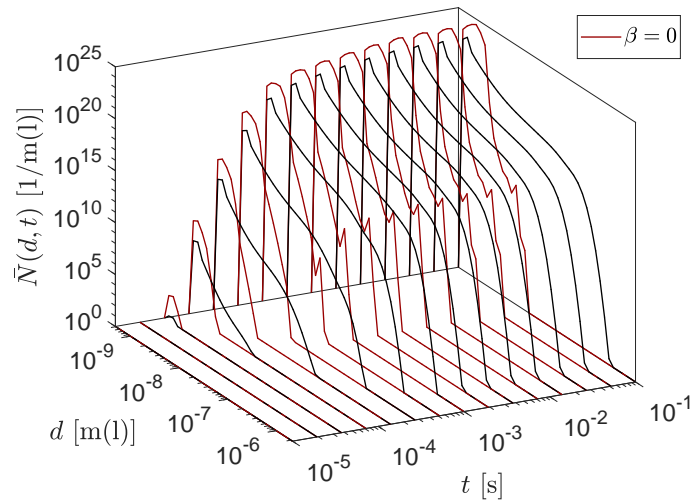


Figure 5.8 Temporal change in the cumulative smoke size distribution $\bar{N}(\cdot)$ integrated across the outflow boundary for $D_{p,0} = 90 \mu\text{m}$. The red lines represent the distributions obtained without coagulation.

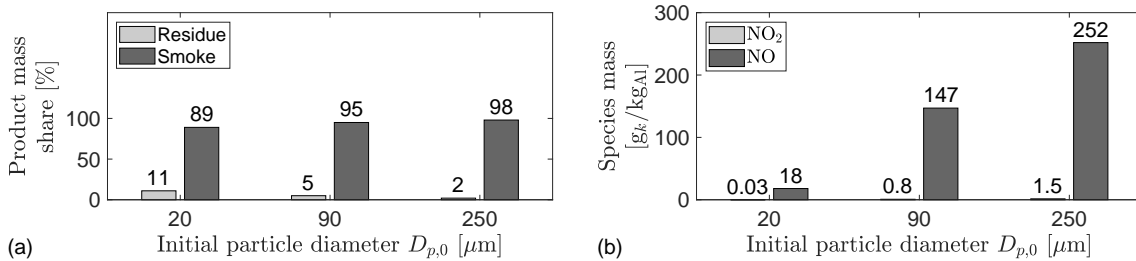


Figure 5.9 Bar plots of the combustion product mass shares of oxide smoke and the residue particle (a) and the amounts of NO and NO₂ formed per kilogram of burnt Al (b) for $D_{p,0} = 20 \mu\text{m}$ (a), $90 \mu\text{m}$ (b) and $250 \mu\text{m}$ (c). Here, coagulation is included.

kilogram of Al burnt (Fig. 5.9(b)) increase from 18 g and 0.03 g, respectively, to 147 g and 0.8 g as well as 252 g and 1.5 g as $D_{p,0}$ changes from $20 \mu\text{m}$ to $90 \mu\text{m}$ and $250 \mu\text{m}$. By contrast, the formation of N₂O and NO₃ is nearly negligible. Apart from the droplet sizes and number, the influence of droplet coagulation on the exhaust composition is very minor. Although the nano-sized smoke encompasses most of the oxide mass, we surmise that the presence of other fuel particles in a dust cloud promotes the scavenging of oxide smoke, leading to larger residues and a smaller smoke fraction [145, 157].

5.5.3 Burning times and residue sizes

Figure 5.10(a) shows our predictions of the particle burning times t_b over the initial diameter $D_{p,0}$ alongside measurements acquired for laser-ignited Al-particles in air at atmo-

5 Unsteady morphological changes of a burning aluminum particle

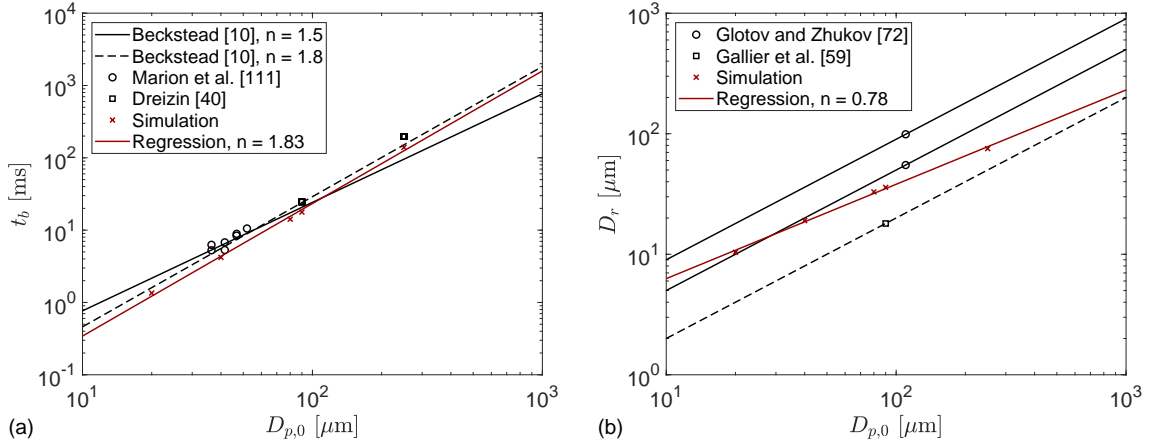


Figure 5.10 Comparison of the predicted particle burning time t_b (a) and residue diameter D_r (b) with experimental measurements and correlations for different initial particle diameters $D_{p,0}$. The black lines in figure (b) represent a constant ratio $D_r/D_{p,0}$.

spheric pressure [40, 111] and the burning time correlations of Beckstead [10],

$$t_b = \frac{a_{\text{cor}} D_{p,0}^{n_{\text{cor}}}}{X_{\text{eff}}^{0.1} T_{p,0}^{0.2}} \quad (5.9)$$

with $n_{\text{cor}} = 1.5$ ($a_{\text{cor}} = 0.0244$) or $n_{\text{cor}} = 1.8$ ($a_{\text{cor}} = 0.00735$), $T_{p,0} = 2550$ K and $X_{\text{eff}} = 0.21$. The agreement of the predictions with the experimental data is very positive. As indicated by the red line in Fig. 5.10(a), our burning time predictions obey a correlation with exponent $n_{\text{cor}} = 1.83$ ($a_{\text{cor}} = 0.0051$) and approximately match the experimental correlation with $n_{\text{cor}} = 1.8$.

In Fig. 5.10(b), predictions of the oxide residue diameter D_r are compared with the data of Refs. [59, 72] for different initial diameters $D_{p,0}$. Contrary to the common hypothesis that the ratio $D_r/D_{p,0}$ remains approximately constant [145], we find the ratio to slightly decrease with $D_{p,0}$, $D_r = 1.04 \times D_{p,0}^{0.78}$. Neither t_b nor D_r are affected by smoke coagulation in the envelope flame.

5.6 Chapter conclusions

In order to support the idea of harnessing metal particles as recyclable and tradable energy carriers and to quantitatively guide the development of dust combustors, we reported on a comprehensive modelling framework for predicting the composition and smoke charge of the envelope flame surrounding a burning Al-particle in a temporally and spatially resolved way. A particular novelty is the incorporation of changes in the particle morphology due

to evaporation, surface oxidation and smoke scavenging. Based on a detailed analysis of the exhaust fumes, including the amounts of nitrogen oxides and the size distribution of dispersed smoke droplets, we found that both the fraction of oxide emitted as smoke and the NO and NO₂ emissions increase with the initial particle size $D_{p,0}$, suggesting the use of finer aluminum powders for the combustion process in order to minimize potential alumina leakage and pollutant emissions. The agreement of our burning time ($t_b \sim D_{p,0}^{1.83}$) and residue size ($D_r \sim D_{p,0}^{0.78}$) predictions with available experimental measurements for a range of initial particle diameters $D_{p,0}$ is very good. Apart from an analysis of the gaseous and condensed phase combustion products, our modelling tool can also be instrumented to inform point-particle descriptions by providing net mass and heat transfer rates in terms of the free-stream conditions u_{in} , \mathbf{Y}_{in} , T_{in} and $N_{in}(\cdot)$ and the particle's degrees of freedom, for example, $m_{p,Al}$, m_{p,Al_2O_3} and the mean particle temperature T_p [157].

Chapter 6

Developments towards a turbulent metal dust flame

6.1 Chapter introduction

In the preceding chapters, we developed a comprehensive PBE-based model formulation for analyzing the combustion characteristics of single aluminum particles with a particular focus on the resolution and prediction of the oxide smoke size distribution. The detailed kinetic framework constitutes the main cornerstone of our model formulation which not only encompasses the rates at which the smoke droplets nucleate, grow or dissociate, coagulate and emit thermal radiation but also includes mass and enthalpy conserving formulations for gas-droplet, gas-surface and droplet-surface interactions. Starting from spatially homogeneous configurations, *i.e.*, the perfectly and partially stirred reactor, which served as test beds for our kinetic framework and represent the dynamics very close to the fuel particle's surface in a laminar and turbulent reactive flow, respectively, we successively increased the model's complexity by including spatial transport phenomena, such as droplet differential diffusion and thermophoresis, and accounting for a temporally varying biphasic fuel particle morphology. The model was then instrumented to conduct an in-depth analysis of the combustion process of single aluminum particles featuring the prediction of oxide size distributions, heat release rates, burning times as well as smoke and pollutant emissions. In particular, the model enabled us to investigate the chemical conversion routes, the pollutant formation processes and the oxide droplet dynamics including the inception, growth and migration of smoke fines inside the micro-diffusion flame embracing individual fuel particles. This small-scale information is not only valuable to understand

the basics of the metal combustion process, but may also be used to inform and calibrate simplified combustion models that are frequently used in large-scale simulations of metal burners, *e.g.*, point-particle descriptions.

Building on the information gleaned from the fundamental investigations on the single particle level, constituting the main part of this thesis, here, we want to build a bridge towards the analysis of turbulent metal dust flames which are frequently encountered in practically relevant large-scale metal burners. While the chemical conversion as well as the smoke inception take place on the smaller scales, it is the interaction of many fuel particles in a dust flame that ultimately determines the overall power density, fuel conversion ratio and emissions of a metal-based burner (Fig. 1.3). In this regard, the developments reported in this chapter may be thought of as an extended outlook which provides the main ideas and concepts of a two-level statistical framework for modelling turbulent metal dust flames. The model formulation is specifically designed to allow for elucidating the interplay of turbulence and polydispersity on part of the metal dust particles and assessing these two physically distinct sources of variability influencing a particle-laden reactive flow individually. Using a recently developed Eulerian Monte Carlo (EMC) solver [154] we target the estimation of particle property statistics rather than resolving the entire property distribution. The key novel feature of the PBE-PDF approach compared to existing Lagrangian stochastic methods [117] lies with the capacity to account for polydispersity and turbulence individually and the possibility to harness detailed kinetics calibrated in laminar flow configurations. Ultimately, we adapt the model formulation to aluminum dust combustion in a partially stirred reactor (PaSR) which, similar to Chapter 3, serves as spatially homogeneous test bed for the novel modelling framework and allows for the tentative assessment of the effects that turbulence and polydispersity may have on the particle temperature and oxide fraction, for example.

In this chapter, we drop the notion of a polydispersed oxide smoke population that may form upon condensation from a supersaturated vapour caused by the evaporation of individual fuel particles and consider a population of metal fuel particles instead. Omitting the particulate nature of the smoke fines for the time being, we are interested in the interaction of metal dust particles with the ambient gas phase through mass and enthalpy transfer. In contrast to the oxide smoke fines which have been in the spotlight of Chapters 2 to 5, metal dust particles are typically characterized by several properties,

e.g., the mass, oxide fraction, temperature and velocity [157]. Particularly the last two properties distinguish dust particles from smoke fines, since the fuel particles are usually so large that the assumption of an instantaneous equilibration in terms of velocity and temperature between particles and the ambient gas ceases to be valid.

This chapter is organized as follows: Starting with a simplified generic demonstration case featuring a single particle property, we introduce the general idea of the PBE-PDF approach and allude to possible advantages it has compared to existing formulations in Section 6.2. Subsequently, we apply the model formulation to aluminum dust combustion in a PaSR including multiple particle properties and provide the governing equations (Section 6.3). Following a tentative discussion of the influence of turbulence and polydispersity on the particle properties, we conclude this chapter in Section 6.4.

6.2 Modelling framework

Before we specify the PBE-PDF modelling framework to a turbulent metal dust flame in a PaSR (Section 6.3), in this section, we concentrate on a generic particle population immersed in an inert environment in order to provide a clear insight in the PBE-PDF modelling approach and demonstrate the formulation's advantages and fidelity. For clarity and the sake of argument, here, we characterize the particles by only a single property $p_p \in \Omega_{p_p} = [0, \infty)$, *e.g.*, size. Adopting a Eulerian perspective, the particles may formally be described in terms of the particle number density $N(p_p, t)$ which contains all statistical information regarding the variability of the property p_p among the particles within the population. Physically, $N(p_p, t) dp_p$ denotes the number density of particles whose property, at time t , lies within the interval $[p_p, p_p + dp_p)$. For future reference, we define the total particle number density

$$\rho_N(N(\cdot, t)) = \int_{\Omega_{p_p}} N(p_p, t) dp_p \quad (6.1)$$

as functional of the particle property distribution $N(\cdot, t)$. Moreover, using the total particle number density $\rho_N(t)$, we may define the probability density function (*pdf*) $f_N(p_p, t)$ associated with $N(p_p, t)$ according to

$$N(p_p, t) \equiv \rho_N(t) f_N(p_p, t) \quad (6.2)$$

which, by construction, satisfies all properties of a *pdf*. The spatially localized dynamics of the particle number density may then be governed by the PBE

$$\begin{aligned} \frac{\partial N(p_p, t)}{\partial t} + \frac{\partial A_p(p_p)N(p_p, t)}{\partial p_p} &= \frac{\partial}{\partial p_p} \left(D_p(p_p) \frac{\partial N(p_p, t)}{\partial p_p} \right) \\ &+ \frac{\partial}{\partial p_p} \left(\frac{p_p - \langle P_p \rangle}{\tau_{\text{int}}} N(p_p, t) \right), \end{aligned} \quad (6.3)$$

which is of a generic type. In Eq. (6.3), $A_p(p_p)$ and $D_p(p_p)$ denote the advection and diffusion rate in p_p -space, respectively, while τ_{int} represents an arbitrary interaction time scale. The last term on the right hand side of Eq. (6.3) represents this interaction between the particles causing their property to approach a mean particle property

$$\langle P_p \rangle = \int_{\Omega_{p_p}} p_p f_N(p_p, t) dp_p. \quad (6.4)$$

Since, in this particular demonstration case, Eq. (6.3) is of advection-diffusion type it conserves the total particle number density, $\rho_N(t) = \rho_N(0) = \rho_N$.

In spatially resolved aluminum dust flames, the particles are usually characterized in terms of at least six properties in addition to the three spatial coordinates and the time parameter [157], rendering the spatially inhomogeneous counterpart of Eq. (6.3) very high-dimensional. Mitigating the curse of dimensionality, Sewerin [154] recently developed an EMC solver which redirects the computational effort to the estimation of the particle property distribution's statistics rather than resolving the entire distribution as briefly outlined in the following section.

6.2.1 Eulerian Monte Carlo scheme

The EMC method applied in this chapter [154] is based on the idea to redefine the particle property distribution according to Eq. (6.2) in terms of the total number density ρ_N and a *pdf* f_N . While, in general, the total number density is only a function of the three spatial coordinates as well as time and obeys a standard (\mathbf{x}, t) -transport equation that is coupled to f_N and can be solved in a computationally efficient manner using a direct discretization scheme, the property distribution f_N itself still obeys a high-dimensional transport equation. In order to circumvent the prohibitive computational effort associated with the direct discretization of high-dimensional transport equations, the EMC scheme

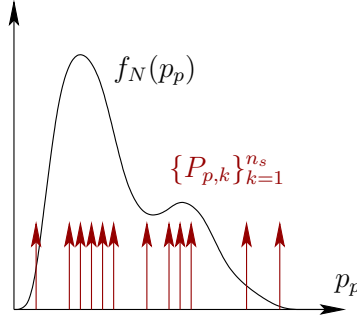


Figure 6.1 Illustration of the particle property distribution $f_N(\cdot)$ represented in terms of a set of particle phase scalars $\{P_{p,k}\}_{k=1}^{n_s}$. Here, the red arrows represent individual Dirac δ -distributions. Note that the density of the samples $P_{p,k}$, $k = 1, \dots, n_s$, correlates with the amplitude in $f_N(p_p)$.

harnesses the notion of representing the particle property distribution $f_N(\cdot, t)$ in terms of n_s particle phase scalars $\{P_{p,k}(t)\}_{k=1}^{n_s}$,

$$f_{N,n_s}(p_p, t) = \frac{1}{n_s} \sum_{k=1}^{n_s} \delta(p_p - P_{p,k}(t)), \quad (6.5)$$

as illustrated in Fig. 6.1. If each of these scalars $P_{p,k}(t)$, $k = 1, \dots, n_s$, parameterizing the property distribution evolves along the characteristic curve

$$dP_{p,k}(t) = \left(A_p(P_{p,k}(t)) + \left. \frac{dD_p(p_p)}{dp_p} \right|_{P_{p,k}(t)} - \frac{P_{p,k}(t) - \langle P_p \rangle_{n_s}}{\tau_{\text{int}}} \right) dt + \sqrt{2D_p(P_{p,k}(t))} d\bar{W}_k(t), \quad (6.6)$$

then f_{N,n_s} is an approximation of f_N with $f_N = \langle f_{N,n_s} \rangle$. In Eq. (6.6), $d\bar{W}_k(t) \sim \mathcal{N}(t; 0, dt)$ represents a Wiener process whose increments are normally distributed with mean 0 and variance dt and $\langle \cdot \rangle_{n_s}$ indicates the evaluation of the expectation with respect to the n_s particle phase scalars and, thus, represents a Monte Carlo estimator for $\langle P_p \rangle$. Recall that Eq. (6.6) is a stochastic differential equation which is physically completely equivalent to the PBE in Eq. (6.3) as it may be transformed into the PBE using a fine-grained *pdf* approach [107] in combination with Itô's formula [61, 124], for instance. Given the evolutions of total number density and particle phase scalars, we are able to estimate (higher-order) statistics of the number density distribution $N(\cdot, t)$ at any point in time. For details on additional spatial transport terms and their discretization using a kinetic FV method, we refer to Reference [154].

6.2.2 Treatment of polydispersity

The parameterization of f_N in terms of particle phase scalars is akin to a random sampling process, $P_{p,k}(t) \sim f_N(\cdot, t)$, and introduces uncontrollable perturbations as the set of particle phase scalars $\{P_{p,k}\}_{k=1}^{n_s}$ changes every time we sample from the same nominal *pdf* $f_N(p_p, t)$. In order to quantify the statistical variability associated with the generation of samples, we formulate a master density $f_{P_{p,1}, \dots, P_{p,n_s}}(p_{p,1}, \dots, p_{p,n_s}, t) = f_{\{P_{p,i}\}}(\{p_{p,i}\}, t)$ [133] that contains all statistical information about the samples. In particular, $f_{\{P_{p,i}\}}(\{p_{p,i}\}, t) d\{p_{p,i}\}$ denotes the joint probability to encounter, at the same time t , each sample $P_{p,k}(t)$ within an interval $[p_{p,k}, p_{p,k} + dp_{p,k})$, $k = 1, \dots, n_s$. An evolution equation governing the master density may either be derived from a fine-grained *pdf* approach [107] or the Chapman–Kolmogorov equation for Markov processes [61]. The latter is based on the notion of a transition *pdf* $f_{\{P_{p,i}\}|\{P'_{p,j}\}}(\{p_{p,i}\}, t|\{p'_{p,j}\}, t')$ which absorbs all the physics (Eq. (6.6)) and defines the probability of transitioning, during the time interval dt , from a state $\{p'_{p,j}\}$ at time t' to a possibly different state $\{p_{p,i}\}$ at time $t = t' + dt$. In this particular case, $f_{\{P_{p,i}\}|\{P'_{p,j}\}}$ represents the dynamics of a drift-diffusion process with mean-field interactions and may be defined as

$$f_{\{P_{p,i}\}|\{P'_{p,j}\}}(\{p_{p,i}\}, t|\{p'_{p,j}\}, t') = \left\langle \prod_{k=1}^{n_s} \delta \left(p_{p,k} - \left(p'_{p,k} + \tilde{A}_p(p'_{p,k}) dt + \sqrt{2D_p(p'_{p,k})} d\bar{W}_k \right) \right) \right\rangle \quad (6.7)$$

with

$$\tilde{A}_p(p'_{p,k}) = A_p(p'_{p,k}) + \left. \frac{dD_p(p_p)}{dp_p} \right|_{p'_{p,k}} - \frac{p'_{p,k} - \langle P'_p \rangle_{n_s}}{\tau_{\text{int}}}. \quad (6.8)$$

Expanding the Dirac distribution in Eq. (6.7) for each sample $k = 1, \dots, n_s$ with $dp'_{p,k} = \tilde{A}_p(p'_{p,k}) dt + \sqrt{2D_p(p'_{p,k})} d\bar{W}_k$ to second order,

$$\delta(p'_{p,k} - p_{p,k}) + \left. \frac{d\delta(p_p)}{dp_p} \right|_{p'_{p,k} - p_{p,k}} dp'_{p,k} + \frac{1}{2} \left. \frac{d^2\delta(p_p)}{dp_p^2} \right|_{p'_{p,k} - p_{p,k}} dp'_{p,k}{}^2, \quad (6.9)$$

inserting this result into Eq. (6.7) and evaluating the expectation yields the transition *pdf*

$$\begin{aligned}
& f_{\{P_{p,i}\}|\{P'_{p,j}\}}(\{p_{p,i}\}, t|\{p'_{p,j}\}, t') \\
&= \prod_{k=1}^{n_s} \delta(p'_{p,k} - p_{p,k}) \\
&+ \sum_{k=1}^{n_s} \prod_{\substack{j=1 \\ j \neq k}}^{n_s} \left(\frac{d\delta(p_p)}{dp_p} \Big|_{p'_{p,k}-p_{p,k}} \tilde{A}_p(p'_{p,k}) + \frac{d^2\delta(p_p)}{dp_p^2} \Big|_{p'_{p,k}-p_{p,k}} D_p(p'_{p,k}) \right) dt,
\end{aligned} \tag{6.10}$$

where we made use of the properties $\langle d\bar{W}_k \rangle = 0$ and $\langle d\bar{W}_k^2 \rangle = dt$ of a Wiener process. Moreover, for the evaluation of the expectation, we omitted all terms which are higher than first order in dt as these will vanish in the limit $dt \rightarrow 0$ (Eq. (6.12) below). Following the Chapman–Kolmogorov equation for Markov processes, the temporal change in the master density $f_{\{P_{p,i}\}}(\{p_{p,i}\}, t)$ is defined in terms of the transition *pdf* according to

$$f_{\{P_{p,i}\}}(\{p_{p,i}\}, t) = \int_{\Omega_{p_p}} f_{\{P_{p,i}\}|\{P'_{p,j}\}}(\{p_{p,i}\}, t|\{p'_{p,j}\}, t') f_{\{P'_{p,j}\}}(\{p'_{p,j}\}, t') d\{p'_{p,j}\}. \tag{6.11}$$

Substituting the expression for the transition *pdf* in Eq. (6.10) into Eq. (6.11), rearranging the resulting expression and letting $dt = t - t'$ tend to 0, we find

$$\begin{aligned}
\frac{\partial f_{\{P_{p,i}\}}}{\partial t} + \sum_{k=1}^{n_s} \frac{\partial}{\partial p_{p,k}} \left(\left(A_p(p_{p,k}) - \frac{p_{p,k} - \langle P_p \rangle_{n_s}}{\tau_{\text{int}}} \right) f_{\{P_{p,i}\}} \right) \\
= \sum_{k=1}^{n_s} \frac{\partial}{\partial p_{p,k}} \left(D_p(p_{p,k}) \frac{\partial f_{\{P_{p,i}\}}}{\partial p_{p,k}} \right)
\end{aligned} \tag{6.12}$$

as evolution equation for the master density. Recall that even if the characteristic curves of each particle phase scalar were deterministic (Eq. (6.6) excluding the Wiener term), the sampling process would still introduce variability.

6.2.3 Treatment of turbulence

The particle property distribution $f_N(p_p)$ from which the random samples are drawn was kept constant up to this point. However, turbulence may cause the property distribution itself to be subject to perturbations such that also $f_N(p_p)$ changes from realization to realization as indicated in Fig. 6.2. In this regard, turbulence may be considered a top-level fluctuation in the initial distribution $f_N(p_p, 0)$ which then propagates in time. In the

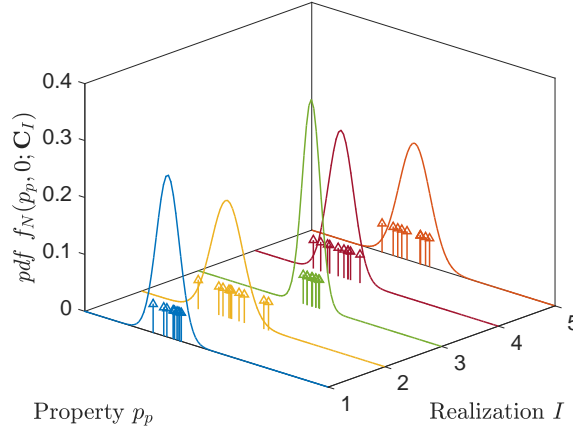


Figure 6.2 Illustration of the top-level fluctuation in the initial property distribution $f_N(p_p, 0; \mathbf{C}_I)$ due to turbulence. Here, both the samples and the *pdfs* are subject to randomness due to a sampling process and turbulence, respectively. In this particular example, the property distributions correspond to Gaussians parameterized by a mean and a variance (\mathbf{C}_I) each drawn from a uniform distribution on a prescribed interval.

example of Fig. 6.2, this top-level fluctuation is parameterized in terms of the parameter set $\mathbf{C} \in \Omega_{\mathbf{c}}$ which is associated with the *pdf* $f_{\mathbf{C}}$ and we may compute the average property distribution according to

$$\langle f_N(p_p, t; \mathbf{C}) \rangle_{\mathbf{C}} = \int_{\Omega_{\mathbf{c}}} f_N(p_p, t; \mathbf{c}) f_{\mathbf{C}}(\mathbf{c}) d\mathbf{c}. \quad (6.13)$$

Here, $\langle \cdot \rangle_{\mathbf{C}}$ denotes the expectation with respect to the variation in the initial distribution parameterized by \mathbf{C} . Superimposing turbulence on the p_p -discrete property distribution f_{N, n_s} (Eq. (6.5)) yields the relation

$$\begin{aligned} \langle f_N(p_p, t; \mathbf{C}) \rangle_{\mathbf{C}} &= \langle \langle f_{N, n_s}(p_p, t; \mathbf{C}) \rangle \rangle_{\mathbf{C}} \\ &= \int_{\Omega_{\mathbf{c}}} \int_{\Omega_{p_p}} \underbrace{\frac{1}{n_s} \sum_{k=1}^{n_s} \delta(p_p - p_{p,k}; \mathbf{c}) f_{\{P_{p,i}\}}(\{p_{p,i}\}, t; \mathbf{c})}_{=f_{N, n_s}(p_p, t; \mathbf{c})} f_{\mathbf{C}}(\mathbf{c}) d\{p_{p,i}\} d\mathbf{c} \end{aligned} \quad (6.14)$$

which links the ensemble-averaged property distribution $\langle f_N \rangle_{\mathbf{C}}$ to the p_p -discrete representation in terms of particle phase scalars $\{P_{p,i}\}$.

The central modelling variable in terms of which the physics is formulated may then be obtained as

$$f_{\{P_{p,i}\}}(\{p_{p,i}\}, t) = \int_{\Omega_{\mathbf{c}}} f_{\{P_{p,i}\}}(\{p_{p,i}\}, t; \mathbf{c}) f_{\mathbf{C}}(\mathbf{c}) d\mathbf{c} \quad (6.15)$$

and accounts for both the variability introduced by the random sampling of a finite num-

ber of particle phase scalars representing polydispersity and randomness in the property distribution caused by turbulence. The evolution equation for the particle property distribution $f_{\{P_{p,i}\}}(\{p_{p,i}\}, t; \mathbf{c})$ parameterized in terms of \mathbf{c} is given in Eq. (6.12). However, since $f_{\mathbf{C}}$ is not a function of time, also $f_{\{P_{p,i}\}}(\{p_{p,i}\}, t)$ defined in Eq. (6.15) obeys Eq. (6.12).

6.2.4 Comparison of stochastic models

In standard Lagrangian stochastic models (see Reference [117], for example) n_s samples drawn from an ensemble-averaged distribution $\langle f_N(p_p, t; \mathbf{C}) \rangle_{\mathbf{C}}$ are evolved in time causing the perturbations introduced by turbulence on part of the initial *pdf* to be blurred with the variability introduced in the sampling process. Consequently, these methods are only suitable if we are interested in combined statistics of the mean property distribution. The key advantage of the PBE-PDF method proposed here, in which we evolve n_s samples drawn from n_r individual realizations, is the capability to assess both effects individually and to estimate higher-order statistics with respect to either turbulence or polydispersity. Figure 6.3 shows the temporal evolution of a property *pdf* using both the PBE-PDF approach (a) and a Lagrangian stochastic method (b). While the Lagrangian stochastic method yields at time $t = 1$ a set of particle phase scalars based on which the statistics of the ensemble-averaged distribution can be estimated, the PBE-PDF method provides information on both the variation in the property distribution due to turbulence and polydispersity and allows for the estimation of the standard deviation around the mean property distribution (grey patch in Fig. 6.3(a)), for example.

In Fig. 6.3, we observe that the averaged distributions (red curves) of the PBE-PDF approach and the Lagrangian stochastic model at the final point in time ($t = 1$) do not coincide anymore as the *pdf* in Fig. 6.3(a) appears to be wider. This is due to the particle interaction term in Eq. (6.3) that is non-linear in N . As we apply the ensemble-averaging operator $\langle \cdot \rangle_{\mathbf{C}}$ to Eq. (6.3) in order to find the evolution equation for the averaged *pdf* $\langle f_N(p_p, t; \mathbf{C}) \rangle_{\mathbf{C}}$ the final term in Eq. (6.3) is rendered unclosed. For the results shown in Fig. 6.3(b), we used a perfect mixing assumption to close this term. By contrast, the PBE-PDF formulation (Fig. 6.3(a)) does not require any closure model to account for non-linear particle interaction terms as it evolves each realization individually.

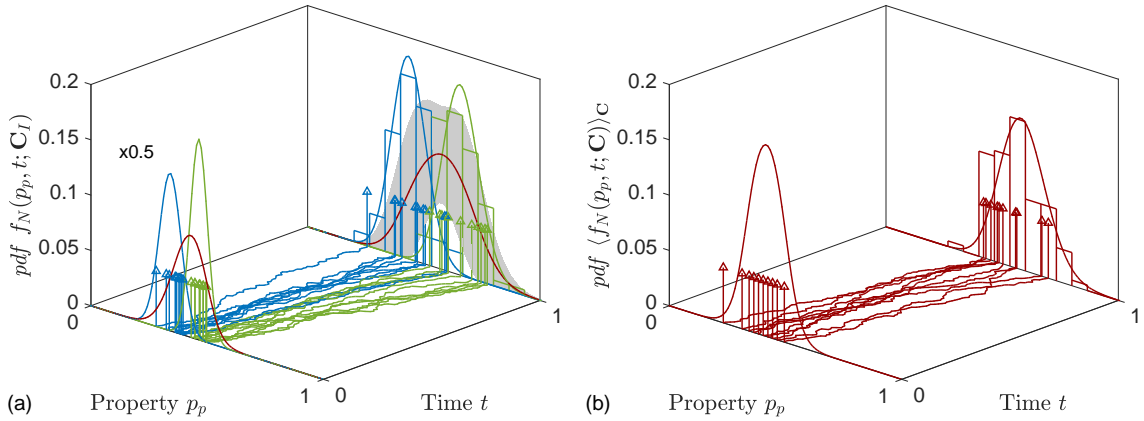


Figure 6.3 Temporal evolution of the property pdf and the individual particle phase scalars obtained using the PBE-PDF approach (a) and the Lagrangian stochastic model (b) [117]. Note that the initial distributions ($t = 0$) in figure (a) are scaled by a factor of 0.5. While the blue and green curves in figure (a) represent individual realizations of f_N (Fig. 6.2), the red line denotes the ensemble-averaged distribution which corresponds to the initial average distribution $\langle f_N(p_p, 0; \mathbf{C}) \rangle_{\mathbf{C}}$ in figure (b). The sample paths depicted in both figures are obtained from evolving the particle phase scalars according to Eq. (6.6) with constant diffusivity and interaction time scale as well as an advection rate that is quadratic in p_p . By contrast, the continuous distributions are obtained by solving Eq. (6.3) with constant ρ_N using an FV solver and resemble the histograms constructed from the evolved samples at $t = 1$. The grey patch in figure (a) denotes plus/minus one standard deviation from the mean distribution.

6.3 A partially stirred reactor for turbulent aluminum dust flames

The previous section focused on the basic concept of the PBE-PDF formulation applied to a generic demonstration case and addressed the advantages it has compared to Lagrangian stochastic models. Within the scope of this introduction, we simplified the model formulation and assumed, for instance, that the particles are characterized by a single property only and do not interact with an ambient gas phase, which is, however, indispensable for the description of turbulent metal dust flames. In this section, we apply the formulation to the combustion of an aluminum dust in a reactive atmosphere within the context of the PaSR configuration and show preliminary predictions.

6.3.1 Governing equations

While the thermochemical state of the multicomponent gas phase remains completely determined by the reactive gas scalars $\Phi(t) = (\mathbf{Y}(t), T(t))^T$ (Sections 2.2.1 and 4.3.1), the polydispersed aluminum dust particles are characterized in terms of $n_{\mathbf{p}_p} = 3$ properties (mass M_p , oxide fraction X_p and temperature T_p), accumulated in the property vector

6.3 A partially stirred reactor for turbulent aluminum dust flames

$\mathbf{p}_p = (m_p, \chi_p, \tau_p)^T \in \Omega_{\mathbf{p}_p}$, and accounted for by the particle number density $N(\mathbf{p}_p, t)$ [157].

As time progresses, the gas composition and particle property distribution may change on account of gas phase reactions as well as mass and heat exchanges between the gas and the particles. While the time evolution of the reactive scalars in a single realization is governed by an ODE system,¹

$$\frac{d\Phi(t)}{dt} = \dot{\mathbf{r}}_g(\Phi(t), N(\cdot, t)), \quad (6.16)$$

the evolution of the particle population is governed by the PBE

$$\frac{\partial N(\mathbf{p}_p, t)}{\partial t} + \nabla_{\mathbf{p}_p} \cdot (\mathbf{A}_p(\mathbf{p}_p, \Phi(t))N(\mathbf{p}_p, t)) = 0, \quad (6.17)$$

where the property advection rate \mathbf{A}_p is now vector-valued. Equation (6.17) is a pure advection equation and, thus, maintains the total particle number, *i.e.*,

$$\begin{aligned} \frac{d\rho_N(t)}{dt} &= \frac{d}{dt} \left(\int_{\Omega_{\mathbf{p}_p}} N(\mathbf{p}_p, t) d\mathbf{p}_p \right) = \int_{\Omega_{\mathbf{p}_p}} \frac{\partial N(\mathbf{p}_p, t)}{\partial t} d\mathbf{p}_p \\ &= - \int_{\Omega_{\mathbf{p}_p}} \nabla_{\mathbf{p}_p} \cdot (\mathbf{A}_p(\mathbf{p}_p, \Phi(t))N(\mathbf{p}_p, t)) d\mathbf{p}_p \\ &= - \int_{\partial\Omega_{\mathbf{p}_p}} \mathbf{A}_p(\mathbf{p}_p, \Phi(t))N(\mathbf{p}_p, t) \cdot \mathbf{n}_{\mathbf{p}_p} d\mathbf{p}_p = 0, \end{aligned} \quad (6.18)$$

where the last equality results from the fact that the boundaries of the property space, $\partial\Omega_{\mathbf{p}_p}$ (with outward-pointing unit normal $\mathbf{n}_{\mathbf{p}_p}$), are chosen in a way that the number density vanishes here. The rates-of-change $\dot{\mathbf{r}}_g$ and \mathbf{A}_p are given in Reference [157].

In line with the developments of Section 6.2, here, we choose the EMC method, which has already been applied within the scope of laminar aluminum dust flames by Sewerin and Finke [157], to solve the high-dimensional PBE in Eq. (6.17). Parameterizing the property distribution $N(\mathbf{p}_p, t)$ in terms of n_s particle phase scalars $\{\mathbf{P}_{p,k}(t)\}_{k=1}^{n_s}$,

$$N_{n_s}(\mathbf{p}_p, t) = \rho_N f_{N, n_s}(\mathbf{p}_p, t) = \frac{\rho_N}{n_s} \sum_{k=1}^{n_s} \delta(\mathbf{p}_p - \mathbf{P}_{p,k}(t)), \quad (6.19)$$

¹Technically, Eq. (6.16) constitutes the counterpart of Eq. (2.15) but the gas-surface interactions are formally accounted for through the dependence on the particle property distribution $N(\cdot, t)$.

and evolving each sample, $k = 1, \dots, n_s$, along its characteristic curve

$$d\mathbf{P}_{p,k}(t) = \mathbf{A}_p(\mathbf{P}_{p,k}(t), \Phi(t)) dt \quad (6.20)$$

provides a solution $N_{n_s}(\mathbf{p}_p, t)$ which is an approximation of $N(\mathbf{p}_p, t)$ with $N(\mathbf{p}_p, t) = \langle N_{n_s}(\mathbf{p}_p, t) \rangle$. Jointly, the total particle number density ρ_N , the particle phase scalars $\{\mathbf{P}_{p,k}(t)\}_{k=1}^{n_s}$ and the gas phase scalars $\Phi(t)$ determine the state of the dispersion at time t .

Based on the physical picture proposed in Fig. 3.1, we adapt the PaSR formulation provided in Chapter 3 to an aluminum dust flame. Here, we consider an ensemble of n_r gas-particle elements with composition $(\Phi(t), \{\mathbf{P}_{p,k}(t)\}_{k=1}^{n_s})$ whose variability across the reactor is characterized by the joint *pdf* $f_{\Phi, \{\mathbf{P}_{p,i}\}}(\phi, \{\mathbf{p}_{p,i}\}, t)$. In particular, the expression $f_{\Phi, \{\mathbf{P}_{p,i}\}}(\phi, \{\mathbf{p}_{p,i}\}, t) d\phi d\{\mathbf{p}_{p,i}\}$ denotes the probability of observing, at time t , a fluid element with gas composition $\Phi(t) \in [\phi, \phi + d\phi]$ and particle phase scalars $\mathbf{P}_{p,k}(t) \in [\mathbf{p}_{p,k}, \mathbf{p}_{p,k} + d\mathbf{p}_{p,k}]$, $k = 1, \dots, n_s$. The fluid elements' states may not only change on account of chemical gas phase reactions and gas-particle interactions but also due to interactions between the fluid elements. This small-scale mass and enthalpy exchange is caused by molecular mixing which homogenizes small-scale heterogeneity induced by the distribution in residence time of the elements. Following the considerations of Chapter 3 and the formulations of Chen [32] and Rigopoulos [140], the dynamics of $f_{\Phi, \{\mathbf{P}_{p,i}\}}$ are governed by

$$\begin{aligned} \frac{\partial f_{\Phi, \{\mathbf{P}_{p,i}\}}}{\partial t} = & - \frac{\partial}{\partial \phi} \cdot \left(f_{\Phi, \{\mathbf{P}_{p,i}\}} \dot{\mathbf{r}}_g(\phi, \{\mathbf{p}_{p,i}\}) \right) + \mathcal{M}_g f_{\Phi, \{\mathbf{P}_{p,i}\}} \\ & - \sum_{k=1}^{n_s} \frac{\partial}{\partial \mathbf{p}_{p,k}} \cdot \left(f_{\Phi, \{\mathbf{P}_{p,i}\}} \mathbf{A}_p(\{\mathbf{p}_{p,i}\}, \phi) \right) + \mathcal{M}_p f_{\Phi, \{\mathbf{P}_{p,i}\}} \\ & + \frac{1}{\tau_{\text{res}}} \left(f_{\Phi, \{\mathbf{P}_{p,i}\}}^{\text{in}} - f_{\Phi, \{\mathbf{P}_{p,i}\}} \right), \end{aligned} \quad (6.21)$$

where τ_{res} denotes the mean residence time after which, on average, a fluid element inside the reactor is replaced by an element drawn from the inflow *pdf*

$$f_{\Phi, \{\mathbf{P}_{p,i}\}}^{\text{in}} = \delta(\phi - \Phi^{\text{in}}) \prod_{k=1}^{n_s} \delta(\mathbf{p}_{p,k} - \mathbf{P}_{p,k}^{\text{in}}) \quad (6.22)$$

with $\mathbf{P}_{p,k}^{\text{in}} \sim f_N^{\text{in}}(\mathbf{p}_p)$. The micro-mixing terms in Eq. (6.21) represent closure models

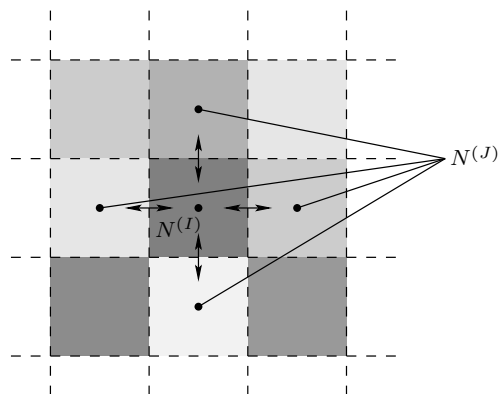


Figure 6.4 Phenomenological illustration of the diffusive particle exchange between different realizations in a PaSR. The different shadings indicate heterogeneity in terms of the particle number density $N^{(I)}$, $I = 1, \dots, n_r$, driving the diffusive exchange.

which have been applied in order to close the spatial diffusion terms of the spatially inhomogeneous *pdf* transport equation [32, 128]. For the molecular exchange on part of the gas phase (\mathcal{M}_g), we employ the IEM model as used in Chapter 3, whereas mixing on part of the dispersed particles (\mathcal{M}_p) is accounted for as follows.

From a phenomenological point of view, micro-mixing on part of the dust particles is considered a diffusive blending of the particle property distributions associated with all realizations². Consequently, we may formulate a discrete diffusion equation for the particle number density $N^{(I)}(\mathbf{p}_p, t)$ in the I -th realization according to

$$\frac{\partial N^{(I)}(\mathbf{p}_p, t)}{\partial t} = \alpha_{\text{mix},p} \mathcal{D}_p(\mathbf{p}_p) \sum_{\substack{J=1 \\ J \neq I}}^{n_r} \left(N^{(J)}(\mathbf{p}_p, t) - N^{(I)}(\mathbf{p}_p, t) \right), \quad I = 1, \dots, n_r, \quad (6.23)$$

which is obtained by discretizing a diffusion equation for the particle number density $N(\mathbf{p}_p, \mathbf{x}, t)$,

$$\frac{\partial N}{\partial t} = \nabla \cdot (\mathcal{D}_p \nabla N), \quad (6.24)$$

in physical space as illustrated in Fig. 6.4. In Eq. (6.23), $\mathcal{D}_p(\mathbf{p}_p)$ denotes the size-dependent Stokes–Einstein diffusion coefficient³ and $\alpha_{\text{mix},p}$ represents a mixing parameter which includes the granularity of the fluid elements, *i.e.*, their surface-to-volume ratio, and a length

²In this context, a realization corresponds to a particular fluid element, associated with a gas composition and a particle charge, inside the PaSR.

³Here, \mathcal{D}_p is evaluated according to Eq. (4.21) discounting for kinetic effects and assuming a constant temperature and viscosity.

scale on which the gradients in $N(\mathbf{p}_p, t)$ are evaluated (Fig. 6.4). Jointly, $\mathcal{D}_p(\mathbf{p}_p)$ and $\alpha_{\text{mix},p}$ may define a particle mixing time scale $\tau_{\text{mix},p}(\mathbf{p}_p) = (\mathcal{D}_p(\mathbf{p}_p)\alpha_{\text{mix},p})^{-1}$. Upon integration of Eq. (6.23) over \mathbf{p}_p -space, we find an evolution equation for the total particle number density of the I -th fluid element,

$$\frac{\partial \rho_N^{(I)}(t)}{\partial t} = \int_{\Omega_{\mathbf{p}_p}} \alpha_{\text{mix},p} \mathcal{D}_p(\mathbf{p}_p) \sum_{\substack{J=1 \\ J \neq I}}^{n_r} \left(N^{(J)}(\mathbf{p}_p, t) - N^{(I)}(\mathbf{p}_p, t) \right) d\mathbf{p}_p. \quad (6.25)$$

Integrating Eqs. (6.23) and (6.25) in time using the forward Euler scheme and parameterizing $N(\mathbf{p}_p, t)$ in terms of the total number density and the particle phase scalars yields

$$\begin{aligned} N^{(I)}(\mathbf{p}_p, t + \Delta t) &= (1 - \alpha_{\text{mix},p} \mathcal{D}_p(\mathbf{p}_p) \Delta t (n_r - 1)) \frac{\rho_N^{(I)}(t)}{n_s} \sum_{k=1}^{n_s} \delta(\mathbf{p}_p - \mathbf{P}_{p,k}^{(I)}(t)) \\ &+ \alpha_{\text{mix},p} \mathcal{D}_p(\mathbf{p}_p) \Delta t \sum_{\substack{J=1 \\ J \neq I}}^{n_r} \frac{\rho_N^{(J)}(t)}{n_s} \sum_{k=1}^{n_s} \delta(\mathbf{p}_p - \mathbf{P}_{p,k}^{(J)}(t)) \end{aligned} \quad (6.26)$$

and

$$\begin{aligned} \rho_N^{(I)}(t + \Delta t) &= \left(1 - \alpha_{\text{mix},p} \langle \mathcal{D}_p(\mathbf{P}_p) \rangle_{n_s}^{(I)} \Delta t (n_r - 1) \right) \rho_N^{(I)}(t) \\ &+ \alpha_{\text{mix},p} \Delta t \sum_{\substack{J=1 \\ J \neq I}}^{n_r} \rho_N^{(J)} \langle \mathcal{D}_p(\mathbf{P}_p) \rangle_{n_s}^{(J)} \end{aligned} \quad (6.27)$$

for the new particle property distribution and its zeroth moment in realization I after mixing. In Eq. (6.27), $\langle \mathcal{D}_p(\mathbf{P}_p) \rangle_{n_s}^{(I)}$ denotes the Monte Carlo estimator for the mean particle diffusivity with respect to \mathbf{p}_p -space in fluid element I . Although the total particle number density remains constant for an individual fluid element in the sense of Eq. (6.18), the interaction among fluid elements due to molecular mixing, however, may cause ρ_N to change in time. Divided by the updated total number density $\rho_N^{(I)}(t + \Delta t)$, the prefactor of each δ -distribution in Eq. (6.26) denotes the probability for a sample to remain, during the time interval Δt , in realization I or to transition from realization J to realization I , respectively. Here, we assume that all fluid elements interact with each other and that the mixing coefficient $\alpha_{\text{mix},p}$ is constant. Since the property distribution in each realization is parameterized in terms of $n_r \times n_s$ samples after the mixing process (Eq. (6.26)), we resample n_s particle phase scalars $\{\mathbf{P}_{p,k}^{(I)}\}_{k=1}^{n_s}$ from the distribution given in Eq. (6.26) for

every realization $I = 1, \dots, n_r$ using a bespoke sampling scheme [154].

6.3.2 Analysis of the interaction between polydispersity and turbulence

Apart from the PBE fractional step, which is now governed by Eq. (6.20) [157], and the surface chemistry, which is part of the PBE step here, the governing PaSR equations are solved using a similar numerical procedure as outlined in Section 3.3 and Appendix B but adapted to an aluminum dust. In order to tentatively analyze the interaction of turbulence and polydispersity in turbulent aluminum dust flames within the scope of the PaSR using the PBE-PDF formulation developed here, we choose an ensemble of $n_r = 64$ fluid elements or realizations each of which carries a gas composition and a particle population represented in terms of $n_s = 32$ particle phase scalars and a total particle number density. Note that we initialize every realization with a specific total number density in order to impose an identical initial dust concentration of 0.4 kg/m^3 [157]. The initial gas composition of the realizations corresponds to air ($[\text{O}_2]/[\text{N}_2]=21/79$) at atmospheric pressure and a temperature $T = 2000 \text{ K}$ and the particle samples are initialized with a temperature $T_p = 298 \text{ K}$, an oxide fraction $X_p = 0$ as well as a mass M_p that corresponds to a particle diameter randomly sampled from the log-normal size distribution given in Reference [157, Eq. (78)]. The inflow composition ($\Phi^{\text{in}}, f_N^{\text{in}}(\mathbf{p}_p)$), moreover, matches the initial conditions.

Figure 6.5 shows the temporal evolutions of different statistics of the particle temperature T_p and oxide fraction X_p for a residence time scale $\tau_{\text{res}} = 10^{-3} \text{ s}$, a mixing time scale $\tau_{\text{mix}} = 10^{-4} \text{ s}$ and a particle mixing parameter $\alpha_{\text{mix},p} = 10^{12} \text{ m}^{-2}$. As indicated by the evolutions of the ensemble means of the average particle temperature $\langle\langle T_p \rangle_{n_s}\rangle_{n_r}$ and oxide fraction $\langle\langle X_p \rangle_{n_s}\rangle_{n_r}$ in Fig. 6.5(a), the particles heat up rapidly and are successively converted until a statistically quasi-steady combustion mode is reached which exhibits an average particle temperature of about 2000 K and an oxide fraction of roughly 0.5 . This quasi-steady mode is maintained by the replacement of burnt-out fluid elements with fresh ensembles and their interactions with other realizations inside the reactor. The variability of the \mathbf{p}_p -averaged properties due to turbulence is a measure for the mixing intensity and is represented by the patches in Fig. 6.5(a) which indicate one standard deviation ($\text{std}_{n_r}(\langle T_p \rangle_{n_s}), \text{std}_{n_r}(\langle X_p \rangle_{n_s})$) about the ensemble-averaged mean particle temperature and oxide fraction. By contrast, the variability of particle temperature and oxide fraction with respect to polydispersity is given by $\langle\text{std}_{n_s}(T_p)\rangle_{n_r}$ and $\langle\text{std}_{n_s}(X_p)\rangle_{n_r}$ in Fig. 6.5(b) which

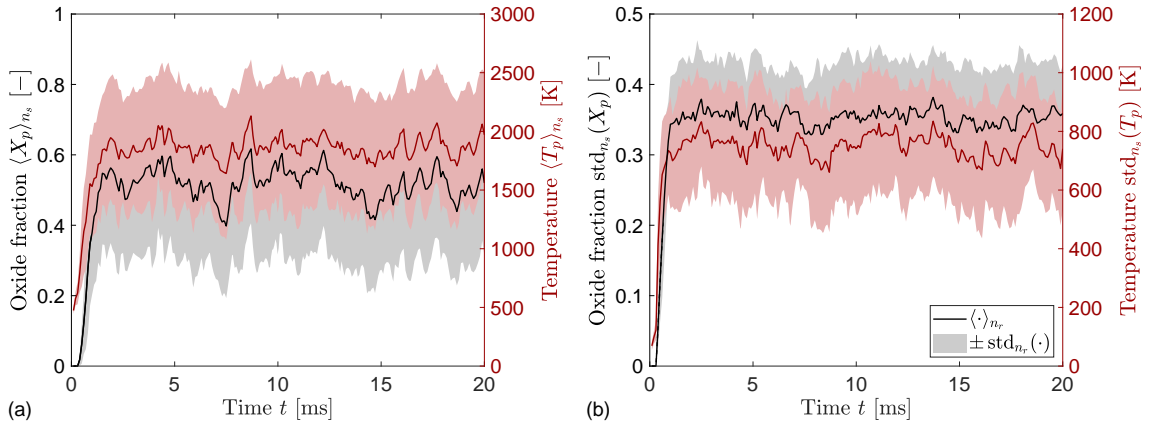


Figure 6.5 Time evolution of ensemble statistics of the particle temperature T_p and oxide fraction X_p during aluminum dust combustion in air in a PaSR. While the shaded areas (plus/minus one standard deviation from the respective mean quantities) reflect randomness due to turbulence, the solid lines represent the ensemble averages of the mean (a) and the standard deviation (b) of T_p and X_p with respect to the n_s samples and are, thus, indicative of the variability associated with polydispersity. Here, the subscript n_s denotes the evaluation of the statistics with respect to the samples in particle property space, whereas the subscript n_r represents an ensemble statistic with respect to the realizations. Since n_s and n_r are finite, all statistics are Monte Carlo estimates.

is slightly more pronounced than the variability due to turbulence. A key advantage of the PBE-PDF formulation is that we are also able to quantify the turbulence-related perturbations in the variation of the particle properties due to polydispersity as indicated by the patches in Fig. 6.5(b) which represent one standard deviation about the ensemble-mean of the temperature and oxide fraction fluctuations ($\text{std}_{n_r}(\text{std}_{n_s}(T_p))$, $\text{std}_{n_r}(\text{std}_{n_s}(X_p))$).

6.4 Chapter conclusions

The generalization of single particle combustion models, such as the one developed in the preceding chapters, for example, to turbulent metal dust flames constitutes an important step towards the prediction of the combustion characteristics, the power density and the emissions associated with large-scale metal burners. In the spirit of an extended outlook, in this chapter, we provided the basic concepts of a two-level statistical Eulerian PBE-PDF description that allows for investigating the effects of turbulence and polydispersity on part of the fuel particles' properties on the combustion of aluminum dusts. The modelling approach harnesses a recently developed Eulerian Monte Carlo solver which targets the predictions of statistics of the particle property distribution. Compared to existing Lagrangian stochastic models, the advantage of the PBE-PDF formulation was shown to be twofold. First, the influence of turbulence, as the first source of variability, and polydis-

persity, the second source of variability, on particle-laden flows can be assessed separately without blurring of these two effects. In particular, the modelling framework enables us to quantify the particle property distribution's variability caused by turbulence. And second, non-linear particle interaction processes can be accounted for straightforwardly without the necessity of closure models.

Following the presentation of the PBE-PDF framework's basic principles, in this chapter, we adapted the partially stirred reactor introduced within the scope of Chapter 3 to the turbulent combustion of a metal dust. In particular, we provided a mechanistic description of micro-mixing on part of the fuel particles that is based on the physics of a diffusion process. Ultimately, we showed tentative results of the time evolutions of particle property statistics in the PaSR and demonstrate the predictive capabilities of the modelling framework. As a next step, the extension of the PBE-PDF description to spatially inhomogeneous turbulent dust flames, possibly through an intermediate stage of several interacting PaSRs, is targeted which is, however, beyond the scope of this thesis.

Chapter 7

Conclusions

7.1 Summary

Metal powders are currently being investigated as carbon-free and reusable energy carriers that aid our transition to a sustainable energy economy. Within the scope of the recently proposed metal fuel cycle, the so-called metal fuels are burned while releasing process heat and producing condensed phase oxides as combustion product, which can be extracted from the exhaust fumes and reconverted to the original metal through a clean reduction step. Due to its suitable properties and a rich database, aluminum is a promising and relevant metal fuel candidate. Particularly for the aluminum-driven metal fuel cycle, however, the formation of very fine oxide smoke droplets upon combustion poses major challenges as these non-inertial smoke fines need to be separated from the carrier gas in order to avoid oxide leakage and preserve the circular nature of the metal fuel cycle. In this thesis, we presented a kinetically detailed modelling framework that accounts for the oxide smoke in a Eulerian fashion on a population level and permits the resolution of the entire smoke droplet size distribution along with gas phase composition and surface composition of the fuel particle. Physically, the direct resolution of droplet size distributions is very important for the analysis of heat release and the smoke dynamics in metal dust flames, since it enables us to elucidate smoke deposition and emission mechanisms and support the design and assessment of potential smoke recovery techniques.

The modelling framework proposed in this work harnesses a population balance approach, in which the smoke droplets are described in terms of a number density and the oxide size distribution is governed by the population balance equation. In order to kinetically inform the PBE-based model formulation with the rates at which droplets nucleate,

grow or dissociate, coagulate and radiate, in a first step, we developed a tailored and detailed kinetic framework for these spatially localized droplet formation and interaction kinetics that is based on first principles and valid across the entire droplet size range from the kinetic to the continuum regime (Chapter 2). Particular features are the computation of the vapour phase's supersaturation in terms of the chemical potentials and the calibration of coagulation enhancement factors to account for the effect of field interactions, *i.e.*, London–van der Waals forces, and hydrodynamic retardation on the coagulation rate. Moreover, our kinetic framework may easily be adapted to other metal fuel candidates, provided the relevant material properties are given. Upon coupling of the PBE with balance laws for mass and enthalpy as well as detailed gas phase and surface reaction mechanisms, including NO_x chemistry, the model was first employed within the scope of a perfectly stirred reactor (Chapter 2) which provides an important test bed as it allows for the spatially homogeneous investigation of the combustion dynamics close to an aluminum fuel particle's reactive surface in a laminar flame. Within the scope of the PSR, we found that the NO_x chemistry has a significant impact on the combustion process and particularly on the quenching mechanism. If NO_x chemistry is neglected, combustion and smoke condensation terminate as soon as all oxygen is consumed, whereas the occupation of the fuel particle's surface by atomic nitrogen and the associated obstruction of the fuel supply is responsible for the extinction of the flame in case NO_x -related reactions are taken into account. However, in both cases, the produced smoke droplets are nano-sized, although coagulation is active. An increase in pressure turns out to slightly increase the droplet's sizes.

Aiming at the assessment of the effect that molecular mixing, a phenomenon that plays an essential role in turbulent metal dust flames, has on the gas composition and oxide smoke size distribution, in Chapter 3, we applied our PBE-based model in a partially stirred reactor. The PaSR appears to be homogeneous on a macroscopic level but features inhomogeneity on the smallest scales and, thus, represents the dynamics in a single grid cell of a solver for a turbulent flame based on a PDF approach. The key contribution of this work was the extension of the PaSR model to accommodate a reactive surface whose surface composition is subject to small-scale heterogeneity, too. In particular, this was realized by introducing a decorrelation time scale that controls the temporally varying association between a dispersion and a surface element. In this way, we were able to

investigate the influence of the micro-mixing intensity on gas and surface composition as well as the smoke droplet size distribution and found that slow mixing reduces the maximum flame temperature and, consequently, the NO_x emissions, while the smoke droplets become larger; a mechanism that is reinforced by an increase in the operating pressure.

Despite the fact that both the PSR and the PaSR are spatially homogeneous and, therefore, simplified flow configurations, the insights we gained from their investigations are valuable and constitute the basis for the spatially resolved single aluminum particle combustion model discussed in Chapter 4. In order to be able to predict the oxide smoke size distribution and gas-droplet as well as droplet-surface interactions at every location inside the spatially resolved boundary layer around a single steadily burning aluminum particle, we embedded the PBE-based framework into a set of tailored balance laws governing the gas species' mass as well as the dispersion's mass, momentum and enthalpy. These balance laws resemble their single-phase counterparts but are specifically adapted to the notion of a gas-droplet dispersion featuring an instantaneous equilibration in terms of temperature and bulk velocity between gas and droplets. Concomitantly, we extended the PBE by spatial transport terms representing droplet diffusion and thermophoretic transport and enhanced the kinetic framework of Chapter 2 accordingly by the respective spatial droplet transport parameters, *i.e.*, the Stokes–Einstein diffusion coefficient and a thermophoretic velocity. Considering the steady combustion of a single aluminum particle in an O_2/Ar mixture, the droplet formation and interaction kinetics were adjusted in such a way that fair agreement with existing experimental measurements is achieved. In particular, this calibration showed not only that the interplay of nucleation (at the rate proposed by Reiss et al. [138, 139]) and dissociation affects the envelope flame through the chemical equilibrium between aluminum suboxides and oxide smoke, but also that the shape of the smoke halo is mainly determined by the droplets' sizes and their diffusional mobility. Concomitantly, we were led to the conclusion that coagulation may not occur in the flame zone, possibly due to electrostatic droplet repulsion induced by thermionic emissions and ionization reactions. Following the consolidation of the droplet formation kinetics, the combustion of an aluminum particle in air was investigated as validation case. For the consolidated droplet formation kinetics, the predicted radial AIO and oxide smoke profiles compared qualitatively very well with the available experimental data, while deviations in the temperature profile remained, for which possible reasons were discussed. A

7 Conclusions

sensitivity analysis with respect to pressure revealed that, at the expense of higher NO_x emissions, the smoke droplet size can be significantly increased with a higher operating pressure, even though the droplets remain nanometric. In combination with coagulation, the enlarging effect of pressure was shown to be reinforced to yield average smoke droplet diameters of about 100 nm at $p = 10$ bar.

With the objective of predicting the amount of oxide smoke and pollutants emitted over the course of a single aluminum fuel particle's conversion, in Chapter 5, we went one step further and extended the single particle modelling framework by a time-varying particle morphology, including the notion of an oxide cap. Physically, the changes in the fuel particle's morphology were found to be mediated by aluminum evaporation, heterogeneous surface oxidation and oxide smoke deposition. An analysis of the cumulative pollutant and smoke emissions revealed that both the fraction of oxide emitted as smoke and the amount of NO and NO_2 , the only relevant NO_x species, increase with the initial particle diameter. The validity of our predictions was corroborated by a very good agreement of our estimated burning times and residue sizes for different initial particle diameters with existing experimental measurements and empirical correlations. In particular, we found the burning time to scale with the initial diameter to the power of 1.83, while the residue size is found to increase with a diameter exponent of 0.78.

In a last step (Chapter 6), we build a bridge from the kinetically detailed single particle combustion model featuring the resolution of the smoke droplet's size distribution at every point in space and time to a turbulent metal dust flame. The metal dust configuration is thought to be more relevant in practice as it provides insight in the combustion dynamics of an entire fuel particle population. In particular, we proposed a preliminary model formulation that is based on a probability density function approach combined with a recently developed Eulerian Monte Carlo solver for the PBE. The PBE-PDF formulation was found to be capable of quantifying fluctuations in the particle property distribution caused by both turbulent effects and polydispersity which constitutes the key advantage compared to existing models. Adapting the PaSR of Chapter 3 to a metal dust flame, we provided tentative predictions of statistics of the particle temperature and oxide fraction in a turbulent flow.

At the end of this section, we would like to summarize the main outcomes of this thesis with regards to the pollutant emissions, the separability of the oxide smoke from exhaust

fumes and the implications for the design of combustors or separation devices. We can conclude the following five major findings:

- At atmospheric conditions, the oxide smoke droplets were found to be nano-sized on average in all three configurations (PSR, PaSR and single particle model) rendering their direct extraction challenging due to the small Stokes numbers. Since the extraction of these smoke fines requires HEPA-type or electrostatic filters and is, hence, energy-intensive and incompatible with the requirements of the metal fuel cycle, the formation or emission of these fines needs to be avoided. Besides our hypothesis that the existence of other fuel particles promotes the collection of smoke, we showed that it is possible to control the smoke droplet size by the adjustment of operating parameters as described in the following point.
- The operating pressure has a substantial impact on the shape of the envelope flame spawned by individual aluminum fuel particles and its increase significantly enhances the smoke droplet's sizes. Consequently, we found a means to control the oxide droplets' sizes.
- Although coagulation is an effective mechanism to increase the size of the smoke fines, particularly in combination with an elevated thermodynamic pressure, a comparison of model predictions and experimental measurements suggests that it may be inhibited within the envelope flame. We hypothesize that this may be due to electrostatic repulsion between droplets that are about to collide. Physically, these repulsive forces may be caused by thermionic emissions and the absorption of free charge carriers.
- The existence of an oxide cap significantly increases the capture of smoke as it provides a low-velocity corridor that favours smoke migration towards the particle surface.
- The fraction of oxide emitted as smoke and the NO_x emissions increase with the initial fuel particle size. In order to reduce potential oxide leakage and the emission of harmful pollutants, smaller aluminum particles should be considered in metal combustors.

7.2 Outlook

In this section, we collect a few ideas that came up during our research reported in this thesis, which we believe may be relevant to look at in the future in order to improve our understanding of metal-fuelled flames, particularly using aluminum. Besides the fact that more experimental investigations and measurements of the aluminum combustion process, necessarily including the smoke droplet size distribution, are needed to support the validation of physical models, in our opinion, there are still some open aspects on the numerical and modelling part that are briefly summarized here.

Aluminum particle cloud Although our single particle combustion model is capable of predicting the smoke dynamics in the vicinity of a fuel particle and estimating the smoke deposition fluxes in terms of the particle temperature and oxide fraction (or surface area of the oxide cap), for example, it was shown that the oxide smoke fraction is considerably smaller in metal dust flames [157]. We surmise that the presence of other fuel particles that feature a substantial oxide cap or are already completely burned serve as smoke collectors, since the droplet mass fluxes were shown to be larger on the oxide part of the fuel particle's surface (Chapter 5). Accompanying the further development of metal dust models, it may also be of interest to shed light on the effect the existence of multiple particles has on the smoke migration by considering a multiple particle arrangement with several spatially resolved metal fuel particles inside the flow domain.

Droplet charging In Section 4.6.1, we concluded that the charging of the smoke droplets, possibly due to thermionic emissions and chemionization reactions, and the associated electrostatic repulsion between colliding droplets could be responsible for coagulation to become ineffective. In our opinion, it is key to understand this potential mechanism better as it strongly controls the smoke dispersion in the vicinity of a fuel particle. Concretely, the effect of droplet charging may be accounted for by augmenting the coagulation enhancement factors (Section A.2) following the theoretical work of Savel'ev and Starik [149] or by considering the droplet charge as another independent variable which ultimately renders the PBE bivariate.

Numerical solution schemes Also on part of the numerical solution schemes that are used to solve the governing equations, there is still potential for alternative, possibly more accurate, methods. First, the first order accurate fractional time stepping [128] we introduced in Section 2.5 could be replaced by a second order fractional time stepping [171], for example. Although the employed scheme is frequently used in the combustion community, yields reasonably accurate results and can be efficiently implemented, it may be of interest to look into higher order schemes as well. Second, the scheme to decouple droplet formation and gas phase chemistry (strategy 4) discussed in Section 4.5.2 still only takes into account the species consumption due to nucleation in the chemistry fractional step and solves for the change in supersaturation brought about by droplet growth or dissociation subsequently. A more direct coupling of droplet formation and chemistry should improve the method's stability. Here, the key challenge is to find a reasonable and straightforward rule how to redistribute the condensed or dissociated droplet mass among the discrete number densities. This step is necessary since, during the chemistry fractional step, we are only able to compute the overall mass exchanged between the droplets and the gas associated with condensation or dissociation. In the subsequent PBE fractional step, there is no information about how to distribute the prescribed droplet mass change within the droplet population.

Informing point-particle descriptions The investigations reported in this thesis are indispensable for understanding the chemical conversion, heat release and smoke inception on the smallest scales and estimating the size distribution of the oxide smoke. However, power density, pollutant emission and performance are macroscopic properties of a metal dust combustor, which can only be predicted on the level of a metal dust flame. At the moment, these metal dust models [157] rely on point-particle descriptions that are limited to simplified boundary layer models that typically invoke assumptions on constant transport properties, a unity Lewis number and reactive passivity and neglect the particulate nature of the smoke. Even though using single particle models as detailed as the one proposed in this work is computationally prohibitive, we ought to use the information gained from resolving the boundary layer to inform point-particle methods with heat and mass transfer rates given the particle's degrees of freedom and the free-stream conditions, in order to improve their predictive capabilities.

Transferability to other metals At this point, we ought to emphasize once again that the PBE-based modelling framework proposed in this thesis may straightforwardly be adapted to other metal fuels, provided the required material properties are known. It would definitely be interesting to consider other metal fuels that tend to produce volatile oxides such as lithium, beryllium or magnesium, for instance.

PBE-PDF framework for spatially inhomogeneous configurations Lastly, the preliminary PBE-PDF modelling framework proposed in Chapter 6 needs to be extended to accommodate spatially inhomogeneous transport phenomena in order for it to be capable of predicting the combustion behaviour in more realistic flow configurations. Here, looking into the interaction of two or multiple PaSRs may constitute a first step towards the formulation of a spatially inhomogeneous *pdf* transport equation.

Bibliography

- [1] J. Adánez and A. Abad. “Chemical-looping combustion: Status and research needs”. In: *Proceedings of the Combustion Institute* 37.4 (2019), pp. 4303–4317.
- [2] J. Adanez, A. Abad, F. Garcia-Labiano, P. Gayan, and L. F. de Diego. “Progress in Chemical-Looping Combustion and Reforming technologies”. In: *Progress in Energy and Combustion Science* 38.2 (2012), pp. 215–282.
- [3] P. Akridis. “Coupled CFD-Population Balance Modelling of Soot Formation in Laminar and Turbulent Flames”. PhD thesis. Department of Mechanical Engineering, Imperial College London, UK, 2016.
- [4] M. K. Alam. “The Effect of van der Waals and Viscous Forces on Aerosol Coagulation”. In: *Aerosol Science and Technology* 6.1 (1987), pp. 41–52.
- [5] P. Atkins, J. de Paula, and J. Keeler. *Atkins’ Physical Chemistry*. 11th ed. Oxford University Press, UK, 2017.
- [6] A. Azhagurajan, N. Selvakumar, and T. L. Thanulingam. “Thermal and sensitivity analysis of nano aluminium powder for firework application”. In: *Journal of Thermal Analysis and Calorimetry* 105.1 (2011), pp. 259–267.
- [7] V. A. Babuk and V. A. Vasilyev. “Model of Aluminum Agglomerate Evolution in Combustion Products of Solid Rocket Propellant”. In: *Journal of Propulsion and Power* 18.4 (2002), pp. 814–823.
- [8] R. Becker and W. Döring. “Kinetische Behandlung der Keimbildung in übersättigten Dämpfen”. In: *Annalen der Physik* 24.5 (1935), pp. 719–752.
- [9] M. W. Beckstead. *A Summary of Aluminum Combustion*. Technical Report, No. RTO-EN-023. Brigham Young University, Provo, Utah, USA, 2004.
- [10] M. W. Beckstead. “Correlating Aluminum Burning Times”. In: *Combustion, Explosion and Shock Waves* 41.5 (2005), pp. 533–546.

Bibliography

- [11] M. W. Beckstead, Y. Liang, and K. V. Pudduppakkam. “Numerical Simulation of Single Aluminum Particle Combustion (Review)”. In: *Combustion, Explosion and Shock Waves* 41.6 (2005), pp. 622–638.
- [12] J. M. Bergthorson. “Recyclable metal fuels for clean and compact zero-carbon power”. In: *Progress in Energy and Combustion Science* 68 (2018), pp. 169–196.
- [13] J. M. Bergthorson, S. Goroshin, M. J. Soo, P. Julien, J. Palecka, D. L. Frost, and D. J. Jarvis. “Direct combustion of recyclable metal fuels for zero-carbon heat and power”. In: *Applied Energy* 160 (2015), pp. 368–382.
- [14] G. A. Bird. *Molecular Gas Dynamics and the Direct Simulation of Gas Flows*. Oxford Engineering Science Series 42. Oxford University Press, UK, 1994.
- [15] V. K. Bityukov, V. A. Petrov, and I. V. Smirnov. “Influence of the Melt Thermal Conductivity on Temperature Fields in Aluminum Oxide upon Heating by Concentrated Laser Radiation”. In: *High Temperature* 55.2 (2017), pp. 233–238.
- [16] M. Blander and J. L. Katz. “The Thermodynamics of Cluster Formation in Nucleation Theory”. In: *Journal of Statistical Physics* 4.1 (1972), pp. 55–59.
- [17] J. F. Blinn. “Floating-Point Tricks”. In: *IEEE Computer Graphics and Applications* 17.4 (1997), pp. 80–84.
- [18] P. Bogacki and L. F. Shampine. “A 3(2) Pair of Runge-Kutta Formulas”. In: *Applied Mathematics Letters* 2.4 (1989), pp. 321–325.
- [19] B. T. Bojko, P. E. DesJardin, and E. B. Washburn. “On modeling the diffusion to kinetically controlled burning limits of micron-sized aluminum particles”. In: *Combustion and Flame* 161.12 (2014), pp. 3211–3221.
- [20] R. W. Brankin, I. Gladwell, and L. F. Shampine. *RKSUITE release 1.0*. 1991. URL: <http://www.netlib.org/ode/rksuite/>.
- [21] P. N. Brown, G. D. Byrne, and A. C. Hindmarsh. “VODE: A Variable-Coefficient ODE Solver”. In: *SIAM Journal on Scientific and Statistical Computing* 10.5 (1989), pp. 1038–1051.
- [22] T. A. Brzustowski and I. Glassman. “Spectroscopic Investigation of Metal Combustion”. In: *Heterogeneous Combustion*. Ed. by H. G. Wolfhard, I. Glassman, and L. Green. Vol. 15. Progress in Astronautics and Rocketry. Elsevier, 1964, pp. 41–73.

- [23] P. Bucher, R. A. Yetter, F. L. Dryer, E. P. Vicenzi, T. P. Parr, and D. M. Hanson-Parr. “Condensed-phase Species Distributions about Al Particles Reacting in Various Oxidizers”. In: *Combustion and Flame* 117.1-2 (1999), pp. 351–361.
- [24] P. Bucher, L. Ernst, F. L. Dryer, R. A. Yetter, T. P. Parr, and D. M. Hanson-Parr. “Detailed Studies on the Flame Structure of Aluminum Particle Combustion”. In: *Solid Propellant Chemistry, Combustion, and Motor Interior Ballistics*. Ed. by V. Yang, T. B. Brill, and W.-Z. Ren. Vol. 185. Progress in Astronautics and Aeronautics. American Institute of Aeronautics and Astronautics, Inc., Reston, Virginia, USA, 2000, pp. 689–722.
- [25] P. Bucher, R. A. Yetter, F. L. Dryer, T. P. Parr, D. M. Hanson-Parr, and E. P. Vicenzi. “Flames structure measurement of single, isolated aluminum particles burning in air”. In: *Symposium (International) on Combustion* 26.2 (1996), pp. 1899–1908.
- [26] P. Bucher, R. A. Yetter, F. L. Dryer, T. P. Parr, and D. M. Hanson-Parr. “PLIF species and ratiometric temperature measurements of aluminum particle combustion in O₂, CO₂ and N₂O oxidizers, and comparison with model calculations”. In: *Symposium (International) on Combustion* 27.2 (1998), pp. 2421–2429.
- [27] A. Burcat and B. Ruscic. *Third Millennium Ideal Gas and Condensed Phase Thermochemical Database for Combustion with Updates from Active Thermochemical Tables*. Technical Report, No. ANL-05/20. Argonne National Laboratory, Illinois, USA, 2005. URL: <http://garfield.chem.elte.hu/Burcat/burcat.html>.
- [28] J. H. Burgoyne and F. Weinberg. “A method of analysis of a plane combustion wave”. In: *Symposium (International) on Combustion* 4.1 (1953), pp. 294–302.
- [29] L. Catoire, J.-F. Legendre, and M. Giraud. “Kinetic Model for Aluminum-Sensitized Ram Accelerator Combustion”. In: *Journal of Propulsion and Power* 19.2 (2003), pp. 196–202.
- [30] S. Chapman and T. G. Cowling. *The Mathematical Theory of Non-Uniform Gases: An Account of the Kinetic Theory of Viscosity, Thermal Conduction and Diffusion in Gases*. 3rd ed. Cambridge University Press, UK, 1990.
- [31] M. W. Chase. “NIST-JANAF Thermochemical Tables Part I, Al-Co”. In: *Journal of Physical and Chemical Reference Data* (1998), pp. 59–173.

Bibliography

- [32] J.-Y. Chen. “Stochastic Modeling of Partially Stirred Reactors”. In: *Combustion Science and Technology* 122.1-6 (1997), pp. 63–94.
- [33] S. Y. Cho, R. A. Yetter, and F. L. Dryer. “A Computer Model for One-Dimensional Mass and Energy Transport in and around Chemically Reacting Particles, Including Complex Gas-Phase Chemistry, Multicomponent Molecular Diffusion, Surface Evaporation, and Heterogeneous Reaction”. In: *Journal of Computational Physics* 102.1 (1992), pp. 160–179.
- [34] M. E. Coltrin, R. J. Kee, F. M. Rupley, and E. Meeks. *SURFACE CHEMKIN-III: A Fortran Package for Analyzing Heterogeneous Chemical Kinetics at a Solid-surface – Gas-phase Interface*. Technical report, No. SAND96-8217. Sandia National Laboratories, Livermore, California, USA, 1996.
- [35] W. G. Courtney. “Remarks on Homogeneous Nucleation”. In: *The Journal of Chemical Physics* 35.6 (1961), pp. 2249–2250.
- [36] P. Debiagi, R. C. Rocha, A. Scholtissek, J. Janicka, and C. Hasse. “Iron as a sustainable chemical carrier of renewable energy: Analysis of opportunities and challenges for retrofitting coal-fired power plants”. In: *Renewable and Sustainable Energy Reviews* 165 (2022), p. 112579.
- [37] L. T. DeLuca, L. Galfetti, G. Colombo, F. Maggi, A. Bandera, V. A. Babuk, and V. P. Sinditskii. “Microstructure Effects in Aluminized Solid Rocket Propellants”. In: *Journal of Propulsion and Power* 26.4 (2010), pp. 724–732.
- [38] B. V. Derjaguin and Y. Yalamov. “Theory of thermophoresis of large aerosol particles”. In: *Journal of Colloid Science* 20.6 (1965), pp. 555–570.
- [39] L. Dombrovsky. *Near-infrared properties of droplets of aluminum oxide melt*. 2010. URL: <https://www.thermopedia.com/content/149>.
- [40] E. L. Dreizin. “On the Mechanism of Asymmetric Aluminum Particle Combustion”. In: *Combustion and Flame* 117.4 (1999), pp. 841–850.
- [41] B. P. M. Duarte and C. M. S. G. Baptista. “Moving Finite Elements Method Applied to Dynamic Population Balance Equations”. In: *AIChE Journal* 54.3 (2008), pp. 673–692.

- [42] R. Duval, A. Soufiani, and J. Taine. “Coupled radiation and turbulent multiphase flow in an aluminised solid propellant rocket engine”. In: *Journal of Quantitative Spectroscopy and Radiative Transfer* 84.4 (2004), pp. 513–526.
- [43] A. Einstein. “Eine neue Bestimmung der Moleküldimensionen”. PhD thesis. Hohe Philosophische Fakultät, Universität Zürich, Switzerland, 1905.
- [44] N. Eisenreich, H. Fietzek, M. del Mar Juez-Lorenzo, V. Kolarik, A. Koleczko, and V. Weiser. “On the Mechanism of Low Temperature Oxidation for Aluminum Particles down to the Nano-Scale”. In: *Propellants, Explosives, Pyrotechnics* 29.3 (2004), pp. 137–145.
- [45] V. P. Elyutin, B. S. Mitin, and Y. S. Anisimov. “Surface tension and density of Al_2O_3 -BeO melts”. In: *Izvestiya Akademii Nauk SSSR, Neorganicheskie Materialy* 9.9 (1973), pp. 1585–1587.
- [46] V. N. Emelyanov, I. V. Teterina, and K. N. Volkov. “Dynamics and combustion of single aluminium agglomerate in solid propellant environment”. In: *Acta Astronautica* 176 (2020), pp. 682–694.
- [47] A. Faghri and Y. Zhang. *Fundamentals of Multiphase Heat Transfer and Flow*. Springer Nature, Switzerland, 2020.
- [48] L. Farkas. “Keimbildungsgeschwindigkeit in übersättigten Dämpfen”. In: *Zeitschrift für Physikalische Chemie* 125.1 (1927), pp. 236–242.
- [49] J. H. Ferziger, M. Perić, and R. L. Street. *Computational Methods for Fluid Dynamics*. 4th ed. Springer Nature, Switzerland, 2020.
- [50] J. Finke. “An integrative approach for investigating the precipitation of aluminum oxide near a burning aluminum particle”. Master’s thesis. Institute of Mechanics and Adaptronics, Technische Universität Braunschweig, 2021.
- [51] J. Finke. “Modelling of aluminum oxide formation using a population balance approach”. Student research project. Institute of Solid Mechanics/Institute of Mechanics and Adaptronics, Technische Universität Braunschweig, 2020.
- [52] J. Finke and F. Sewerin. “A combined PBE-CFD approach for modelling the formation and dispersion of oxide smoke in homogeneous aluminum combustors and around a burning aluminum particle”. In: *Proceedings of the 11th European Com-*

Bibliography

- bustion Meeting* (2023), pp. 1826–1831. URL: https://nuage.insa-rouen.fr/index.php/s/kwmTR2jWJHjJ6SS/download/ECM2023_Proceedings.pdf.
- [53] J. Finke and F. Sewerin. “A population balance approach for predicting the size distribution of oxide smoke near a burning aluminum particle”. In: *Combustion and Flame* 265 (2024), p. 113464.
- [54] J. Finke and F. Sewerin. “An unsteady PBE-CFD analysis of the asymmetric smoke-laden flame around a burning aluminum particle”. In: *Proceedings of the Combustion Institute* 40.1-4 (2024), p. 105564.
- [55] J. Finke and F. Sewerin. “Combining a population balance approach with detailed chemistry to model the condensation of oxide smoke during aluminum combustion in spatially homogeneous reactors”. In: *Combustion and Flame* 248 (2023), p. 112510.
- [56] R. H. French. “Origins and Applications of London Dispersion Forces and Hamaker Constants in Ceramics”. In: *Journal of the American Ceramic Society* 83.9 (2000), pp. 2117–2146.
- [57] J. Frenkel. *Kinetic Theory of Liquids*. Ed. by R. H. Fowler, P. Kapitza, and N. F. Mott. The International Series of Monographs on Physics. Oxford University Press, UK, 1947.
- [58] S. K. Friedlander. *Smoke, Dust, and Haze: Fundamentals of Aerosol Dynamics*. 2nd ed. Oxford University Press, UK, 2000.
- [59] S. Gallier, J.-G. Kratz, N. Quaglia, and G. Fouin. “Detailed analysis of a quench bomb for the study of aluminum agglomeration in solid propellants”. In: *Progress in Propulsion Physics* 8 (2016), pp. 197–212.
- [60] S. Gallier, A. Braconnier, F. Godfroy, F. Halter, and C. Chauveau. “The role of thermophoresis on aluminum oxide lobe formation”. In: *Combustion and Flame* 228 (2021), pp. 142–153.
- [61] C. Gardiner. *Stochastic Methods: A Handbook for the Natural and Social Sciences*. 4th ed. Springer Series in Synergetics. Springer-Verlag Berlin Heidelberg, Germany, 2009.

- [62] A. Garmory and E. Mastorakos. “Aerosol nucleation and growth in a turbulent jet using the Stochastic Fields method”. In: *Chemical Engineering Science* 63.16 (2008), pp. 4078–4089.
- [63] S. L. Girshick and C.-P. Chiu. “Kinetic nucleation theory: A new expression for the rate of homogeneous nucleation from an ideal supersaturated vapor”. In: *The Journal of Chemical Physics* 93.2 (1990), pp. 1273–1277.
- [64] P. Glarborg, J. A. Miller, B. Ruscic, and S. J. Klippenstein. “Modeling nitrogen chemistry in combustion”. In: *Progress in Energy and Combustion Science* 67 (2018), pp. 31–68.
- [65] I. Glassman. “Combustion of metals: Physical considerations”. In: *Solid propellant rocket research*. Ed. by M. Summerfield. Vol. 1. Academic Press, Inc., New York, USA, 1960, pp. 253–258.
- [66] V. Glasziou, C. Chauveau, S. Courtiaud, and F. Halter. “Measurement of the temperature of burning aluminum particles using multi-spectral pyrometry”. In: *Combustion Science and Technology* 196.13 (2024), pp. 1–14.
- [67] J. Glorian. “Cinétique hétérogène pour la combustion de l’aluminium”. PhD thesis. ENSTA ParisTech, France, 2014.
- [68] J. Glorian, L. Catoire, S. Gallier, and N. Cesco. “Gas-surface thermochemistry and kinetics for aluminum particle combustion”. In: *Proceedings of the Combustion Institute* 35.2 (2015), pp. 2439–2446.
- [69] J. Glorian, S. Gallier, and L. Catoire. “On the role of heterogeneous reactions in aluminum combustion”. In: *Combustion and Flame* 168 (2016), pp. 378–392.
- [70] B. Glorieux, F. Millot, J.-C. Rifflet, and J.-P. Coutures. “Density of Superheated and Undercooled Liquid Alumina by a Contactless Method”. In: *International Journal of Thermophysics* 20.4 (1999), pp. 1085–1094.
- [71] B. Glorieux, F. Millot, and J. C. Rifflet. “Surface Tension of Liquid Alumina from Contactless Techniques”. In: *International Journal of Thermophysics* 23.5 (2002), pp. 1249–1257.

Bibliography

- [72] O. G. Glotov and V. A. Zhukov. “The Evolution of 100- μm Aluminum Agglomerates and Initially Continuous Aluminum Particles in the Flame of a Model Solid Propellant. II. Results”. In: *Combustion, Explosion, and Shock Waves* 44.6 (2008), pp. 671–680.
- [73] S. Gordon and B. J. McBride. *Computer Program for Calculation of Complex Chemical Equilibrium Compositions and Applications. I. Analysis*. Technical report, No. NASA 1311. NASA Lewis Research Center, Cleveland, Ohio, USA, 1994.
- [74] S. Gordon and B. J. McBride. *Computer Program for Calculation of Complex Chemical Equilibrium Compositions, Rocket Performance, Incident and Reflected Shocks, and Chapman-Jouguet Detonations*. Technical report, No. NASA SP-273. NASA Lewis Research Center, Cleveland, Ohio, USA, 1976.
- [75] E. Hairer and G. Wanner. *Solving Ordinary Differential Equations II: Stiff and Differential-Algebraic Problems*. 2nd ed. Springer Series in Computational Mathematics. Springer-Verlag Berlin Heidelberg, Germany, 1996.
- [76] E. Hairer, S. P. Nørsett, and G. Wanner. *Solving Ordinary Differential Equations I: Nonstiff Problems*. 2nd ed. Springer Series in Computational Mathematics. Springer-Verlag Berlin Heidelberg, Germany, 1993.
- [77] H. C. Hamaker. “The London–van der Waals attraction between spherical particles”. In: *Physica* 4.10 (1937), pp. 1058–1072.
- [78] J. Harrison and M. Q. Brewster. “Analysis of thermal radiation from burning aluminium in solid propellants”. In: *Combustion Theory and Modelling* 13.3 (2009), pp. 389–411.
- [79] C. B. Henderson. “A Proposed Combustion Scheme for the Gaseous Oxidation Reactions of Beryllium and Aluminum”. In: *Combustion Science and Technology* 1.4 (1970), pp. 275–278.
- [80] R. A. Higgins. *Engineering Metallurgy Part I: Applied Physical Metallurgy*. 6th ed. Edward Arnold, London, UK, 1993.
- [81] J. Hou, F. Simons, and R. Hinkelmann. “Improved total variation diminishing schemes for advection simulation on arbitrary grids”. In: *International Journal for Numerical Methods in Fluids* 70.3 (2012), pp. 359–382.

- [82] H. M. Hulburt and S. Katz. “Some problems in particle technology: A statistical mechanical formulation”. In: *Chemical Engineering Science* 19.8 (1964), pp. 555–574.
- [83] W. P. Jones, F. di Mare, and A. J. Marquis. *LES-BOFFIN: User’s Guide*. Technical report. Department of Mechanical Engineering, Imperial College London, UK, 2002.
- [84] P. Julien and J. M. Bergthorson. “Enabling the metal fuel economy: green recycling of metal fuels”. In: *Sustainable Energy & Fuels* 1.3 (2017), pp. 615–625.
- [85] V. I. Kalikmanov. *Nucleation Theory*. Lecture Notes in Physics 860. Springer Science+Business Media Dordrecht, Netherlands, 2013.
- [86] V. V. Karasev, A. A. Onischuk, O. G. Glotov, A. M. Baklanov, A. G. Maryasov, V. E. Zarko, V. N. Panfilov, A. I. Levykin, and K. K. Sabelfeld. “Formation of charged aggregates of Al_2O_3 nanoparticles by combustion of aluminum droplets in air”. In: *Combustion and Flame* 138.1-2 (2004), pp. 40–54.
- [87] A. Kasztankiewicz, K. Gańczyk-Specjalska, A. Zygmunt, K. Cieślak, B. Zakościelny, and T. Gołofit. “Application and properties of aluminum in rocket propellants and pyrotechnics”. In: *Journal of Elementology* 23.1 (2018).
- [88] J. L. Katz. “The Critical Supersaturations Predicted by Nucleation Theory”. In: *Journal of Statistical Physics* 2.2 (1970), pp. 137–146.
- [89] J. L. Katz and H. Wiedersich. “Nucleation Theory without Maxwell Demons”. In: *Journal of Colloid and Interface Science* 61.2 (1977), pp. 351–355.
- [90] R. J. Kee, M. E. Coltrin, P. Glarborg, and H. Zhu. *Chemically Reacting Flow: Theory, Modeling, and Simulation*. John Wiley & Sons, Inc., Hoboken, New Jersey, USA, 2017.
- [91] V.-M. Kerminen. “Simulation of Brownian Coagulation in the Presence of van der Waals Forces and Viscous Interactions”. In: *Aerosol Science and Technology* 20.2 (1994), pp. 207–214.
- [92] M. K. King. “Aluminum combustion in a solid rocket motor environment”. In: *Proceedings of the Combustion Institute* 32.2 (2009), pp. 2107–2114.

Bibliography

- [93] B. Koren. “A Robust Upwind Discretization Method for Advection, Diffusion and Source Terms”. In: *Numerical Methods for Advection-Diffusion Problems*. Ed. by C. B. Vreugdenhil and B. Koren. Vol. 45. Notes on Numerical Fluid Mechanics and Multidisciplinary Design. Vieweg Verlag, Wiesbaden, Germany, 1993, pp. 117–138.
- [94] J. Lam, D. Amans, C. Dujardin, G. Ledoux, and A.-R. Allouche. “Atomistic Mechanisms for the Nucleation of Aluminum Oxide Nanoparticles”. In: *The Journal of Physical Chemistry A* 119.33 (2015), pp. 8944–8949.
- [95] D. Langbein. “Non-retarded dispersion energy between macroscopic spheres”. In: *Journal of Physics and Chemistry of Solids* 32.7 (1971), pp. 1657–1667.
- [96] D. Langbein. “Retarded Dispersion Energy between Macroscopic Bodies”. In: *Physical Review B* 2.8 (1970), pp. 3371–3383.
- [97] D. Langbein. “Theory of Van der Waals Attraction”. In: *Springer Tracts in Modern Physics*. Ed. by M. Bhattacharya, Y. Chen, A. Fujimori, M. Getzlaff, T. Mannel, E. Mucciolo, W. C. Stwalley, and J. Yang. Vol. 72. Springer-Verlag Berlin Heidelberg, Germany, 1974, pp. 1–139.
- [98] D. Laraqui, O. Allgaier, C. Schönnenbeck, G. Leyssens, J.-F. Brillhac, R. Lomba, C. Dumand, and O. Guézet. “Experimental study of a confined premixed metal combustor: Metal flame stabilization dynamics and nitrogen oxides production”. In: *Proceedings of the Combustion Institute* 37.3 (2019), pp. 3175–3184.
- [99] B. van Leer. “Towards the Ultimate Conservative Difference Scheme. II. Monotonicity and Conservation Combined in a Second-Order Scheme”. In: *Journal of Computational Physics* 14.4 (1974), pp. 361–370.
- [100] M. Leitner, T. Leitner, A. Schmon, K. Aziz, and G. Pottlacher. “Thermophysical Properties of Liquid Aluminum”. In: *Metallurgical and Materials Transactions A* 48.6 (2017), pp. 3036–3045.
- [101] R. J. LeVeque. *Finite Volume Methods for Hyperbolic Problems*. Cambridge Texts in Applied Mathematics. Cambridge University Press, UK, 2002.
- [102] M.-C. Lin et al. “An ultrafast rechargeable aluminium-ion battery”. In: *Nature* 520.7547 (2015), pp. 324–328.

- [103] R. P. Lindstedt and S. A. Louloudi. “Joint-scalar transported PDF modeling of soot formation and oxidation”. In: *Proceedings of the Combustion Institute* 30.1 (2005), pp. 775–783.
- [104] A. Liu and S. Rigopoulos. “A conservative method for numerical solution of the population balance equation, and application to soot formation”. In: *Combustion and Flame* 205 (2019), pp. 506–521.
- [105] A. Liu, C. E. Garcia, F. Sewerin, B. A. O. Williams, and S. Rigopoulos. “Population balance modelling and laser diagnostic validation of soot particle evolution in laminar ethylene diffusion flames”. In: *Combustion and Flame* 221 (2020), pp. 384–400.
- [106] S. Louloudi. “Transported probability density function modeling of turbulent jet flames”. PhD thesis. Department of Mechanical Engineering, Imperial College London, UK, 2003.
- [107] T. S. Lundgren. “Distribution Functions in the Statistical Theory of Turbulence”. In: *The Physics of Fluids* 10.5 (1967), pp. 969–975.
- [108] A. Lyngfelt, B. Leckner, and T. Mattisson. “A fluidized-bed combustion process with inherent CO₂ separation; application of chemical-looping combustion”. In: *Chemical Engineering Science* 56.10 (2001), pp. 3101–3113.
- [109] P. Maas, M. Schiemann, V. Scherer, P. Fischer, D. Taroata, and G. Schmid. “Lithium as energy carrier: CFD simulations of LI combustion in a 100 MW slag tap furnace”. In: *Applied Energy* 227 (2018), pp. 506–515.
- [110] I. H. Malitson. “Refraction and Dispersion of Synthetic Sapphire”. In: *Journal of the Optical Society of America* 52.12 (1962), pp. 1377–1379.
- [111] M. Marion, C. Chauveau, and I. Gökalp. “Studies on the Ignition and Burning of Levitated Aluminum Particles”. In: *Combustion Science and Technology* 115.4-6 (1996), pp. 369–390.
- [112] W. H. Marlow. “Derivation of aerosol collision rates for singular attractive contact potentials”. In: *The Journal of Chemical Physics* 73.12 (1980), pp. 6284–6287.

Bibliography

- [113] W. H. Marlow. “Lifshitz–van der Waals forces in aerosol particle collisions. I. Introduction: Water droplets”. In: *The Journal of Chemical Physics* 73.12 (1980), pp. 6288–6295.
- [114] S. Mathur, P. K. Tondon, and S. C. Saxena. “Thermal conductivity of binary, ternary and quaternary mixtures of rare gases”. In: *Molecular Physics* 12.6 (1967), pp. 569–579.
- [115] R. McGraw. “Description of Aerosol Dynamics by the Quadrature Method of Moments”. In: *Aerosol Science and Technology* 27.2 (1997), pp. 255–265.
- [116] J. A. Meijerink and H. A. van der Vorst. “Guidelines for the usage of incomplete decompositions in solving sets of linear equations as they occur in practical problems”. In: *Journal of Computational Physics* 44.1 (1981), pp. 134–155.
- [117] J.-P. Minier. “On Lagrangian stochastic methods for turbulent polydisperse two-phase reactive flows”. In: *Progress in Energy and Combustion Science* 50 (2015), pp. 1–62.
- [118] M. F. Modest. *Radiative Heat Transfer*. 3rd ed. Academic Press, Boston, Massachusetts, USA, 2013.
- [119] D. O’Sullivan and S. Rigopoulos. “A conservative finite volume method for the population balance equation with aggregation, fragmentation, nucleation and growth”. In: *Chemical Engineering Science* 263 (2022), p. 117925.
- [120] D. W. Oxtoby. “Homogeneous nucleation: theory and experiment”. In: *Journal of Physics: Condensed Matter* 4.38 (1992), pp. 7627–7650.
- [121] P.-F. Paradis and T. Ishikawa. “Surface Tension and Viscosity Measurements of Liquid and Undercooled Alumina by Containerless Techniques”. In: *Japanese Journal of Applied Physics* 44.7 (2005), pp. 5082–5085.
- [122] S. H. Park, K. W. Lee, E. Otto, and H. Fissan. “The log-normal size distribution theory of Brownian aerosol coagulation for the entire particle size range: Part I—analytical solution using the harmonic mean coagulation kernel”. In: *Journal of Aerosol Science* 30.1 (1999), pp. 3–16.

- [123] S. V. Patankar. *Numerical Heat Transfer and Fluid Flow*. Series in Computational Methods in Mechanics and Thermal Sciences. Hemisphere Publishing Corporation, Washington, D.C., USA, 1980.
- [124] G. A. Pavliotis. *Stochastic Processes and Applications: Diffusion Processes, the Fokker-Planck and Langevin Equations*. Vol. 60. Texts in Applied Mathematics. Springer Science+Business Media New York City, New York, USA, 2014.
- [125] M. Perez, M. Dumont, and D. Acevedo-Reyes. “Implementation of classical nucleation and growth theories for precipitation”. In: *Acta Materialia* 56.9 (2008), pp. 2119–2132.
- [126] T. Poinsoot and D. Veynante. *Theoretical and Numerical Combustion*. 3rd. ed. Edited by T. Poinsoot, 2011.
- [127] N. I. Poletaev. “Formation of Condensed Combustion Products in Metal Dust Flames: Nucleation Stage”. In: *Combustion, Explosion, and Shock Waves* 51.3 (2015), pp. 299–312.
- [128] S. B. Pope. “PDF methods for turbulent reactive flows”. In: *Progress in Energy and Combustion Science* 11.2 (1985), pp. 119–192.
- [129] S. M. Pourmortazavi, S. S. Hajimirsadeghi, I. Kohsari, M. Fathollahi, and S. G. Hosseini. “Thermal decomposition of pyrotechnic mixtures containing either aluminum or magnesium powder as fuel”. In: *Fuel* 87.2 (2008), pp. 244–251.
- [130] S. E. Pratsinis. “Simultaneous Nucleation, Condensation, and Coagulation in Aerosol Reactors”. In: *Journal of Colloid and Interface Science* 124.2 (1988), pp. 416–427.
- [131] J. L. Prentice and L. S. Nelson. “Differences between the Combustion of Aluminum Droplets in Air and in an Oxygen-Argon Mixture”. In: *Journal of the Electrochemical Society* 115.8 (1968), pp. 809–812.
- [132] S. Qamar, M. P. Elsner, I. A. Angelov, G. Warnecke, and A. Seidel-Morgenstern. “A comparative study of high resolution schemes for solving population balances in crystallization”. In: *Computers & Chemical Engineering* 30.6-7 (2006), pp. 1119–1131.
- [133] D. Ramkrishna. *Population Balances: Theory and Applications to Particulate Systems in Engineering*. Academic Press, San Diego, California, USA, 2000.

Bibliography

- [134] I. Ranc-Darbord, G. Baudin, M. Genetier, D. Ramel, P. Vasseur, J. Legrand, and V. Pina. “Emission of Gas and Al_2O_3 Smoke in Gas-Al Particle Deflagration: Experiments and Emission Modeling for Explosive Fireballs”. In: *International Journal of Thermophysics* 39.3 (2018), p. 36.
- [135] R. Reed and V. Calia. “Review of Aluminum Oxide Rocket Exhaust Particles”. In: *AIAA 28th Thermophysics Conference Meeting Paper* (1993), p. 2819.
- [136] D. Reguera. “Nucleation phenomena: The non-equilibrium kinetics of phase change”. In: *Contributions to Science* 11.2 (2015), pp. 173–180.
- [137] D. Reguera and J. M. Rubí. “Non-equilibrium Thermodynamics for Nucleation Kinetics”. In: *Experimental Thermodynamics Volume X: Non-equilibrium Thermodynamics with Applications*. Ed. by D. Bedeaux, S. Kjelstrup, and J. V. Sengers. The Royal Society of Chemistry, Cambridge, UK, 2015, pp. 314–337.
- [138] H. Reiss, W. K. Kegel, and J. L. Katz. “Resolution of the Problems of Replacement Free Energy, $1/S$, and Internal Consistency in Nucleation Theory by Consideration of the Length Scale for Mixing Entropy”. In: *Physical Review Letters* 78.23 (1997), pp. 4506–4509.
- [139] H. Reiss, W. K. Kegel, and J. L. Katz. “Role of the Model Dependent Translational Volume Scale in the Classical Theory of Nucleation”. In: *The Journal of Physical Chemistry A* 102.44 (1998), pp. 8548–8555.
- [140] S. Rigopoulos. “PDF method for population balance in turbulent reactive flow”. In: *Chemical Engineering Science* 62.23 (2007), pp. 6865–6878.
- [141] S. Rigopoulos and A. G. Jones. “Finite-Element Scheme for Solution of the Dynamic Population Balance Equation”. In: *AIChE Journal* 49.5 (2003), pp. 1127–1139.
- [142] C. Ruan, Z. Wu, J. Sun, N. Jüngst, E. Berrocal, M. Aldén, and Z. Li. “Ignition, stabilization and particle-particle collision in lifted aluminum particle cloud flames”. In: *Proceedings of the Combustion Institute* 40.1-4 (2024), p. 105596.
- [143] M. Saba, T. Kato, and T. Oguchi. “Reaction modeling study on the combustion of aluminum in gas phase: The $\text{Al} + \text{O}_2$ and related reactions”. In: *Combustion and Flame* 225 (2021), pp. 535–550.

- [144] V. Sabel'nikov and O. Soulard. "Rapidly decorrelating velocity-field model as a tool for solving one-point Fokker-Planck equations for probability density functions of turbulent reactive scalars". In: *Physical Review E* 72.1 (2005), p. 016301.
- [145] M. Salita. "Deficiencies and Requirements in Modeling of Slag Generation in Solid Rocket Motors". In: *Journal of Propulsion and Power* 11.1 (1995), pp. 10–23.
- [146] V. Sarou-Kanian, F. Millot, and J.-C. Rifflet. "Surface Tension and Density of Oxygen-Free Liquid Aluminum at High Temperature". In: *International Journal of Thermophysics* 24.1 (2003), pp. 277–286.
- [147] A. M. Savel'ev and A. M. Starik. "An improved model of homogeneous nucleation for high supersaturation conditions: aluminum vapor". In: *Physical Chemistry Chemical Physics* 19.1 (2017), pp. 523–538.
- [148] A. M. Savel'ev and A. M. Starik. "The formation of $(\text{Al}_2\text{O}_3)_n$ clusters as a probable mechanism of aluminum oxide nucleation during the combustion of aluminized fuels: Numerical analysis". In: *Combustion and Flame* 196 (2018), pp. 223–236.
- [149] A. M. Savel'ev and A. M. Starik. "On Coagulation Mechanisms of Charged Nanoparticles Produced by Combustion of Hydrocarbon and Metallized Fuels". In: *Journal of Experimental and Theoretical Physics* 108.2 (2009), pp. 326–339.
- [150] A. M. Savel'ev and D. A. Yagodnikov. "Mechanism of Electric Charging of Aluminum Oxide Particles When Burning Solid Fuels". In: *Journal of Propulsion and Power* 38.5 (2022), pp. 771–782.
- [151] M. Schiemann, J. Bergthorson, P. Fischer, V. Scherer, D. Taroata, and G. Schmid. "A review on lithium combustion". In: *Applied Energy* 162 (2016), pp. 948–965.
- [152] A. Schmidt-Ott and H. Burtscher. "The Effect of van der Waals Forces on Aerosol Coagulation". In: *Journal of Colloid and Interface Science* 89.2 (1982), pp. 353–357.
- [153] J. H. Seinfeld and S. N. Pandis. *Atmospheric Chemistry and Physics: From Air Pollution to Climate Change*. 3rd ed. John Wiley & Sons, Inc., Hoboken, New Jersey, USA, 2016.

Bibliography

- [154] F. Sewerin. “A Eulerian Monte Carlo method for the numerical solution of the multivariate population balance equation”. In: *Journal of Computational Physics* 509 (2024), p. 113024.
- [155] F. Sewerin. “A methodology for solving the population balance equation based on an embedded reduced order representation”. In: *Chemical Engineering Science* 252 (2022), p. 117101.
- [156] F. Sewerin. “An efficient implementation of a conservative finite volume scheme with constant and linear reconstructions for solving the coagulation equation”. In: *Chemical Engineering Science* (2023), p. 119020.
- [157] F. Sewerin and J. Finke. “A Eulerian population balance/Monte Carlo approach for simulating laminar aluminum dust flames”. In: *Particuology* 88 (2024), pp. 323–343.
- [158] F. Sewerin and S. Rigopoulos. “Algorithmic Aspects of the LES-PBE-PDF Method for Modeling Soot Particle Size Distributions in Turbulent Flames”. In: *Combustion Science and Technology* 191.5-6 (2019), pp. 766–796.
- [159] F. Sewerin and S. Rigopoulos. “An explicit adaptive grid approach for the numerical solution of the population balance equation”. In: *Chemical Engineering Science* 168 (2017), pp. 250–270.
- [160] F. Sewerin and S. Rigopoulos. “An LES-PBE-PDF approach for predicting the soot particle size distribution in turbulent flames”. In: *Combustion and Flame* 189 (2018), pp. 62–76.
- [161] E. E. Shpilrain and K. Yakimovich. “Experimental study of the density of liquid alumina up to 2750 C”. In: *High Temperatures - High Pressures* 5.2 (1973), pp. 191–198.
- [162] H. Sinn, B. Glorieux, L. Hennet, A. Alatas, M. Hu, E. E. Alp, F. J. Bermejo, D. L. Price, and M.-L. Saboungi. “Microscopic Dynamics of Liquid Aluminum Oxide”. In: *Science* 299.5615 (2003), pp. 2047–2049.
- [163] M. von Smoluchowski. “Drei Vorträge über Diffusion, Brownsche Molekularbewegung und Koagulation von Kolloidteilchen”. In: *Physikalische Zeitschrift* 17 (1916), pp. 557–571, 587–599.

- [164] M. von Smoluchowski. “Versuch einer mathematischen Theorie der Koagulationskinetik kolloider Lösungen”. In: *Zeitschrift für Physikalische Chemie* 92.1 (1917), pp. 129–168.
- [165] L. A. Spielman. “Viscous Interactions in Brownian Coagulation”. In: *Journal of Colloid and Interface Science* 33.4 (1970), pp. 562–571.
- [166] A. M. Starik, A. M. Savel’ev, and N. S. Titova. “Specific Features of Ignition and Combustion of Composite Fuels Containing Aluminum Nanoparticles (Review)”. In: *Combustion, Explosion, and Shock Waves* 51.2 (2015), pp. 197–222.
- [167] V. B. Storozhev and A. N. Yermakov. “On the Interplay of Chemical and Physical Processes during the Combustion of Aluminum in Water Vapor”. In: *Russian Journal of Physical Chemistry B* 8.5 (2014), pp. 672–679.
- [168] V. B. Storozhev. Private communication. 2020.
- [169] V. B. Storozhev and A. N. Yermakov. “Combustion of nano-sized aluminum particles in steam: Numerical modeling”. In: *Combustion and Flame* 162.11 (2015), pp. 4129–4137.
- [170] V. B. Storozhev and A. N. Yermakov. “Effect of suboxides on dynamics of combustion of aluminum nanopowder in water vapor: Numerical estimate”. In: *Combustion and Flame* 190 (2018), pp. 103–111.
- [171] G. Strang. “On the construction and comparison of difference schemes”. In: *SIAM Journal on Numerical Analysis* 5.3 (1968), pp. 506–517.
- [172] D. S. Sundaram, P. Puri, and V. Yang. “A general theory of ignition and combustion of nano- and micron-sized aluminum particles”. In: *Combustion and Flame* 169 (2016), pp. 94–109.
- [173] S. Suzuki, K. Kuwana, and R. Dobashi. “Effect of particle morphology on thermophoretic velocity of aggregated soot particles”. In: *International Journal of Heat and Mass Transfer* 52.21-22 (2009), pp. 4695–4700.
- [174] M. T. Swihart and L. Catoire. “Thermochemistry of Aluminum Species for Combustion Modeling from Ab Initio Molecular Orbital Calculations”. In: *Combustion and Flame* 121.1-2 (2000), pp. 210–222.

Bibliography

- [175] M. T. Swihart, L. Catoire, B. Legrand, I. Gökalp, and C. Paillard. “Rate constants for the homogeneous gas-phase Al/HCl combustion chemistry”. In: *Combustion and Flame* 132.1-2 (2003), pp. 91–101.
- [176] L. Talbot, R. K. Cheng, R. W. Schefer, and D. R. Willis. “Thermophoresis of particles in a heated boundary layer”. In: *Journal of Fluid Mechanics* 101.4 (1980), pp. 737–758.
- [177] L. C. Thijs, C. E. A. G. van Gool, W. J. S. Ramaekers, J. A. van Oijen, and L. P. H. de Goey. “Resolved simulations of single iron particle combustion and the release of nano-particles”. In: *Proceedings of the Combustion Institute* 39.3 (2023), pp. 3551–3559.
- [178] Y. S. Touloukian, R. W. Powell, C. Y. Ho, and P. G. Klemms. *Thermal Conductivity: Metallic Elements and Alloys*. Thermophysical Properties of Matter: The TPRC Data Series. Volume 1. Purdue Research Foundation, IFI/Plenum Data Corporation, New York City, New York, USA, 1970.
- [179] K. A. Trowell, S. Goroshin, D. L. Frost, and J. M. Bergthorson. “Aluminum and its role as a recyclable, sustainable carrier of renewable energy”. In: *Applied Energy* 275 (2020), p. 115112.
- [180] H. Vehkamäki. *Classical Nucleation Theory in Multicomponent Systems*. Springer-Verlag Berlin Heidelberg, Germany, 2006.
- [181] G. di Veroli and S. Rigopoulos. “Modeling of Turbulent Precipitation: A Transported Population Balance-PDF Method”. In: *AIChE Journal* 56.4 (2010), pp. 878–892.
- [182] V. I. Vishnyakov, G. S. Dragan, and A. V. Florko. “The Formation of Negatively Charged Particles in Thermoemission Plasmas”. In: *Journal of Experimental and Theoretical Physics* 106.1 (2008), pp. 182–186.
- [183] M. Volmer and A. Weber. “Keimbildung in übersättigten Gebilden”. In: *Zeitschrift für Physikalische Chemie* 119.1 (1926), pp. 277–301.
- [184] H. A. van der Vorst. “Bi-CGSTAB: A Fast and Smoothly Converging Variant of Bi-CG for the Solution of Nonsymmetric Linear Systems”. In: *SIAM Journal on Scientific and Statistical Computing* 13.2 (1992), pp. 631–644.

- [185] J. Wang, N. Wang, X. Zou, W. Yu, and B. Shi. “Modeling of micro aluminum particle combustion in multiple oxidizers”. In: *Acta Astronautica* 189 (2021), pp. 119–128.
- [186] J. Warnatz. “Influence of Transport Models and Boundary Conditions on Flame Structure”. In: *Numerical Methods in Laminar Flame Propagation*. Ed. by N. Peters and J. Warnatz. Vol. 6. Notes on Numerical Fluid Mechanics. Springer Fachmedien Wiesbaden, Germany, 1982, pp. 87–111.
- [187] E. B. Washburn, J. A. Webb, and M. W. Beckstead. “The simulation of the combustion of micrometer-sized aluminum particles with oxygen and carbon dioxide”. In: *Combustion and Flame* 157.3 (2010), pp. 540–545.
- [188] C. R. Wilke. “A Viscosity Equation for Gas Mixtures”. In: *The Journal of Chemical Physics* 18.4 (1950), pp. 517–519.
- [189] F. A. Williams. *Combustion Theory: The Fundamental Theory of Chemically Reacting Flow Systems*. 2nd ed. Combustion Science and Engineering Series. The Benjamin/Cummings Publishing Company, Inc., Menlo Park, California, USA, 1985.
- [190] N. Yilmaz, B. Donaldson, and W. Gill. “Aluminum Particle Ignition Studies with Focus on Effect of Oxide Barrier”. In: *Aerospace* 10.1 (2023), p. 45.
- [191] F. J. Zeleznik and S. Gordon. “Calculation of complex chemical equilibria”. In: *Industrial & Engineering Chemistry* 60.6 (1968), pp. 27–57.

Ehrenerklärung

Ich versichere hiermit, dass ich die vorliegende Arbeit vollständig ohne unzulässige Hilfe Dritter und ohne Benutzung anderer als der angegebenen Hilfsmittel angefertigt habe.

Alle verwendeten fremden und eigenen Quellen sind als solche kenntlich gemacht und im Falle einer Ko-Autorenschaft, insbesondere im Rahmen einer kumulativen Dissertation, ist der Eigenanteil richtig und vollständig ausgewiesen. Insbesondere habe ich nicht die Hilfe einer kommerziellen Promotionsberaterin/eines kommerziellen Promotionsberaters in Anspruch genommen. Dritte haben von mir weder unmittelbar noch mittelbar geldwerte Leistungen für Arbeiten erhalten, die im Zusammenhang mit dem Inhalt der vorgelegten Dissertation stehen.

Ich habe insbesondere nicht wissentlich:

- Ergebnisse erfunden oder widersprüchliche Ergebnisse verschwiegen,
- statistische Verfahren absichtlich missbraucht, um Daten in ungerechtfertigter Weise zu interpretieren,
- fremde Ergebnisse oder Veröffentlichungen plagiiert,
- fremde Forschungsergebnisse verzerrt wiedergegeben.

Mir ist bekannt, dass Verstöße gegen das Urheberrecht Unterlassungs- und Schadensersatzansprüche der Urheberin/des Urhebers sowie eine strafrechtliche Ahndung durch die Strafverfolgungsbehörden begründen können.

Ich erkläre mich damit einverstanden, dass die Dissertation ggf. mit Mitteln der elektronischen Datenverarbeitung auf Plagiate überprüft werden kann.

Die Arbeit wurde bisher weder im Inland noch im Ausland in gleicher oder ähnlicher Form als Dissertation eingereicht und ist als Ganzes auch noch nicht veröffentlicht.

Magdeburg, 12.12.2024

Jannis Finke

List of Publications

The author declares that parts of this thesis are taken from the publications listed below.

- **J. Finke** and F. Sewerin. “An unsteady PBE-CFD analysis of the asymmetric smoke-laden flame around a burning aluminum particle”. In: *Proceedings of the Combustion Institute* 40 (2024), p. 105564.
- **J. Finke** and F. Sewerin. “A population balance approach for predicting the size distribution of oxide smoke near a burning aluminum particle”. In: *Combustion and Flame* 265 (2024), p. 113464.
- **J. Finke** and F. Sewerin. “A combined PBE-CFD approach for modelling the formation and dispersion of oxide smoke in homogeneous aluminum combustors and around a burning aluminum particle”. In: *Proceedings of the 11th European Combustion Meeting* (2023), pp. 1826–1831.
- **J. Finke** and F. Sewerin. “Combining a population balance approach with detailed chemistry to model the condensation of oxide smoke during aluminum combustion in spatially homogeneous reactors”. In: *Combustion and Flame* 248 (2023), p. 112510.

Appendices

Appendix A

Droplet formation kinetics

A.1 Changes in the chemical potential during gas-to-liquid phase transitions

Following Kalikmanov [85, Chapter 3] and Vehkamäki [180, Chapter 2], the difference between the chemical potential μ_v^i of a bulk gas molecule of substance i [J] and the chemical potential of a bulk liquid molecule μ_l^i is controlled by the thermal state (p, T) as well as the mole fraction X_i of gas species i ,

$$\Delta\mu^i = \mu_v^i(p, X_i, T) - \mu_l^i(p, T). \quad (\text{A.1})$$

In a vapour that is supersaturated with respect to species i , $\Delta\mu^i$ is positive, rendering the conversion into bulk liquid energetically favourable. Since, in our case, the bulk liquid phase consists of pure $\text{Al}_2\text{O}_3(\text{l})$, the chemical potential $\mu_l^i(p, T)$ for $i = \text{Al}_2\text{O}_3(\text{l})$ coincides with that of the pure substance, $\mu_l^i(p, T) = \mu_l^{i,\text{pure}}(p, T)$. In a multicomponent ideal gas, moreover, every component i behaves as if it were alone at pressure $p_v^i = X_i p$, whence μ_v^i may be approximated in terms of the chemical potential of the pure gaseous substance i , $\mu_v^i(p, X_i, T) \approx \mu_v^{i,\text{pure}}(p_v^i, T)$, leading to

$$\Delta\mu^i = \mu_v^{i,\text{pure}}(p_v^i, T) - \mu_l^{i,\text{pure}}(p, T). \quad (\text{A.2})$$

Since, in the remainder of this section, we focus on species $i = \text{Al}_2\text{O}_3$ or $i = \text{Al}_2\text{O}_3\text{c}$, the superscript i is omitted for brevity and p_v is defined as in Eq. (2.28). The chemical potentials of pure substances can be related to their thermodynamic properties which are,

A Droplet formation kinetics

however, commonly specified at the standard pressure $p_0 = 1 \text{ atm}$. In order to evaluate μ_v^{pure} and μ_l^{pure} at a pressure p_1 that may be different from p_0 , the relation [85, Chapter 2]

$$d\mu^{\text{pure}}(p, T) = -\tilde{s}_1(p, T)dT + \tilde{v}_1(p, T)dp \quad (\text{A.3})$$

obtained from the Gibbs–Duhem equation is employed. Here, \tilde{s}_1 and \tilde{v}_1 denote the entropy and the volume per molecule, respectively. Since we intend to evaluate the chemical potential only at a different pressure, maintaining the same temperature, we have $dT = 0$ and $d\mu^{\text{pure}} = \tilde{v}_1 dp$ or, upon integration over the pressure range $[p_0, p_1]$,

$$\int_{p_0}^{p_1} d\mu^{\text{pure}}(p, T) = \mu^{\text{pure}}(p_1, T) - \mu^{\text{pure}}(p_0, T) = \int_{p_0}^{p_1} \tilde{v}_1(p, T) dp. \quad (\text{A.4})$$

For an ideal vapour (subscript v), substitution of the ideal gas law $\tilde{v}_1(p, T) = k_B T/p$ gives [191]

$$\mu_v^{\text{pure}}(p_1, T) = \mu_v^{\text{pure}}(p_0, T) + k_B T \ln \left(\frac{p_1}{p_0} \right). \quad (\text{A.5})$$

Similarly, taking $\tilde{v}_1 = v_1 = \text{const.}$ in Eq. (A.4) for the liquid phase (subscript l) yields

$$\mu_l^{\text{pure}}(p_1, T) = \mu_l^{\text{pure}}(p_0, T) + v_1 (p_1 - p_0). \quad (\text{A.6})$$

By substituting Eqs. (A.5) and (A.6) with $p_1 = p_v$ and $p_1 = p$, respectively, into Eq. (A.2), we finally obtain for the change in chemical potential on transition of a pure Al_2O_3 or $\text{Al}_2\text{O}_3\text{c}$ molecule from the gaseous to the bulk liquid phase

$$\Delta\mu = \mu_v^{\text{pure}}(p_0, T) + k_B T \ln \left(\frac{p_v}{p_0} \right) - \mu_l^{\text{pure}}(p_0, T) - v_1 (p - p_0). \quad (\text{A.7})$$

Since, in the present case, bulk $\text{Al}_2\text{O}_3(1)$ may form from a vapour that encompasses the two condensing species Al_2O_3 and $\text{Al}_2\text{O}_3\text{c}$, the chemical potential of an $\text{Al}_2\text{O}_3/\text{c}$ vapour molecule is evaluated as

$$\mu_v^{\text{pure}} = \frac{X_{\text{Al}_2\text{O}_3} \mu_v^{\text{Al}_2\text{O}_3, \text{pure}} + X_{\text{Al}_2\text{O}_3\text{c}} \mu_v^{\text{Al}_2\text{O}_3\text{c}, \text{pure}}}{X_{\text{Al}_2\text{O}_3} + X_{\text{Al}_2\text{O}_3\text{c}}}. \quad (\text{A.8})$$

A.2 Theory of enhancement factors for particle collisions

For a pure species, the chemical potential coincides with the Gibbs free energy $G_\mu(p, T)$ [5, 153]; specifically, at standard pressure p_0 , we have

$$\mu^{\text{pure}}(p_0, T) = \mu^0(T) = G_\mu^0(T) = H^0(T) - TS^0(T), \quad (\text{A.9})$$

where H^0 and S^0 are the enthalpy and entropy, respectively, and the superscript 0 indicates standard pressure. H^0 and S^0 can be obtained from standard thermodynamic databases in the form of JANAF polynomials.

In a final step, the chemical potential difference in Eq. (A.7) is recast in terms of the supersaturation. For an ideal gas and an incompressible liquid at a temperature not too close to the critical point, $\Delta\mu$ and S are related according to [16, 57, 85, 180]

$$k_B T \ln S = \Delta\mu \quad \Leftrightarrow \quad S = \exp\left(\frac{\Delta\mu}{k_B T}\right). \quad (\text{A.10})$$

Inserting Eq. (A.7) into Eq. (A.10) ultimately yields Eq. (2.29) for the supersaturation S in terms of the thermal state (p, T) and the vapour pressure p_v .

A.2 Theory of enhancement factors for particle collisions

In the continuum regime, the viscous correction of the relative diffusion coefficient \mathcal{D}_{12} for two colliding particles with radii r_1 and r_2 that are a distance \tilde{r} apart is given by [4]

$$\tilde{\mathcal{D}}(\tilde{r}) = \frac{\mathcal{D}_{12}}{\mathcal{D}'_{12}} = 1 + \frac{2.6r_1r_2}{(r_1 + r_2)^2} \sqrt{\frac{r_1r_2}{(r_1 + r_2)(\tilde{r} - r_1 - r_2)}} + \frac{r_1r_2}{(r_1 + r_2)(\tilde{r} - r_1 - r_2)}. \quad (\text{A.11})$$

Here, \mathcal{D}'_{12} represents the relative particle diffusion coefficient that includes the effect of viscous retardation. Equation (A.11) is incorporated into Eq. (A.19) below for the enhancement factor \mathcal{W}^{con} in the continuum regime.

Following Friedlander [58, Chapter 7], the attractive London–van der Waals force can be derived from the London–van der Waals potential,

$$F_{\text{LvdW}}(\tilde{r}) = -\frac{d\Phi_{\text{LvdW}}(\tilde{r})}{d\tilde{r}}, \quad (\text{A.12})$$

where \tilde{r} is the distance between the centers of two particles. The London–van der Waals potential $\Phi_{\text{LvdW}}(\tilde{r})$ for two macroscopic, spherical bodies was first described by Hamaker

A Droplet formation kinetics

[77] who formulated the potential energy

$$\Phi^{\text{Ha}}(\tilde{r}) = -\frac{A_H}{6} \left(\frac{2r_1 r_2}{\tilde{r}^2 - (r_1 + r_2)^2} + \frac{2r_1 r_2}{\tilde{r}^2 - (r_1 - r_2)^2} + \ln \left(\frac{\tilde{r}^2 - (r_1 + r_2)^2}{\tilde{r}^2 - (r_1 - r_2)^2} \right) \right). \quad (\text{A.13})$$

Here, A_H is the Hamaker constant, a material parameter. For two solid alumina particles in air, the Hamaker constant is barely temperature dependent and amounts to $A_H = 165 \times 10^{-21}$ J [56], a value that we adopt also for liquid $\text{Al}_2\text{O}_3(\text{l})$. Hamaker's formula was found to describe the London–van der Waals forces only approximately as it neglects screening, retardation and many-body interactions. Retardation is, in this case, different from the viscous effect considered above and is caused by the finite speed at which an electric field propagates as well as the time frame required for the field to orientate and respond to perturbations. This inertia results in an impediment of the attractive London–van der Waals forces and weakens the interaction [152].

Based on series expansions, Langbein [95] proposed an exact solution for the non-retarded interaction energy of two spherical particles including screening. Since these expressions are impractical for numerical solution schemes [4], we employ the upper and lower limits of the London–van der Waals potential for the non-retarded case (indicated by the superscript N) which Langbein [95] provides,

$$|\Phi^N(\tilde{r})| \geq |\Phi_L^N(\tilde{r})| = |\Phi^{\text{Ha}}(\tilde{r})|, \quad (\text{A.14})$$

$$|\Phi^N(\tilde{r})| \leq |\Phi_U^N(\tilde{r})| = \left| -\frac{A_H r_1 r_2}{3} \left(\frac{1}{\tilde{r}^2 - (r_1 + r_2)^2} + \frac{1}{\tilde{r}^2 - (r_1 - r_2)^2} - \frac{2}{\tilde{r}^2 - r_1^2} - \frac{2}{\tilde{r}^2 - r_2^2} + \frac{2}{\tilde{r}^2} \right) \right|. \quad (\text{A.15})$$

For the retarded case (indicated by the superscript R), Langbein [96, 97] also derived an exact expression which was approximated by Schmidt-Ott and Burtscher [152] as

$$\Phi^R(\tilde{r}) = -\frac{C_R}{\tilde{r}} \left(\frac{\tilde{\chi}_1 \tilde{\chi}_2}{(\tilde{r} - \tilde{\chi}_1 - \tilde{\chi}_2)^2} - \frac{\tilde{\chi}_1 + \tilde{\chi}_2}{\tilde{r} - \tilde{\chi}_1 - \tilde{\chi}_2} - \ln(\tilde{r} - \tilde{\chi}_1 - \tilde{\chi}_2) \right) \Bigg|_{-r_1}^{r_1} \Bigg|_{-r_2}^{r_2}, \quad (\text{A.16})$$

where the evaluation at $\{-r_1, r_1\}$ applies to $\tilde{\chi}_1$ and the evaluation at $\{-r_2, r_2\}$ pertains to $\tilde{\chi}_2$. In Eq. (A.16), C_R is a material constant which can be evaluated by applying the continuity condition

$$\Phi^R(r_R) = \Phi^N(r_R) \quad (\text{A.17})$$

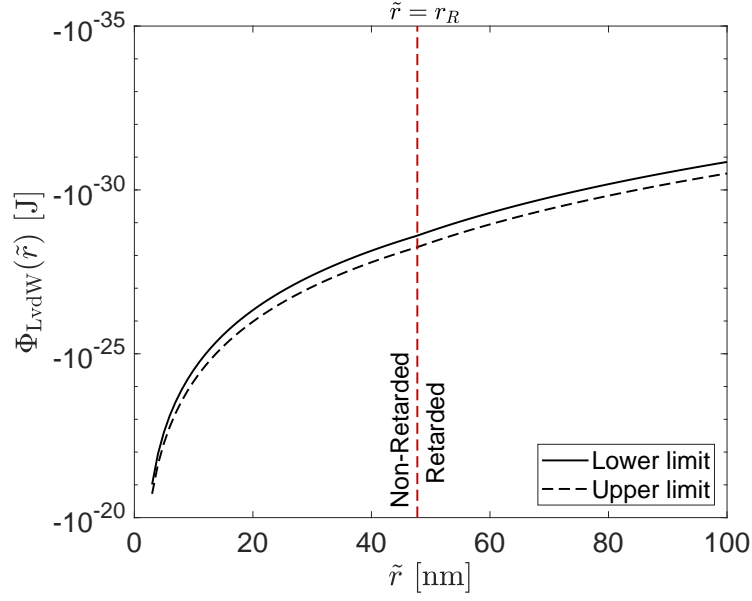


Figure A.1 Upper and lower limits of the London-van der Waals potentials for the non-retarded ($\tilde{r} < r_R$) and retarded ($\tilde{r} > r_R$) cases.

at the separation distance r_R beyond which retardation begins to be effective. According to Schmidt-Ott and Burtscher [152], the retardation distance can be roughly approximated by Planck's law yielding

$$r_R = \frac{3\hbar_P c}{4\pi A_H} + r_1 + r_2, \quad (\text{A.18})$$

where $\hbar_P = h_P/(2\pi)$ is the reduced Planck constant and c is the speed of light. Because the continuity condition in Eq. (A.17) yields a different constant C_R depending on whether Φ^R is matched with the upper or the lower limit of the non-retarded potential Φ^N , the distinction between upper and lower bounds also carries over to Φ^R . The upper and lower limits of $\Phi_{\text{LvdW}}(\tilde{r})$ for both the non-retarded ($\tilde{r} < r_R$) and the retarded ($\tilde{r} > r_R$) cases are depicted in Fig. A.1.

According to Marlow [112, 113], Schmidt-Ott and Burtscher [152] and Alam [4], the enhancement factors for the coagulation rates in the continuum and kinetic regimes may be computed, respectively, from

$$\begin{aligned} \mathcal{W}^{\text{con}}(r_1, r_2, T) = \frac{1}{r_1 + r_2} & \left(\int_{r_1+r_2}^{r_R} \frac{\tilde{\mathcal{D}}(\tilde{r})}{\tilde{r}^2} \exp\left(\frac{\Phi^N(\tilde{r})}{k_B T}\right) d\tilde{r} \right. \\ & \left. + \int_{r_R}^{\infty} \frac{\tilde{\mathcal{D}}(\tilde{r})}{\tilde{r}^2} \exp\left(\frac{\Phi^R(\tilde{r})}{k_B T}\right) d\tilde{r} \right)^{-1} \end{aligned} \quad (\text{A.19})$$

A Droplet formation kinetics

and

$$\begin{aligned}
\mathcal{W}^{\text{kin}}(r_1, r_2, T) = & - \frac{1}{2(r_1 + r_2)^2 k_B T} \\
& \times \left(\int_{r_1+r_2}^{r_R} \tilde{r}^2 \left(\frac{d\Phi^N(\tilde{r})}{d\tilde{r}} + \tilde{r} \frac{d^2\Phi^N(\tilde{r})}{d\tilde{r}^2} \right) \right. \\
& \quad \left. \exp \left(-\frac{1}{k_B T} \left(\frac{\tilde{r}}{2} \frac{d\Phi^N(\tilde{r})}{d\tilde{r}} + \Phi^N(\tilde{r}) \right) \right) d\tilde{r} \right. \\
& \quad \left. + \int_{r_R}^{\infty} \tilde{r}^2 \left(\frac{d\Phi^R(\tilde{r})}{d\tilde{r}} + \tilde{r} \frac{d^2\Phi^R(\tilde{r})}{d\tilde{r}^2} \right) \right. \\
& \quad \left. \exp \left(-\frac{1}{k_B T} \left(\frac{\tilde{r}}{2} \frac{d\Phi^R(\tilde{r})}{d\tilde{r}} + \Phi^R(\tilde{r}) \right) \right) d\tilde{r} \right). \tag{A.20}
\end{aligned}$$

In Eq. (A.19), $\tilde{D}(\tilde{r})$ is the viscous correction factor of Eq. (A.11). Some authors take into account a so-called Fuchs jump distance [91, 112] which determines the distance between two approaching particles below which the transport is governed by kinetic theory. However, since we compute the enhancement factors for both regimes separately, the Fuchs jump distance is not accounted for here. In order to render the integration limits in Eqs. (A.19) and (A.20) finite, it is advantageous to apply the integral transformation $\tilde{x} = \bar{\tilde{x}}(\tilde{r}) = r_2/\tilde{r}$, $r_2 > r_1$, with inverse Jacobian $d\tilde{r}/d\tilde{x} = -r_2/\tilde{x}^2$ [4]. Our implementation of Eqs. (A.19) and (A.20) was cross-checked by reproducing the results of Schmidt-Ott and Burtscher [152, Table 1] and approximating, based on estimates of the material parameters invoked by Alam [4], also the absolute values of the enhancement factors reported by Alam [4, Figure 7].

The computed enhancement factors are depicted in Fig. A.2 for a temperature of 3045 K. Since upper and lower limits of the interaction potentials and the enhancement factors are given, the final values are obtained as simple averages. While the van der Waals attraction promotes the coagulation of small particles in the kinetic regime ($\mathcal{W}^{\text{kin}} \geq 1$), viscous retardation dominates in the continuum regime, hindering coagulation ($\mathcal{W}^{\text{con}} \leq 1$). In both regimes, the enhancement factors become extremal for equally-sized particles. The computations were carried out in quadruple precision using a Fortran program.

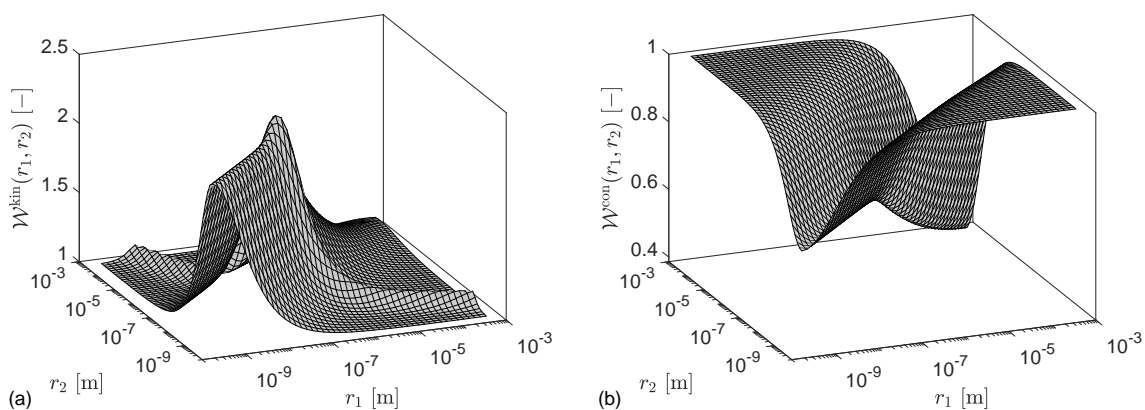


Figure A.2 Enhancement factors for the coagulation of two $\text{Al}_2\text{O}_3(\text{l})$ droplets in the kinetic (a) and continuum regime (b) at $T = 3045\text{ K}$ for $A_H = 165 \times 10^{-21}\text{ J}$.

A.3 Overview of physical assumptions

As a guide for potential model extensions and kinetic amendments, the following list contains the key physical assumptions inherent in the kinetic framework (Figs. 2.4 and 2.2) we presented:

1. The dispersed oxide droplets exchange heat instantaneously with the ambient gas such that both phases possess a common temperature.
2. The heat flux from the reactive surface into the bulk $\text{Al}(\text{B})/\text{Al}_2\text{O}_3(\text{B})$ phase vanishes. (This point only applies to the spatially homogeneous reactors considered in Chapters 2 and 3.)
3. The nucleation of $\text{Al}_2\text{O}_3(\text{l})$ droplets from a supersaturated $\text{Al}_2\text{O}_3/\text{c}$ vapour proceeds through $(\text{Al}_2\text{O}_3/\text{c})_n$ cluster formation and is commensurate with the capillarity assumptions (CNT).
4. The $\text{Al}_2\text{O}_3(\text{l})$ droplets do not emit thermal radiation outside the wavelength range $[\lambda_{w,\text{min}}, \lambda_{w,\text{max}}]$.
5. None of the gaseous species radiate thermally.
6. The gas-droplet dispersion is optically thin.
7. The Hamaker constant A_H of solid Al_2O_3 in air remains valid also in the melt, *i.e.*, for $\text{Al}_2\text{O}_3(\text{l})$.

A Droplet formation kinetics

8. The site density of a liquid aluminum surface coincides with the one of its crystalline counterpart Al(1 1 1).

Appendix B

Monte Carlo method for a PaSR featuring a reactive surface

The stochastic solution method we apply to solve the *pdf* equation in Eq. (3.6) is based on a semi-discrete representation of $f_{\Phi, \Psi, \mathbf{H}}(\phi, \psi, \mathbf{h}; t)$ in terms of an ensemble of n_f realizations $\mathbf{Z}^{(i)}$, $i = 1, \dots, n_f$, with

$$\mathbf{Z}^{(i)}(t) = \begin{pmatrix} \Phi^{(i)}(t) \\ \Psi^{(i)}(t) \\ \mathbf{H}^{(i)}(t) \end{pmatrix} \quad (\text{B.1})$$

such that

$$f_{\Phi, \Psi, \mathbf{H}}(\phi, \psi, \mathbf{h}; t) = \frac{1}{n_f} \sum_{i=1}^{n_f} \delta(\phi - \Phi^{(i)}(t)) \delta(\psi - \Psi^{(i)}(t)) \delta(\mathbf{h} - \mathbf{H}^{(i)}(t)). \quad (\text{B.2})$$

The realizations are indicated by a parenthesized superscript index and are often termed stochastic particles because the dynamical equations they obey are reminiscent of Lagrangian equations of motion of physical particles. Based on Eq. (B.2), expectations with respect to $f_{\Phi, \Psi, \mathbf{H}}$ may be estimated in terms of the ensemble $\{\mathbf{Z}^{(i)}(t)\}_{i=1}^{n_f}$. For example, considering the general observable $Q(\phi, \psi, \mathbf{h})$, the expectation $\langle Q(\Phi(t), \Psi(t), \mathbf{H}(t)) \rangle$ is obtained as

$$\langle Q(\Phi(t), \Psi(t), \mathbf{H}(t)) \rangle = \frac{1}{n_f} \sum_{i=1}^{n_f} Q(\Phi^{(i)}(t), \Psi^{(i)}(t), \mathbf{H}^{(i)}(t)). \quad (\text{B.3})$$

The dynamical system governing the trajectory of any single realization $\mathbf{Z} = \mathbf{Z}^{(i)}$ is determined in such a way that the *pdf* $f_{\mathbf{Z}}(\mathbf{z}; t)$ associated with $\mathbf{Z}(t)$ evolves according to

Eq. (3.6). Incorporating a fractional time stepping, the algorithm we invoke to solve this dynamical system and advance $\{\mathbf{Z}^{(i)}(t)\}_{i=1}^{n_f}$ over a time step Δt_n is an extension of the scheme by Chen [32]; the main steps are summarized in Fig. B.1.

Input: $\{\mathbf{Z}^{(i)}\}_{i=1}^{n_f}$ and γ at time t_n , Δt_n , Φ^{in} , \mathbf{H}^{in}

1. Inflow/outflow step:
 - 1.1 Define $n_{\text{out}} = \lfloor r_{\text{out}} \rfloor$ with $r_{\text{out}} = n_f \min(\Delta t_n / \tau_{\text{res}}, 1)$. Generate a uniformly distributed random variable $\xi_{\text{out}} \in [0, 1]$. If $\xi_{\text{out}} \leq r_{\text{out}} - n_{\text{out}}$, then increment n_{out} by one
 - 1.2 Select n_{out} distinct samples from the ensemble $\{\mathbf{Z}^{(i)}\}_{i=1}^{n_f}$ and replace their gas and droplet phase scalars $\Phi^{(i)}$ and $\mathbf{H}^{(i)}$ by Φ^{in} and \mathbf{H}^{in} , respectively, leaving $\Psi^{(i)}$ unchanged
 - 1.3 Evaluate the mean dispersion density $\langle \rho \rangle$ using Eqs. (3.8) and (B.3). Subsequently, solve Eq. (3.7) with $\langle \dot{s}_k \rangle = 0$ for $k \in \mathcal{G}$ to update the surface density γ
2. Advective mixing:
 - 2.1 Define $n_{\text{adv}} = \lfloor r_{\text{adv}} \rfloor$ with $r_{\text{adv}} = n_f \min(\Delta t_n / \tau_{\text{adv}}, 1)$. Generate a uniformly distributed random variable $\xi_{\text{adv}} \in [0, 1]$ and increment n_{adv} by one if $\xi_{\text{adv}} \leq r_{\text{adv}} - n_{\text{adv}}$
 - 2.2 Select n_{adv} distinct samples from the ensemble $\{\mathbf{Z}^{(i)}\}_{i=1}^{n_f}$ and replace their surface compositions $\Psi^{(i)}$ by the surface compositions of n_{adv} randomly chosen samples (selection with replacement)
3. Combined reaction/PBE step:
 - 3.1 For every sample $\mathbf{Z}^{(i)}$, solve Eqs. (2.15), (2.16) and (2.26) over the time step Δt_n , possibly invoking a nested fractional steps decomposition (Section 2.5)
 - 3.2 Evaluate $\langle \rho \rangle$ using Eqs. (3.8) and (B.3) and compute $\langle \dot{s}_k \rangle$ for $k \in \mathcal{G}$. Update the surface density γ by advancing Eq. (3.7) in time
4. IEM-micro-mixing step:
 - 4.1 Compute the mean gas composition $\langle \Phi \rangle$ and the mean droplet phase scalars $\langle \mathbf{H} \rangle$ from Eq. (B.3)
 - 4.2 Define $\alpha_{\text{mix}} = \exp(-C_{\text{mix}} \Delta t_n / (2\tau_{\text{mix}}))$ and, for every sample $\mathbf{Z}^{(i)}$, replace the gas phase scalars $\Phi^{(i)}$ by $\alpha_{\text{mix}}(\Phi^{(i)} - \langle \Phi \rangle) + \langle \Phi \rangle$. Similarly, replace the droplet phase scalars $\mathbf{H}^{(i)}$ by $\alpha_{\text{mix}}(\mathbf{H}^{(i)} - \langle \mathbf{H} \rangle) + \langle \mathbf{H} \rangle$
 - 4.3 Evaluate $\langle \rho \rangle$ using Eqs. (3.8) and (B.3) and update the surface density γ by solving Eq. (3.7) with $\langle \dot{s}_k \rangle = 0$ for $k \in \mathcal{G}$

Output: $\{\mathbf{Z}^{(i)}\}_{i=1}^{n_f}$ and γ at time $t = t_n + \Delta t_n$

Figure B.1 Algorithmic steps for solving the evolution equations describing a PaSR with a reactive surface (Eqs. (3.6) and (3.7)) using a stochastic particle method. Here, the pdf $f_{\Phi, \Psi, \mathbf{H}}(\phi, \psi, \mathbf{h}; t) = f_{\mathbf{Z}}(\mathbf{z}; t)$ is discretely represented in terms of an ensemble of realizations $\mathbf{Z}^{(i)}(t)$, $i = 1, \dots, n_f$ (Eqs. (B.1) and (B.2)). Note that the operator $\lfloor \cdot \rfloor$ returns the largest integer that is smaller than or equal to the input number.

Appendix C

Derivation of the dispersion balance laws

A particular feature of our physical description of the gas-droplet dispersion is that both phases instantaneously exchange momentum and heat in such a way that a common temperature T and bulk velocity \mathbf{u} are maintained. In order to formally account for this equilibration in terms of temperature and velocity, we invoked in Section 4.3.3 combined-phase balance laws that encompass the transport and localized changes of the mass, momentum and enthalpy carried by both phases. Here, the physical rationales and assumptions underlying these balance laws are summarized.

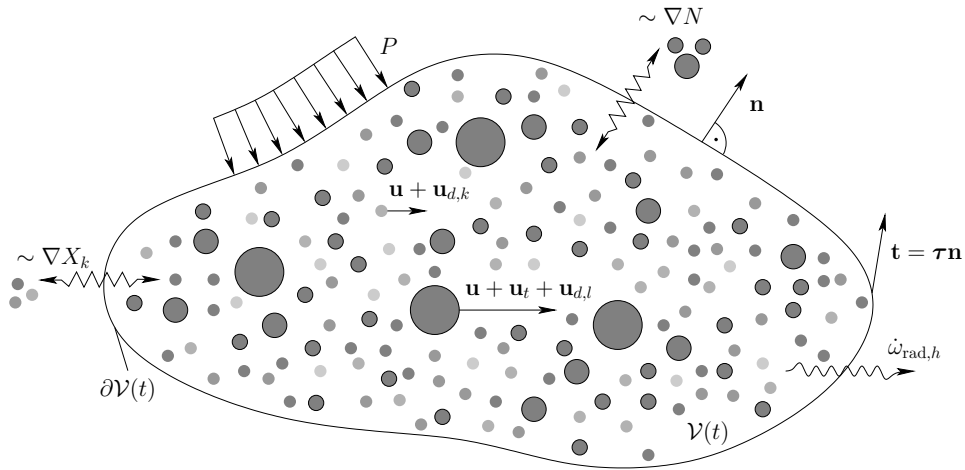


Figure C.1 Schematic illustration of a material volume $\mathcal{V}(t) \subseteq \Omega_{\mathbf{x}}$ of the gas-droplet dispersion.

Figure C.1 illustrates a material volume $\mathcal{V}(t) \subseteq \Omega_{\mathbf{x}}$ which is occupied by the gas-droplet dispersion and whose contained mass $M(t)$, linear momentum $\mathbf{L}(t)$ and enthalpy $H(t)$ may change in time. These changes are brought about by the action of external forces communicated through mechanical traction as well as radiative and conductive heat losses. Due to thermophoretic and diffusive transport, the droplets' velocities differ, in general,

from the bulk gas velocity $\mathbf{u}(\mathbf{x}, t)$ at a location \mathbf{x} in physical space $\Omega_{\mathbf{x}}$ and time t .

C.1 Mass

By construction, the mass $M(t)$ inside *any* material volume $\mathcal{V}(t)$ of the gas-droplet dispersion remains unchanged in time,

$$\frac{dM(t)}{dt} = \frac{d}{dt} \int_{\mathcal{V}(t)} \rho(\mathbf{x}, t) d\mathbf{x} = 0 \quad \forall \mathcal{V}(t). \quad (\text{C.1})$$

In view of the Reynolds transport theorem, mass may only accumulate inside a fixed control volume that momentarily coincides with $\mathcal{V}(t)$ if species or droplet mass fluxes cross the control volume's surface $\partial\mathcal{V}(t)$,

$$\begin{aligned} \frac{d}{dt} \int_{\mathcal{V}(t)} \rho d\mathbf{x} &= \int_{\mathcal{V}(t)} \frac{\partial \rho}{\partial t} d\mathbf{x} \\ &+ \int_{\partial\mathcal{V}(t)} \left(\sum_{k \in \mathcal{G}} \rho_k \varepsilon_g \mathbf{u}_k + \rho_l \int_{\Omega_v} v N(v) \mathbf{u}_l(v) dv \right) \cdot \mathbf{n} d\mathbf{x} \quad \forall \mathcal{V}(t), \end{aligned} \quad (\text{C.2})$$

where $\mathbf{n}(\mathbf{x}, t)$ represents the outward pointing unit surface normal on $\partial\mathcal{V}(t)$. Upon substitution of Eqs. (4.7) and (4.10), the mass flow rate of the gas per unit of surface area reduces to

$$\sum_{k \in \mathcal{G}} \rho_k \varepsilon_g \mathbf{u}_k = \sum_{k \in \mathcal{G}} \rho_g \varepsilon_g Y_k \left(\mathbf{u} + \mathbf{u}^c - \mathcal{D}_k \frac{\nabla X_k}{X_k} \right) = \rho_g \varepsilon_g \mathbf{u}. \quad (\text{C.3})$$

Similarly, by Eqs. (4.13) and (4.25), the droplet mass flux reads

$$\rho_l \int_{\Omega_v} v N(v) \mathbf{u}_l(v) dv = \rho_l \varepsilon_l \left(\mathbf{u} + \mathbf{u}_t + \mathbf{u}_{d,l}^{\varepsilon_l} \right). \quad (\text{C.4})$$

The right hand side of Eq. (C.4) indicates that both droplet thermophoresis and diffusion induce net transport on part of the dispersed phase, causing the droplets' velocity to deviate from the bulk velocity \mathbf{u} . By introducing Eqs. (C.3) and (C.4) into Eq. (C.2) and applying the divergence and localization theorems, we obtain Eq. (4.28).

C.2 Momentum

Following along a similar rationale as in Section C.1, the change of momentum inside a material volume $\mathcal{V}(t) \subseteq \Omega_{\mathbf{x}}$ is given by

$$\begin{aligned}
\frac{d\mathbf{L}(t)}{dt} &= \frac{d}{dt} \int_{\mathcal{V}(t)} \left(\rho_g \varepsilon_g \mathbf{u} + \int_{\Omega_v} \rho_l v N(v) \mathbf{u}_l(v) dv \right) d\mathbf{x} \\
&= \int_{\mathcal{V}(t)} \frac{\partial}{\partial t} \left(\rho_g \varepsilon_g \mathbf{u} + \int_{\Omega_v} \rho_l v N(v) \mathbf{u}_l(v) dv \right) d\mathbf{x} \\
&\quad + \int_{\partial\mathcal{V}(t)} \left(\sum_{k \in \mathcal{G}} \rho_k \varepsilon_g \mathbf{u}_k \otimes \mathbf{u}_k \right) \cdot \mathbf{n} d\mathbf{x} \\
&\quad + \int_{\partial\mathcal{V}(t)} \left(\int_{\Omega_v} \rho_l v N(v) \mathbf{u}_l(v) \otimes \mathbf{u}_l(v) dv \right) \cdot \mathbf{n} d\mathbf{x} \quad \forall \mathcal{V}(t).
\end{aligned} \tag{C.5}$$

The parenthesized terms inside the first integral on the right hand side of Eq. (C.5) correspond to the momentum carried by the gas-droplet dispersion per unit of volume and may be reformulated, on substitution of Eq. (4.13), as

$$\rho_g \varepsilon_g \mathbf{u} + \int_{\Omega_v} \rho_l v N(v) \mathbf{u}_l(v) dv = \rho \mathbf{u} + \rho_l \varepsilon_l \left(\mathbf{u}_t + \mathbf{u}_{d,l}^{\varepsilon_l} \right). \tag{C.6}$$

With the aid of Eq. (4.7), moreover, the dyadic product of the species velocities in the second term on the right hand side of Eq. (C.5) can be expanded as

$$\begin{aligned}
\sum_{k \in \mathcal{G}} \rho_k \varepsilon_g (\mathbf{u}_k \otimes \mathbf{u}_k) &= \rho_g \varepsilon_g \left(\mathbf{u} \otimes \mathbf{u} - \mathbf{u}_c \otimes \mathbf{u}_c \right. \\
&\quad \left. + \sum_{k \in \mathcal{G}} \mathcal{D}_k \frac{W_k}{W} \nabla X_k \otimes \mathcal{D}_k \frac{\nabla X_k}{X_k} \right).
\end{aligned} \tag{C.7}$$

Similarly, we obtain from Eq. (4.13) for the dyadic product in the final term of Eq. (C.5)

$$\begin{aligned}
\int_{\Omega_v} \rho_l v N(v) \mathbf{u}_l(v) \otimes \mathbf{u}_l(v) dv &= \rho_l \varepsilon_l (\mathbf{u} \otimes \mathbf{u}) + \rho_l \varepsilon_l \left(\mathbf{u} \otimes \left(\mathbf{u}_t + \mathbf{u}_{d,l}^{\varepsilon_l} \right) \right) \\
&\quad + \int_{\Omega_v} \rho_l v N(v) (\mathbf{u}_t + \mathbf{u}_{d,l}(v)) \otimes \mathbf{u}_l(v) dv.
\end{aligned} \tag{C.8}$$

Physically, the change in momentum in Eq. (C.5) is caused by the forces exerted by the ambience on the material surface $\partial\mathcal{V}(t)$ through the mechanical pressure P and the Cauchy

C Derivation of the dispersion balance laws

traction $\mathbf{t}(\mathbf{x}, t) = \boldsymbol{\tau} \mathbf{n}$,

$$\frac{d\mathbf{L}}{dt} = \int_{\partial\mathcal{V}(t)} (-P\mathbf{I} + \boldsymbol{\tau}) \cdot \mathbf{n} \, d\mathbf{x} \quad \forall \mathcal{V}(t), \quad (\text{C.9})$$

where $\boldsymbol{\tau}(\mathbf{x}, t) = \mu (\nabla \mathbf{u} + (\nabla \mathbf{u})^T)$ is the viscous stress tensor. Following common practice, the isotropic part of the stress tensor, $2\mu \nabla \cdot \mathbf{u}/3$, was absorbed into the mechanical pressure P . In evaluating the viscous stresses, the presence of the droplets is accounted for through the viscosity of the dispersion (Eq. (4.17)), but we neglect any additional velocity gradients induced by thermophoretic or diffusive droplet transport. By equating Eqs. (C.5) and (C.9), introducing Eqs. (C.6) to (C.8) and applying the divergence and localization theorems, we obtain after substitution of Eq. (4.28) the following local balance equation for the dispersion's momentum

$$\begin{aligned} & \rho \frac{\partial \mathbf{u}}{\partial t} + \left((\rho \mathbf{u} + \rho_l \varepsilon_l (\mathbf{u}_t + \mathbf{u}_{d,l}^{\varepsilon_l})) \cdot \nabla \right) \mathbf{u} \\ & + \nabla \cdot \left(\rho_g \varepsilon_g \left(\sum_{k \in \mathcal{G}} \mathcal{D}_k \frac{W_k}{W} \nabla X_k \otimes \mathcal{D}_k \frac{\nabla X_k}{X_k} - \mathbf{u}_c \otimes \mathbf{u}_c \right) \right) \\ & + \frac{\partial}{\partial t} (\rho_l \varepsilon_l (\mathbf{u}_t + \mathbf{u}_{d,l}^{\varepsilon_l})) + \nabla \cdot \left(\int_{\Omega_v} \rho_l v N(v) (\mathbf{u}_t + \mathbf{u}_{d,l}(v)) \otimes \mathbf{u}_l(v) \, dv \right) \\ & = -\nabla P + \nabla \cdot (\mu (\nabla \mathbf{u} + (\nabla \mathbf{u})^T)). \end{aligned} \quad (\text{C.10})$$

In order for the standard form of the Navier–Stokes equations to be recovered in the limit $\varepsilon_l = 0$, we assume the dyadic products in the third term on the left hand side of Eq. (C.10) to cancel. This is tantamount to the assumption that the gas momentum is advected by the bulk velocity field \mathbf{u} . In fact, the appearance of the species diffusion velocities and the correction velocity in Eq. (C.7) shows that, while the correction velocity eliminates any net mass transport due to Hirschfelder–Curtiss diffusion, it may cause a net momentum transport. The fourth and fifth terms on the left hand side of Eq. (C.10) represent the inertia associated with changes in the droplets' thermophoretic and diffusional momentum. Since we assume that \mathbf{u}_t and $\mathbf{u}_{d,l}^{\varepsilon_l}$ are related algebraically to \mathbf{Y} , T and $N(\cdot)$ without intervening dynamics or inertia, these terms are omitted here. Keeping only the leading two terms on the left hand side of Eq. (C.10), we ultimately arrive at the balance law in Eq. (4.29).

C.3 Enthalpy

If the viscous heating contribution $\boldsymbol{\tau} : \nabla \mathbf{u}$ is negligible compared to the sensible enthalpy released by chemical reactions, then the enthalpy $H(t)$ inside the material volume $\mathcal{V}(t) \subseteq \Omega_{\mathbf{x}}$ of Fig. C.1 changes in time according to

$$\begin{aligned}
\frac{dH(t)}{dt} &= \int_{\mathcal{V}(t)} \dot{\omega}_{\text{rad},h} - \nabla \cdot \mathbf{q} \, d\mathbf{x}, \\
&= \int_{\mathcal{V}(t)} \frac{\partial \rho h}{\partial t} \, d\mathbf{x} + \int_{\partial \mathcal{V}(t)} \left(\sum_{k \in \mathcal{G}} \rho_k h_k \varepsilon_g \mathbf{u}_k \right) \cdot \mathbf{n} \, d\mathbf{x} \\
&\quad + \int_{\partial \mathcal{V}(t)} \left(\rho_l h_l \int_{\Omega_v} v N(v) \mathbf{u}_l(v) \, dv + \sigma_l \sqrt[3]{36\pi} \int_{\Omega_v} v^{2/3} N(v) \mathbf{u}_l(v) \, dv \right) \cdot \mathbf{n} \, d\mathbf{x} \\
&= - \int_{\partial \mathcal{V}(t)} \mathbf{q} \cdot \mathbf{n} \, d\mathbf{x} + \int_{\mathcal{V}(t)} \dot{\omega}_{\text{rad},h} \, d\mathbf{x} \quad \forall \mathcal{V}(t)
\end{aligned} \tag{C.11}$$

where $\mathbf{q}(\mathbf{x}, t) = -\lambda \nabla T$ is the conductive heat flux. Note that the right hand side of Eq. (C.11) does not contain the time derivative of the thermodynamic pressure because a constant pressure system is considered. Upon substitution of Eqs. (4.7), (4.13), (4.25) and (4.26) into Eq. (C.11), we obtain, after application of the divergence theorem and upon localization, Eq. (4.31) for the dispersion enthalpy.

Appendix D

Newton method for solving the triple point angle equation

Since the residual in Eq. (5.8) is periodic in α (Fig. D.1) and features sharp gradients, the Newton scheme is rendered unstable unless the triple point angle is restricted to $\alpha \in [-\pi/2, \pi/2]$ by replacing its value after each iteration according to

$$\alpha \leftarrow \alpha - 2\pi \left\lfloor \frac{\alpha}{2\pi} + \frac{1}{2} \right\rfloor. \quad (\text{D.1})$$

In this way, the convergence radius of the scheme was proven to be enhanced significantly, permitting to choose the initial guesses for α from a much broader range.

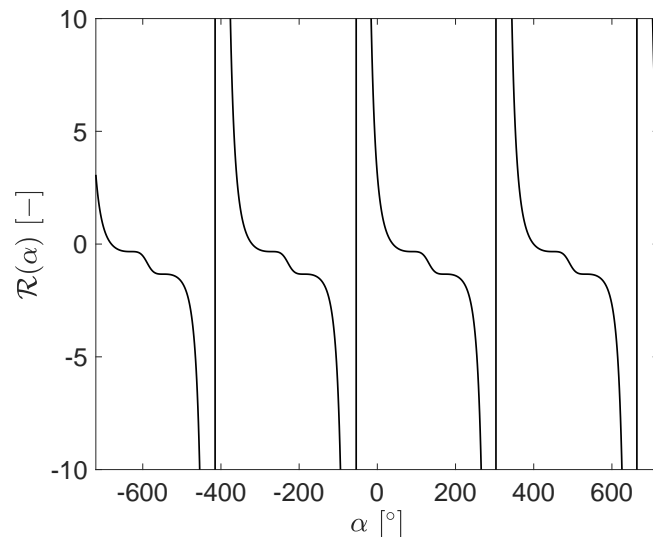


Figure D.1 Residual of the non-linear equation governing the triple point angle α (Eq. (5.8)).

In order to solve the non-linear Eq. (5.8) for the triple point angle α using a Newton

D Newton method for solving the triple point angle equation

method, the computation of the Jacobian $d\mathcal{R}(\alpha)/d\alpha$ is required. Here, we chose to use the analytical derivative given by

$$\begin{aligned}
\mathcal{K}(\alpha) &= \frac{d\mathcal{R}(\alpha)}{d\alpha} \\
&= \left(\left(-3 \cos^2 \alpha \sin \alpha (1 - \sin(\alpha - \varphi_{12}))^2 (2 + \sin(\alpha - \varphi_{12})) \right. \right. \\
&\quad - 2 \cos^3 \alpha (1 - \sin(\alpha - \varphi_{12})) \cos(\alpha - \varphi_{12}) (2 + \sin(\alpha - \varphi_{12})) \\
&\quad \left. \left. + \cos^3 \alpha (1 - \sin(\alpha - \varphi_{12}))^2 \cos(\alpha - \varphi_{12}) \right) \cos^{-3}(\alpha - \varphi_{12}) \right. \\
&\quad + 3 \cos^3 \alpha (1 - \sin(\alpha - \varphi_{12}))^2 (2 + \sin(\alpha - \varphi_{12})) \sin(\alpha - \varphi_{12}) \cos^{-4}(\alpha - \varphi_{12}) \\
&\quad + \left(-3 \cos^2 \alpha \sin \alpha (2 + \sin(\varphi_1 - \alpha)) (1 - \sin(\varphi_1 - \alpha))^2 \right. \\
&\quad \quad - \cos^3 \alpha \cos(\varphi_1 - \alpha) (1 - \sin(\varphi_1 - \alpha))^2 \\
&\quad \quad \left. + 2 \cos^3 \alpha (2 + \sin(\varphi_1 - \alpha)) (1 - \sin(\varphi_1 - \alpha)) \cos(\varphi_1 - \alpha) \right) \cos^{-3}(\varphi_1 - \alpha) \\
&\quad - 3 \cos^3 \alpha (2 + \sin(\varphi_1 - \alpha)) (1 - \sin(\varphi_1 - \alpha))^2 \sin(\varphi_1 - \alpha) \cos^{-4}(\varphi_1 - \alpha) \left. \right) \\
&\quad \times \left((1 + \sin \alpha)^2 (2 - \sin \alpha) \right. \\
&\quad \quad \left. - \cos^3 \alpha (2 + \sin(\varphi_1 - \alpha)) (1 - \sin(\varphi_1 - \alpha))^2 \cos^{-3}(\varphi_1 - \alpha) \right)^{-1} \\
&\quad - \left(2 (1 + \sin \alpha) \cos \alpha (2 - \sin \alpha) - (1 + \sin \alpha)^2 \cos \alpha \right. \\
&\quad \quad - \left(-3 \cos^2 \alpha \sin \alpha (2 + \sin(\varphi_1 - \alpha)) (1 - \sin(\varphi_1 - \alpha))^2 \right. \\
&\quad \quad \quad - \cos^3 \alpha \cos(\varphi_1 - \alpha) (1 - \sin(\varphi_1 - \alpha))^2 \\
&\quad \quad \quad \left. \left. + 2 \cos^3 \alpha (2 + \sin(\varphi_1 - \alpha)) (1 - \sin(\varphi_1 - \alpha)) \cos(\varphi_1 - \alpha) \right) \cos^{-3}(\varphi_1 - \alpha) \right. \\
&\quad \quad \left. \left. + 3 \cos^3 \alpha (2 + \sin(\varphi_1 - \alpha)) (1 - \sin(\varphi_1 - \alpha))^2 \sin(\varphi_1 - \alpha) \cos^{-4}(\varphi_1 - \alpha) \right) \right) \\
&\quad \times \left(\cos^3 \alpha (1 - \sin(\alpha - \varphi_{12}))^2 (2 + \sin(\alpha - \varphi_{12})) \cos^{-3}(\alpha - \varphi_{12}) \right. \\
&\quad \quad \left. + \cos^3 \alpha (2 + \sin(\varphi_1 - \alpha)) (1 - \sin(\varphi_1 - \alpha))^2 \cos^{-3}(\varphi_1 - \alpha) \right) \\
&\quad \times \left((1 + \sin \alpha)^2 (2 - \sin \alpha) \right. \\
&\quad \quad \left. - \cos^3 \alpha (2 + \sin(\varphi_1 - \alpha)) (1 - \sin(\varphi_1 - \alpha))^2 \cos^{-3}(\varphi_1 - \alpha) \right)^{-2}.
\end{aligned} \tag{D.2}$$